The star formation history of early-type galaxies in the fornax cluster

Kuntschner, Harald

The Star Formation History of Early-Type Galaxies in the Fornax Cluster

by
Harald Kuntschner

A thesis submitted to the University of Durham
in accordance with the regulations for
admittance to the Degree of Doctor of Philosophy.

Department of Physics
University of Durham
October 1998

"Astronomy compels the soul to look upwards and leads us from this world to another."

Plato (The Republic)

Abstract

We have measured central line strengths and line-strength gradients for a complete sample of early-type galaxies in the Fornax cluster, comprising 11 elliptical and 11 lenticular galaxies, more luminous than $M_B = -17$. We find that the centres of Fornax ellipticals follow the locus of galaxies of fixed age in Worthey's models and have metallicities varying roughly from half solar to 2.5 times solar. Line-strength gradients indicate that elliptical galaxies do not show age gradients with radius but do exhibit a decrease of ~ 0.4 dex in [Fe/H] between the centre and one effective radius. The centres of lenticular galaxies however exhibit a substantial spread to younger luminosity weighted ages indicating a more extended star formation history. Metallicity gradients are generally shallower than for ellipticals. Five of the faint S0s have experienced a central starburst on top of an underlying older stellar population.

Our conclusions are based on several age/metallicity diagnostic diagrams in the Lick/IDS system comprising established indices such as [MgFe] and Hβ as well as new and more sensitive indices such as C4668, Fe3 and Hγ_A. The inferred difference in the age distribution between lenticular and elliptical galaxies is a robust conclusion as the models generate consistent relative ages using different age and metallicity indicators even though the absolute ages remain uncertain. The absolute age uncertainty is caused by the effects of non-solar abundance ratios which are not accounted for in the stellar population models. We find that Es are generally overabundant in magnesium where the most luminous galaxies show stronger overabundances. The luminosity weighted stellar populations of young S0s are consistent with solar abundance ratios, however the bulges of the two large S0s in our sample have [Mg/Fe] > 0.

We have analysed in detail the sources of scatter in the Mg–σ_0 relation by investigating the effects of age, metallicity and [Mg/Fe] variations. We find that young stellar populations are responsible for most of the scatter towards weak Mg-absorption. However, for the roughly coeval ellipticals the scatter at a given σ_0 is correlated with [Mg/Fe] variations; metallicity and age effects seem to be less important.

The young luminosity weighted ages of the faint S0s in the Fornax cluster are consistent with the recent discovery that the fraction of S0 galaxies in intermediate redshift clusters is a factor of 2-3 lower than found locally, and suggests that a fraction of the cluster spiral galaxy population has evolved into these faint S0s in the 5 Gyrs interval from $z = 0.5$ to the present. One of the proposed transformation mechanisms is the galaxy harassment picture. The properties of young S0s with large bulge to disk ratios in our sample are remarkably similar to the proposed end-products of galaxy harassment. However, we note that there are young disky S0s which are unlikely to be the result of harassment. Two of the faintest lenticular galaxies in our sample have blue continua and extremely strong Balmer-line absorption suggesting starbursts < 2 Gyrs ago.

Preface

The work described in this thesis was undertaken between Oct 1995 and Oct 1998 whilst the author was a research student under the supervision of Prof. Roger L. Davies in the Department of Physics at the University of Durham. This work has not been submitted for any other degree at the University of Durham or at any other University.

The majority of the work contained in this thesis is the authors own. The measurements of central velocity dispersions presented in Section 3.5.3 were obtained using the FCQ program and MIDAS routines written by Ralf Bender and Roberto Saglia. The line-strength measurement program which is used throughout this thesis is based on a code written by Glenn Baggley.

A number of results presented here have appeared in the following papers:

- Harald Kuntschner and Roger L. Davies, *The ages and metallicities of early-type galaxies in the Fornax cluster*, 1998, *MNRAS*, **295**, 29L
- Harald Kuntschner, Roger L. Davies and Ralf Bender, *Line-strength indices and kinematics in Fornax*, in "Galaxy Scaling Relations: Origins, Evolution and Applications", page 363, 1997, editors: L N da Costa and A Renzini, ESO Astrophysics Symposia, Springer Verlag (Berlin)

Acknowledgements

First of all I would like to thank my supervisor, Roger Davies, for his continuous encouragement and invaluable guidance over the last three years. However, I'm also indebted to him for giving me enough freedom and support to develop my own ideas. I should also thank Richard Bower, John Lucey, Reynier Peletier, Ray Sharples, Ian Smail and many others for useful discussions on various astronomical topics. Perhaps even more important to the completion of my thesis was the never ending support of Alan Lotts, the Durham computer system manager.

I would also like to express my thanks to Ralf Bender who not only provided me with software and the data obtained at the ESO NTT, but also encouraged me in the first place to come to Durham.

On the financial side I am grateful to the Dr. Carl Duisberg Stiftung and the German government for generous support during my first year in Durham. For the last two years, my living was supported by the Department of Physics and a University of Durham Research Studentship.

Arriving in Durham on one of those typical dark, rainy evenings in September 1995 did not seem to me as a good sign for the future. However, thanks to my office mates Claire, Eric, Fiona, Katherine and Scott, I was wrong. My time in Durham was and in fact is a wonderful tour through British customs such as having crisps during the morning break, drinking horrible tea and complaining about the weather. After three years I'm an expert in the latter. Special thanks go to Katherine who taught me the more colloquial aspects of the English language. I also want to thank Claire, Eric and Fiona for reading the drafts of this thesis and converting my German-English into something more useful.

I also have to thank my friends who took great care to rescue me from the world of astronomy from time to time, thanks to Anthony, Belma, Nathalie, and Thani. Special thanks must go to Claudia. Without her immense patience, support, and encouragement I wouldn't have been able to complete this thesis.

Finally, I must thank my parents for their unconditional support and deep trust in me over so many years.

Contents

Abstract ii

Preface iii

Acknowledgements iv

Contents v

List of Figures viii

List of Tables xiii

1 Introduction 1

1.1 The Properties of Elliptical & S0 Galaxies 2

1.1.1 Morphology and Kinematics 2

1.1.2 The Stellar Populations of Early-Type Galaxies 4

1.1.3 Global Scaling relations 7

1.1.4 Galaxy Formation and Evolution Scenarios 8

1.1.5 Summary 10

1.2 The Fornax Cluster and Sample Selection 11

1.3 Aim and Outline of this Thesis 17

2 Long-Slit Spectroscopy 18

2.1 Introduction 18

2.2 Instrument Description 18
2.3 Basic Data Reduction 19
2.3.1 Overscan and Trim 21
2.3.2 Bias Correction 21
2.3.3 Dark Current 21
2.3.4 Bad Columns 22
2.3.5 Flat Fielding 22
2.3.6 Cosmic Rays 23
2.3.7 Wavelength Calibration and Distortion Correction 23
2.3.8 Sky Subtraction 24
2.4 Further Data Reduction 25
2.4.1 Extracting 1d Stellar Spectra 25
2.4.2 Extracting Central Galaxy Spectra 26
2.4.3 Extracting 1d Spectra for Line-Strength Gradients 26
2.4.4 Lick/IDS Resolution Correction 27
2.5 Summary of Observations 30

3 Line-Strength Measurements **35**

3.1 Introduction: The Lick/IDS Library 35
3.2 Definition of Lick/IDS Indices 36
3.3 Measuring Line-Strength Indices 41
3.3.1 The `ls1d` Program 41
3.3.2 Poisson Error Estimation 41
3.4 Transformation to the Lick/IDS System 41
3.5 Velocity Dispersion Measurements and Corrections 48
3.5.1 The Fourier Cross Correlation Method – `fxcor` task 50
3.5.2 The FCQ Setup 52
3.5.3 Central Velocity Dispersions 53

3.5.4 Velocity Dispersion Correction 59
3.6 Final Central Absorption Line-Strength 60

4 Nuclear Stellar Populations **65**
4.1 Introduction 65
4.2 Worthey (1994) Models 66
4.3 Nuclear Age and Metallicity Estimates 68
4.3.1 The Hβ *vs* [MgFe] Diagram 68
4.3.2 New Indices: $C_2$4668 & Hγ_A 73
4.3.3 Two Post-Starburst or Starburst Galaxies 77
4.3.4 Emission in Early-Type Galaxies 78
4.4 The Effects of Varying Metal Abundance Ratios 84
4.4.1 The Mg-Overabundance 85
4.4.2 Are Other Elements Overabundant? 95
4.4.3 Absolute Age and Metallicity Estimates 98
4.5 Conclusions from Central Line-Strength Analysis 103

5 Nuclear Stellar Populations and Central Velocity Dispersions **107**
5.1 Introduction 107
5.2 Mg–σ_0 Relation in the Fornax Cluster 108
5.3 Other Indices *vs* σ_0 112
5.4 What Causes the Spread in the Mg–σ_0 Relation? 124
5.5 Conclusions from Index–σ_0 Relations 130

6 Velocity Dispersion Profiles & Rotation Curves **132**
6.1 Introduction 132
6.2 Literature Comparison 132
6.3 Results 134

7 Line Strength Gradients in Early-Type Galaxies **141**

7.1 Introduction 141
7.2 Establishing the Lick/IDS offset for NTT Data 142
7.3 Extracting Line-Strength Gradients 143
7.4 Literature and Run-to-Run Comparison 148
7.5 Results 153
7.5.1 Index-Gradients 153
7.5.2 Age and Metallicity Gradients 162
7.5.3 The S0 Galaxy NGC1381: When and How was the Disk Formed? . . 172
7.6 Conclusions from Line-Strength Gradients 180

8 Conclusions **182**
8.1 Elliptical Galaxies 182
8.2 S0-Type Galaxies 183
8.3 Discussion and General Conclusions 184
8.4 Future Work 186

Bibliography **187**

A Final Line-Strength Measurements for Stars **196**

B Line-Strength Gradients **198**

List of Figures

1.1 The Hubble Diagram 1

1.2 DSS Image of the Central Area of the Fornax Cluster 12

1.3 Finding Chart for the Fornax Sample 14

1.4 Luminosity and Redshift Distribution of the Fornax Sample 16

2.1 Spatial Cut Through Standard Star Frame 24

2.2 Fit to the Galaxy Centre of NGC1351 27

2.3 Focus Variations in NGC1351 28

2.4 Calibrated Spectrum of NGC1339 30

3.1 Definition of Lick/IDS Indices 37

3.2 Position of Lick/IDS Indices 40

3.3 Lick/IDS Offset : AAT96 44

3.4 Lick/IDS Offset: AAT96, Linear Comparison 46

3.5 Index *vs* Index Comparisons for Fe-Indices 47

3.6 Index *vs* Index Comparison for Mg-Indices 48

3.7 Index *vs* Index Comparison for Balmer Indices 49

3.8 Velocity Dispersion Calibration Curve for `fxcor` 52

3.9 Velocity Dispersion Comparison with Smith (1998) 55

3.10 Velocity Dispersion Comparison with McElroy (1995) 56

3.11 Velocity Dispersion Comparison with D'Onofrio et al. (1995) 57

3.12 Velocity Dispersion Comparison with Graham et al. (1998) 58

3.13 Velocity Dispersion Corrections 61

4.1 Hβ *vs* [MgFe] Diagram for González's Galaxies 70

4.2 Hβ *vs* [MgFe] Diagram 71

4.3 Hγ_A *vs* $C_2$4668 Diagram 74

4.4 G4300 *vs* $C_2$4668 Diagram 76

4.5 Spectra of ESO358-G25, ESO359-G02 and NGC1336 77

4.6 Residual Emission Spectra 81

4.7 [OIII]λ5007 Emission 82

4.8 Effects of the Mg-Overabundance 86

4.9 Estimates of the Mg-Overabundance 89

4.10 Comparison of Fe3 with other Fe-Lines 91

4.11 Mg-Overabundance Estimated with Fe3 92

4.12 Mg/<Fe> *vs* Hβ and Hγ_A Diagram 93

4.13 The Correction of $C_2$4668 for Overabundance Problems 96

4.14 $C_2$4668 *vs* Other Metal Lines 97

4.15 Age/Metallicity Diagnostic Diagram with Hγ_A, Fe3 and $C_2$4668c 100

4.16 Ages and Metallicities of the Fornax Sample 101

4.17 Absolute Blue Luminosity Plotted Against Various Indices and Estimates . 104

5.1 Mgb' & Mg_2–log σ_0 Relation 110

5.2 Residuals of the Mgb' & Mg_2–log σ_0 Relation 111

5.3 Fe3′–log σ_0 Relation 114

5.4 Various Metal Indices *vs* log σ_0 116

5.5 Residuals from Various Metal Indices *vs* log σ_0 117

5.6 Balmer Lines *vs* log σ_0 118

5.7 Metallicity and Age *vs* log σ_0 120

5.8 Residuals from log age *vs* [Fe/H] Relation 122

5.9 Model Mg_2, Mgb' and Fe3′–σ_0 Relations 123

5.10 Mg/Fe *vs* $\log \sigma_0$ 125

5.11 Residuals from Mg–σ_0 *vs* other Residuals (a) 128

5.12 Residuals from Mg–σ_0 *vs* other Residuals (b) 129

6.1 Comparison of Kinematics for NGC1427 134

6.2 Comparison of Kinematics for NGC1404 135

6.3 Comparison of Kinematics for NGC3379 136

6.4 Kinematics of Fornax Sample (a) 138

6.5 Kinematics of Fornax Sample (b) 139

6.6 Kinematics of Fornax Sample (c) 140

7.1 Lick/IDS offset : NTT92 144

7.2 Lick/IDS offset : NTT92, Linear Comparison 145

7.3 Lick/IDS offset : NTT93 146

7.4 Lick/IDS offset : NTT93, Linear Comparison 147

7.5 Comparison of Line-Strength Gradients for NGC1427 150

7.6 Comparison of Line-Strength Gradients for NGC1404 151

7.7 Comparison of Line-Strength Gradients for NGC3379 152

7.8 Fitting Gradients: An Example 154

7.9 Sky Subtraction: Test for NGC1427 156

7.10 Sky Subtraction: Test for NGC1373 157

7.11 Correlations of Line-Strength Gradients with Other Parameters 161

7.12 [MgFe] *vs* Hβ Diagrams for Individual Galaxies: S0s 164

7.13 [MgFe] *vs* Hβ Diagrams for Individual Galaxies: Es 165

7.14 Fe3 *vs* Hγ_A Diagrams for Individual Galaxies: S0s 166

7.15 Fe3 *vs* Hγ_A Diagrams for Individual Galaxies: Es 167

7.16 DSS Images of the 11 Fornax S0s 168

7.17 Summary of Metallicity Gradients in Ellipticals 170

7.18 Mg*b* *vs* Fe3 Diagrams for Individual Galaxies: S0s 173

7.19 Mgb *vs* Fe3 Diagrams for Individual Galaxies: Es 174

7.20 DSS Image of NGC1381 175

7.21 Age/Metallicity Diagnostic Diagram for NGC1381 176

7.22 Mg-Overabundance in NGC1381 178

7.23 Mg_2 *vs* Mgb Diagram for NGC1381 179

B.1 Line-Strength Gradients: NGC1316 (AAT96) 199

B.2 Line-Strength Gradients: NGC1336 (NTT92) 200

B.3 Line-Strength Gradients: NGC1336 (NTT93) 201

B.4 Line-Strength Gradients: NGC1336 (AAT96) 202

B.5 Line-Strength Gradients: NGC1339 (NTT92) 203

B.6 Line-Strength Gradients: NGC1339 (AAT96) 204

B.7 Line-Strength Gradients: NGC1351 (NTT93) 205

B.8 Line-Strength Gradients: NGC1351 (AAT96) 206

B.9 Line-Strength Gradients: NGC1373 (NTT93) 207

B.10 Line-Strength Gradients: NGC1373 (AAT96) 208

B.11 Line-Strength Gradients: NGC1374 (AAT96) 209

B.12 Line-Strength Gradients: NGC1375 (AAT96) 210

B.13 Line-Strength Gradients: NGC1379 (AAT96) 211

B.14 Line-Strength Gradients: NGC1380 (AAT96) 212

B.15 Line-Strength Gradients: NGC1380A (AAT96) 213

B.16 Line-Strength Gradients: NGC1381 (AAT96) 214

B.17 Line-Strength Gradients: NGC1381 (AAT96) 215

B.18 Line-Strength Gradients: NGC1381 (AAT96) 216

B.19 Line-Strength Gradients: NGC1399 (NTT92) 217

B.20 Line-Strength Gradients: NGC1399 (AAT96) 218

B.21 Line-Strength Gradients: NGC1399 (AAT96) 219

B.22 Line-Strength Gradients: NGC1404 (NTT92) 220

B.23 Line-Strength Gradients: NGC1404 (AAT96) 221

B.24 Line-Strength Gradients: NGC1419 (AAT96) 222

B.25 Line-Strength Gradients: NGC1427 (NTT93) 223

B.26 Line-Strength Gradients: NGC1427 (AAT96) 224

B.27 Line-Strength Gradients: NGC1427 (AAT96) 225

B.28 Line-Strength Gradients: NGC1427 (AAT96) 226

B.29 Line-Strength Gradients: IC1963 (AAT96) 227

B.30 Line-Strength Gradients: IC2006 (AAT96) 228

B.31 Line-Strength Gradients: E359-G02 (AAT96) 229

B.32 Line-Strength Gradients: E358-G06 (AAT96) 230

B.33 Line-Strength Gradients: E358-G25 (AAT96) 231

B.34 Line-Strength Gradients: E358-G50 (AAT96) 232

B.35 Line-Strength Gradients: E358-G59 (AAT96) 233

B.36 Line-Strength Gradients: ESO358-G59 (NTT92) 234

B.37 Line-Strength Gradients: NGC3379 (AAT96) 235

List of Tables

1.1 A Collection of Distance Measurements to Fornax 13

1.2 Details of the Fornax Galaxy Sample 15

2.1 Instrumental Parameters and Setups : NTT92 19

2.2 Instrumental Parameters and Setups : NTT93 20

2.3 Instrumental Parameters and Setups : AAT96 20

2.4 Lick/IDS Resolution 28

2.5 Log of Observations - Galaxies 31

2.5 Log of Observations - Galaxies 32

2.6 Log of Observations - Comparison Stars : NTT92 33

2.7 Log of Observations - Comparison Stars : NTT93 33

2.8 Log of Observations - Comparison Stars : AAT96 34

3.1 Definitions of Lick/IDS Indices 39

3.2 Adopted Lick/IDS Offsets for AAT96 43

3.3 Adopted Recession Velocities and Central Velocity Dispersions - AAT96 Run 59

3.4 Central Index Measurements 63

4.1 Simple Statistics and K-S Tests 72

4.2 Nebular Emission Lines 79

4.3 HI Recombination Lines 83

4.4 Emission in Fornax Early-Type Galaxies 83

4.5 Spectral Index Response to Abundance Changes: Cool Giant 90

4.6 The $C_2$4668-Index Before and After Correction 96

4.7 The Ages and Metallicities of Fornax Early-Type Galaxies. 102

7.1 Adopted Lick/IDS Offsets for NTT92 and NTT93 148

7.2 Line-Strength Gradients 159

7.3 Average Line-Strength Gradients 159

7.4 Average [Fe/H] Gradients for Es 172

A.1 Index Measurements of Lick/IDS Comparison Stars 197

Chapter 1

Introduction

The main topic of this thesis are the stellar populations of early-type galaxies as probed in the nearby Fornax cluster. In this introduction we will give a brief description of the general properties of early-type galaxies, summarize the properties of the Fornax cluster and conclude with an outline of this thesis. Note that at the beginning of each Chapter in this thesis we give a further, more detailed introduction into the topic.

Galaxies are one of the grandest structures of the universe. Their sizes range from as small as $10^6 M_\odot$ to as much as $10^{13} M_\odot$, being built of stars, interstellar gas, dust and perhaps dark matter. Yet galaxies were recognized only early in this century (1920s) as vast assemblages of stars, distinct from our own Galaxy. Edwin P. Hubble (1889 - 1953) was one of the pioneers in this field. He introduced a classification diagram for galaxies, now widely known as the Hubble tuning fork diagram (Hubble, 1936, see Figure 1.1 for a revised Hubble diagram).

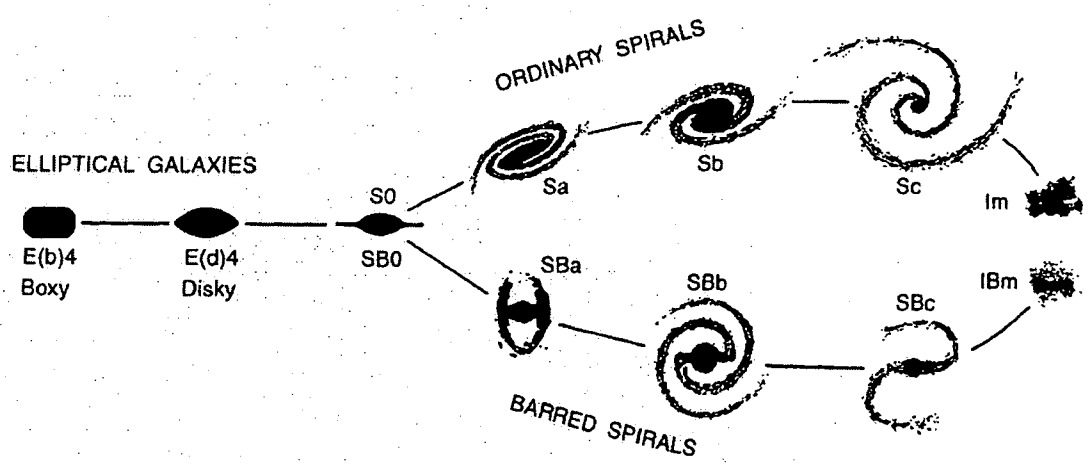

Figure 1.1: Revised "Hubble tuning fork" diagram taken from Kormendy and Bender (1996).

Early-type (E and S0) galaxies are located on the left hand side of this diagram. Hubble incorrectly thought that this diagram described an evolutionary sequence, extending from left to right. Therefore we call ellipticals and S0s today *early-type* galaxies and spirals *late-type* galaxies. For a modern morphological classification scheme see e.g., Sandage and Bedke (1994).

Elliptical-type galaxies have been observed since 1749 (Le Gentil, M32) and up to the end of the 1970s these galaxies were interpreted as systems devoid of any substructure, without cold gas, flattened by rotation and consisting entirely of (metal rich) population II stars created in the single collapse of a gigantic gas cloud shortly after the beginning of the Universe. However, research during the last two decades has revealed a substantially more complex picture. In Section 1.1 we will provide a brief summary of recent research in this field.

1.1 The Properties of Elliptical & S0 Galaxies

Elliptical and S0 galaxies represent a sizeable fraction of galaxies brighter than $M_B \sim -18$. Using a magnitude limited catalogue of galaxies such as the RSA (Sandage and Tammann, 1987, complete to $B_T \sim 12.0$), 13% and 11% of the total sample are classified as E+E/S0 and S0+S0/a respectively. Furthermore, the fraction of nearby bright elliptical galaxies is a function of the local density, ranging from about 10% in low-density regions to 40% in dense clusters of galaxies. In contrast, the fraction of bright S0s stays roughly constant at 40% for all environments (Dressler, 1980; Dressler et al., 1997).

1.1.1 Morphology and Kinematics

The radial surface brightness profiles of elliptical galaxies are very smooth and show a strong concentration towards the centre. They can be fit reasonably well by a $r^{1/4}$ law (de Vaucouleurs, 1948) over a wide range of radii and ellipticities. Yet, recent results from the Hubble Space Telescope (HST) show that the cores of elliptical galaxies seem to deviate from a $r^{1/4}$ law (Faber et al., 1997). The existence of cores was in fact recognized much earlier on, see e.g., Lauer (1985). Additionally, a significant fraction of Es show evidence for fine structure i.e., faint shells and ripples in their outer envelopes (e.g., Malin and Carter, 1983; Schweizer et al., 1990). The largest elliptical galaxies, the cDs, exhibit faint extended envelopes (in fact this is one of their classification criteria).

For a long time it was believed that the observed flattening of ellipticals, in analogy to the (disky) S0s, was due to rotation (e.g., Larson, 1975). This picture drastically changed when Bertola and Capaccioli (1975) and Illingworth (1977) showed that most of the luminous Es do not rotate fast enough to explain the observed flattening. Binney (1976) suggested that velocity dispersion anisotropy could be responsible for the flattening.

However, not all elliptical galaxies are supported by anisotropic velocity dispersions. For example, Davies et al. (1983) demonstrated that low luminosity elliptical galaxies rotate almost as rapidly as predicted for oblate systems with isotropic velocity dispersions. In terms of their kinematical properties the cores of Es are a special place. For example Kormendy et al. (1996) demonstrated by utilizing the superb resolution of the HST that the central velocity dispersion of NGC3115 reaches $\sim$ 440 kms^{-1} whereas ground based data suggested values of only $\sim$ 300 kms^{-1}. This is interpreted as strong evidence for a $2 \times 10^9 M_\odot$ central black hole. It was also found that about 20%-30% of giant elliptical galaxies exhibit kinematically-decoupled cores (KDC), or even counter rotating cores (e.g., Franx and Illingworth, 1988; Hau, 1998). The majority of current models which are able to explain the existence of kinematically distinct cores are based on merger scenarios (for a review see Schweizer, 1998). This is in strong contrast to the traditional formation scenario of elliptical galaxies i.e., fast dissipational collapse of a primordial gas cloud. Note that these peculiar cores can survive for a long time and therefore do not necessarily indicate a recent merger.

Detailed studies of the isophote shapes (contours of constant surface brightness) in the late 1980s showed that many elliptical galaxies do not appear to be perfectly elliptical when projected on the sky (Carter, 1987; Bender, 1988). The deviations from a perfect ellipsoid are generally very small (<1%) and one can classify them in two groups: disky isophotes and boxy isophotes. Note that some intermediate types exist also. Disky Es are thought to contain faint disks which contribute between a few percent and up to 30% of the total light of a galaxy (Rix and White, 1990; Scorza and Bender, 1995).

With this in mind, Kormendy and Bender (1996) proposed a revision of the Hubble sequence for elliptical galaxies, based on the isophote shape. They suggest that elliptical galaxies can be divided into basically two groups (see also Figure 1.1):

1. **Boxy Es:** Generally these are luminous ($M_V \lesssim -22.0$) galaxies which are supported by anisotropic velocity dispersions. Often they show hot X-ray gas or radio emission. The fact that they also often show signs of kinematically peculiar cores is interpreted as a natural by-product of mainly stellar mergers. Recent HST images suggest that they have shallow core profiles (Faber et al., 1997).

2. **Disky Es:** These are usually fainter systems ($M_V \gtrsim -20.5$) and are rotationally supported. HST images do not show signs of a distinct core although there could be small distinct cores hidden below the resolution limit of HST (de Jong et al., 1998). X-ray emission from hot gas and kinematically peculiar cores are rare. Together with the presence of (faint) disks, this may indicate that dissipation was essential for their formation. Note that this includes dissipational mergers.

   Elliptical galaxies of intermediate luminosity ($-22.0 \lesssim M_V \lesssim -20.5$) are present in both classes. Note that the sequence E (boxy) - E (disky) is not necessarily a continuous sequence (Kormendy and Bender, 1996).

S0s are by definition the combination of a bulge and a clearly visible disk without spiral arms. From a morphological point of view the S0s are very close to the disky Es. Therefore it seems natural to see the sequence of spiral galaxy, S0 to disky E as a continuous sequence of decreasing disk-to-bulge ratio of systems which formed mainly dissipationally (Bender et al., 1992).

This trend may be connected to the stellar populations in these galaxies. For example de Jong and Davies (1997) found a weak trend in the sense that disky Es have stronger Hydrogen line absorption as measured using the Hβ line. With the help of stellar population models, this indicates that disky Es have younger luminosity weighted ages. However, it is important to bear in mind that disks in elliptical galaxies have a variety of spatial scales and densities. The study by de Jong and Davies referred mostly to the presence of disky isophotes in the outer parts of elliptical galaxies. Yet HST images of elliptical galaxies in the Coma cluster reveal many small (from the ground invisible) central disks. Sometimes these small disks are accompanied by dust lanes reminiscent of those in spiral galaxies. Future studies should account for disks on this range of scales, as they might have very different origins.

1.1.2 The Stellar Populations of Early-Type Galaxies

Understanding the properties, e.g., the ages and metallicities, of the stellar populations in early-type galaxies is a difficult and long-standing problem. Since we can only study the integrated light of these galaxies (dwarf Es in the local group are an exception), and since velocity broadening makes it impossible to study weak absorption features, it has up to now been impossible to *uniquely* determine the average age and metallicity of early-type galaxies.

The prevailing view until the mid 1970s was that elliptical galaxies are old ($\sim$15 Gyrs), coeval and span a range in mean metallicity. Characteristic for early-type galaxies is their colour with $B-V$values of usually 0.8 - 1.1 mag (Peletier et al., 1990). This is consistent with most of the light originating from G-K dwarfs & giants. In fact, the spectra of early-type galaxies in the optical closely resemble G-KIII stars. With age effects having only minor influence, metallicity was thought to be the driving parameter in relations such as the colour-magnitude relation where galaxy colours become redder with increasing luminosity (Sandage and Visvanathan, 1977). This was based on the idea that elliptical galaxies are formed in a monolithic collapse and burst of star formation shortly after the "Big-Bang" passively evolving afterwards (Larson, 1974, 1975). In this simple picture, bigger galaxies contain more metal rich stellar populations because they are able to hold on to the products of stellar nucleosynthesis longer due to their deeper potential wells (Calberg, 1984; Arimoto and Yoshii, 1987).

The steady progress in stellar population synthesis over the last 20 years resulted in

a bewildering variety of new insights into the stellar populations of early-type galaxies without reaching a final conclusion about their formation mechanisms. For example, it was realized quite early on that the stars in our own galaxy do not exactly match elliptical galaxy spectra. O'Connell (1976) concluded in his analysis of the central stellar populations in giant ellipticals that the absorption features of Mg I and Na I are enhanced with respect to the Fe absorption features in solar neighbourhood stars. Today we call this the Mg-overabundance or in general α-element overabundance. Furthermore, there is a growing body of evidence that not all elliptical galaxies harbour an entirely old stellar population. Most notably, the dwarf elliptical M32, a satellite of the Andromeda Galaxy (M31), shows signs of an intermediate age stellar population (e.g., O'Connell, 1980; Freedman, 1992). Finally, the existence of E+A galaxies (e.g., Zabludoff et al., 1996), which show the spectrum of an old elliptical but with superimposed strong Balmer lines (characteristic of A-type stars) and no emission features, are evidence for secondary star-formation in Es.

However, the results by O'Connell were based on relatively simplistic stellar population synthesis models. Up-to-date evolutionary stellar population synthesis models (e.g., Bruzual and Charlot, 1993; Worthey, 1994; Weiss et al., 1995; Kodama and Arimoto, 1997; Vazdekis et al., 1996) use the information of large stellar libraries to determine how the spectral energy distribution (SED) changes with parameters such as stellar gravity, metallicity and temperature. Then they couple this information with theoretical stellar evolutionary isochrones and stellar flux distributions to produce the SED of a model population. By varying input parameters such as age, metallicity and Initial Mass Function (IMF) one can determine a best fit model SED to a given integrated spectrum of the object under study.

In principle, one would expect it to be a relatively easy task to vary the input age and metallicity of a model stellar population and so find the best fitting combination (assuming usually a Salpeter like IMF). However, as demonstrated by Worthey (1994), the influence of age and metallicity on the integrated SED of an old stellar population are mostly degenerate. In other words the SEDs of old stellar populations look almost identical when Δ age [Gyrs] $\approx -3/2\,\Delta$ Z [fraction of metals] is preserved. Worthey dubbed this behaviour the "3/2 rule".

Despite this age/metallicity degeneracy, Worthey and González (1993) identified certain absorption lines in the optical which are preferentially driven by either age or metallicity changes. These absorption lines are measured in the Lick/IDS system (Burstein et al., 1984; Worthey et al., 1994; Trager et al., 1998) which is described in detail in Chapter 3. There are other line-strengths systems in use which use different absorption lines (e.g., Rose, 1985). However, the most commonly used one is the Lick/IDS system in combination with Worthey's (1994) models which we will use throughout this thesis (see Charlot et al. (1996) for a recent comparison of some population synthesis models).

Using the age and metallicity indicators in the Lick/IDS system combined with Worthey's models González (1993) analysed the central stellar populations of 41 nearby elliptical galaxies in primarily low density environments. He found compelling evidence for luminosity weighted ages ranging from as young as $\sim$ 2 Gyrs to up to $\sim$17 Gyrs with only a limited range in metallicity. This is in strong contrast to the traditional picture of E galaxy formation and gave rise to an ongoing and controversial debate about the star-formation history of early-type galaxies.

A few years earlier Schweizer et al. (1990) found many signs of disturbance in a sample of 36 giant elliptical galaxies located mostly in the field and groups. These galaxies exhibit e.g., weak ripples and jets. Combining these findings with the absorption strength of the Hβ line they concluded that the disturbed galaxies are younger and likely to be the products of disk-disk mergers.

González did not only find young elliptical galaxies but also verified earlier findings (O'Connell, 1976; Peletier, 1989; Worthey et al., 1992) that for elliptical galaxies the strengths of Magnesium lines compared to Fe lines is stronger than for stars in the solar neighborhood. This is strong evidence for non solar abundance ratios in elliptical galaxies, i.e., $[\mathrm{Mg/Fe}] \equiv \log((\mathrm{Mg/Fe})/(\mathrm{Mg/Fe})_{\odot}) > 0$.

So far we have considered only the central stellar populations of elliptical galaxies yet it has been known for a long time that the stellar populations change with position in the galaxy. In fact the analysis of colours showed that elliptical galaxies become bluer with increasing radius (e.g., Franx et al., 1989a; Peletier et al., 1990). Furthermore, line-strength gradients in Es show weaker metal lines with increasing radius (e.g., Davies et al., 1993; Carollo et al., 1993). Generally these findings are interpreted as an average decrease in metallicity with increasing radius. Line strength gradients are naturally accounted for in a dissipational formation scenario (Larson, 1976; Calberg, 1984).

The previous discussion focused mainly on the stellar populations of *elliptical* galaxies because little is known about those of S0s. The analysis of the latter type of galaxies is complicated by their structure, i.e., bulge + disk component. Early results, based on IR photometry, suggested that the disks of S0s would be 3-5 Gyrs younger than their bulges (Bothun and Gregg, 1990). This has been challenged by Peletier and Balcells (1996) who found no significant age gradients and very shallow metallicity gradients along the major axis in a sample of early-type spirals. A comprehensive study of line-strength gradients in S0s was performed by Fisher et al. (1996). They concluded that the centres of S0s, i.e., the bulges, are very similar to elliptical galaxies, and the disks along the major axis show only small age or metallicity gradients.

1.1.3 Global Scaling relations

Despite the rather complex picture of stellar populations in early-type galaxies as presented in the previous Section, these galaxies appear to be extremely homogeneous when viewed from the perspective of scaling relations.

Their appearance is very uniform with almost perfectly elliptical isophotes and smooth $r^{1/4}$ luminosity profiles (Burkert, 1993). Secondly, the colour of an elliptical galaxy strongly correlates with its luminosity, where the more luminous ellipticals are redder (Sandage and Visvanathan, 1978; Bower et al., 1992; Terlevich, 1998). This is usually referred to as the colour-magnitude-relation (CMR). The stellar populations are also tightly connected to their dynamical properties as demonstrated in the Mg–σ_0 relation. Here the Mg-absorption strength (at $\sim$ 5175 Å) becomes stronger with increasing central velocity dispersion. The scatter about both the CMR and the Mg–σ_0 relation is very small. This is usually interpreted as strong evidence for a tight scaling of the stellar populations with galaxy mass. However, recently Bower et al. (1998) showed that considerably complex star-formation histories can be "hidden" in the spread of the CMR as long as the bulk of the stars is formed at high redshift. In particular, small secondary bursts of star formation are consistent with the observed scatter in the CMR.

In fact, all of the previously mentioned scaling relations can be traced back to a "master" relation called the Fundamental Plane (FP) of elliptical galaxies. Djorgovski and Davis (1987) and Dressler et al. (1987) discovered that ellipticals populate only a band (or "plane") in the three dimensional space of central velocity dispersion, σ_0, effective radius, r_e, and mean effective surface brightness, $< \mathrm{SB} >_e$. The equation of the plane is (e.g., Bender et al., 1997):

$$\log r_e = 1.25 \log \sigma + 0.32 < \mathrm{SB} >_e + const. \qquad (1.1)$$

Remarkably, the S0-type galaxies and bulges of spirals follow a very similar FP (Bender et al., 1992). The typical scatter in r_e for a cluster of galaxies is $\sim$20%, however, for the well studied Coma cluster Jørgensen et al. (1993) find only a scatter of $\sim$ 11%. The existence of the fundamental plane is thought to stem from the virial theorem (Faber et al., 1987). Yet, the FP shows a tilt which is not consistent with this interpretation. Analysing the FP in detail, Renzini and Ciotti (1993) argued that at any location in the FP the spread in the mass to light ratio (M/L) is less then 12% and that the tilt of the plane implies a variation of less than a factor of three in M/L. For a somewhat different interpretation of the tilt in the FP see Pahre et al. (1998).

Most recently Colless et al. (1998) have combined the constraints placed by the Mg-σ_0 relation and the FP for a sample of 736 mostly early-type galaxies in 84 clusters to

estimate the maximum spread in age or metallicity inferred from the intrinsic spread in these relations. They conclude that for reasonable correlations between age and metallicity the distributions in log *age* and log $Z/Z_{\odot}$ are $\delta age/age = 15 - 32\%$ and $\delta Z/Z = 23 - 28\%$ at fixed galaxy mass. Taken together, these results illustrate that the star-formation *and* galaxy formation history of *nearby* early-type galaxies give rise to a remarkable degree of homogeneity (Davies, 1996).

However, Worthey et al. (1996) point out that there might be an age/metallicity conspiracy at work keeping the scaling relations tight. They suggest that younger galaxies (weaker metal lines) are also more metal rich (stronger metal lines) and that the combined effect keeps the galaxy close to the mean relation. This of course involves metallicities in excess of 2 $Z_{\odot}$ for the young stellar populations, and it is not at all clear whether this is reasonable.

Another way to investigate the homogeneity of early-type galaxies is to observe clusters at medium to high redshift, i.e., cosmologically significant look-back times, and probe the existence of scaling relations. The CMR has been probed at up to z = 1.3 (Stanford et al., 1997) and found to be well established. Its evolution is well described by a passive evolution of an old stellar population with little increase in the scatter at high redshift. Other scaling relations, such as the Mg–σ_0 relation (Ziegler and Bender, 1997) at $z \simeq 0.4$ and the FP (van Dokkum et al., 1998a) at z = 0.83 also provide evidence for a formation redshift of ellipticals at $z \gtrsim 2$ and passive evolution afterwards. The existence of these scaling relations at high redshift implies that most of the nearby Es are old[1]. For S0s the situation is not so clear, as some groups have found evidence for significant evolution (Dressler et al., 1997; van Dokkum et al., 1998b). The reason for this might be a true evolution in the population of the S0s, but as Andreon (1998) points out, it could be caused by morphological classification problems at high redshift. The selection criteria and morphological classification schemes are a crucial and perhaps ill-understood part of the interpretation of scaling relations at higher redshift.

1.1.4 Galaxy Formation and Evolution Scenarios

As already mentioned elliptical galaxies were thought to be created dissipationally in a rapid, single burst of star formation some 15 Gyrs ago (Larson, 1975; Calberg, 1984, and references therein). After that the galaxies would evolve passively without merging, resulting in a population of old Es where the mean metallicity scales with galaxy mass.

However, today there is no doubt about the existence of young stellar populations in at least some elliptical galaxies. In the 1970s Toomre suggested that elliptical galaxies could also be created in a merger of two spiral-type galaxies. In fact, he suggested that all star-formation might take place in disks and that Es might all be formed by the merger of

[1] In a statistical sense, i.e., assuming that clusters at high redshift will develop into today's clusters.

stellar disks (Toomre, 1977). This opened an entirely new mechanism of galaxy formation.

Recent, and perhaps also the most successful, galaxy formation models follow the evolution of galaxies from primordial density fluctuations up to the present day. These models are usually referred to as semi-analytic hierarchical galaxy formation models in the framework of the Cold Dark Matter model[2] (e.g., Baugh et al., 1996; Kauffmann, 1996). In these models dark matter halos evolve through a sequence of hierarchical mergers. The gas located within these dark matter halos forms stars quiescently in a disk until they may be disrupted into a spheroidal configuration (i.e., elliptical galaxies) by major mergers. Of course merger induced stellar bursts are likely if there is gas present. Remarkably, this all happens in a universe which is dominated by collisionless dark matter. The luminous matter (i.e., what we observe) is only a tiny fraction of the total mass. Due to secondary gas infall these spheroidal galaxies may grow disks again. This scenario actually implies that galaxies can pass through various phases of morphology (disk+disk - spheroidal - S0) during their evolution.

A natural prediction of hierarchical merging is that small structures form first which would appear to be in contradiction to the existence of luminous *and* old cluster elliptical galaxies. This paradox is solved via the following prediction of the models: In clusters the galaxy formation is enhanced and the expected decrease in age with increasing mass is negligible. The inclusion of chemical enrichment together with the prediction that more massive ellipticals are formed from more massive disks can also plausibly produce the observed colour-magnitude relation (White, 1997; Kauffmann and Charlot, 1998).

In summary these models predict that the bulk of the stars in today's cluster elliptical galaxies formed at high redshifts ($z \sim 2-3$) in disks and are therefore old. The inclusion of chemical enrichment also accounts for the observed scaling of mean metallicity with galaxy mass. This is, at least in a qualitative sense, very much in agreement with observations. Although the stars form very early in these models, the actual galaxy formation continues until lower redshifts, i.e., there are still *stellar* major mergers without further significant star-formation. The separation of star-formation and galaxy formation in a morphological sense is an important and strong prediction of hierarchical merging.

This kind of idea was already proposed by Bender et al. (1992). Analysing the FP for dynamically hot galaxies in κ-space (a coordinate transformation of the traditionally FP parameters) they suggested a gas/stellar continuum to explain the smooth variations of ellipticals with increasing mass: larger galaxies are formed by systematically more stellar (and less gaseous) mergers than smaller galaxies.

The predictions for the field galaxy population are different. Recent CDM models (Kauffmann and Charlot, 1998) suggest that the age spread is considerably larger than for

[2]These models are extremely successful despite the fact that a suitable candidate for CDM particles has yet to be discovered.

the cluster galaxies whereas the metallicities are similar. It follows that scaling relations such as the CMR and the FP should show more scatter for the field. Good quality data for field early-type galaxies is sparse. Perhaps the most homogeneous study is that of Larson et al. (1980). They found an increased scatter in the CMR for field Es; however, S0s in their field sample did not show such a trend. Also Guzmán and Lucey (1993) found some evidence that early-type galaxies in low density regions are younger than cluster galaxies. Most recently Kodama et al. (1998) analysed the CMR of 35 early-type galaxies in the Hubble Deep Field with a median redshift of 0.9. Perhaps in contradiction to the predictions of the hierarchical models they find a red sequence (with considerable scatter) well-described by passive evolution of an intrinsically old stellar population. Major observational programs to probe the stellar populations of field galaxies are now underway and will shed more light onto the galaxy formation history of these galaxies.

1.1.5 Summary

Elliptical and S0-type galaxies emerge as complex individuals when we analyse their detailed structure, internal dynamics and stellar populations. However, they also behave highly uniformly when viewed from the perspective of global scaling relations. Different galaxy and star formation scenarios are discussed in the literature. Perhaps the most important are the hierarchical merger scenarios and some modified early collapse models.

It is not clear at all which scenario matches the observational evidence best. However, there are some conclusions common to all scenarios:

1. The bulk of the stellar population in cluster elliptical galaxies and bulges of S0s is old. This implies *star* formation redshifts of $z \gtrsim 2$.
2. Some early-type galaxies have been created in mergers occuring as recently as the present epoch which involved significant amounts of secondary star-formation, giving young luminosity weighted ages.
3. Star formation and morphological galaxy formation do not have to happen at the same time. So one has to carefully differentiate between these two formation mechanisms and their time scales.

Of course there are many problems and open questions. Some of the more important ones we list in the following:

1. One of the main obstacles on our way to understand the stellar populations and galaxy formation mechanisms is the age/metallicity degeneracy. New model predictions and better defined indices will help us to break the degeneracy and uniquely determine the ages and metallicities.

2. How important is merging in terms of galaxy formation and when exactly did it happen? If merging is a basic ingredient to the formation history of early-type galaxies then it is crucial to establish the amount of dissipation in each of the mergers. Some observations, such as those of line-strength gradients seem to be a mystery without dissipational star-formation.

3. Is the formation mechanism of field galaxies substantially different to cluster galaxies and as a result of this how do their stellar populations compare to a cluster environment?

4. When we speak about the age of the Milky Way we talk about the oldest stars. An interesting question is: what is the age of the oldest stars in early-type galaxies? Due to the fact that we see only the luminosity weighted integrated spectra of distant galaxies this question is very difficult to answer.

1.2 The Fornax Cluster and Sample Selection

We have chosen to probe the stellar populations of early type galaxies in the nearby Fornax cluster. In this Section we give a brief summary about the cluster and describe our sample selection.

The Fornax cluster is located in the southern hemisphere at $\alpha \sim 3^h35^m$ and $\delta \sim -35°.7$. It is a small, compact cluster of galaxies dominated by the central cD NGC1399. Compared to Virgo the central number density of galaxies in Fornax is ~ 2 times higher (Ferguson and Sandage, 1988). Figure 1.2 shows a Digital Sky Survey (DSS) image of the central $2°.5 \times 2°.5$ region of the Fornax cluster centred on NGC1399.

The Fornax cluster represents an important step in the extragalactic distance scale. It is close enough that planetary nebulae (McMillan et al., 1993) and Cepheids can be detected (Silbermann et al., 1998), but also distant enough that its velocity perturbation by the Virgocentric flow is negligible (Bureau et al., 1996). Furthermore the cluster does not show any significant substructure and has a core dominated by early-type galaxies which makes it ideal for distance calibration purposes. In Table 1.1 we present a selection of up-to-date distance estimates for the Fornax cluster. Throughout this thesis we adopt the distance modulus inferred from the I-band Surface Brightness Fluctuations (SFB): $m - M = 31.2$. This is equivalent to a distance of $\simeq 17$ Mpc.

Ferguson (1989) performed a major photographic galaxy survey over $\sim 40\,\square°$ on the Fornax cluster (The Fornax Cluster Catalogue, FCC). He lists in his catalogue of likely Fornax members 340 galaxies where the completeness limit of the survey is $B_T \sim 18$. Our sample was drawn from this catalogue to include all early-type galaxies (ellipticals & S0s, but no dE or barred S0s) brighter then $B_T = 14.2$. Additionally we included IC2006 which is a confirmed member of Fornax but just outside the area covered by the photographic

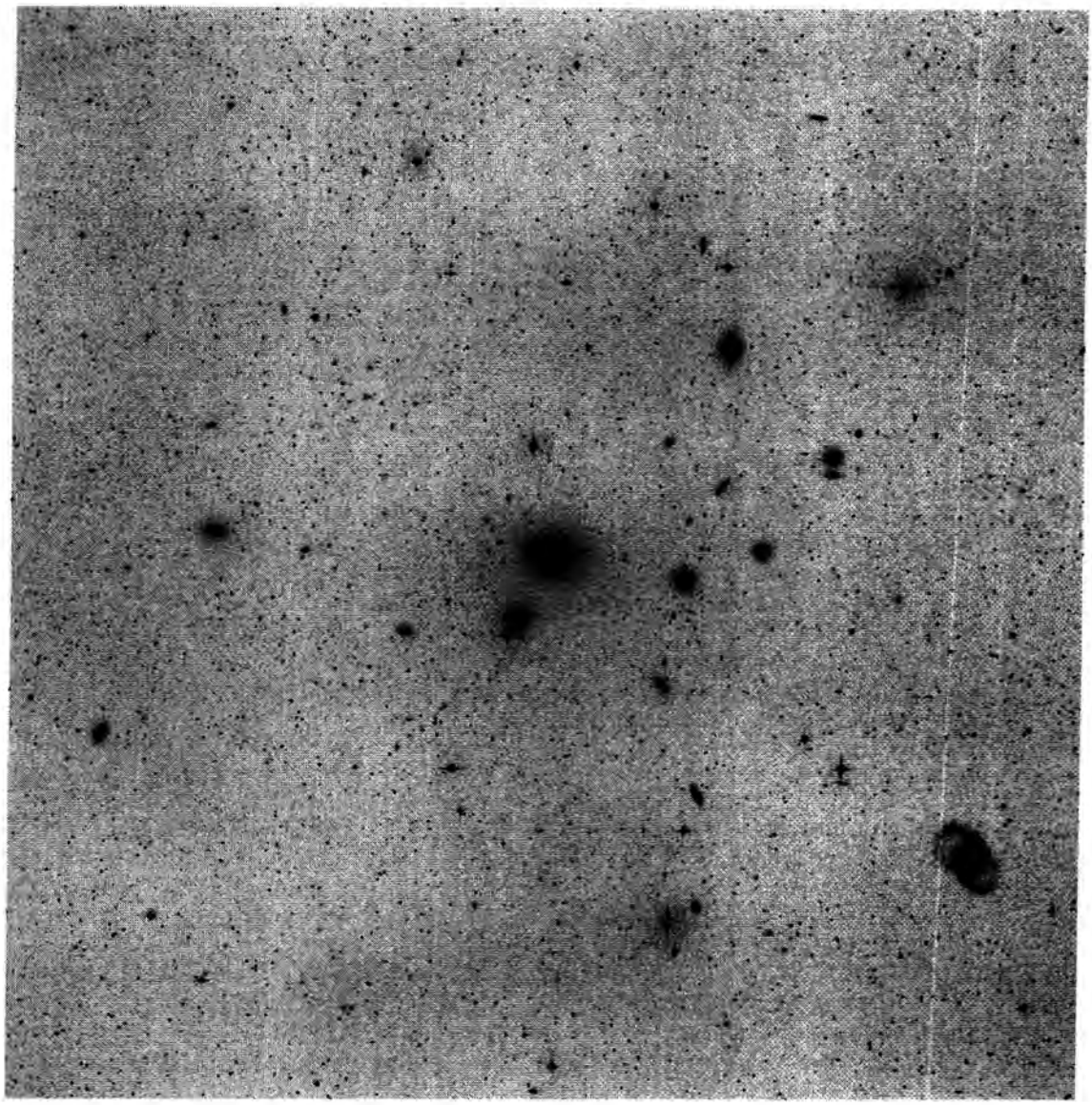

Figure 1.2: A Digital Sky Survey (DSS) image of the central 2°.5 × 2°.5 region of the Fornax cluster. See Figure 1.3b for identification of galaxies.

Table 1.1: A Collection of Distance Measurements to Fornax

$m-M$	Method	Reference
31.31±0.27	Cepheid	Silbermann et al. (1998)
31.22±0.06	I-band SBF	Jensen et al. (1998)
31.32±0.24	K′-band SBF	Jensen et al. (1998)
30.94±0.33	I-band TFR	Bureau et al. (1996)
31.07±0.13	V-band GCLF	Kohle et al. (1996)
30.85±0.11	I-band GCLF	Kohle et al. (1996)
31.14±0.14	PNLF	McMillan et al. (1993)

SBF: Surface Brightness Fluctuations
TFR: Tully-Fisher relation
PNLF: Planetary Nebulae Luminosity Functions
GCLF: Globular Cluster Luminosity Functions

survey of Ferguson. In total we selected 23 early-type galaxies. Note, that one galaxy (NGC1428) has a bright star close to its centre and has therefore been excluded from the spectroscopic sample giving a total of 22 galaxies. The standard elliptical NGC3379 was observed as a calibration galaxy.

Figure 1.3 shows the location of our sample galaxies within the Fornax cluster. The area shown in Figure 1.3b corresponds to the DSS image shown in Figure 1.2 and can be used to identify the galaxies. We have adopted the morphological classifications given by Ferguson and checked them with images we obtained on the Siding Spring 40″ telescope. From these we noted a central dust lane in ESO359-G02 and a central disk in ESO358-G59 which led us to classify them as lenticular galaxies. We classified IC2006 as elliptical, as it was not classified by Ferguson.

In Table 1.2 we list the name, adopted type and total apparent magnitude of our sample galaxies along with the heliocentric velocity as derived in this work [column (1)-(4)]. In column (5) and (6) we list the major and minor axis effective radii as measured by Caon et al. (1994) if not stated otherwise; in column (7) the major axis position angles (PA) as taken from the RC3 (de Vaucouleurs et al., 1991) are shown if not stated otherwise.

In order to characterize our sample in more detail we present in Figure 1.4 the absolute luminosity distribution (upper panel, solid line) assuming a distance modulus of 31.2 mag. The dashed line in the same plot represents the luminosity distribution of all galaxies listed in the FCC but using the same luminosity cut-off as in our sample. In total our sample comprises ∼45% of all galaxies in Fornax brighter than $B_T = 14.2$. The lower panel in Figure 1.4 shows the redshift distribution (solid line) of our sample. The mean recession velocity is $v_{helio} = 1442$ kms^{-1}.

In the literature one can find two important studies of stellar populations in the Fornax cluster. Note that neither used the Lick/IDS system. (1) Pickles (Pickles, 1985a,b;

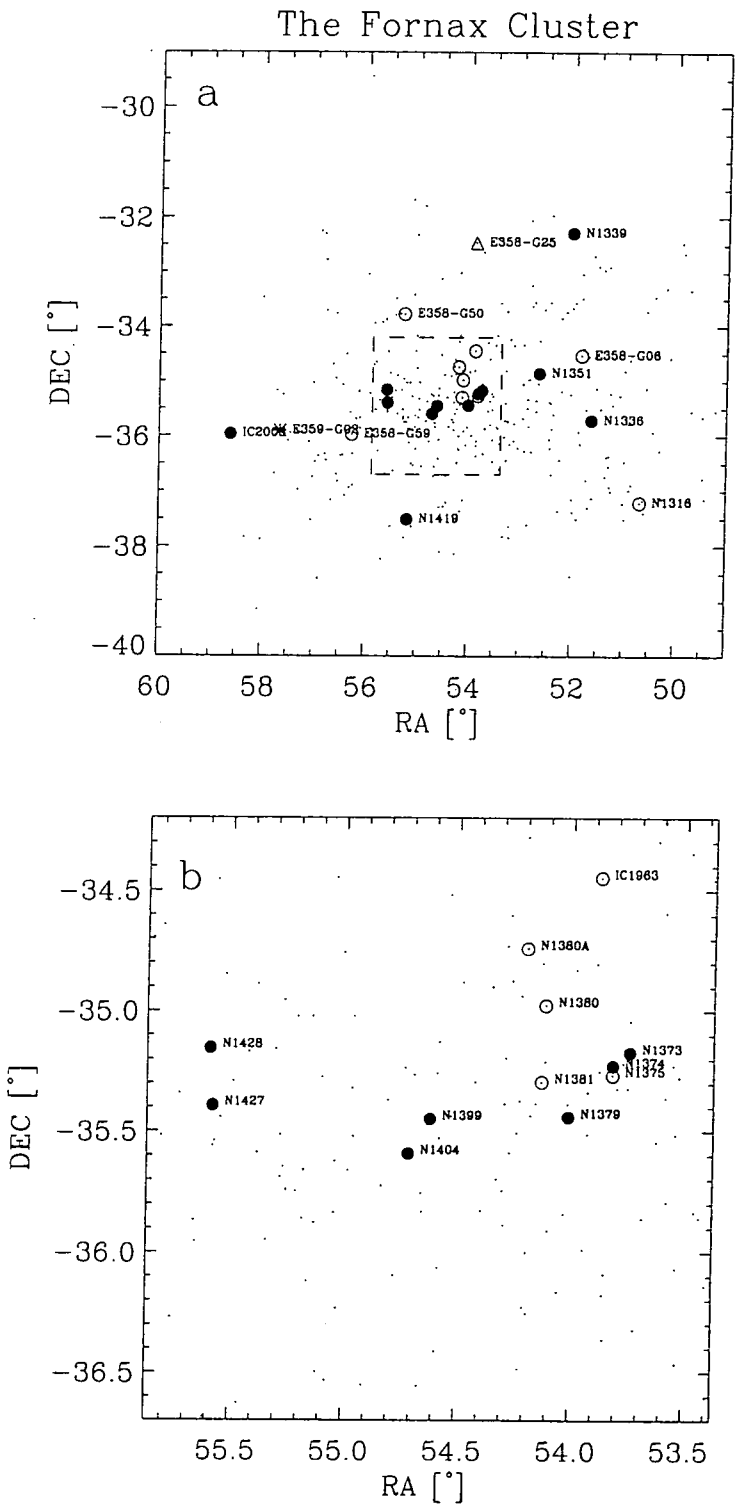

Figure 1.3: (a) The spatial distribution of the Fornax sample. Filled circles and open circles represent ellipticals and S0s respectively. The cross and open triangle represent possible post-starburst and starburst galaxies respectively. Note that for completeness NGC 1428 was included. The small dots represent the total sample of 340 Fornax galaxies identified by Ferguson (1989). (b) The central area of the Fornax cluster indicated by a dashed box in panel (a) is shown. Note that the area covered by panel (b) is identical to the DSS image shown in Figure 1.2.

Table 1.2: Details of the Fornax Galaxy Sample

Name	Type	B_T [a] [mag]	v_{helio} [kms^{-1}]	r_e maj[b] [″]	r_e min[b] [″]	PA maj[c] [°]
NGC1316	S0	9.4	1744±16	132.2	90.5	50
NGC1336	E4	13.1	1439±11	30.8	22.9	22
NGC1339	E4	12.5	1355±12	15.7	11.1	172
NGC1351	E5	12.5	1529±13	33.7	22.3	140
NGC1373	E3	14.1	1341±10	11.1	8.5	131
NGC1374	E0	12.0	1349±13	26.6	24.2	118[e]
NGC1375	S0	13.2	726±13	24.0	9.3	91
NGC1379	E0	11.8	1360±11	23.9	23.3	182[e]
NGC1380	S0	10.9	1858±14	52.4	26.6	7
NGC1380A	S0	13.3	1545±11	32.4	7.1	179
NGC1381	S0	12.4	1726±12	23.5	8.0	139
NGC1399	E0	10.6	1431±28	134.1	120.8	110[e]
NGC1404	E2	11.0	1923±17	26.0	23.0	157[e]
NGC1419	E0	13.5	1574±10	9.4	9.3	188[e]
NGC1427	E4	11.8	1416±10	39.2	27.1	76
IC1963	S0	12.9	1608±08	11.3[g]	...	84
IC2006	E	12.2	1371±12	24.2[d]	21.8[d]	40[d]
E359-G02	S0	14.2	1461±18	19.8	12.3	45
E358-G06	S0	13.9	1259±12	18.7	8.0	32
E358-G25	S0	13.8	1408±19	20.5	11.8	60
E358-G50	S0	13.9	1302±11	20.9	9.3	173
E358-G59	S0	14.0	1006±12	13.3	8.1	155
NGC3379[h]	E1	10.2	896±14	35.3[f]	31.4[f]	111[f]

[a] from Nasa/IPAC Extragalactic Database (NED)
[b] from Caon et al. (1994)
[c] from RC3 (de Vaucouleurs et al., 1991)
[d] from Schweizer et al. (1989)
[e] from de Carvalho et al. (1991)
[f] from Goudfrooij et al. (1994b)
[g] mean r_e from Ferguson (1989)
[h] calibration galaxy; non Fornax member

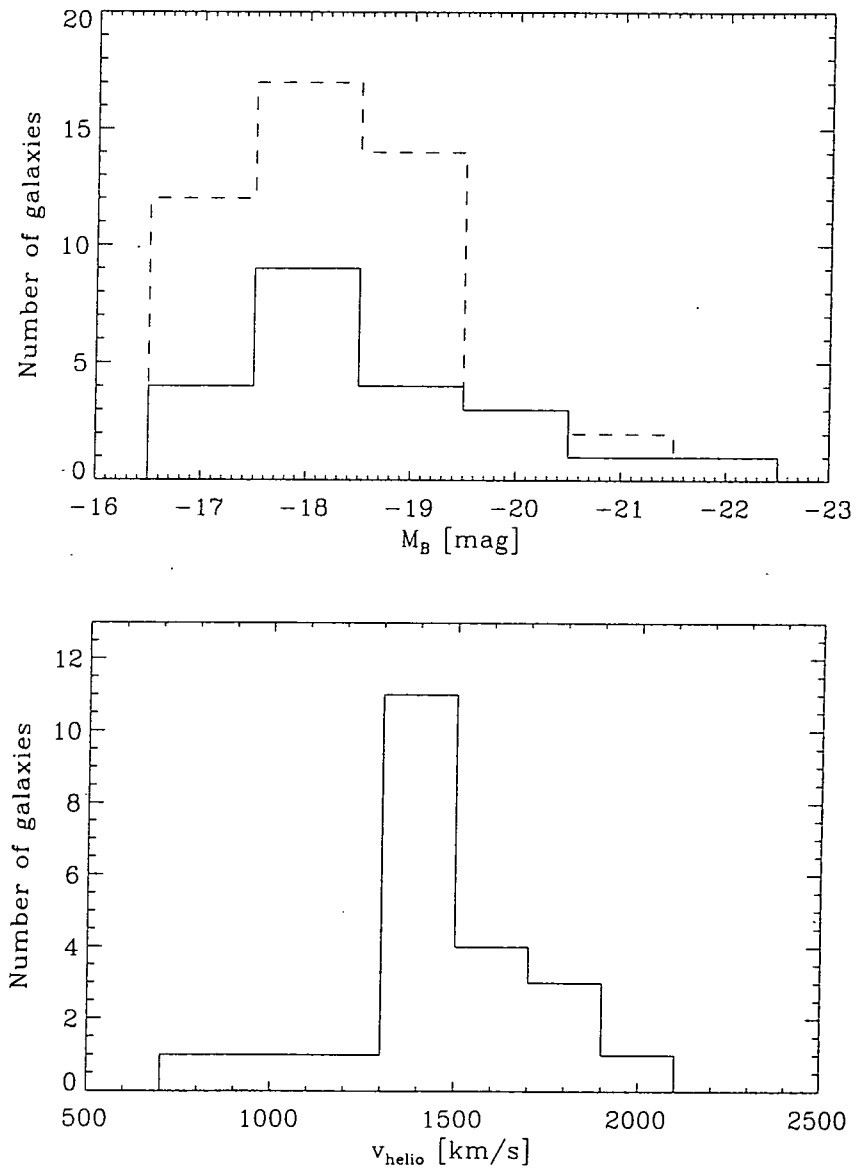

Figure 1.4: **Upper panel:** The absolute blue luminosity distribution of all early-type galaxies in our sample (solid line). The dashed line represents the distribution of all galaxy types in the Fornax cluster for the same luminosity range as our sample. For both distributions we used the catalogue values by Ferguson (1989) and assumed a distance modulus of 31.2 mag. Note that the galaxy IC2006 was added to Ferguson's catalogue. The mean luminosity of our sample is $M_B \simeq -18.5$. **Lower Panel:** The redshift distribution of our sample. Measurements are from this work. Mean redshift of the our sample: 1442 kms^{-1}.

Pickles and Visvanathan, 1985) analysed a sample of 12 elliptical and five lenticular galaxies in the Fornax cluster. Using an early version of population synthesis models he concluded that the ellipticals show relatively young main-sequence turnoff ages of 6-10 Gyrs. He also pointed out that there is strong evidence for small amounts of current star formation in the brightest Es. Finally, he noted that the elliptical galaxies follow a metallicity sequence where the brightest galaxies have 2 to 3 times solar metallicity. In fact, in this thesis we will confirm some of his results with up-to-date model predictions. (2) Held and Mould (1994) observed 10 nucleated dwarf elliptical galaxies (dEs). They conclude that the dEs cover a wide range in metallicity (-1.4 $\lesssim$ [Fe/H] $\lesssim$ -0.7) and also show Hydrogen lines of varying strength. The strong Balmer absorption is interpreted as a sign of an intermediate-age stellar population in those galaxies.

1.3 Aim and Outline of this Thesis

Early-type galaxies appear to be extremely homogeneous when viewed in the light of scaling relations such as the Mg–σ_0 relation or the fundamental plane. From the tightness of these relations one can infer that the stellar populations are very homogeneous. However, recent results give rise to doubts about the correctness of former conclusion.

The main aim of this thesis is to investigate the stellar populations of cluster early-type galaxies in order to probe the origin of the scaling relations. The first part of this thesis deals with the data reduction of our long-slit spectroscopy (Chapter 2) and the description of the Lick/IDS line-strength system which we use to interpret the stellar populations (Chapter 3). In Chapter 4 we will investigate the central stellar populations of our sample galaxies in the framework of the Lick/IDS system and Worthey's (1994) stellar population models. We analyse the spectra in previously established age/metallicity diagnostic diagrams as well as making use of new index combinations. The validity and caveats of the models and their application to early-type galaxies is critically reviewed with an emphasis on non-solar abundance ratios. We conclude with our best estimates of the central ages and metallicities of early-type galaxies in the Fornax cluster.

In Chapter 5 we will investigate the correlation between central index measurements and central velocity dispersions. In particular we will analyse the sources of scatter in the Mg–σ_0 relation. However, we also present other index–σ_0 relations such as Fe–σ_0. Velocity dispersion profiles and rotation curves of our galaxies are presented in Chapter 6. These will be used in Chapter 7 to correct the line-strength gradients within galaxies for velocity broadening. The line-strength gradients will allow us to analyse galaxies as a whole rather than concentrating on the bright centre. This is important as the centres of galaxies can be quite different from the outer regions. We will establish age and metallicity gradients within galaxies and also derive estimates on the total metal content in elliptical galaxies.

Finally in Chapter 8 we will discuss our general conclusions and give an outlook to future work.

Chapter 2

Long-Slit Spectroscopy

2.1 Introduction

In this Chapter we describe the basic reduction steps performed in order to extract useful scientific information from the raw CCD observations. Our main aim is to study various absorption lines in the optical wavelength range in order to deduce information on the integrated stellar populations of early-type galaxies in the Fornax cluster.

Section 2.2 describes the telescopes and CCD we have used during our three observing runs. To begin with the data is stored on the CCD as a two dimensional array of counts which not only shows the spectrum of the object but also some signature of the CCD itself, such as pixel to pixel gain variations. However, what we actually need for our analysis is a wavelength calibrated spectrum of the target object free of all CCD effects. In Section 2.3 we describe the basic data-reduction procedure to remove all the structure due to the CCD itself (e.g., bias, bad columns, pixel to pixel variations, etc.) and also how the wavelength calibration was achieved. The line-strength analysis technique adopted in this thesis requires further treatment of the spectra such as continuum and resolution correction which is described in Section 2.4. Finally, Section 2.5 summarizes the observations of galaxies and standard stars during all three observing runs.

2.2 Instrument Description

The observations for this thesis were carried out in three observing runs from 1992 to 1996. We used the ESO Multi-Mode Instrument (EMMI) at the 3.6m New Technology Telescope (NTT) on La Silla 19-21 December 1992 and 12-13 December 1993. EMMI is a dual-beam instrument. We used the dichroic mode (DIMD) for long-slit spectroscopy in which a dichroic beamsplitter is inserted in the beam in order to perform medium dispersion long-slit spectroscopy in the red and blue channel simultaneously.

In December 6-8, 1996 we used the 4m Anglo-Australian-Telescope (AAT) at Siding Spring equipped with the Royal Greenwich Observatory (RGO) Spectrograph at the Cassegrain (f/8) focus.

Throughout this thesis we will refer to the three observing runs by the following abbreviations: **NTT92**, **NTT93**, **AAT96**. Table 2.1, Table 2.2 and Table 2.3 summarize the main setup characteristics of all three observing runs.

Table 2.1: Instrumental Parameters and Setups : NTT92

Observer	R. Bender	
Dates	19 - 21 December 1992	
Instrument	EMMI	
Beam	red arm	blue arm
Spectral range	4528 - 5560 Å	3730 - 4660 Å
Grating	#7 (600 grooves/mm)	#12 (600 grooves/mm)
λ_c	5000 Å	4100 Å
Dispersion	56 Å/mm	36 Å/mm
	1.08 Å/pixel	0.91 Å/pixel
Resolution (FWHM)	$\sim$ 4.5 Å	$\sim$ 4.8 Å
Resolution (velocity)	$\sigma \simeq 115\ km/s$ [a]	$\sigma \simeq 150\ km/s$ [b]
Spatial Scale	0.″44/pixel	0.″39/pixel
Slit Width	2″	2″
Detector	THX31156 (ESO#18)	TK1024 AF (ESO#31)
Detector size	1024 × 1024 pixel	1024 × 1024 pixel
Pixel size	19 × 19 μm^2	24 × 24 μm^2
Gain	2.10 e^-/ADU	3.3 e^-/ADU
Read-out-noise	4.90 e^- rms	7 e^- rms
Seeing	1-2″	1-2″

[a] at 5000 Å
[b] at 4100 Å

2.3 Basic Data Reduction

The data from all three observing runs was reduced using IRAF (Image Reduction And Analysis Facility). This is a very versatile data reduction environment that provides a large set of tools to perform standard reductions and also allows one to write personal, specialized reduction routines. All data in this thesis has been acquired using CCDs (Mackay, 1986). In many respects, CCDs are within a small factor of being perfect photon detectors. However, carriers are created in silicon not only by light but also by various other effects such as thermal sources. Raw CCD data as taken from the telescope must therefore be corrected using some standard steps described in the next paragraphs. All three observing runs have been reduced in the same way.

Table 2.2: Instrumental Parameters and Setups : NTT93

Observer	A. Paquet	
Dates	12/13 December 1993	
Instrument	EMMI	
Beam	red arm	blue arm
Spectral range	4550 - 5818 Å	3710 - 4604 Å
Grating	#7 (600 grooves/mm)	#12 (600 grooves/mm)
λ_c	5200 Å	4100 Å
Dispersion	56 Å/mm	36 Å/mm
	0.87 Å/pixel	0.92 Å/pixel
Resolution (FWHM)	$\sim$ 5.0 Å	$\sim$ 5.0 Å
Resolution (velocity)	$\sigma \simeq 125\ km/s$ [a]	$\sigma \simeq 155\ km/s$ [b]
Spatial Scale	0.″35/pixel	0.″39/pixel
Slit Width	2 ″	2 ″
Detector	LORAL 2048	TK1024 AF (ESO#31)
Detector size	2048 × 2048 pixel	1024 × 1024 pixel
Pixel size	15 × 15 μm^2	24 × 24 μm^2
Gain	1.37 e^-/ADU	3.3 e^-/ADU
Read-out-noise	6.7 e^- rms	7 e^- rms
Seeing	1-1.5″	1-1.5″

[a] at 5000 Å
[b] at 4100 Å

Table 2.3: Instrumental Parameters and Setups : AAT96

Observer	R. L. Davies & H. Kuntschner
Dates	6-8 December 1996
Instrument	RGO spectrograph
Spectral range	4243 - 5828 Å
Grating	600 V
λ_c	5000 Å
Dispersion	66 Å/mm
	1.55 Å/pixel
Resolution (FWHM)	$\sim$ 4.1 Å
Resolution (velocity)	$\sigma \simeq 105\ km/s$ [a]
Spatial Scale	0.″77/pixel
Slit Width	2.″3
Detector	Tek1k #2
Detector size	1024 × 1024 pixel
Pixel size	24 × 24 μm^2
Gain	1.36 e^-/ADU
Read-out-noise	3.6 e^- rms
Seeing	$\sim$1″

[a] at 5000 Å

2.3.1 Overscan and Trim

A typical CCD controller adds to the CCD a DC-baseline charge level (normally called bias) to avoid negative counts in the analog-to-digital converter. The information about the bias level is usually stored in an area at one side of the CCD frame called overscan region (this region is not really part of the CCD chip, it is added to the data during the read out). Within IRAF one can define the overscan region and the bias level will be removed to first-order by averaging for each line separately. Unfortunately the Loral chip we used for NTT93 (Table 2.2) in the red arm provides only an useful overscan region of about 5 pixels (typically there are $\sim$ 30 pixels), hence the average over 5 pixel is not very stable and might introduce some row to row variations.

After the removal of the bias level the overscan region is no longer useful and is chopped off. This latter step usually trims off not only the overscan region but also the first and last few rows and columns of the CCD area, because most of the CCDs are larger than the projected slit.

2.3.2 Bias Correction

In addition, there may be column-to-column variations in the structure of the bias level, and this would obviously not have been removed by the overscan correction. For that reason we obtained frames with a zero integration time, called 'zero' or 'bias frames'. Usually 5 to 10 bias frames per night are combined with a median rejection algorithm to obtain one "master" bias frame to correct for the pixel to pixel variations. Unfortunately the bias frames from the observing run NTT92 show a wave like pattern ($\sim 2-3$ ADU level) which is *not* stable with time. A likely cause of the patterns is "pick-up-noise". These patterns are sometimes visible even in the object frames and cannot be removed. As the patterns are not stable with time we decided not to correct for pixel to pixel variations for the NTT92 run. Consequently the spectra extracted from the NTT92 run will be noisier than photon counts would suggest. This is reflected in the poor quality of the line-strength measurements (see Section 7.2 on page 142). Observations NTT93 and AAT96 do not suffer from pick-up-noise and therefore have been bias corrected.

2.3.3 Dark Current

On some CCDs there is a non-negligible amount of background added during long exposures. There are electronic bias, dark current, and leaks. For the NTT92 run we obtained 3 'dark' frames for each channel i.e., we exposed for 30 min but did not open the shutter. The average dark current in the detector was only 0.1 (red) and 3 (blue) counts per 30 min. The dark current in the NTT93 run was of the same order. Since our exposure time was usually only 45 min we decided not to correct for the dark current. The remaining dark

current will anyway be removed during sky subtraction. Furthermore the dark frames did not show any structure throughout the whole chip and were free of leaks. Exposures times for the AAT96 run were short enough to ignore any dark current.

2.3.4 Bad Columns

All CCDs used in our observing runs exhibited bad columns. We detected in the NTT92 data about 13 bad columns on the red CCD and only five bad columns on the blue CCD. They were removed by linearly interpolating over the regions. As long as there are only single columns this does not affect later reduction or analysing steps. However, the red CCD had four bad columns clustered together which makes a substantial wavelength region unusable. Unfortunately this region is located in one of the Fe-absorption features which makes the determination of this index very unreliable.

In the NTT93 run the new Loral 2048 chip in the red arm exhibited more than 50 bad columns which were difficult to locate and seemed to "bleed" into neighbouring pixels. Again we removed them as well as possible by interpolating over the region. Some of the bad columns show only on individual frames so it is likely that some of the weak bad columns remain on the chip.

The Tek-chip of the AAT96 run showed only a few bad columns. Hence the quality of the line-strength indices is very good.

2.3.5 Flat Fielding

The next step in removing the instrumental signature is to flat-field the data. There are pixel-to-pixel gain variations caused by the chip itself or for example dust on the CCD-window. Furthermore there are large-scale spatial variations. To obtain the short-scale sensitivity map we can use any source that has only long scale structure, both along the spatial and along the dispersion directions, like a quartz lamp reflected at the dome of the telescope (Dome Flats). The removal of large-scale variations can be accomplished using sky frames.

Usually at the beginning of the night domeflats were taken. The domeflats of each night were combined using a median rejection algorithm resulting in a "master domeflat".

For spectroscopic data one might want to remove the large scale, wavelength-dependent structure that is peculiar to the flat field itself, e.g., removing bumps and wiggles which are found in the flat field source but not found in the stellar sky spectrum. These bumps, wiggles, and color effects can exist due to

- the lamps being of a very different temperature than the celestial sources you are observing,

- transmission features in any color balance filters used with the projector lamps, and
- the wavelength-dependence reflectivity of whatever the projection lamps shine on.

The combined domeflats were normalized by fitting a cubic spline of high order (40-50) to the average continuum in wavelength direction and dividing each row by this fit. The resulting frames are referred to as "response" frames. The rms amplitude, which represents the pixel-to-pixel variations in sensitivity, was typically 3-4%. Usually the quartz lamp does not illuminate the detector in exactly the same way as the light from the targets, so one would expect illumination variations in the slit direction. To correct for this we took twilight sky frames and combined them again with a median rejection algorithm. The resulting sky frame was first divided by a response frame. The vignetting along the slit was then determined by interactively fitting a cubic spline in each of 10 to 15 wavelength bins. A final illumination frame was produced by interpolating between the fitted points. Typically the illumination correction is $< 0.5\%$ for most of the detector area apart from the edges where the illumination correction was sometimes up to 10%.

The final step in flat-fielding was to multiply each response frame with the illumination frame from the appropriate night and divide each science frame by the resulting final flat field.

2.3.6 Cosmic Rays

Due to the long exposure times there are lots of cosmic rays all over the object (galaxy) frames. The standard IRAF way of removing cosmic rays did not give good results as it was not able to distinguish between real cosmic rays and the steep continuum of the galaxy profile. Therefore the frames were cleaned with a routine (`cleanest`) provided by the REDUCEME package (Cardiel et al., 1998). This routine automatically detects cosmic rays via a sophisticated deviation algorithm, while at the same time one is able to check each cosmic ray by eye. All comic rays in the area where the galaxy is recorded on the chip were manually removed and checked. This combination of automatic and manual removal resulted in a very efficient and highly successful cleaning of cosmic rays. Typically 400 cosmic rays had to be removed for a 2700s exposure.

2.3.7 Wavelength Calibration and Distortion Correction

Having cleaned the data from cosmic rays one can transform the science frames onto a linear wavelength scale. In order to remove the distortion in wavelength direction we obtained spectra of e.g., a Th-Ar-comparison lamp before and after most of the galaxy observations. A 'distortion map' in wavelength direction of the whole detector was then prepared from each set of comparison spectra by fitting a two dimensional polynomial to

the wavelength as a function of column and row to the position of 15 - 25 spectral lines. Nevertheless the galaxy spectrum is probably not aligned precisely along the CCD rows as later reduction programs will show. Additionally to the arc lamps we obtained spectra of standard stars such as K-giants. In order to uniformly illuminate the slit we moved the star several times perpendicular to the slit and additionally along the slit (NTT92 & AAT96; for NTT93 only trailed stars were obtained, see Section 2.4.1). This procedure results in so called "rocked" stars with several spectra of the same star stepped in the spatial direction (see Figure 2.1).

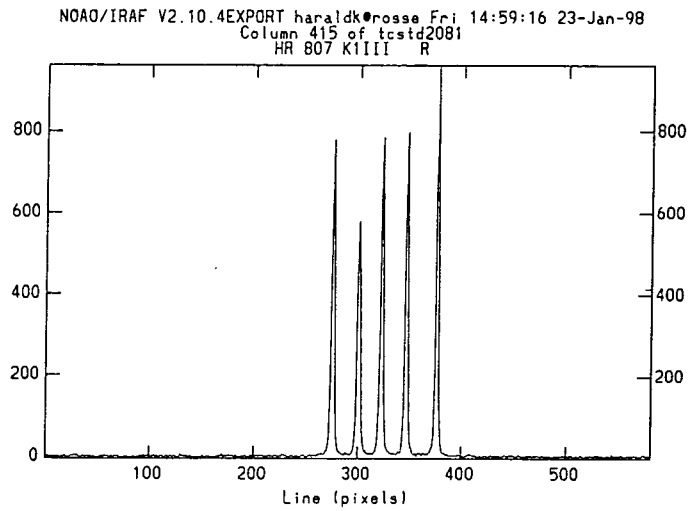

Figure 2.1: A "rocked" star seen in spatial direction. The y-axis denotes counts in ADU.

By using the spectra of "rocked" stars one can detect the misalignments of the wavelength direction with the rows on the CCD and correct the distortion maps for it. The distortion maps were used to transform each galaxy and comparison star to a linear wavelength scale in Å. The galaxy spectra were usually aligned to the rows of the detector to better than $\pm$ 1 pixel. The rms residual in the wavelength fit was typically 0.1 - 0.2 Å.

2.3.8 Sky Subtraction

As the galaxy spectrum should now be parallel to the physical x-axis of our frames it is easy to remove the background (sky). A polynomial of first order ($f(x) = mx + t$) was fitted to each column of the image and the resulting fit subtracted. This works well as long as the frames provide enough clean sky beside the galaxy spectrum. One has to make sure that there is no light 'pollution' from the object itself which can be a problem for large ellipticals. Therefore only a region close to the edges of the images (about 80-100 pixels on each side of the galaxy) was used. A similar procedure has been performed with the comparison stars as most of them were taken in twilight.

After this final reduction step the clean science frames are wavelength calibrated on a linear scale (x-axis) and roughly rectified for distortion in the spatial direction (y-axis). These frames are the basis for any further reduction i.e., extracting 1d-spectra from the 2d-frames and measuring velocity-dispersion or line-strength indices.

2.4 Further Data Reduction

After the basic data reduction one has to extract the scientific information from each of the frames which depends highly on the aim of the project. Here we are mainly interested in line-strength indices in the centres of early-type galaxies but it is also of interest to us how those indices change with position in the galaxy. The smallest independent unit on the CCD is a single pixel (neglecting seeing effects), hence one could extract row by row spectra of the science frame in question and determine indices. This might be a valid approach in the centre of the galaxy but in the outer parts the S/N will be not good enough to give reliable results. Thus in general one extracts and averages a couple of rows in order to achieve high enough signal but preserve the best spatial resolution as possible. In the next paragraphs we describe how useful spectra were extracted from the 2d-frames.

2.4.1 Extracting 1d Stellar Spectra

For many calibration and measuring purposes we need 1d stellar-spectra. As shown in Figure 2.1 most of the stars were observed as so called "rocked" stars. Each single spectrum on a science frame was extracted with the IRAF routine `apall`. This routine fits a low order polynomial to the spectrum in the wavelength direction and extracts it by maximizing the S/N. Each of those extractions were then cross-correlated (see Section 3.5.1 for a detailed description of the cross-correlation procedure) against each other and outliers, typically the outermost extractions, were discarded. Finally the remaining spectra were combined with a 3σ-clipping algorithm into one 1d spectrum. The NTT93 run did not have "rocked" stars instead the stars were trailed along the slit. For these stars several regions along the slit were extracted and then treated in the same way as the "rocked" stars.

After this reduction step, the spectra are in 1d format but still have their radial velocities. These velocities have to be removed before one can measure line-strength indices or use the stars as templates to derive accurate velocities for galaxies. In principle, if one knew the exact wavelength of some un-blended absorption lines, one could de-redshift the stars to laboratory wavelength. For our observing runs we used only a medium dispersion grating and therefore most of the lines are blends and cannot be used. To overcome this problem we used a set of 4 stars (G,K-giants), taken at 1.5 Å resolution FWHM (kindly provided by Claire Halliday) and measured the wavelength of four un-blended lines: two ion lines at 5269.9 Å and 5328.2 Å and two Mg lines at 5183.6 Å and 5172.8 Å. These

lines are very clear and provided an accurate redshift to ± 8 kms^{-1} rms. In turn the de-redshifted high-resolution stars were used as templates for a cross-correlation with the stars from our observing runs. Here a nominal error of $\pm$5-6 kms^{-1} (internal estimate of the `fxcor` task) was achieved. The total error in redshift for the stars from NTT92, NTT93 & AAT96 which have been used in all subsequent analysis is estimated to be $\pm$10-15 kms^{-1} (equivalent to $\pm$0.2 Å at 5200 Å).

2.4.2 Extracting Central Galaxy Spectra

Galaxy frames are treated in a slightly different way. For all observing runs the galaxies were put in the centre of the slit. This results in a spatially extended spectrum of the galaxy in the middle of the CCD. For the AAT96 run a central spectrum for each galaxy was extracted by fitting a low order polynomial to the position of the centre along the wavelength direction, re-sampling the data in spatial direction and finally co-adding the spectra within a 3.″85 aperture (=5 pixel). So the spectra for our central line-strength analysis (see Chapter 4) correspond to an effective aperture of 2.″3×3.″85.

The continuum shape of galaxy as well as star spectra (AAT96) were corrected for the spectral response of the CCD using the spectro-photometric standard star gd108 (Oke, 1990). This means that the continuum shape of the spectra is very similar to a truly fluxed spectrum but the counts do not represent the absolute flux per unit frequency.

Note that this procedure was only performed for the AAT96 run as no good photometric standard stars were available for the other observing runs. However in order to establish a similar spectral shape for all runs, galaxies in common with the AAT96 run were used to determine a mean continuum correction for each NTT92 and NTT93.

2.4.3 Extracting 1d Spectra for Line-Strength Gradients

Both observing runs at the NTT and some exposures at the AAT were aimed at deep exposures of elliptical galaxies to extract spectra along the spatial axis and provide line-strength **gradients**.

For many galaxies there are two exposures of the same position angle (PA) available which were combined to give a single 2d-frame of high S/N. In order to do that the absolute position of the spectra on the CCD has to be exactly the same in both frames. Unfortunately due to the long exposure times the centre of the galaxy can move slightly ($\sim$1 pixel) as a function of wavelength. Furthermore some frames showed a small variation of the FWHM of the galaxy profile with wavelength, which is caused by focus variations. To correct for the first problem a low order Legendre function was fitted to the galaxy centre (see Figure 2.2) and then exactly aligned with a predefined row on the chip. Then a Gaussian was fitted to extractions of the central galaxy profile (average of 10-20 columns)

and plotted as a function of wavelength (see Figure 2.3). Each galaxy exposure was checked for focus variations and if present each column was convolved with a Gaussian of small width such that the galaxy profile showed an approximately constant width with wavelength. The aligned and focus corrected frames were then co-added to give a single high S/N 2d frame.

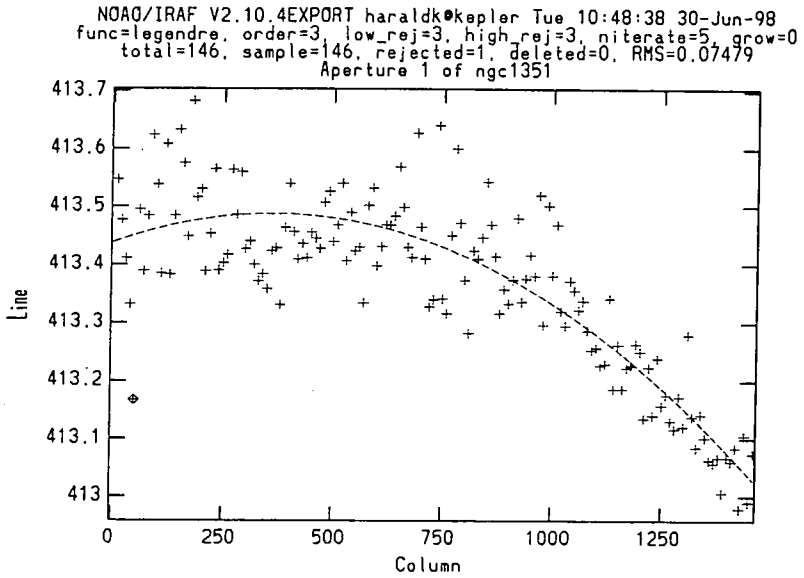

Figure 2.2: A third order Legendre function is fitted to the centre of NGC1351. The maximum change of position is ~0.5 pixel whereas the rms error of the fit is only 0.07 pixel.

Using a fortran program incorporated in IRAF, the now fully corrected frames were used to extract 1d-spectra of a given and constant S/N in spatial direction. Each side of the galaxy was treated independently and the S/N was determined just bluewards of the Mg_2 feature in an approximately 100 Å long range (NTT92 and NTT93 only for the red beam). As the response function of the CCD falls off to the blue this means that spectra have a slightly higher S/N in the red and a lower S/N in the blue compared with the mean S/N set in the program. Note that any error estimates are based on the local S/N rather than on the mean S/N. During the extraction the redshift and velocity dispersion of each extraction is determined and the 1d-spectra are continuum corrected and resolution corrected (see next paragraph).

2.4.4 Lick/IDS Resolution Correction

When measuring line-strength one has to calibrate the indices to a standard system such as the Lick/IDS system (see Section 3.4). In order to avoid any systematic offsets we applied corrections to reproduce the spectral shape of the original Lick/IDS spectra as accurately

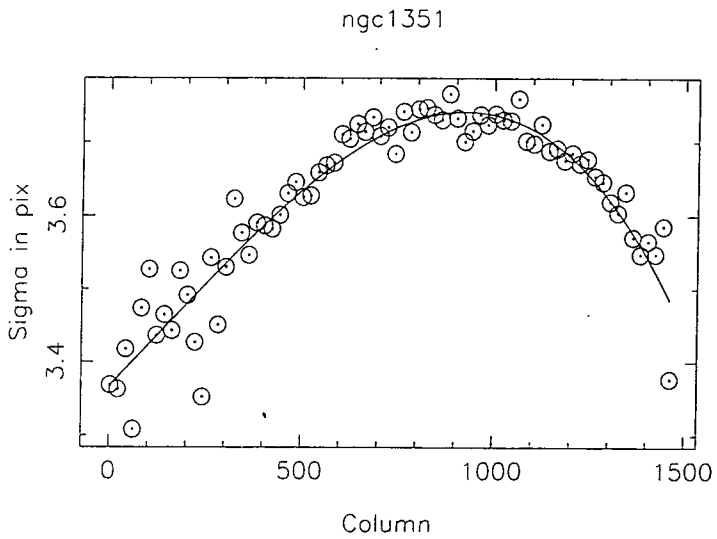

Figure 2.3: Focus variations for NGC1351 plotted as a function of column i.e., wavelength. The y-axis shows the width of the fitted Gaussian measured in pixels. The wavelength range spanned is 4550 - 5818 Å. The low S/N in the blue region of the spectrum is reflected in somewhat noisier data points.

as possible. One of the essential problems here is the instrumental resolution of the Lick/IDS system. Recently Worthey and Ottaviani (1997) determined the instrumental resolution of the Lick/IDS system which is summarized in Table 2.4. Note that the resolution is a function of wavelength and degrades to the blue and red end.

Table 2.4: Lick/IDS Resolution

Wavelength [Å]	FWHM [Å]
4000	11.5
4400	9.2
4900	8.4
5400	8.4
6000	9.8

From Worthey and Ottaviani (1997)

In order to determine the resolution of our spectra we used the comparison arc lamp frames. Assuming that all un-blended lines have a Gaussian profile the FWHM (Full Width at Half Maximum) in Å was determined for a range of lines. Generally the FWHM was constant with wavelength. The measured resolutions for all observing runs are listed in Tables 2.1, 2.2 and 2.3. Sometimes resolution is also quoted in kms^{-1} at a particular wavelength such as the instrumental velocity dispersion σ (Eqn. 2.6). Equation 2.1 to 2.4

provide the mathematical background.

$$f(x) = \frac{1}{\sqrt{2\pi}\,\sigma} e^{-\frac{x^2}{2\sigma^2}} \tag{2.1}$$

$$f(\sigma) = \frac{1}{\sqrt{2\pi e}\,\sigma} \tag{2.2}$$

$$FWHM = 2 \times x\left(\frac{1}{2} f(0)\right) = 2\sigma\sqrt{2\,ln2} \tag{2.3}$$

$$\frac{FWHM}{\sigma} = 2\sqrt{2\,ln2} \simeq 2.35 \tag{2.4}$$

The actual calculation of the instrumental resolution in σ [kms^{-1}] can be performed by

$$v = \frac{\text{FWHM [Å]}}{\lambda} \times c[\text{kms}^{-1}] \tag{2.5}$$

$$\sigma = \frac{v}{2.35}\ [\text{kms}^{-1}] \tag{2.6}$$

where c is the velocity of light and λ is the wavelength where one has measured the FWHM.

Now, to correct for the resolution difference between the Lick/IDS spectra and ours the spectra were convolved with a Gaussian of wavelength dependent width, such that the Lick/IDS resolution was best matched. Some stellar spectra were compared with original Lick/IDS spectra by overplotting (after continuum subtraction) and found to be in excellent agreement. Note that the resolution correction for galaxy spectra is applied after the determination of redshift and velocity dispersion, but before measuring the line-strength indices. An example of a continuum and resolution corrected spectrum can be seen in Figure 2.4. This kind of spectrum is then used to measure line-strength indices in the Lick/IDS system. All spectra were rebinned to a log-wavelength sampling with fixed parameters as this is the required input format for cross-correlations (`fxcor`) and the line-strength measuring program (`lsid`).

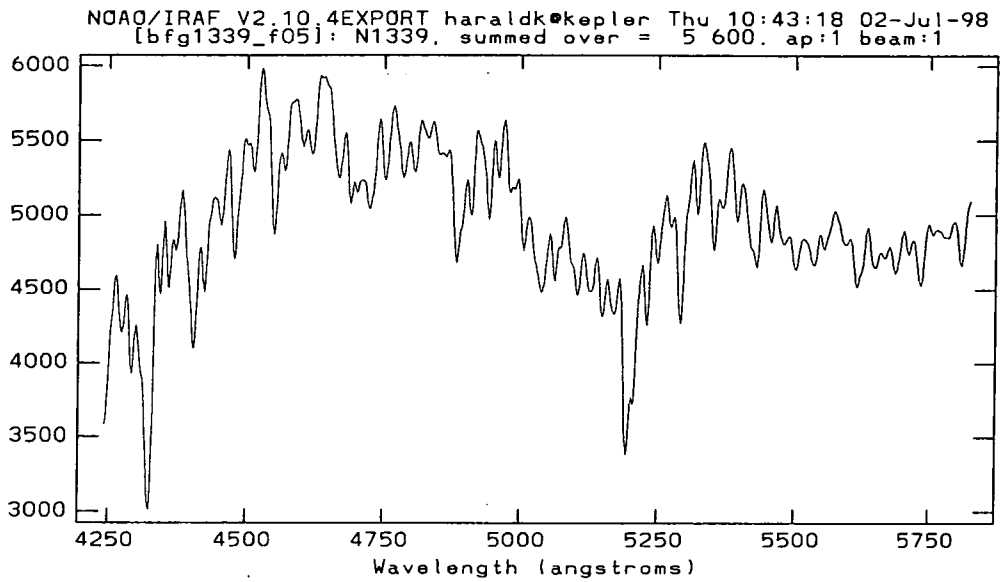

Figure 2.4: The spectrum of NGC1339 after continuum- and resolution-correction is shown. The y-axis denotes counts in ADU.

2.5 Summary of Observations

Table 2.5 gives the log of galaxy observations during all three observing runs. The galaxies are sorted by name (column 1) starting with NGC numbers. Columns 2-5 state the date of observation, the telescope, the exposure time and the PA of the slit respectively. Column 6 shows the PA of the major axis. Column 7-8 state the adopted galaxy type and B_T (taken from NED).

Table 2.6 lists all stellar observations taken during the NTT92 observing run. Column 1-6 state the names of the star, the date of observation, the exposure time, the spectral type and the V magnitude respectively. Column 7 shows whether the star was observed by the Lick group as well.

Table 2.7 and 2.8 summarize the same information for observing runs NTT93 and AAT96 respectively.

Table 2.5: Log of Observations - Galaxies

Galaxy	Date	Tel.	exp.	PA obs	PA maj	type	B_T	comment
NGC 1316	08. Dec 1996	AAT96	300s	90°	50°	S0 pec	9.4	
NGC 1336	20. Dec 1992	NTT92	2700s	110°	22°	E4	13.1	clouds
			2700s	110°				clouds
	12. Dec 1993	NTT93	2700s	20°				
	13. Dec 1993		2700s	110°				
	08. Dec 1996	AAT96	1200s	90°				
NGC 1339	19. Dec 1992	NTT92	2700s	175°	172°	E4	12.5	
			2700s	175°				
			2700s	85°				
			2700s	85°				
	07. Dec 1996	AAT96	600s	90°				
NGC 1351	12. Dec 1993	NTT93	2700s	143°	140°	E5	12.5	
			2700s	143°				
	13. Dec 1993		2700s	53°				
			2700s	53°				
	07. Dec 1996	AAT96	900s	90°				
NGC 1373	12 .Dec 1993	NTT93	2700s	135°	131°	E3	14.1	
			2700s	135°				
	13. Dec 1993		2700s	45°				
			2700s	45°				
	08. Dec 1996	AAT96	1200s	90°				
NGC 1374	07. Dec 1996	AAT96	900s	90°	118°	E0	12.0	
NGC 1375	08. Dec 1996	AAT96	900s	90°	91°	S0	13.2	
NGC 1379	13. Dec 1993	NTT93	1800s	70°	182°	E0	11.8	
	07. Dec 1996	AAT96	600s	90°				
			600s	90°				
NGC 1380	08. Dec 1996	AAT96	300s	90°	7°	S0	10.9	
NGC 1380A	08. Dec 1996	AAT96	900s	90°	179°	S0	13.3	
NGC 1381	08. Dec 1996	AAT96	480s	90°	139°	S0	12.4	
NGC 1381			900s	140°				
NGC 1381			900s	50°				
NGC 1381			1800s	50°				offset
NGC 1399	20. Dec 1992	NTT92	1200s	110°	110°	E0	10.6	clouds
	07. Dec 1996	AAT96	300s	90°				
	08. Dec 1996		600s	180°9				
NGC 1404	20. Dec 1992	NTT92	1200s	110°	157°	E2	11.0	clouds
	07. Dec 1996	AAT96	300s	90°				

Table 2.5: Log of Observations - Galaxies

Galaxy	Date	Tel.	exp.	PA obs	PA maj	type	B_T	comment
	08. Dec 1996		300s	90°				
NGC 1419	07. Dec 1996	AAT96	1200s	90°	188°	E0	13.5	
NGC 1427	12. Dec 1993	NTT93	1800s	80°	76°	E4	11.8	
	08. Dec 1996	AAT96	600s	90°				
			1800s	79°				
			1800s	169°				
IC 1963	08. Dec 1996	AAT96	600s	90°	84°	S0	12.9	
IC 2006	08. Dec 1996	AAT96	600s	90°	40°	E	12.2	
ESO 359-G02	08. Dec 1996	AAT96	1200s	90°	45°	S0	14.2	
ESO 358-G06	08. Dec 1996	AAT96	1800s	90°	32°	S0	13.9	
ESO 358-G25	08. Dec 1996	AAT96	1200s	90°	60°	S0 pec	13.8	
ESO 358-G50	08. Dec 1996	AAT96	1200s	90°	173°	S0	13.9	
ESO 358-G59	20. Dec 1992	NTT92	2700s	152°	155°	S0	14.0	clouds
			2300s	152°				clouds
	08. Dec 1996	AAT96	1200s	90°				

Observations of galaxies which are not members of Fornax

NGC 3379	08. Dec 1996	AAT96	300s	90°	71°	E1	10.2	
NGC 3923	12. Dec 1993	NTT93	2700s	48°	50°	E4-5	10.8	
	13. Dec 1993		2100s	48°				
			2700s	138°				
			2800s	138°				

Table 2.6: Log of Observations - Comparison Stars : NTT92

name 1	name 2	date	exp.	type[a]	Vmag[a]	Lick star[b]	comment
HD54810	HR2701	19 Dec 1992	120s	K0III	4.92	*	
HD58972	HR2854		120s	K3III	4.32	*	
HD15004	HR0704	20 Dec 1992	60s	A0III	6.33		clouds
HD15257	HR0717		60s	F0III	5.30		clouds
HD15652	HR0735		60s	M0III	6.10		clouds
HD16825	HR0796		60s	F5V	5.98		clouds
HD16975	HR0805		60s	G8III	5.96		clouds
HD17006	HR0807		60s	K1III	6.06		clouds
HD06203	HR0296	21 Dec 1992	120s	K0III	5.43	*	clouds
HD15379	HR0722		120s	M5III	6.41		clouds

[a] from Simbad
[b] all marked stars are Lick/IDS line-strength standard stars

Table 2.7: Log of Observations - Comparison Stars : NTT93

name 1	name 2	date	exp.	type[a]	Vmag[a]	Lick star[b]	comment
HD37160	HR1907	12 Dec 1993	10s	K0IIIb	4.09	*	saturated
HD47138	HR2423		60s	G8/K0III	5.70		
HD47306	HR2435		30s	A0II	4.40		saturated
HD54810	HR2701		60s	K0III	4.92	*	
HD58972	HR2854		60s	K3III	4.32	*	
gd108	-		60s	sd:B	13.56		
-	-	13 Dec 1993	no stars observed				

[a] from Simbad
[b] all marked stars are Lick/IDS line-strength standard stars

Table 2.8: Log of Observations - Comparison Stars : AAT96

name 1	name 2	date	exp.	type[a]	Vmag[a]	Lick star[b]	comment
HD037160	HR1907	07 Dec 1996	120s	K0IIIb	4.09	*	clouds
HD040657	HR2113		60s	K1.5III	4.53		clouds
HD047205	HR2429		60s	K1III	3.96	*	
HD050778	HR2574		120s	K4III	4.05	*	clouds
HD050778	HR2574		60s	K4III	4.05	*	clouds
HD058972	HR2854		60s	K3III	4.32	*	
HD061935	HR2970		60s	G9III	3.93	*	
HD066141	HR3145		60s	K2III	4.39	*	
L745-46A	-		120s	DF	12.98		clouds
L745-46A	-		300s	DF	12.98		clouds
gd108	-		600s	sd:B	13.56		
HD004656	HR0224	08 Dec 1996	58s	K4IIIb	4.43	*	
HD040657	HR2113		58s	K1.5III	4.53		
HD054810	HR2701		58s	K0III	4.92	*	
HD061935	HR2970		58s	G9III	3.93	*	
HD071597	-		58s	K2III	7.31		
HD083618	HR3845		58s	K2.5III	3.91	*	
HD088284	-		58s	K0III	3.61	*	
HD095272	HR4287		58s	K1III	4.07	*	
HD219449	HR8841		60s	K0III	4.21	*	
HD221148	HR8924		60s	K3IIIvar	6.25	*	
gd108	-		300s	sd:B	13.56		

[a] from Simbad

[b] all marked stars are Lick/IDS line-strength standard stars

Chapter 3

Line-Strength Measurements

3.1 Introduction: The Lick/IDS Library

In the early 1970s, S. Faber and collaborators started a sustained effort to comprehend the stellar populations of early-type galaxies. They collected an extensive library of galaxy and globular cluster spectra as well as spectra of field and cluster giants, subgiants and dwarfs, in the spectral range ~4000 - 6400 Å with ~8 Å resolution at 5200 Å. All the measurements were obtained at the Shane 3m Telescope of Lick Observatory from 1972 to 1984 with the same detector, the Image Dissector Scanner (hereafter IDS) (Robinson and Wampler, 1972). Since they could use the same instrument for the whole project this is perhaps the most reliable and stable published library at present. In a series of papers they have defined the Lick/IDS absorption-line index system, presented observations of globular clusters & stars and derived absorption-line index fitting functions (Burstein et al., 1984; Faber et al., 1985; Burstein et al., 1986; Gorgas et al., 1993). Worthey et al. (1994) expanded the original eleven-index system to 21 indices and presented the complete library of stellar data. It turned out that there is only one good age indicator among the 21 indices, namely Hβ. As the higher order Balmer lines Hγ and Hδ are also covered by the Lick/IDS wavelength range, Worthey and Ottaviani (1997) included 4 new indices in the Lick/IDS system measuring Hγ and Hδ, each with a narrow and a wide central passband. Most recently Trager et al. (1998) presented the final and fully calibrated library of extragalactic objects comprising 381 nearby galaxies and 38 globular clusters. The strength of the Lick/IDS system is that it is accompanied by single-burst stellar population (SSP) models (Worthey et al., 1994; Worthey and Ottaviani, 1997, see also Section 4.2 on page 66). These models are able to predict for a given single burst age, given metallicity and given initial mass function (IMF) the strength of 25 absorption features in integrated stellar populations (age $\geq$ 2 Gyrs). So, by comparing the observed strength of well chosen indices to the model predictions one can infer, under certain assumptions, estimates of the age and metallicity of the integrated stellar populations. Many authors have used the Lick/IDS system to analyse their spectra and compare with the Lick results

e.g., González (1993); Davies et al. (1993); Fisher et al. (1995, 1996); Ziegler and Bender (1997); Kuntschner and Davies (1998).

However measuring line-strength indices in integrated spectra of extragalactic objects is complicated by a number of problems:

- in the optical wavelength range the true continuum is not visible due many metal absorption lines,
- the strength of an absorption feature generally depends on the spectral resolution which is achieved with the spectrograph,
- different detector response functions will alter the continuum shape and thus lead to systematically offset index measurements unless the spectra are corrected for continuum shape,
- galaxies with different internal velocity broadening mimic different resolutions and hence different strengths of absorption features.

In this Chapter we describe our general method of determining line-strength indices from 1d spectra. First we introduce the Lick/IDS index-system which we will use throughout this thesis (Section 3.2). Then Section 3.3 describes how we actually measure the indices. The evaluation and correction of offsets to the adopted standard system is described in Section 3.4. For galaxy spectra we have to apply further corrections for the internal velocity broadening which are described in Section 3.5. Finally in Section 3.6 we present our fully corrected central index measurements of the AAT96 run.

3.2 Definition of Lick/IDS Indices

The continuum level is essential for the exact measurement of the equivalent width of an absorption line. Unfortunately in a typical early-type galaxy the optical spectrum is dominated by numerous metal absorption lines which can completely deplete the true continuum level. However, to measure a line strength empirically a true continuum level is not necessary as long as a pseudo-continuum can be defined in a standard way. In the Lick/IDS system there are three passbands defined for each index - one for the absorption feature itself and two passbands which define a pseudo-continuum to the red and blue of the absorption feature. The pseudo-continuum passbands cover no strong or highly variable lines, providing a stable continuum. The mean height in each of the pseudo-continuum regions is determined, and a straight line is drawn through the midpoint of each one. The difference in flux between this line and the observed spectrum within the central passband determines the index. This is illustrated in Figure 3.1 were the two pseudo-continuum passbands are indicated by dashed lines and the central index passband is indicated by dot-dashed lines. The solid line represents the pseudo-continuum.

Absorption features seen in galaxies with a large internal velocity dispersion are broadened. In order not to "loose" any absorbed flux the central passbands in the Lick/IDS system cover always a much broader region than would be necessary for only stellar objects. The velocity broadening does not only affect the absorption feature itself but can also influence the two continuum passbands for very large velocity dispersions. The absorption feature will "grow" out of the central passband and into the side-passbands lowering the pseudo-continuum. In order to compare with the model predictions, which are based on a stellar library at instrumental (IDS) resolution, one has to correct indices measured in galaxies to zero velocity dispersion. See Section 3.5.4 for details.

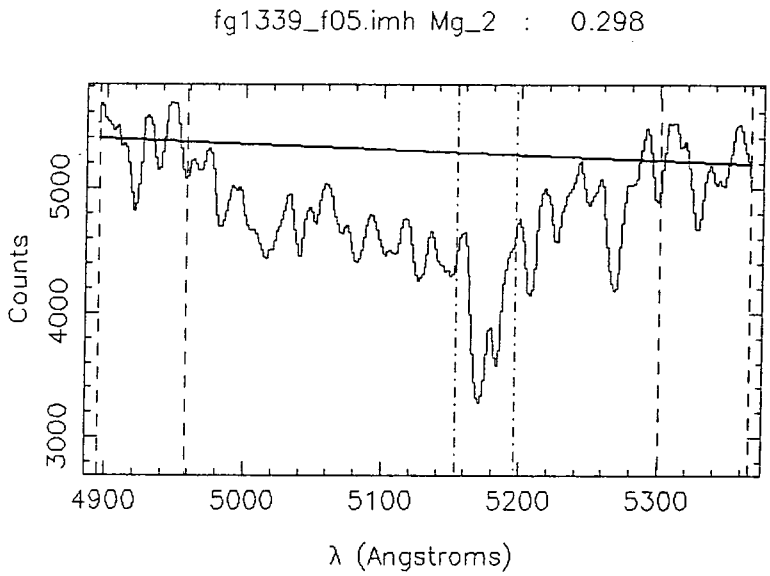

Figure 3.1: The definition of Lick indices. The two pseudo continuum passbands (dashed lines) and the central passband (dot-dashed lines) are indicated for the Mg_2 index. The thick solid line represents the pseudo-continuum. The spectrum is that of NGC1339 shown at the instrumental resolution of the AAT96 run.

For historical reasons, atomic features are measured in equivalent width (EW), while predominantly molecular features are specified as magnitudes of the average unabsorbed flux. The average pseudo-continuum flux level is defined as:

$$F_P = \left(\frac{1}{\lambda_2 - \lambda_1}\right) \int_{\lambda_1}^{\lambda_2} F_\lambda d\lambda, \tag{3.1}$$

where λ_1 and λ_2 are the wavelength limits of the pseudo-continuum sideband. If $F_{C\lambda}$ represents the straight line connecting the midpoints of the blue and red pseudo-continuum levels, an equivalent width is then

$$\mathrm{EW} = \int_{\lambda_1}^{\lambda_2} \left(1 - \frac{F_{I\lambda}}{F_{C\lambda}}\right) d\lambda, \tag{3.2}$$

where $F_{I\lambda}$ is the observed flux per unit wavelength and λ_1 and λ_2 are the wavelength limits of the feature passband. Similarly, an index measured in magnitudes is defined as:

$$\mathrm{Mag} = -2.5 \log \left[\left(\frac{1}{\lambda_2 - \lambda_1} \right) \int_{\lambda_1}^{\lambda_2} \frac{F_{I\lambda}}{F_{C\lambda}} d\lambda \right]. \tag{3.3}$$

All integrals in Equation 3.2 to 3.3 were computed adding first all the spectral bins (pixels) that fit completely within the passband, and interpolating fractional pixels.

Table 3.1 summarizes the wavelength definitions for all 25 Lick/IDS indices defined in Worthey et al. (1994) & Worthey and Ottaviani (1997). The units of the indices are shown in column 5. In column 6 the dominant elements which are measured by the index (taken from Tripicco and Bell (1995) where available) are presented in order of strength. Elements in brackets control the index in a negative sense. Note that some of the Fe-indices are also strongly dependent on other, lighter elements. Note further that the original Lick/IDS index Fe4668 has been renamed to $C_2$4668 by Trager et al. (1998). Column 7 states the average error for each index in the Lick/IDS stellar library (same units as index). For reference we show in Figure 3.2 the position of most of the Lick/IDS indices used in the AAT96 run overplotted on a galaxy spectrum.

González (1993) quotes in his thesis two non-standard Lick/IDS indices which are combinations of existing Lick/IDS indices. They were created in order to define a good mean metallicity indicator. First, the two indices Fe5270 and Fe5335 are substituted by their mean to give the new iron index <Fe> (Equation 3.4). Then the [MgFe] index is defined as the geometric mean of Mgb and <Fe> (Equation 3.5). These indices will be used later in this work.

$$\mathrm{<Fe>} = \frac{\mathrm{Fe5270} + \mathrm{Fe5335}}{2} \tag{3.4}$$

$$[\mathrm{MgFe}] = \sqrt{\mathrm{Mg}b \cdot \mathrm{<Fe>}} \tag{3.5}$$

Table 3.1: Definitions of Lick/IDS Indices

#	Name	Index Bandpass	Pseudocontinua	Units	Measures	Error	Notes
01	CN_1	4142.125-4177.125	4080.125-4117.625 4244.125-4284.125	mag	C, N, (O), (Mg)	0.018	1
02	CN_2	4142.125-4177.125	4083.875-4096.375 4244.125-4284.125	mag	C, N, (O), (Mg)	0.019	1
03	Ca4227	4222.250-4234.750	4211.000-4219.750 4241.000-4251.000	Å	(C), Ca, O	0.25	
04	G4300	4281.375-4316.375	4266.375-4282.625 4318.875-4335.125	Å	C, (O), Ti	0.33	
05	Fe4383	4369.125-4420.375	4359.125-4370.375 4442.875-4455.375	Å	Fe, C, (Mg)	0.46	
06	Ca4455	4452.125-4474.625	4445.875-4454.625 4477.125-4492.125	Å	(Fe), (C), Cr	0.22	
07	Fe4531	4514.250-4559.250	4504.250-4514.250 4560.500-4579.250	Å	Ti, (Si), Cr	0.37	
08	C_24668	4634.000-4720.250	4611.500-4630.250 4742.750-4756.500	Å	C, (O), (Si)	0.57	2
09	Hβ	4847.875-4876.625	4827.875-4847.875 4876.625-4891.625	Å	Hβ, (Mg)	0.19	
10	Fe5015	4977.750-5054.000	4946.500-4977.750 5054.000-5065.250	Å	(Mg), Ti, Fe	0.41	
11	Mg_1	5069.125-5134.125	4895.125-4957.625 5301.125-5366.125	mag	C, Mg, (O), (Fe), (Si)	0.006	2
12	Mg_2	5154.125-5196.625	4895.125-4957.625 5301.125-5366.125	mag	Mg, C, (Fe), (O), (Si)	0.007	
13	Mg*b*	5160.125-5192.625	5142.625-5161.375 5191.375-5206.375	Å	Mg, (C), (Cr), (Fe)	0.20	
14	Fe5270	5245.650-5285.650	5233.150-5248.150 5285.650-5318.150	Å	Fe, C, (Mg)	0.24	
15	Fe5335	5312.125-5352.125	5304.625-5315.875 5353.375-5363.375	Å	Fe, (C), (Mg)	0.22	
16	Fe5406	5387.500-5415.000	5376.250-5387.500 5415.000-5425.000	Å	Fe	0.18	
17	Fe5709	5696.625-5720.375	5672.875-5696.625 5722.875-5736.625	Å	(C), Fe	0.16	
18	Fe5782	5776.625-5796.625	5765.375-5775.375 5797.875-5811.625	Å	Cr	0.19	
19	Na D	5876.875-5909.375	5860.625-5875.625 5922.125-5948.125	Å	Na, C, (Mg)	0.21	
20	TiO_1	5936.625-5994.125	5816.625-5849.125 6038.625-6103.625	mag	C	0.006	3
21	TiO_2	6189.625-6272.125	6066.625-6141.625 6372.625-6415.125	mag	C, V, Sc	0.005	3
22	Hδ_A	4083.500 4122.250	4041.600 4079.750 4128.500 4161.000	Å	Hδ	0.64	
23	Hγ_A	4319.750 4363.500	4283.500 4319.750 4367.250 4419.750	Å	Hγ	0.48	
24	Hδ_F	4091.000 4112.250	4057.250 4088.500 4114.750 4137.250	Å	Hδ	0.40	
25	Hγ_F	4331.250 4352.250	4283.500 4319.750 4354.750 4384.750	Å	Hγ	0.33	
...	Hβ_G	4851.320 4871.320	4815.000 4845.000 4880.000 4930.000	Å	Hβ	...	4

[1] C, N are dominant as CN.
[2] C is dominant as C_2.
[3] TiO appears at M0 and cooler.
[4] Hβ-index definition from González (1993).

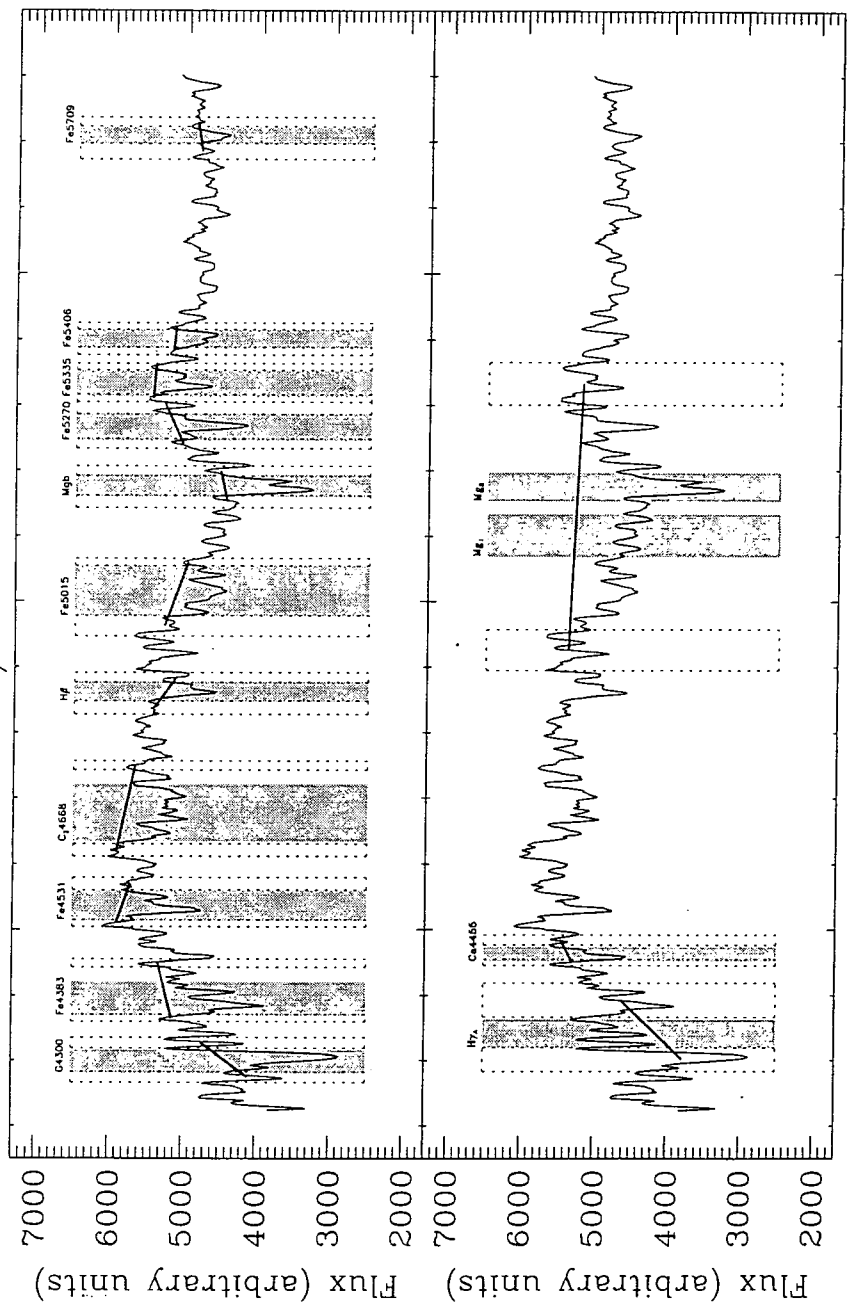

Figure 3.2: Shown are the passbands of most of the Lick/IDS indices measured in the AAT96 run. Central passbands are indicated by the shaded areas, while the sidebands are indicated by the dashed boxes. The pseudo-continuum is indicated by a solid line for each index. The galaxy used in this example is NGC 1339 at instrumental resolution.

3.3 Measuring Line-Strength Indices

3.3.1 The lsld Program

To measure line-strength indices a FORTRAN program, incorporated into the IRAF environment, called lsld was used. This program reads in 1d-spectra with log-wavelength binning. Then it shifts the index passbands to the appropriate redshift of the spectrum stored as a keyword in the header. It then measures the line-strength indices according to Equation 3.1 to 3.3. Fractions of pixels are interpolated in a simple linear way. The program automatically determines which indices from Table 3.1 are in the wavelength range and writes the results, i.e., the index values and the associated errors, to an output file. Note that for all line-strength measurements the input spectra were continuum corrected and broadened to the Lick/IDS resolution.

3.3.2 Poisson Error Estimation

Obviously, the suitability of line-strength indices to investigate stellar populations relies on a proper determination of the associated errors. Even small errors ($\sim$0.20 Å) in the Lick/IDS indices Mgb , Fe5270 and Hβ translate into $\Delta[Fe/H] \simeq 0.18$ dex and Δage $\simeq$ 6 Gyrs respectively (for a composite population of 10 Gyrs and metallicity around [Fe/H] = 0.3, Cardiel et al. (1998)). The ideal method to estimate errors in indices is to process parallel to the science frame an error frame through the whole data-reduction. Unfortunately at the time the data reduction for this thesis was performed no such software was available in IRAF.

Here the errors are estimated from pure photon statistics (Poisson) taking into account the readout noise, the gain of the CCD and the continuum shape correction. Note that these errors do not include any errors from flat-fielding, sky subtraction or any other systematic errors.

3.4 Transformation to the Lick/IDS System

In order to compare our measurements with the stellar population model predictions (Worthey, 1994; Worthey and Ottaviani, 1997) which are based on the Lick/IDS stellar library and the fitting functions (see Section 4.2 on page 66) one has to calibrate the data as accurately as possible to the Lick/IDS system. Ideally one would like to use the same telescope and instrument as the Lick group, but this is obviously not possible. Hence the effects of using a different telescope, spectrograph and recording device (CCD instead of IDS) have to be corrected for.

For the Lick/IDS system all stars and galaxies were observed with IDS. The instru-

mental resolution proved to be approximately constant around 5000 Å with a FWHM of 8.4 Å but degrades to a FWHM of ~10-11 Å at the blue and red end of the spectra. Table 2.4 on page 28 summarizes the dependence of resolution on wavelength (Worthey and Ottaviani, 1997). The Lick/IDS spectra were not fluxed by means of a flux-standard star but normalized to a quartz-iodide tungsten lamp. The resulting continuum shape cannot be reproduced and causes significant offsets for indices with a broad wavelength coverage (e.g., Mg_2; see Table 3.2). Most Lick/IDS spectra of galaxy nuclei were taken through a spectrograph entrance aperture of $1\farcs4 \times 4''$, with a second aperture for sky subtraction located at $21''$ or $35''$ away. The wavelength calibration was performed with helium, neon, mercury, and later cadmium lamps. However, due to instrument flexure and variable stray magnetic fields, shifts and stretches of the wavelength scale of up to 3 Å could occur (Trager et al., 1998) which can cause significant offsets for individual Lick/IDS measurements.

The first step in the calibration is to reproduce the spectral shape of the Lick/IDS spectra as well as possible. Hence we continuum corrected all our data and degraded the spectra to the Lick/IDS resolution. Of course there are still small systematic differences present. The best way to establish any remaining offsets to the Lick/IDS system is to observe as many stars which have been previously observed by the Lick group as possible. Then one can compare the measurements and determine the necessary offset for each index. The two observing runs at the NTT were originally not aimed at a Lick/IDS analysis. However, the observing run at the AAT was specifically designed to serve as a standard for this thesis and to be transfered to the Lick/IDS system. For that reason we observed 13 different stars (G9III - K4III) and 8 galaxies in common with the Lick/IDS stellar library (see Table 2.8 on page 34). Note that for our central line-strength analysis (Chapter 4 & 5) we will use only the data from the AAT96 run as we are unable to calibrate the NTT runs independently. However, for the line-strength gradients (Chapter 7) we make use of the data from all observing runs; the Lick/IDS calibration for the NTT data is described in Chapter 7.

The wavelength range of the AAT96 run allows us to measure 16 different indices in the Lick/IDS system. Namely index #4-17 and #23,25 in Table 3.1. It is straightforward to compare the stars after continuum- and resolution correction, but in order to compare the galaxies, we have to take several other things into account. Most extended objects show line-strength indices which vary with position in the object. Therefore it is crucial to observe the same area in the galaxy as Lick (standard aperture of $1\farcs4 \times 4''$). The slit width of the AAT96 run was $2\farcs3$. Matching the observed area of Lick/IDS and AAT96 gives an aperture of $2\farcs3 \times 2\farcs44$; approximately equivalent to a three pixels extraction over the centre of a galaxy. Nevertheless the apertures are not exactly the same and one would expect some differences if there is a steep line-strength gradient present. Maybe even more important are seeing effects which can also change the central index strength of a galaxy. Furthermore the line strength measurements for galaxies have to be corrected for internal

velocity broadening which is described in detail in Section 3.5.4.

Figure 3.3 compares the line strength measurements for 16 indices in common with Lick/IDS for 12 stars[1] (open triangles) and 8 galaxies (filled circles; NGC 1339, 1375, 1379, 1380, 1374, 1399, 1404, 3379). Each mini-plot in Figure 3.3 shows Lick/IDS - AAT96 *vs* the average of Lick/IDS and AAT96 for a particular index *after* the offset correction which is presented in Table 3.2 has been applied. Note, that only the stars have been used to evaluate the offset to the Lick/IDS system and no offset was applied when the offset was smaller than the 1σ error. On top of each mini-plot the remaining offset and the 1σ error is shown as a number (units are the same as for the index). The error in the offset is evaluated by the mean standard deviation of the stars (with respect to the dashed line) divided by $\sqrt{12-1}$.

Table 3.2: Adopted Lick/IDS Offsets for AAT96

Index	offset
G4300	$+0.21 \pm 0.09$ Å
Fe4383	$+0.60 \pm 0.13$ Å
Ca4455	$+0.37 \pm 0.06$ Å
Fe4531	$+0.00 \pm 0.10$ Å
$C_2$4668	-0.19 ± 0.17 Å
Hβ	-0.05 ± 0.04 Å
Fe5015	$+0.00 \pm 0.08$ Å
Mg_1	$+0.003 \pm 0.002$ mag
Mg_2	$+0.023 \pm 0.003$ mag
Mgb	$+0.15 \pm 0.09$ Å
Fe5270	$+0.07 \pm 0.05$ Å
Fe5335	$+0.00 \pm 0.08$ Å
Fe5406	$+0.00 \pm 0.04$ Å
Fe5709	$+0.00 \pm 0.06$ Å
Hγ_A	$+0.45 \pm 0.28$ Å
Hγ_F	$+0.00 \pm 0.14$ Å

All offsets: Lick/IDS - AAT96

Most off the indices show zero or small offsets to the Lick/IDS system, a possible exception is Fe4383. The rather large offset in Mg_2 is due to a well known difference in continuum shape. With the possible exception of G4300 (which is at the blue end of our spectra) there are also no signs of any offset-dependence on line-strength. The galaxies show for all indices more scatter than the stars which is somewhat reflected in the bigger error bars, but there are also some "dubious" outliers. This is not surprising recalling the problems of matching the Lick/IDS galaxy observations discussed earlier and the fact that the Lick group had to observe these Fornax galaxies at a very high airmass. However,

[1]Note that the star HD221148 was excluded from our sample, because it proved to be very different to the Lick/IDS measurement – possibly due to misidentification.

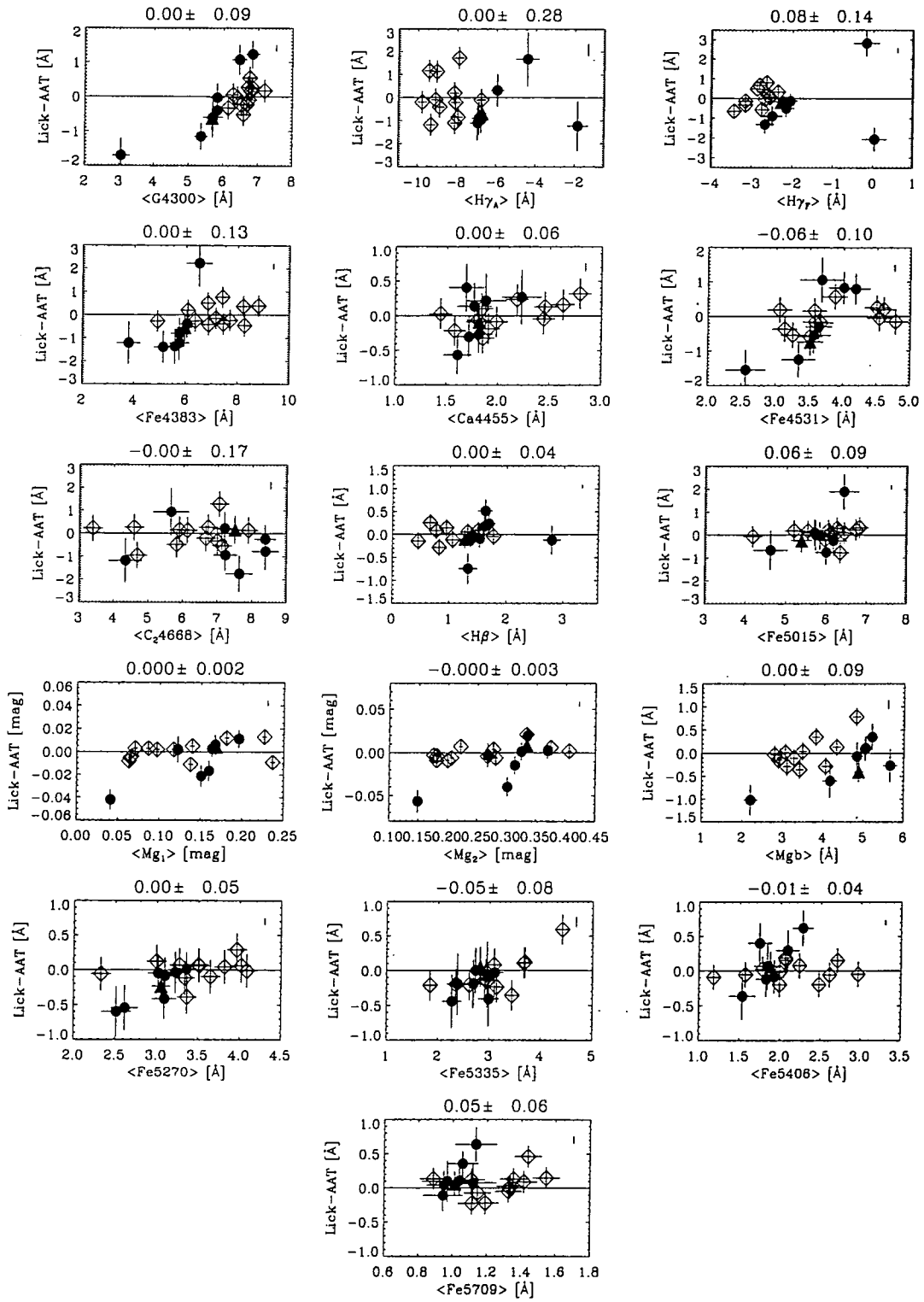

Figure 3.3: Comparison of 16 indices between Lick/IDS and AAT96 *after* Lick/IDS offset correction (see Table 3.2). Open diamonds, filled circles and the filled triangle represent stars, Fornax-galaxies and NGC3379 respectively. The remaining offset and the associated 1σ-error for each index are shown above the mini-plots. The error in the offset is also shown as an error bar in the upper right corner of each mini-plot.

with the possible exception of the indices G4300 and Fe4383 the galaxy offset is consistent with the stellar data.

Figure 3.4 shows the *offset-corrected* measurements in a linear comparison. Strictly speaking these transformations to the Lick/IDS system are only valid in the line-strength range which is covered by the comparison stars. For indices such as $H\gamma_A$ and Fe4383 this can possibly create a problem because the galaxies are located somewhat outside the stellar data. For the Balmer lines and Mg*b* the stars mostly show an absorption that is too weak indicating that *galactic* G,K giants do not necessarily resemble the spectra of early-type galaxies. As we will demonstrate in Section 4.3 particular S0-type galaxies show on average a stronger absorption in $H\beta$.

Table A.1 in Appendix A on page 196 summarizes our line-strength measurements for the 12 Lick/IDS comparison stars and the two velocity standards obtained during the AAT96 run calibrated onto the Lick/IDS system.

Direct comparison of stars and galaxies observed in common with the Lick/IDS library has shown that after corrections for continuum shape, resolution and index offset, our line-strength measurements are calibrated to the Lick/IDS system. Another way to check this is to investigate plots of indices against each other which measure similar elements and compare the results with the original Lick/IDS galaxy sample (Trager et al., 1998). Here we present plots of nine indices which are used in this thesis and are a basic ingredient for the interpretation of stellar populations in early-type galaxies.

Figure 3.5 shows a comparison of three important Fe-indices: <Fe>, Fe5015 & Fe5406. The sample of galaxies from the AAT96 run are represented as filled circles whereas the Lick/IDS galaxy sample is shown as small dots. Furthermore our sample of comparison stars is shown as "five pointed" stars. The mean error of the Lick/IDS galaxies is shown as big error bar in the upper left corner. The smaller error bar represents the error in the offset to the Lick/IDS system for our measurements. From these plots it is clear that our data agree very well with the original Lick/IDS measurements. This is supported by the fact that single stellar population models (Worthey, 1994, see Section 4.1 on page 65 for explanation) which are shown in Figure 3.5 as well, predict accurately the relation between these indices.

A similar comparison can be made when one uses instead of Fe-indices the three Mg-indicators Mg_1, Mg_2 and Mg*b* which is shown in Figure 3.6. Again the AAT96 measurements are following very well the relation set by the Lick/IDS galaxy sample. However, the model predictions deviate from the observed values for large metallicities when Mg2 is plotted *vs* Mg_1 or Mg*b* (see also Chapter 5 in Worthey, 1992). Note that this is an effect which is inert to the Lick/IDS system and the associated models and cannot be attributed to a calibration error in our data. At this point we just note the discrepancy of model predictions and the observed relation between index measurements of galaxies. But later (see Section 7.5.3 on page 172) when we use the model predictions

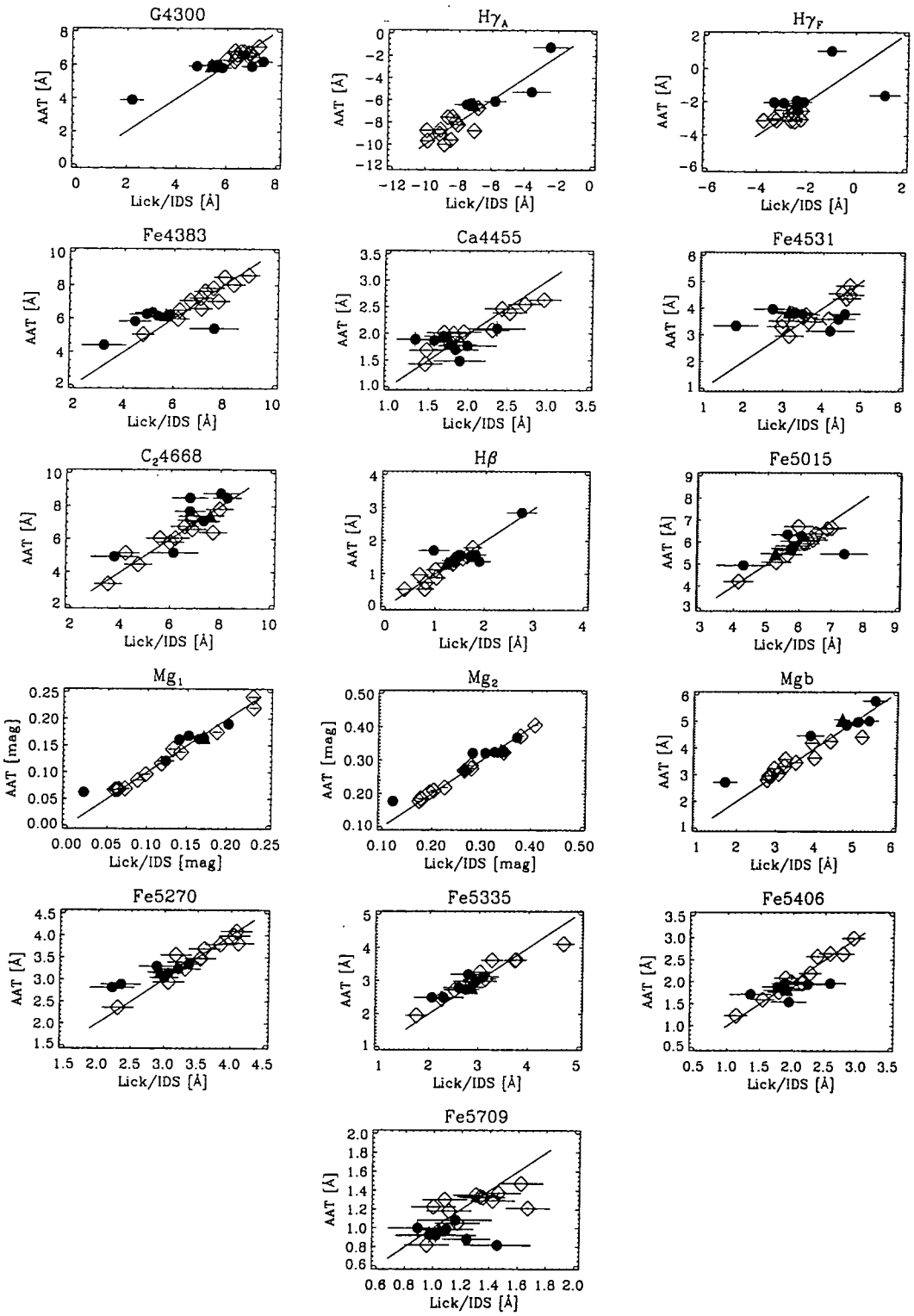

Figure 3.4: Linear comparison of 16 indices between Lick/IDS and AAT96 **after** Lick/IDS offset correction (see Table 3.2). Symbol definitions as in Figure 3.3.

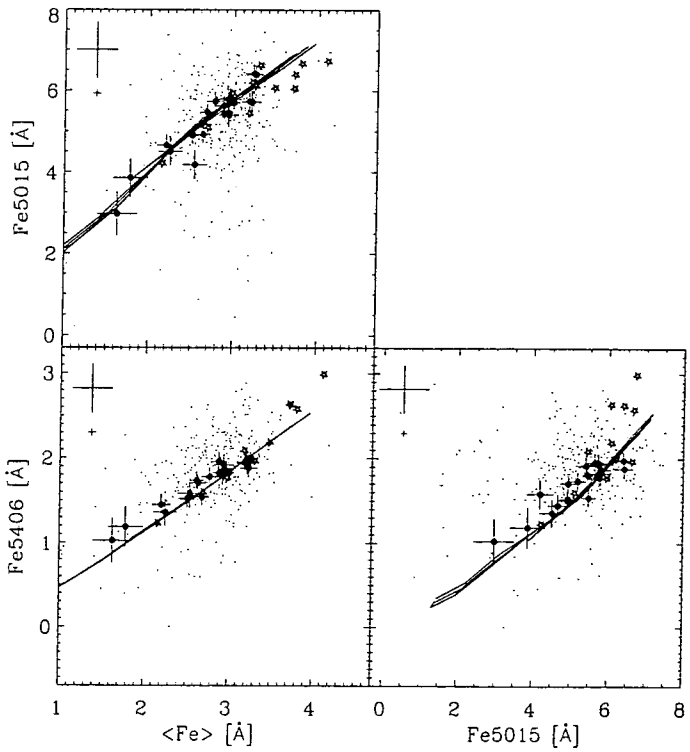

Figure 3.5: Shown are index *vs* index plots for three well established Fe-indicators in the Lick/IDS system. The filled circles and small dots represent AAT96 and Lick/IDS galaxy measurements respectively. The five pointed stars represent the comparison stars observed during the AAT96 run. The big error bar in the upper left corner represents the mean error for Lick/IDS galaxies whereas the small error bar shows the error in the offset to the Lick/IDS system for the AAT96 run. Overplotted are model predictions by Worthey (1994).

to analyse the stellar populations of NGC1381 we will elaborate further on this point.

One further remark on Figure 3.6: For strong Mgb absorption the comparison stars (G-K giants) are not able to produce the kind of absorption seen in galaxies. Usually K-giants are regarded as a good representation of the spectra of early type-galaxies, but here it is obvious that galactic G-K-giants alone cannot resemble the detailed spectral features of metal rich early-type galaxies.

The last indices which we will investigate at this point are the Blamer lines Hβ, Hγ_A and Hγ_F. These will be particularly helpful in later analysis to establish age estimates of early-type galaxies. The results[2] are presented in Figure 3.7. The agreement between our measurements and Lick/IDS is very good with perhaps a slight offset for model predictions at weak Balmer absorption. Note that the spread of the Hβ index for Lick/IDS galaxies is rather large and many data points are well outside the model predictions. However the

[2]The set of Lick/IDS Hγ_A and Hγ_F measurements was kindly provided by S. Trager

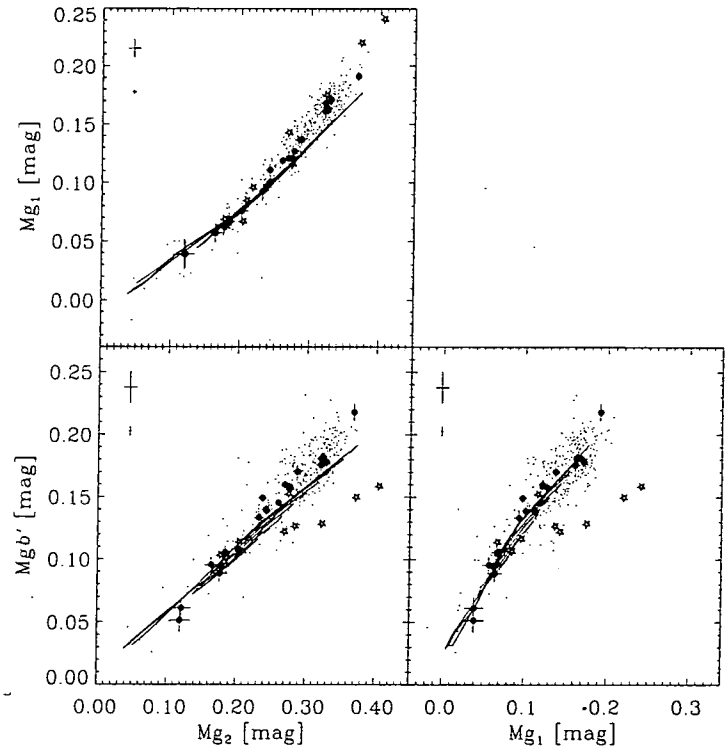

Figure 3.6: Shown are index *vs* index plots for three Mg lines in the Lick/IDS system. Symbol definitions as in Figure 3.5. For a definition of the Mgb' index see Equation 5.1 on page 108.

two indices which measure Hγ absorption show a very tight relation.

To conclude we have shown by comparing stellar as well as galaxy observations (after correcting our data for continuum shape, spectral resolution and individual index-offsets) that our line-strength measurements are very accurately calibrated to the Lick/IDS system. This is essential as we will use single stellar population (SSP) models based on the Lick/IDS stellar library to analyse the stellar population of the early-type galaxies in the Fornax cluster. We note that the model predictions agree well with the general relations for the Fe- and Balmer-indices. However, when Mg indices are compared then small deviations are evident.

3.5 Velocity Dispersion Measurements and Corrections

In order to correct the line-strength indices as measured in galaxies for velocity dispersion broadening we need to evaluate the velocity dispersion for each extraction of the sample galaxies. In the AAT96 run we used a long-slit setup despite the fact that we integrated only for short times. Hence only a central 5 pixels region was extracted from all galaxy spectra, yielding an effective aperture of $2''.3 \times 3''.85$. This is our standard aperture for the

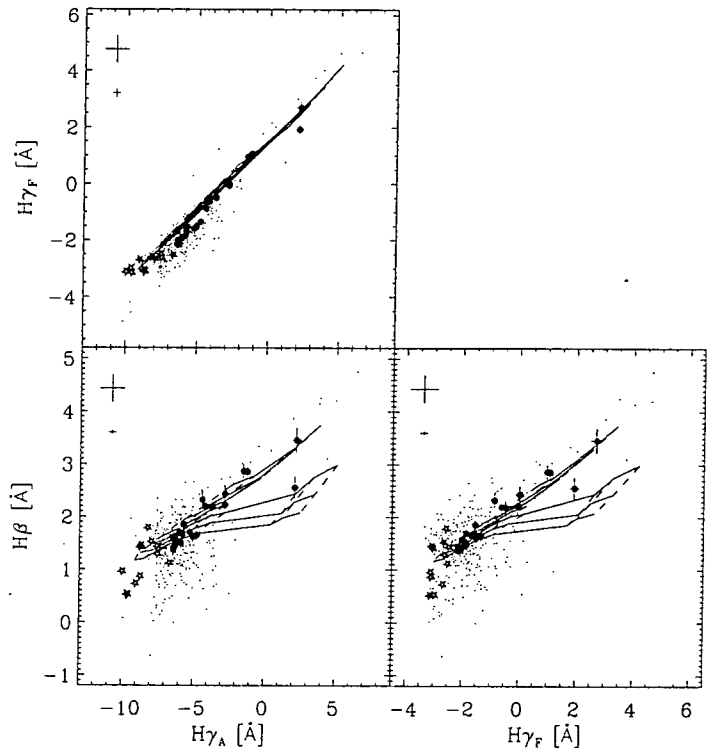

Figure 3.7: Shown are index *vs* index plots for three Balmer lines in the Lick/IDS system. Symbol definitions as in Figure 3.5.

analysis of the central stellar populations which we present in Chapter 4.

Usually rotation and velocity dispersion profiles of early-type galaxies are obtained by using either the Fourier quotient technique (Sargent et al., 1977) or the correlation method (Tonry and Davis, 1979). A common property of these methods is that they assume intrinsically Gaussian velocity distributions. Bender (1990) introduced the Fourier correlation quotient (FCQ) method which is based on the deconvolution of the peak of the template-galaxy correlation function with the peak of the autocorrelation function of the template star. This method does not assume a purely Gaussian broadening function and is able to measure detailed deviation from it. Furthermore this procedure is less sensitive to template mismatching. There is also a variety of other software using similar techniques. Note that there are also programs which evaluate velocity dispersions in real space.

Sophisticated software programs like FCQ deliver potentially better results than simple cross-correlation methods but carry the disadvantage that they need high quality and high S/N data. The spectral resolution of the AAT96 run was unfortunately rather low but the central spectra are of very high S/N. We decided to follow a two-folded approach and measure the central velocity dispersions with FCQ (fitting only a Gaussian and no higher order terms) as well as with `fxcor`, a cross-correlation program in the IRAF environment (see also Section 3.5.1). For extended galaxy spectra, i.e., spectra of lower S/N, which

we will analyse in Chapter 7, we use only the `fxcor` program. For a thorough description of the FCQ technique the reader is referred to Bender (1990). What now follows is a description of how we used the `fxcor` task to measure velocity dispersions followed by a summary of our specific FCQ setup.

3.5.1 The Fourier Cross Correlation Method – `fxcor` task

The cross-correlation method was first employed to measure the redshift of the galaxy spectra in order to evaluate the required wavelength shift for the index-passbands. But at the same time one can make use of the measured width (FWHM) of the correlation peak and estimate the velocity-dispersion.

For the following discussion let $G(n)$ be the spectrum of a galaxy whose redshift and velocity dispersion are to be determined and $S(n)$ the spectrum of a template star at zero redshift, similar spectral type to the galaxy and at instrumental resolution. The spectra have been continuum subtracted and end-masked, and are each sampled in N bins of equal $\log\lambda$ spacing. A velocity shift is then a linear function of the spacing $\Delta\log\lambda$, with velocity increments Δv as follows:

$$\Delta v = c \times \Delta \ln\lambda \tag{3.6}$$

$$= c \times \ln(10) \times \Delta\log\lambda \tag{3.7}$$

where c is the speed of light. Now the normalized cross correlation function is defined as:

$$c(n) = G(m) \otimes S(n) = \frac{1}{N\sigma_G\sigma_S}\sum_{m=0}^{N} G(m)S(m-n) \tag{3.8}$$

where σ_G and σ_S are the RMS deviations:

$$\sigma_G^2 = \frac{1}{N}\sum_{n=0}^{N} G(n)^2 \tag{3.9}$$

$$\sigma_S^2 = \frac{1}{N}\sum_{n=0}^{N} S(n)^2 \tag{3.10}$$

The cross correlation is best performed in Fourier space, which also enables easy filtering of high and low frequency noise. Let $\tilde{G}(s)$ be the Fourier transform of $G(n)$, and $\tilde{S}(s)$ the transform of $S(n)$. The Fourier transform of equation 3.8 is then:

$$\tilde{C}(s) = \frac{1}{N\sigma_G\sigma_S}\tilde{G}(s)\tilde{S}^*(s) \tag{3.11}$$

where $\tilde{C}(s)$ is the Fourier transform of $c(n)$, and * denotes the complex conjugate. The cross-correlation function will show a peak at n_{peak} corresponding to the redshift of the galaxy divided by Δv. The width of the peak will be related to the broadening of the galaxy absorption lines compared to the instrumental resolution of the template star.

The dependence of the width of the cross-correlation peak on the velocity-dispersion of the galaxy has to be calibrated. The easiest way is to broaden template stars with a Gaussian to mimic velocity dispersions in a certain range and cross-correlate those with the unbroadened template spectra. In order to achieve a good calibration curve it is essential to use a range of template stars, matching the spectral characteristics of the galaxies as well as possible. Here stars, ranging from G9 to K4 giants (see also Table 2.8) were broadened with a Gaussian to velocity dispersion of 20 to 400 kms^{-1} in steps of 20 kms^{-1} and used for the `fxcor` calibration.

Prior to the `fxcor` analysis, the raw spectra and template stars were rebinned onto a log-wavelength scale, where there start and end wavelength were kept constant. Within the `fxcor` task the spectra of object and template were continuum subtracted and cut to a user defined wavelength range. Then the Fourier transform was computed and a "ramp" filter applied to remove large scale variations as well as noise from the spectra. The wavelength region for the AAT96 run was 4700 to 5600 Å. This includes the strong Mg feature at 5200 Å and also the Fe lines redwards of it. The `fxcor` program calculates the correlation function, locates the highest peak and fits a Gaussian to obtain an accurate FWHM of the cross-correlation peak.

The final calibration curve derived from all stars is presented in Figure 3.8 where the solid line represents the mean relation which is stored in a look-up table. The instrumental resolution of the AAT96 run was approximately 105 kms^{-1} so it is not surprising that the curve shows little power below 70 kms^{-1} and hence one cannot measure any velocity dispersions below $\sim$ 70 kms^{-1} with this method.

Some of our galaxies show very strong absorption in Hβ, which can even approach the strength of F-type stars (e.g., ESO359-G02 and ESO358-G25). In this kind of stars Balmer lines are intrinsically broad mimicking a large velocity dispersion. While the metal absorption lines are usually weak in young galaxies, the Balmer absorption is very prominent. This leads to an over-weighting of the Balmer lines in `fxcor` resulting in too large velocity dispersion estimates.

To check for this effect the whole sample was reanalysed with `fxcor` using a wavelength range which excludes Hβ (4900-5600 Å) but all other parameters were kept the same. Table 3.3 summarizes the velocity dispersions measured with `fxcor` for both wave-

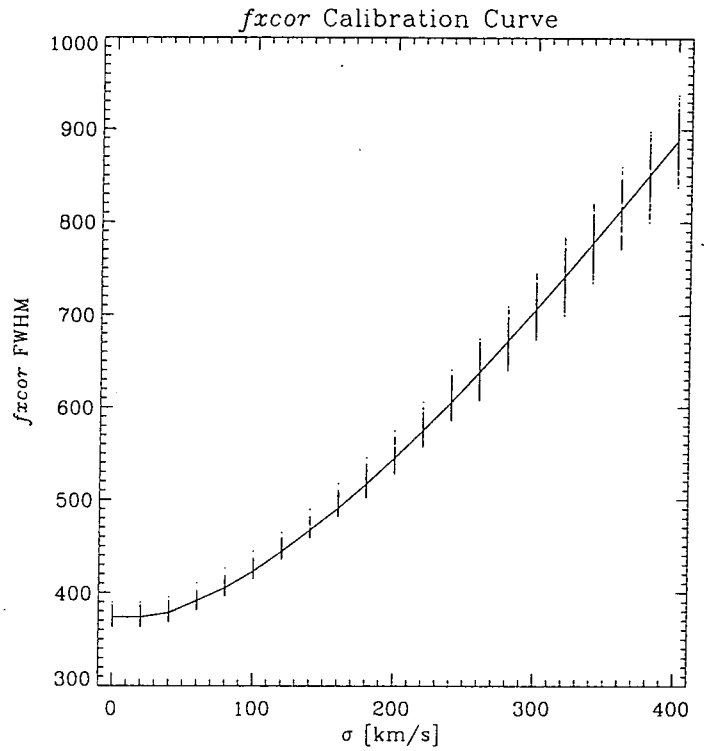

Figure 3.8: fxcor calibration curve for AAT96 run (short wavelength range). Detailed setup described in the text. The solid line connects mean values in each σ-bin. For a given galaxy FWHM the velocity dispersion can be found by tracing horizontally to the curve, then down to the abscissa.

length regions. As can be seen for most of the galaxies, both wavelength ranges give very similar results. But for Hβ strong galaxies, the long wavelength range (including Hβ) gives always larger velocity dispersions. Multiple observations of the same galaxy were averaged. Errors are derived from a comparison with literature data (see Section 3.5.3) and are quoted in column 8.

3.5.2 The FCQ Setup

Having measured central velocity dispersions with a simple correlation method we will now describe briefly the measurements with the FCQ-program (version FCQ8). The program is implemented in MIDAS so all spectra were transferred via the FITS format into the MIDAS environment. Again galaxies and template stars were rebinned to the same wavelength range (4876 to 5653 Å, just excluding Hβ) and step size in $\log\lambda(\sim 0.7$ Å). Note that in order to give a better determined cross-correlation peak the pixel sampling was doubled compared to the original instrumental sampling. For each galaxy we measured the velocity dispersion by using a set of eight different template stars. Note that only a simple Gaussian was fit to the broadening function and no higher order terms were investigated.

For galaxies with a central velocity dispersion of $\sigma_0 \geq 90$ kms^{-1}, all eight stars gave very similar results and an average value was adopted. When using FCQ one can check the results by visually inspecting the broadening function of the galaxy and overplotting the fit of the FCQ-program. Furthermore the program provides the user with a spectrum of the template star broadened to the measured velocity dispersion of the galaxy. Overplotting allows a check for unreasonable fits and severe template mismatching to be made. For galaxies with $\sigma_0 < 90$ kms^{-1} some template stars did not give a good fit and were excluded from the template sample. The remaining measurements were averaged. Using this procedure velocity-dispersions as low as ~ 50 kms^{-1} could be recovered, although the rms error here is about three times bigger than for galaxies with $\sigma \geq 90$ kms^{-1}. This was tested by running simulations and changing slightly parameters such as wavelength range, continuum fitting etc. Table 3.3 summarizes the results.

3.5.3 Central Velocity Dispersions

Both, `fxcor` and FCQ determined remarkably similar velocity dispersions for galaxies with $\sigma > 70$ kms^{-1}. However for smaller galaxies `fxcor` could not deliver reliable results. Hence we adopted as our final velocity dispersion measurements for central galaxy extractions the FCQ values (see Table 3.3 column 5 and 6).

To ensure that the velocity dispersions measured here are on the same system as those of other studies, we have compared the results with the literature. Velocity dispersions of Fornax early-type galaxies are listed in McElroy (1995); Smith (1998); D'Onofrio et al. (1995); Graham et al. (1998). We corrected the measurements of Smith (1998); D'Onofrio et al. (1995); Graham et al. (1998) for aperture effects, i.e., to match the AAT96 aperture. The data from McElroy (1995) was not corrected because the data in the catalogue is already inhomogeneous and an accurate aperture correction is impossible. The results from the literature comparison are presented in Figures 3.9 to 3.11. The quoted offsets in the figures are the median offsets for all galaxies with $\sigma \geq 75$ kms^{-1}. There is an excellent agreement between Smith (1998), McElroy (1995) and Graham et al. (1998) with the AAT96 measurements. D'Onofrio et al. (1995) seems to have a small offset to the standard system in the sense that their values are too big.

Certain galaxies require more attention. For example, the velocity dispersion of NGC1419 (labeled in all plots) deviates by more than 2σ from the mean relation in the comparison with Smith (1998) and is also discrepant in McElroy (1995). We note that the velocity dispersion of this galaxy is based on low resolution spectra and that the authors quote a large error bar for this galaxy. However, Graham et al. (1998) quote a velocity dispersion very close to our measurement. The galaxy with the largest velocity dispersion (NGC1399) has a very steep velocity dispersion profile in the centre and it is therefore not surprising to find larger offsets probably due to seeing and aperture effects. Overall we find the best agreement between our measurements with the new compilations by Smith

(1998) and Graham et al. (1998). This is not surprising as both compilations are based on good quality data and excellent use of analysing techniques. We regard the bigger scatter found in the McElroy (1995) catalogue as a sign of the somewhat inhomogeneous sources from which the catalogue was compiled from.

The errors in $\log \sigma$ quoted in column 7 of Table 3.3 were derived in the following way. The datasets of Smith (1998) and Graham et al. (1998) were corrected for the small offsets to our system and then the external 1σ error for all galaxies with average $\sigma \geq 70$ kms^{-1} was calculated. The external error is 0.035 in $\log \sigma$ units or 8.4%. When we exclude the discrepant data point of the Smith (1998) sample (NGC1419, 3.3 $\times$ standard error offset) then we find an external error of 0.024 in $\log \sigma$ units or 5.7%. The latter error was assigned to all galaxies with $\sigma \geq 70$ kms^{-1}. For galaxies with smaller velocity dispersion we cannot be sure that our velocity dispersion estimates are very accurate, so we adopted three times the external error.

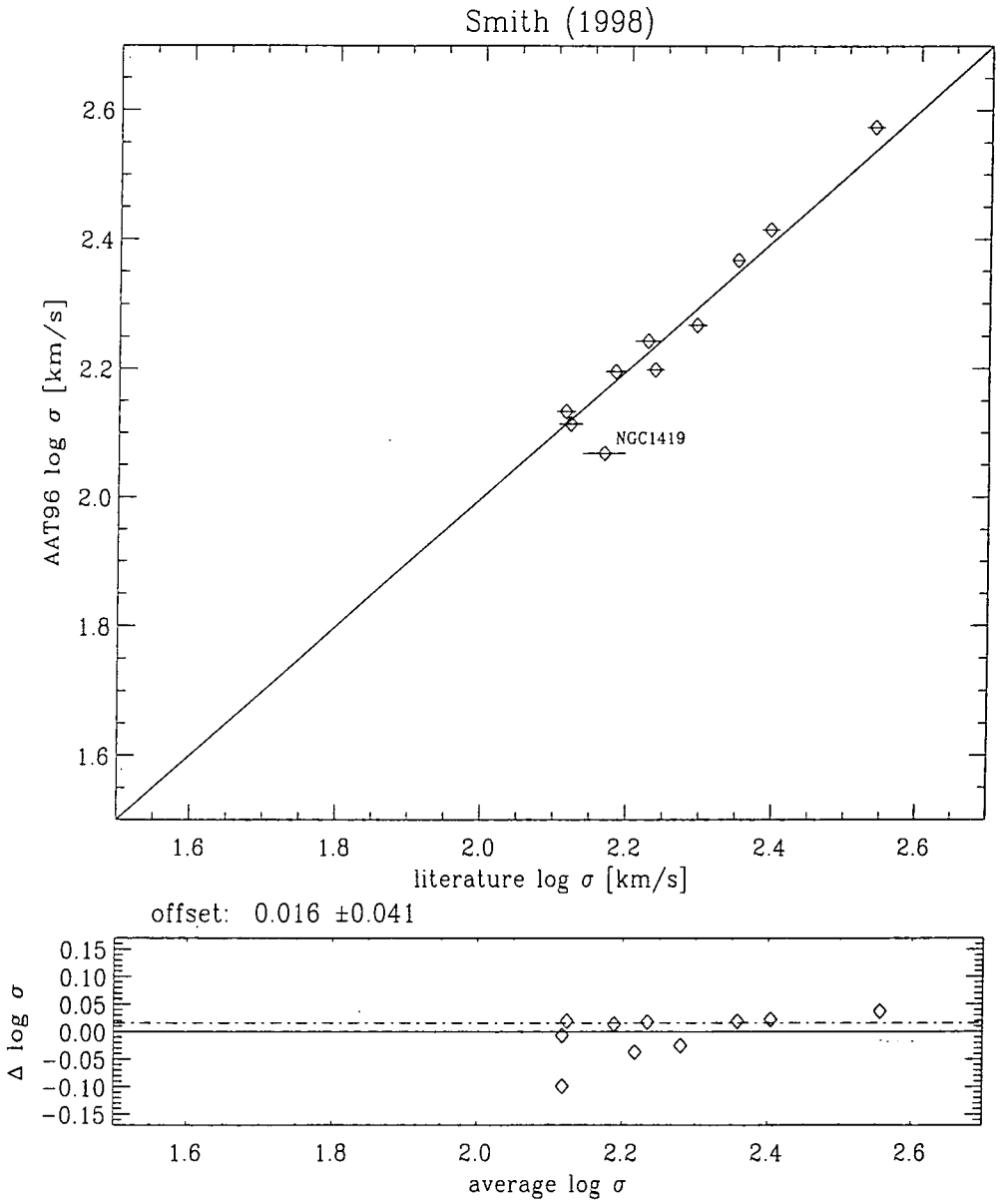

Figure 3.9: Comparison of our AAT96 central velocity dispersions with the compilation from Smith (1998). Plotted are AAT96 velocity dispersions *vs* literature values (top panel) and $\Delta \log \sigma$ in the sense AAT96 - literature *vs* average velocity dispersion (lower panel). The median offset for all galaxies with average velocity dispersion $\geq$ 75 kms^{-1} is shown by a dashed dotted line (lower panel). This offset is also quoted as a number just above the lower panel.

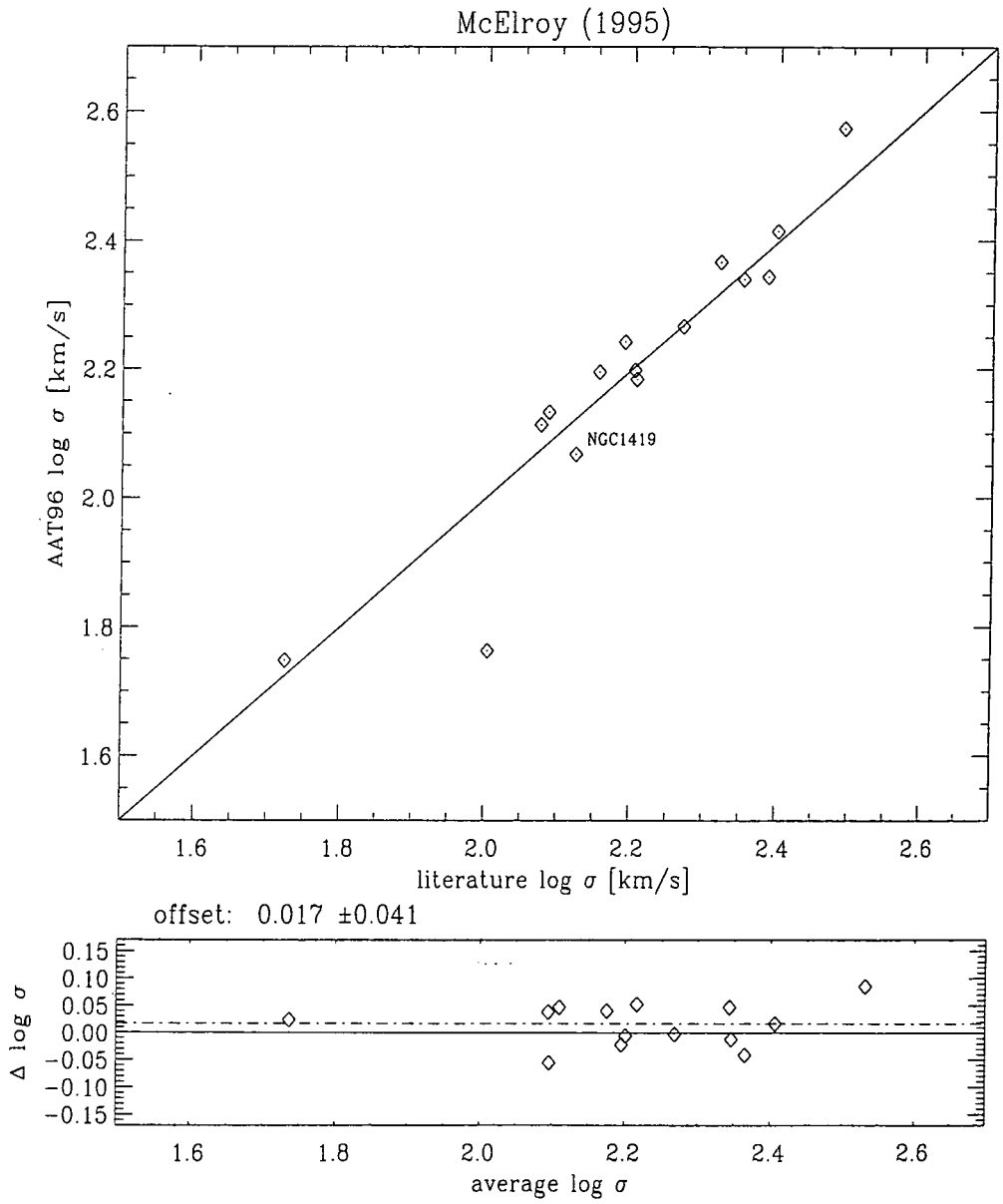

Figure 3.10: Comparison of our (AAT96) velocity dispersions with the compilation from McElroy (1995). Notations as in Figure 3.9

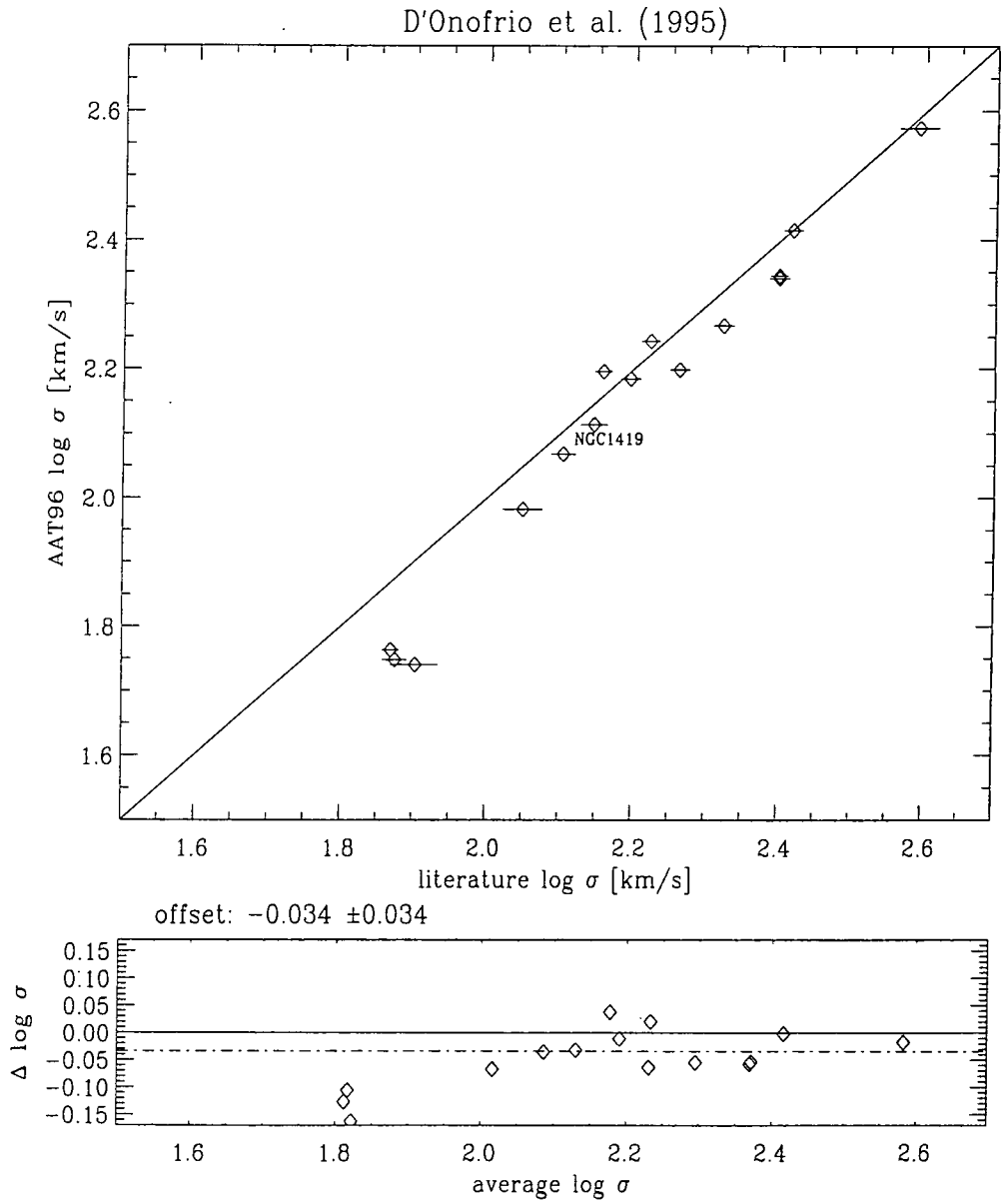

Figure 3.11: Comparison of our (AAT96) velocity dispersions with the data from D'Onofrio et al. (1995). Notations as in Figure 3.9

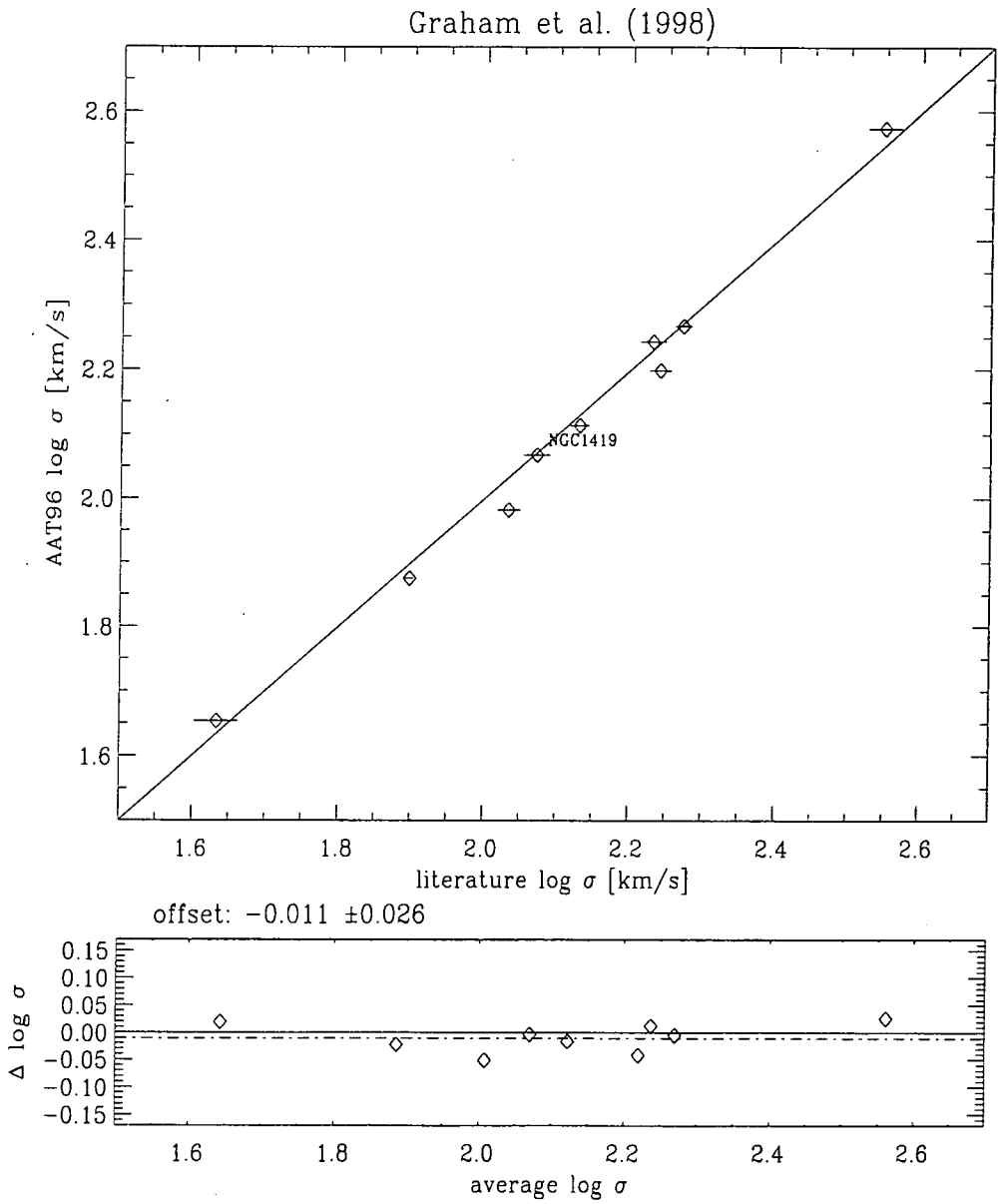

Figure 3.12: Comparison of our (AAT96) velocity dispersions with the data from Graham et al. (1998). Notations as in Figure 3.9.

Table 3.3: Adopted Recession Velocities and Central Velocity Dispersions - AAT96 Run

Name	fxcor v_{helio} kms^{-1}	fxcor [a] σ_0 kms^{-1}	fxcor [b] σ_0 kms^{-1}	FCQ σ_0 kms^{-1}	adopted $\log\sigma_0$	error $\log\sigma_0$
NGC1316	1744±16	236	222	221	2.344	0.024
NGC1336	1439±11	99	99	96	1.982	0.024
NGC1339	1355±12	159	161	158	2.199	0.024
NGC1351	1529±13	153	155	157	2.196	0.024
NGC1373	1341±10	71	70	75	1.875	0.024
NGC1374	1349±13	188	186	185	2.267	0.024
NGC1375	726±13	59	26	56	1.748	0.072
NGC1379	1360±11	134	132	130	2.114	0.024
NGC1380	1858±14	216	217	219	2.340	0.024
NGC1380A	1545±11	53	32	55	1.740	0.072
NGC1381	1726±12	153	153	153	2.185	0.024
NGC1399	1431±28	364	373	375	2.574	0.024
NGC1404	1923±17	256	254	260	2.415	0.024
NGC1419	1574±10	121	118	117	2.068	0.024
NGC1427	1416±10	173	174	175	2.243	0.024
IC1963	1608±08	48	44	58	1.763	0.072
IC2006	1371±12	135	136	136	2.134	0.024
ESO359-G02	1461±18	78	24	45	1.653	0.072
ESO358-G06	1259±12	53	27	58	1.763	0.072
ESO358-G25	1408±19	85	30	58	1.763	0.072
ESO358-G50	1302±11	48	29	49	1.690	0.072
ESO358-G59	1006±12	36	0	54	1.732	0.072
NGC3379	896±14	226	229	233	2.367	0.024

Notes:
All values are derived from an effective central aperture of 2.″3×3.″85.
The adopted central velocity dispersions, σ_0 and $\log\sigma_0$ are given in column 5 and 6 respectively. The adopted errors are given in column 7.

[a] 4700-5600 Å. Including Hβ
[b] 4900-5600 Å. Excluding Hβ

3.5.4 Velocity Dispersion Correction

The observed spectrum of a galaxy is the convolution of the integrated spectrum of its stellar population(s) by the instrumental broadening and the distribution of line-of-sight velocities of the stars. The instrumental resolution and the velocity dispersion broaden the spectral features, in general reducing the observed line-strength compared to the intrinsic values. In this Section we discuss the corrections required to calibrate the indices to a reference velocity dispersion and resolution.

As the indices will be compared to stellar population models based on the Lick/IDS

stellar observations (Worthey, 1994), the indices are corrected to zero velocity dispersion. Spectra of 15 G9-K4 giant stars were used to calculate the velocity dispersion corrections. The stars were first broadened to the Lick/IDS resolution and then broadened using a Gaussian filter to $\sigma = 20 - 360$ kms^{-1} in steps of 20 kms^{-1}. The indices are than measured for each star and σ and a correction factor, $C(\sigma)$, such that $C(\sigma)$ =Index(0)/Index(σ) is determined.

Figure 3.13 shows the dependence of the correction factor on σ for 16 indices. The stars are represented by dots. Note that for the molecular indices Mg_1 and Mg_2 and the index $H\gamma_F$ [3] the correction factor is defined as $C(\sigma)$ = Index(0) − Index(σ). The scatter in $C(\sigma)$ at 360 kms^{-1} was $\leq 5\%$ for all indices but Hβ.

It is worth looking in detail why the Hβ correction seems to be so insecure. The derived correction factors are only useful if the stars used for the simulations resemble the galaxy spectra. In principle one might expect a dependence of the correction factor on line-strength - but most indices do not show such a behaviour. In fact Hβ is the only index where we find a significant influence of line-strength on the correction factor at a given σ. It turns out that stars which exhibit Hβ-absorption $\leq$ 1.1 Å lead to correction factors of $\leq$ 1.0 and stars with Hβ-absorption $>$ 1.1 Å imply positive corrections. In the Fornax sample there are no galaxies with a Hβ line-strength of less than 1.4 Å, hence only stars with a Hβ index greater 1.4 Å have been used to evaluate the correction factor.

Another way to check the accuracy of the velocity dispersion corrections is to use galaxy spectra with a low velocity dispersion as templates and treat them in the same way as stars. The galaxies, NGC1373, NGC1380A, NGC1336, IC1963 and ESO358-G59 were used for this purpose. They span a range in Hβ absorption of $\sim$ 1.7 to 3 Å. In Figure 3.13 the galaxies are represented by open circles and they agree very well with the stellar correction for most of the indices. As expected for Hβ, the galaxies match the results from stars with a Hβ absorption $>$ 1.1.

The final correction factors are derived by taking the mean of 15 stars and five galaxies in each σ-bin (solid line in Figure 3.13). For Hβ, only stars with Hβ-absorption $>$ 1.1 and the galaxies are used. The values and their respective 1σ errors are stored in a look-up table.

3.6 Final Central Absorption Line-Strength

The velocity dispersion corrections and the offset to the Lick/IDS system are applied by a FORTRAN program which reads in the raw index-measurements from continuum corrected and resolution corrected galaxy spectra. For each galaxy and index it applies first an

[3] This index is actually not a molecular index but typical index values are close to zero hence a correction *factor* can degenerate.

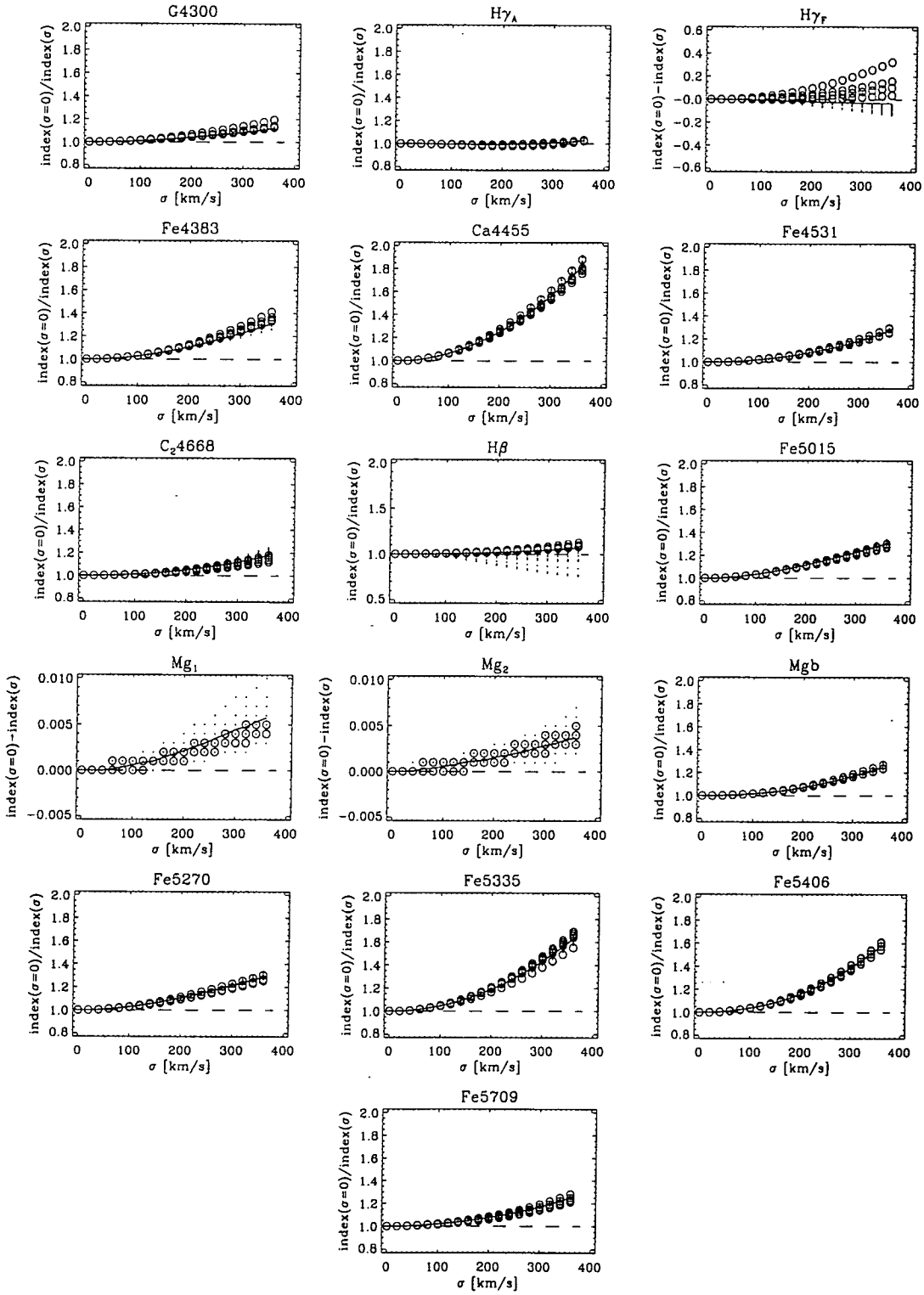

Figure 3.13: Velocity dispersion corrections. Dots and open circles represent stars and galaxies respectively. The solid line connects the mean of all data points in each σ-bin. Note that for Hβ only stars with equivalent width of Hβ > 1.1 Å have been used to determine the mean. See text for details.

correction for velocity dispersion using the results from Section 3.5.4 and 3.5.1. After that it applies a constant offset for each index (see Section 3.4) in order to transform our system onto the Lick/IDS system. The program linearly interpolates between σ-bins and also adds the error from the velocity-dispersion factor to the raw Poisson error of the spectra. As the error in the correction factor is much bigger than any error caused by uncertainties in σ, we assumed the velocity dispersion of the galaxies to be error free. Note that the Lick/IDS offset error is a constant value and does not depend on the velocity dispersion of the galaxy itself. Therefore we did not include the former error in the individual index errors but rather quote for each index a common offset error (see Figure 3.3 and Table 3.2). The final corrected central ($2''.\times3''.85$) index measurements and associated errors for the Fornax galaxies and NGC3379 are presented in Table 3.4. For each galaxy we give the index measurement in the first row whereas the 1σ error is given in the second row.

Note that for the galaxies NGC1381 and NGC1427 we combined three exposures yielding a very high S/N spectrum. Here our index-error estimation taking into account only the Poisson error becomes invalid because of systematic errors such as wavelength calibration. By comparing individual exposures we established that 1.5 $\times$ the original Poisson error estimate is a good indicator of the true error. Former adjusted error was adopted in Table 3.4 and for any further analysis.

Table 3.4: Fully corrected Lick/IDS indices for the central (2″×3″.85) extraction of the AAT96 run

Name	G4300 [Å]	Fe4383 [Å]	Ca4455 [Å]	Fe4531 [Å]	C4668 [Å]	Hβ [Å]	Fe5015 [Å]	Mg_1 [mag]	Mg_2 [mag]	log σ_0
NGC1316	5.14	5.95	2.02	3.57	8.02	2.20	5.70	0.119	0.260	2.344
±	0.11	0.16	0.09	0.12	0.19	0.07	0.16	0.003	0.004	0.024
NGC1336	5.47	4.85	1.49	3.03	4.70	1.64	4.90	0.097	0.237	1.982
±	0.15	0.21	0.11	0.16	0.23	0.09	0.21	0.005	0.006	0.024
NGC1339	5.93	6.15	1.88	3.78	7.69	1.52	5.63	0.168	0.321	2.199
±	0.17	0.25	0.14	0.18	0.26	0.11	0.25	0.006	0.007	0.024
NGC1351	6.04	5.56	1.73	3.26	5.54	1.50	5.74	0.137	0.287	2.196
±	0.16	0.23	0.13	0.17	0.25	0.10	0.23	0.005	0.006	0.024
NGC1373	5.98	5.83	1.78	3.36	5.41	1.85	5.18	0.101	0.243	1.875
±	0.15	0.21	0.11	0.16	0.24	0.10	0.21	0.005	0.006	0.024
NGC1374	6.21	5.80	1.85	3.58	7.07	1.57	5.82	0.164	0.323	2.267
±	0.15	0.22	0.13	0.16	0.24	0.09	0.22	0.005	0.006	0.024
NGC1375	3.90	4.40	1.48	3.33	4.93	2.85	5.47	0.062	0.177	1.748
±	0.14	0.19	0.10	0.15	0.22	0.09	0.20	0.005	0.006	0.072
NGC1379	5.99	5.37	1.76	3.14	5.16	1.70	4.93	0.121	0.269	2.114
±	0.14	0.21	0.11	0.16	0.23	0.09	0.21	0.005	0.006	0.024
NGC1380	5.92	6.26	1.70	3.84	8.50	1.37	5.72	0.161	0.321	2.340
±	0.18	0.27	0.16	0.19	0.29	0.11	0.27	0.006	0.007	0.024
NGC1380A	4.16	5.04	1.67	3.53	5.43	2.87	5.79	0.076	0.202	1.740
±	0.20	0.28	0.15	0.21	0.32	0.13	0.29	0.007	0.009	0.072
NGC1381	6.09	5.82	1.85	3.42	5.99	1.70	5.45	0.121	0.274	2.185
±	0.11	0.15	0.08	0.11	0.16	0.06	0.15	0.003	0.005	0.024
NGC1399	5.90	6.49	2.18	4.06	8.93	1.41	6.41	0.191	0.368	2.574
±	0.17	0.29	0.16	0.17	0.39	0.08	0.24	0.004	0.004	0.024
NGC1404	6.03	6.26	1.96	3.81	8.52	1.58	6.39	0.162	0.325	2.415
±	0.14	0.20	0.12	0.14	0.24	0.08	0.20	0.004	0.004	0.024
NGC1419	5.75	5.28	1.56	3.18	4.97	1.62	4.92	0.111	0.242	2.068
±	0.15	0.22	0.12	0.16	0.24	0.10	0.22	0.005	0.006	0.024
NGC1427	5.95	5.92	1.89	3.61	6.20	1.67	5.43	0.127	0.277	2.243
±	0.09	0.12	0.07	0.09	0.14	0.05	0.12	0.003	0.003	0.024
IC1963	5.08	6.03	1.81	3.31	5.98	2.33	5.39	0.093	0.232	1.763
±	0.19	0.27	0.14	0.21	0.31	0.13	0.28	0.007	0.008	0.072
IC2006	5.95	6.18	1.98	3.74	8.50	1.44	5.73	0.171	0.329	2.134
±	0.15	0.22	0.12	0.16	0.23	0.10	0.22	0.005	0.006	0.024
E359-G02	1.64	2.77	1.30	2.23	1.58	3.46	2.97	0.039	0.119	1.653
±	0.35	0.50	0.26	0.39	0.61	0.23	0.55	0.013	0.016	0.072
E358-G06	5.00	4.05	1.22	2.64	2.60	2.22	4.51	0.057	0.164	1.763
±	0.23	0.33	0.17	0.25	0.38	0.15	0.34	0.008	0.010	0.072
E358-G25	1.58	2.28	0.70	2.01	1.25	2.56	3.86	0.039	0.121	1.763
±	0.30	0.43	0.23	0.34	0.53	0.21	0.47	0.012	0.014	0.072
E358-G50	4.85	4.22	1.46	2.64	3.76	2.44	4.18	0.064	0.176	1.690
±	0.24	0.35	0.18	0.27	0.41	0.16	0.36	0.009	0.011	0.072
E358-G59	5.04	4.84	1.52	3.00	4.71	2.19	4.66	0.067	0.184	1.732
±	0.19	0.26	0.14	0.20	0.30	0.12	0.27	0.007	0.008	0.072
NGC3379	6.02	6.30	1.90	3.92	7.48	1.33	5.56	0.166	0.329	2.367
±	0.15	0.23	0.13	0.16	0.24	0.09	0.21	0.004	0.005	0.024

continued on next page

Name	Mgb [Å]	Fe5270 [Å]	Fe5335 [Å]	Fe5406 [Å]	Fe5709 [Å]	Hγ_A [Å]	Hγ_F [Å]	Fe4930[a] [Å]	Hβ_G [b] [Å]	log σ_0
NGC1316	4.08	3.10	2.90	1.82	1.04	-4.18	-0.64	2.38	2.49	2.344
±	0.08	0.08	0.10	0.07	0.05	0.11	0.08	0.19	0.04	0.024
NGC1336	4.17	2.70	2.33	1.51	0.81	-4.82	-1.34	1.72	1.92	1.982
±	0.10	0.12	0.13	0.10	0.08	0.17	0.10	0.15	0.06	0.024
NGC1339	4.99	3.04	2.72	1.96	0.93	-6.11	-1.91	1.90	1.89	2.199
±	0.12	0.13	0.16	0.11	0.09	0.20	0.12	0.19	0.07	0.024
NGC1351	4.72	3.03	2.51	1.78	0.98	-5.89	-1.85	1.95	1.85	2.196
±	0.11	0.12	0.15	0.11	0.09	0.18	0.11	0.17	0.07	0.024
NGC1373	3.90	2.95	2.29	1.74	0.89	-5.74	-1.55	1.90	2.19	1.875
±	0.10	0.12	0.13	0.10	0.08	0.17	0.11	0.15	0.06	0.024
NGC1374	5.01	3.13	2.76	1.87	0.98	-6.40	-2.02	2.07	1.86	2.267
±	0.10	0.12	0.14	0.10	0.08	0.17	0.11	0.18	0.06	0.024
NGC1375	2.71	2.88	2.49	1.54	1.08	-1.24	1.06	2.27	3.06	1.748
±	0.10	0.11	0.13	0.10	0.08	0.14	0.09	0.14	0.06	0.072
NGC1379	4.45	2.80	2.47	1.71	0.92	-5.26	-1.59	1.73	1.94	2.114
±	0.10	0.11	0.13	0.10	0.08	0.17	0.10	0.15	0.06	0.024
NGC1380	4.86	3.24	3.18	1.93	1.00	-6.43	-2.16	2.14	1.77	2.340
±	0.13	0.14	0.17	0.13	0.09	0.20	0.13	0.24	0.08	0.024
NGC1380A	3.09	3.01	2.84	1.83	1.01	-1.52	0.96	2.00	3.12	1.740
±	0.15	0.16	0.19	0.14	0.12	0.21	0.13	0.20	0.09	0.072
NGC1381	4.42	3.15	2.71	1.80	0.97	-5.99	-1.87	2.09	2.04	2.185
±	0.07	0.08	0.09	0.07	0.05	0.12	0.08	0.13	0.04	0.024
NGC1399	5.91	3.36	3.11	1.88	0.83	-6.40	-2.04	2.05	1.83	2.574
±	0.16	0.11	0.17	0.11	0.07	0.12	0.14	0.55	0.05	0.024
NGC1404	5.00	3.37	3.14	1.98	0.88	-6.29	-1.99	1.84	1.95	2.415
±	0.10	0.10	0.13	0.09	0.06	0.13	0.10	0.23	0.05	0.024
NGC1419	3.93	2.72	2.30	1.53	0.82	-5.08	-1.50	1.84	1.95	2.068
±	0.10	0.12	0.14	0.10	0.08	0.17	0.11	0.16	0.07	0.024
NGC1427	4.40	3.13	2.64	1.82	0.99	-5.80	-1.68	2.04	2.02	2.243
±	0.06	0.06	0.07	0.05	0.04	0.09	0.07	0.13	0.03	0.024
IC1963	3.76	3.06	2.82	1.92	1.04	-4.41	-0.88	1.91	2.52	1.763
±	0.14	0.15	0.17	0.13	0.11	0.22	0.14	0.19	0.09	0.072
IC2006	4.92	3.19	3.17	1.95	0.96	-6.32	-2.13	2.17	1.91	2.134
±	0.10	0.12	0.14	0.10	0.08	0.18	0.11	0.16	0.06	0.024
E359-G02	1.50	1.87	1.38	1.02	0.77	2.19	2.69	1.42	3.50	1.653
±	0.28	0.31	0.36	0.27	0.22	0.33	0.20	0.37	0.16	0.072
E358-G06	2.74	2.54	1.95	1.36	0.60	-2.81	-0.07	1.30	2.48	1.763
±	0.17	0.19	0.22	0.16	0.14	0.25	0.15	0.23	0.10	0.072
E358-G25	1.78	1.99	1.57	1.19	0.52	2.09	1.92	1.23	2.46	1.763
±	0.24	0.28	0.32	0.24	0.20	0.28	0.17	0.33	0.14	0.072
E358-G50	2.55	2.74	2.34	1.58	0.95	-2.82	0.00	1.63	2.67	1.690
±	0.18	0.20	0.23	0.17	0.15	0.27	0.16	0.25	0.11	0.072
E358-G59	3.02	2.30	2.11	1.45	0.89	-3.72	-0.49	1.96	2.42	1.732
±	0.13	0.15	0.17	0.13	0.11	0.21	0.13	0.18	0.08	0.072
NGC3379	5.13	3.21	2.86	1.89	0.99	-6.39	-2.20	2.05	1.80	2.367
±	0.11	0.11	0.14	0.10	0.07	0.16	0.11	0.22	0.06	0.024

Notes:

[a] Fe4930-index definition from González (1993)

[b] Hβ-index definition from González (1993)

Chapter 4

Nuclear Stellar Populations

4.1 Introduction

Having measured the central line-strength indices one can hope to determine the luminosity weighted ages and metallicities of the integrated stellar populations by comparing observed quantities with model predictions. All indices are measured in the Lick/IDS system, which narrows the choice of model to those which have used the so called "fitting functions" of the Lick group (Gorgas et al., 1993; Worthey et al., 1994; Worthey and Ottaviani, 1997). These fitting functions are polynomial fits to the Lick/IDS stellar library and give index strength as a function of stellar temperature (T_e), gravity (log g) and metallicity ([Fe/H]). The first population synthesis model which used these fitting functions to predict index strength in old stellar populations was Worthey's (1994). However, now there are a large variety of models available which use the Lick/IDS fitting functions but have otherwise different population synthesis prescriptions. Here Worthey's (1994) models have been chosen for the analysis of line-strength indices in the Fornax cluster. For a comparison with other stellar population synthesis models see Charlot et al. (1996).

The conventional view that luminous elliptical galaxies are coeval and created about 10-15 Gyrs ago has been established over many decades. In this picture the global spectrophotometric relations observed for ellipticals, for example the colour-magnitude relation (Sandage and Visvanathan, 1977; Larson et al., 1980; Bower et al., 1992; Terlevich, 1998), are accounted for by the steady increase in the abundance of heavy elements with increasing galaxy mass. This arises naturally in e.g., galactic wind models such as those of Arimoto and Yoshii (1987) and Kodama and Arimoto (1997). This view has received support from the small scatter observed in the Fundamental Plane (Renzini and Ciotti, 1993) and from the small scatter in the Mg–σ_0 relation (Bender et al., 1993; Colless et al., 1998) both of which appear to be difficult to establish if there is any significant age spread amongst elliptical galaxies. Recent observations of line-strength indices have however challenged this conventional interpretation of the data (González, 1993; Faber et al., 1995) and

suggested that large age variations may be present amongst elliptical galaxies.

The 41 elliptical galaxies studied by González (1993) have a large range in Hβ absorption strength and a limited range in metal line strength [MgFe]. Combined with Worthey's (1994) models these indicate a large range in age, from $\sim$2 to $\sim$17 Gyrs, with a modest spread in metallicity from solar to roughly three times solar. González's sample is largely drawn from relatively low density environments, with only a few galaxies taken from nearby clusters. It was not intended to be a complete sample.

Jones and Worthey (1995) identified more sensitive metallicity and age indicators: the $C_2$4668 feature and Hγ_{HR} measured at high resolution. Trager (1997) recently revisited González's data and analysed the original Lick/IDS sample of extragalactic objects using $C_2$4668 and the new higher order Balmer line indices modelled by Worthey and Ottaviani (1997) to extend the application of the models with greater certainty. He confirmed González's result, while he concluded that the line-strength index errors (e.g., Hβ) of the original Lick/IDS galaxy sample are too large to allow a fruitful analysis. He ascribed the differences in the absolute ages of galaxies derived from different pairs of indices to the well known over-abundance (with respect to the solar ratios) of magnesium compared to iron in luminous ellipticals (Peletier, 1989; Worthey et al., 1992; Davies et al., 1993; Greggio, 1997). Furthermore Trager found evidence that elliptical galaxies populate a plane in age-metallicity-σ, where the Mg–σ_0 and colour-magnitude relations are mere edge-on projections of the former plane. This relation implies that at fixed σ, metal rich galaxies are younger.

In this Chapter we present a detailed analysis of the central stellar population of the *complete* sample of early-type galaxies in the Fornax cluster brighter than $M_B = -17$[1]. Section 4.2 gives a brief introduction into the stellar population models we are going to employ. In Section 4.3.1 we introduce the underlying idea of measuring ages and metallicities with line-strength indices, and in Section 4.3.2 we expand the analysis to new index combinations. Some comments about the role of emission in early-type galaxies and in particular for the Fornax sample are given in Section 4.3.4. Having established first estimates of the ages and metallicities we present a critical study of the reliability and caveats of the models (and data) in Section 4.4. Section 4.4.3 gives our best estimates of the central ages and metallicities of Fornax early-type galaxies. Finally we present our conclusions in Section 4.5.

4.2 Worthey (1994) Models

In this Section a brief description of the Worthey (1994) models is given. The single-burst stellar population (SSP) models depend only on three input variables:

[1] Adopting a distance modulus of $m - M = 31.2$

1. global metallicity in the range $-2 <$ [Fe/H] < 0.5,
2. single burst age in the range $1 <$ age < 18 Gyrs, and
3. Initial Mass Function (IMF), here chosen to have Salpeter form.

The IMF is defined as the relative number of stars as a function of initial stellar mass:

$$dN(m) = Cm^{-x}dm, \quad m_l \leq m \leq m_u \tag{4.1}$$

where N is the number of stars per mass interval and m_l and m_u are the lower and upper limits of initial stellar mass, respectively. The Salpeter (1955) mass function has a slope $x = 2.35$ in this definition. The coefficient C is a normalization constant.

The model itself is based on three major ingredients: isochrones and opacities, a flux library, and absorption line strength, derived from fitting functions.

- **Isochrones and opacities:** The Worthey (1994) models use a combination of isochrones by VandenBerg and collaborators (VandenBerg, 1985; VandenBerg and Bell, 1985; VandenBerg and Laskarides, 1987) and the Revised Yale Isochrones (Green et al., 1993). Evolution beyond the tip of the red giant branch (RGB) is approximated as a single red clump plus a theoretical prescription for evolution from the early asymptotic giant branch (AGB) to the tip of the AGB. Note at low metallicities ($-1 <$ [Fe/H] < -0.5) the horizontal branch morphology shifts from an extended M3-like[2] branch to a red clump. This effect is only included for the higher order Balmer line indices Hγ and Hδ and not for the original 21 Lick/IDS indices (Worthey and Ottaviani, 1997).

- **Flux library:** To derive observational properties from these models, a flux library is needed for every stellar luminosity, temperature, gravity, and composition. As no observational library of fluxed stellar spectra exists which covers the entire parameter space spanned by the models, Worthey (1994) chose to use model atmospheres of Kurucz (1992) for stars hotter than 3500 K, and a combination of model atmospheres of Bessel et al. (1989, 1991) and observed fluxed spectra of Gunn and Stryker (1983) for cooler M giants.

- **Absorption-line strength:** The novel feature of the Worthey (1994) models is the inclusion of empirically calibrated absorption line strengths. Using the Lick/IDS stellar spectra data, Gorgas et al. (1993) and Worthey et al. (1994) derived polynomial fitting functions for 21 Lick/IDS indices as a function of $1/T_{eff}$, [Fe/H], and

[2] M3 is a typical intermediate metallicity globular cluster.

surface gravity. Worthey and Ottaviani (1997) have extended this analysis to include the higher order Balmer lines Hδ and Hγ.

For a given age and metallicity, an isochrone is selected. Each star on the isochrone is assigned a spectral energy distribution (SED) from the flux library and a set of absorption line strengths. The final model outputs are the integrated fluxed SED (from which colours and magnitudes can be derived) and absorption line strengths on the Lick/IDS system.

As pointed out by Worthey (1994) the determination of the ages of old stellar populations is complicated by the similar effects that age and metallicity have on the integrated spectral energy distributions. Broad band colours and most of the indices are degenerate along the locus of Δ age $\approx -3/2\,\Delta$ Z. Worthey dubbed this behaviour the "3/2 rule". In other words the integrated SED of an old (> 2 Gyrs) stellar population looks almost identical when age is doubled and Z reduced by a factor of three at the same time. Only a few narrow band absorption line-strength indices have so far been identified which can break this degeneracy. In terms of age, the Balmer lines Hβ, Hγ and Hδ are the most promising features, being clearly more sensitive to age than metallicity; a possible further candidate is the G-band. Features which are more metal sensitive, and thus less age sensitive than the average are: $C_2$4668, Fe5270, Fe5335 and Fe4383. By plotting an age sensitive index and a metallicity sensitive index against each other one can break the degeneracy and estimate the age and metallicity of the integrated stellar population (see Figure 4.1).

4.3 Nuclear Age and Metallicity Estimates

In this Section Worthey (1994) single-burst stellar population models are compared to observed central ($2\farcs3\times3\farcs85$ aperture) line-strength indices of a complete sample of Fornax early-type galaxies obtained at the AAT. The NTT data cannot be used for this Chapter as its Lick/IDS calibration relies on the AAT96 observing run and thus would not give independent measurements. Note that parts of the following discussion have been published in Kuntschner and Davies (1998).

4.3.1 The Hβ *vs* [MgFe] Diagram

González (1993) successfully used a combination of Hβ and [MgFe] (for definition of the latter see Equation 3.5 on page 38) to disentangle the effects of age and metallicity. To make a direct comparison we will first analyse our data using the same line-strength indices as González. In Figure 4.1a González's sample of 41 galaxies[3] is reproduced and models

[3] A search in the RC3 (de Vaucouleurs et al., 1991) showed that in González's sample only five galaxies are classified as non standard elliptical (i.e., S0s or dE galaxies). Yet five of the elliptical galaxies are classified as LINERs.

from Worthey (1994) are overplotted. Note that these models are slightly different to the ones used in González thesis. The data values are taken from Table 4.7 in his thesis and represent ($R_e/8$) central values. Compared with the overplotted models most of the galaxies are above solar metallicity and exhibit a large range in luminosity weighted age.

In Figure 4.2 we show a plot of Hβ equivalent width *vs* [MgFe] equivalent width for a complete sample of 22 early-type galaxies in the Fornax cluster. The error bars on the individual data points represent the photon noise and the error in the velocity dispersion correction. The elliptical galaxies in Fornax (filled circles) have weak Hβ absorption spanning a modest range in [MgFe]. The S0s (open circles) on the other hand span a larger range of values in this diagram, typically having stronger Hβ absorption. Note that there are two S0s (NGC 1380 and NGC 1381) with weak Hβ absorption among the elliptical galaxies. The two galaxies with the lowest [MgFe] values and strong Hβ absorption (ESO359-G02, cross and ESO358-G25, open triangle) appear to be different from the rest of the sample. These galaxies are likely to be post-starburst or starburst galaxies and will be treated separately from the rest of the galaxies; for discussion see Section 4.3.3.

Following González we overplot predictions from single-burst stellar population models (Worthey, 1994). Although the absolute age calibration may be insecure, we see that our sample of Fornax ellipticals are old and of similar age. According to the models the metallicity ranges from just sub-solar to about three times solar. The Fornax S0 galaxies however extend to much lower luminosity weighted ages and a greater range in metallicity. This seems to be in conflict to what González found. His elliptical galaxies exhibit a large spread in luminosity weighted age from greater than 12 Gyrs to less than 2 Gyrs – in fact González's sample of elliptical galaxies looks much more like the Fornax S0s than the Fornax ellipticals.

This comparison deserves a little more attention. González's sample of galaxies was drawn from very different environments, where at least 10 galaxies are relatively isolated ellipticals and only a few are from cluster environments such as Virgo. In panels (b)-(d) of Figure 4.1 we present González's sample split up in three categories: galaxies which have been classified as disturbed by Schweizer et al. (1990) ($\Sigma > 1.0$), galaxies with no clear disturbance ($\Sigma \leq 1.0$) and galaxies with no classification by Schweizer et al. (1990). The symbol sizes in panel (b)-(d) are scaled such that the area covered by the symbol is proportional to the central velocity dispersion of the galaxy. One can see that all galaxies with no signs of disturbance are old and that most of the galaxies with no classification have Hβ absorption of $\sim$1.7 Å which is consistent with the findings in Fornax (see also Table 4.1). In panel (c) there are only four "young" galaxies of which two are S0s and the two Es (NGC7454 and NGC6702) are located in very low density environments.

A Kolmogorov-Smirnov (K-S) test for the Hβ distributions of all González galaxies compared to the ellipticals in the Fornax sample gives the following result: The null hy-

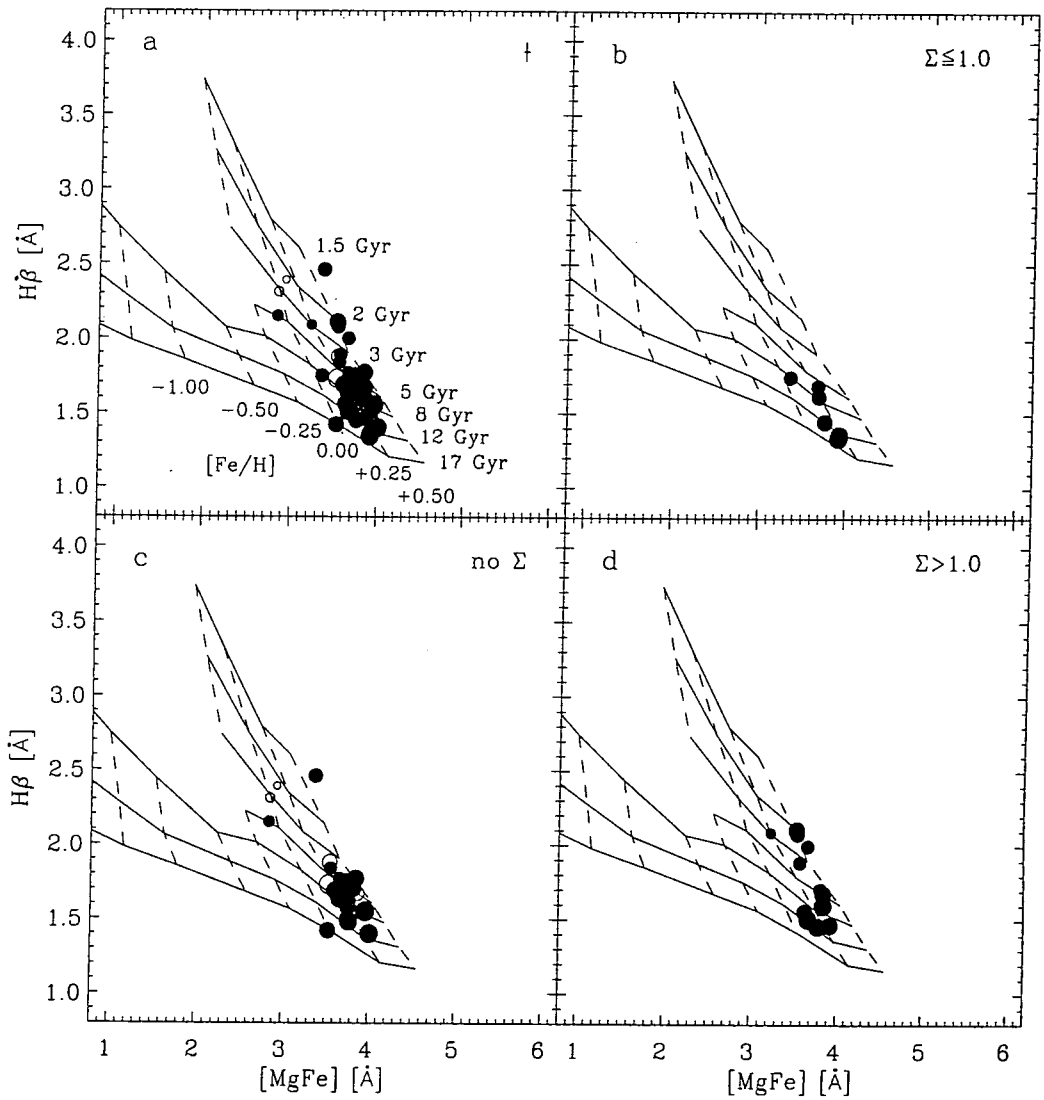

Figure 4.1: (a) Hβ equivalent width *vs* [MgFe] equivalent width diagram for the González (1993) sample of 41 galaxies ($R_e/8$ central values). Es and S0s + dE are represented by filled and open circles respectively (morphologies taken from RC3; de Vaucouleurs et al. (1991)). The area covered by the symbols is proportional to the central velocity dispersion of the galaxy. The cross in the right upper corner of panel (a) indicates the rms uncertainty in the transformation to the Lick/IDS system. In panels (b)-(d) we present González's sample split up in three categories: galaxies with no obvious signs of disturbance after Schweizer et al. (1990) ($\Sigma \leq 1.0$), galaxies with no classification by Schweizer et al. (1990) and galaxies which have been classified as disturbed by Schweizer et al. (1990) ($\Sigma > 1.0$). Overplotted are models by Worthey (1994).

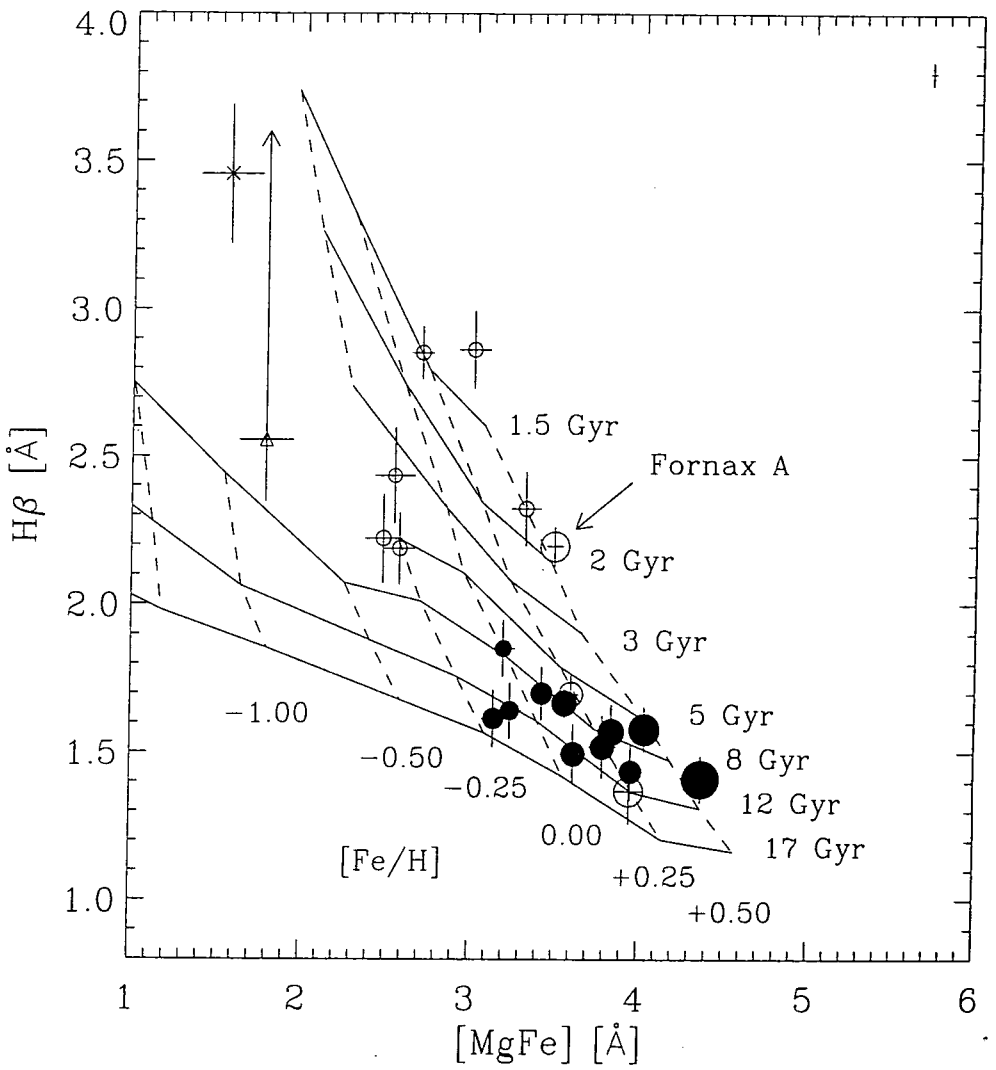

Figure 4.2: Hβ equivalent width *vs* [MgFe] equivalent width diagram for the complete sample of Fornax early-type galaxies (central 2.″0×3.″85 aperture). Overplotted are models by Worthey (1994). The solid lines represent isoage lines whereas the dashed lines are lines of constant metallicity. Filled circles and open circles represent ellipticals and S0s respectively. The cross and open triangle represent possible post-starburst and starburst galaxies respectively. The area covered by the symbols is proportional to the central velocity dispersion of the galaxy. The cross in the right upper corner indicates the rms uncertainty in the transformation to the Lick/IDS system. The arrow attached to the galaxy ESO358-G25 (open triangle) indicates an emission correction, for details see Section 4.3.3.

pothesis that the two samples are drawn from the same distribution cannot be securely rejected. As can be seen in Table 4.1 the difference between the two cumulative distribution functions (Kolmogorov-Smirnov d) is only 0.35 with a probability of 17.7% that the estimate of d is too large (see column significance level). This is not surprising as the means of the two distributions are very similar and we suggest that after all both samples are likely to be drawn from the same parent sample. Note that the Fornax sample is a complete sample. When a K-S test is performed for the S0s against the González sample, it turns out that these two samples are drawn from very different distributions; the same is true when the Fornax Es are compared with the Fornax S0s. See Table 4.1 for the significance levels and values of d.

Table 4.1: Simple Statistics and K-S Tests for the Hβ Distributions

sample	number of galaxies	mean Hβ	std deviation
González all	41	1.73	0.28
Fornax Es	11	1.59	0.13
Fornax S0s [a]	9	2.24	0.48
Fornax all [a]	20	1.88	0.47

K-S tests

sample 1	sample 2	d	significance level
Fornax Es	González all	0.35	0.177
Fornax S0s [a]	González all	0.70	0.001
Fornax all [a]	González all	0.28	0.214
Fornax S0s [a]	Fornax Es	0.71	0.006

Notes:
[a] excluding ESO359-G02 and ESO358-G25
d: Kolmogorov-Smirnov d
sig. level: Probability that d > observed

In summary we find that our sample of cluster elliptical galaxies do not show signs of young stellar populations. We ascribe the fact that González finds some young elliptical galaxies to their origin from low density environments and furthermore that his sample seems to contain many galaxies with signs of disturbance. Note however, that the majority of González's Es show Hβ absorption strength similar to the Fornax sample. In González's sample there is a lack of old and metal poor ellipticals evident. We ascribe this to a selection effect in the sense that González does not probe the luminosity function of ellipticals deep enough to see metal poor i.e., small and therefore faint ellipticals.

Some of the S0 galaxies in Fornax appear to be extremely young ($\sim$ 1Gyr). At this point one should recall that the stronger Hβ absorption found in S0s indicates a younger *mean* age, but line-strength indices reflect only the integrated, luminosity weighted, prop-

erties in a galaxy. As young populations tend to be much more luminous than old ones, a *small* (in mass) young population can dramatically change the strength of indices, in particular Hβ. de Jong and Davies (1997) and Trager (1997) have demonstrated this and showed that the high Hβ galaxies in González sample tend to have disky isophotes. de Jong and Davies (1997) suggested that ongoing star-formation might be associated with the presence of a disk. In the Fornax sample, Fornax A (NGC 1316, see Figure 4.2), often cited as the product of a recent merger, might be a typical example of a galaxy with an old stellar population which looks young due to recent star-formation in a central region (disk?). Less dramatically, the same effect could influence many lenticular galaxies.

4.3.2 New Indices: $C_2$4668 & Hγ_A

Using two indices it was shown in the previous Section that the age/metallicity degeneracy can be broken and that there seems to be a morphological separation in age for Fornax early-type galaxies. But are these results consistent with other index combinations within the Lick/IDS system? This is a crucial test to convince ourselves whether the model predictions are trustworthy or not. In this Section we apply a more sensitive and more accurately determined metallicity index $C_2$4668, and a new age index, Hγ_A, that is also more precisely determined and less sensitive to contamination by emission.

González found nebular emission in more than half of the galaxies in his sample. The strength of the *stellar* absorption at Hβ is therefore uncertain and requires a correction for the estimated infilling due to emission. González adopted an empirical prescription based on the strength of the [OIII]λ5007 emission but the validity of this has been challenged by Carrasco et al. (1996) who propose that no correction should be made. Here we do not attempt to correct Hβ for emission (see Section 4.3.4 for a discussion), rather we use the Hγ_A index which is less sensitive to contamination by emission. The relative strength of nebular emission decreases rapidly with the order of the Balmer-line (Osterbrock, 1989) so that the dilution effect is much reduced. Hγ_A is a more sensitive age indicator than Hβ because the models predict a much wider range in equivalent width for the same age difference. In addition Hγ_A is more precisely determined as (i) the wide sidebands produce improved photon statistics, (ii) there is a smaller rms error in the velocity dispersion corrections.

In Figure 4.3 a plot of Hγ_A equivalent width *vs* $C_2$4668 equivalent width is presented. The symbol definitions are the same as in Figure 4.2. The subscript "A" on Hγ indicates a "wide" (~40 Å) central passband[4]. We have overplotted new model predictions (Worthey and Ottaviani, 1997). In this diagram the ellipticals follow a tight relation at low Hγ_A values varying mostly in $C_2$4668. S0s are distributed to much higher central values of Hγ_A absorption. The distribution is similar to that in the Hβ *vs* [MgFe] diagram, in

[4]The negative values of the Hγ_A index seen in Figure 4.3 do not indicate emission but are the result of the definition of the pseudo-continuum passbands (see e.g., Figure 3.2 on page 40).

addition the precision of both age and metallicity is increased. Remarkably the scatter of elliptical galaxies is reduced and for metallicities greater than solar they exhibit more-or-less constant $H\gamma_A$. The new, more accurate, indicators confirm our principal result that the lenticular galaxies in the Fornax cluster have lower luminosity weighted ages than the elliptical galaxies which appear to be roughly coeval and vary mainly in metallicity.

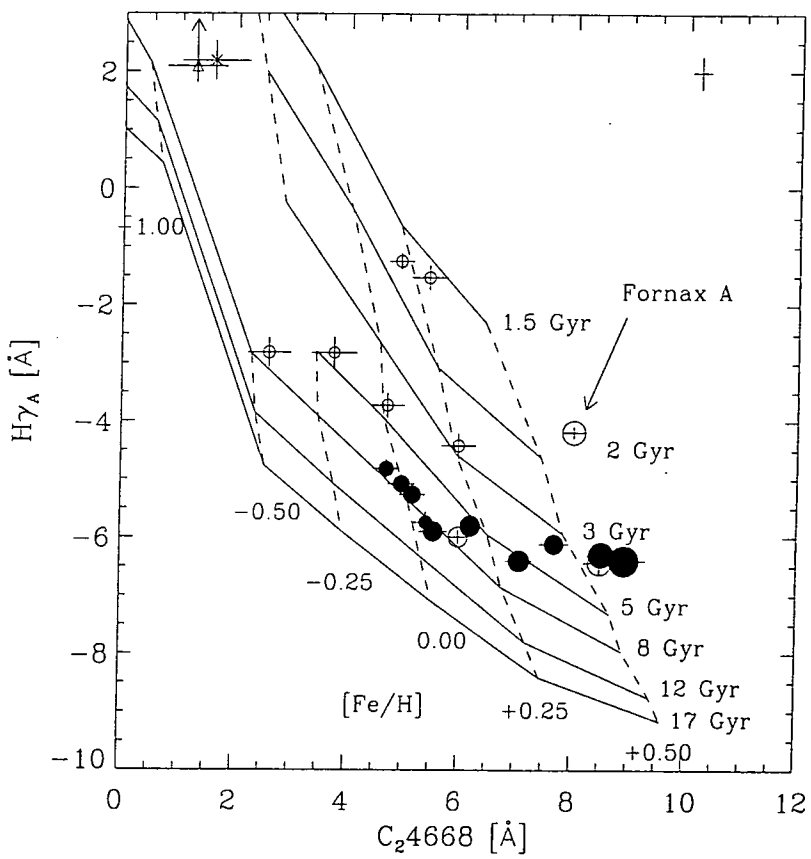

Figure 4.3: $H\gamma_A$ equivalent width *vs* $C_2$4668 equivalent width diagram for a complete sample of Fornax early-type galaxies. Symbol definitions as in Figure 4.2. Overplotted are models by Worthey and Ottaviani (1997). The negative values in $H\gamma_A$ *do not* indicate emission but are created entirely by the definition of the pseudo-continuum passbands. Note that ESO358-G25 (open triangle) moves to a much younger age with respect to Figure 4.2.

Note that the galaxy ESO358-G25 (open triangle) moves to much younger ages, even to the same strength in $H\gamma_A$ absorption as ESO359-G02 (cross). In the spectrum of ESO358-G25 one can see Balmer emission on top of the stellar absorption for both $H\beta$ and $H\gamma$ (see Figure 4.5). ESO358-G02 *does not* show any obvious emission. This shows that the $H\gamma_A$ index is indeed much less affected by emission and therefore is superior to the $H\beta$ index. Furthermore as none of the other galaxies move significantly to younger ages, emission seems to be a rare phenomenon in the Fornax sample. This is confirmed

separately by an analysis of the [OIII]λ5007 emission, described in Section 4.3.4.

There is a hint that the most metal rich ellipticals seem to be younger by $\sim$3 Gyrs than their metal poor brethren. While the absolute age calibration is not secure the relative ages should be valid, nevertheless the apparent reduction in the luminosity weighted ages of the most luminous galaxies may be an artifact of the models. As we will see in Section 4.4 and Section 4.4.2 metallicity estimation is strongly influenced by the abundance ratios and can lead to spuriously young age estimates. Furthermore the behaviour of Balmer lines at high metallicities seems to be quite uncertain. For example, Gregg (1994) found, analysing a sample of globular clusters, that the strength of the Balmer lines is only poorly correlated with metallicity above [Fe/H]=-0.7. New calculations by Mowlavi et al. (1998) show that very metal-rich stars ($Z \geq 0.05$) exhibit properties that deviate from extrapolation of the known characteristics at lower metallicities. In particular they are more luminous and hotter than their metal poorer brethren. This could mean that in diagrams such as presented in Figure 4.3 the locus of very metal rich populations overlaps with metal poorer ones, i.e., the position of some metal rich populations would not be uniquely determined. Certainly a better calibration of the Balmer lines at high metallicities is required to investigate this.

So far only Balmer lines have been used as age indicators. Balmer line indices measure mainly the temperature of the turn off point from the main sequence and thus allow a well determined age estimate of the integrated stellar population (e.g., Buzzoni et al., 1994). Note that the turn off temperature is a function of metallicity and therefore the strength of the Balmer absorption is not only a function of age but also a function of metallicity. As already demonstrated by using a plot of age-indicator *vs* metallicity indicator one can separate the age/metallicity effects. But there are some concerns that stars from other evolutionary phases (e.g., horizontal branch; hereafter HB) might contribute significantly to the Balmer absorption. A study of globular clusters by de Freitas Pacheco and Barbuy (1995) showed that blue HB stars may give a substantial contribution to the Hβ absorption. Furthermore they suggest that the HB morphology is correlated with the degree of central concentration in the globular cluster. Whether elliptical galaxies are subject of these effects is not yet known.

Worthey identified beside the Balmer lines also the G-band (index: G4300) as a possible age indicator. The G-band offers an age indicator which is independent of the Balmer series[5] and also is not affected by nebular emission.

In Figure 4.4 a plot of G4300 equivalent width *vs* $C_2$4668 equivalent width is presented. There are several important things to mention. Firstly the G-band is a very age sensitive feature, but unfortunately for ages > 8 Gyrs and high metallicity it becomes

[5]Note that this is not entirely true, because the red pseudo-continuum of the G4300 index includes the Hγ absorption feature. Nevertheless the effects on the continuum are negligible unless the Hγ absorption reaches very high values

degenerate. The relative positions of the galaxies in this diagram are very similar to the other age/metallicity index combinations. Hence the general conclusion that the ellipticals are old and the S0s have on average younger luminosity weighted ages still holds. ESO358-G25 (open triangle) which shows obvious signs of emission is at the same position as ESO359-G02 (cross), thus confirming the result from using $H\gamma_A$ instead of $H\beta$ as age indicator. Overall the galaxies move to older ages with the oldest ellipticals being outside the model grid. Therefore using two different age indicators with the same metallicity indicator can lead to different *absolute* age estimates. Comparing Figs. 4.4, 4.3 & 4.2 one can see that the absolute ages increase but the relative age distribution stays the same. This re-confirms the conclusion of Worthey (1996) and Worthey et al. (1996) that absolute ages in the Lick/IDS system are not secure but relative age changes are readily visible.

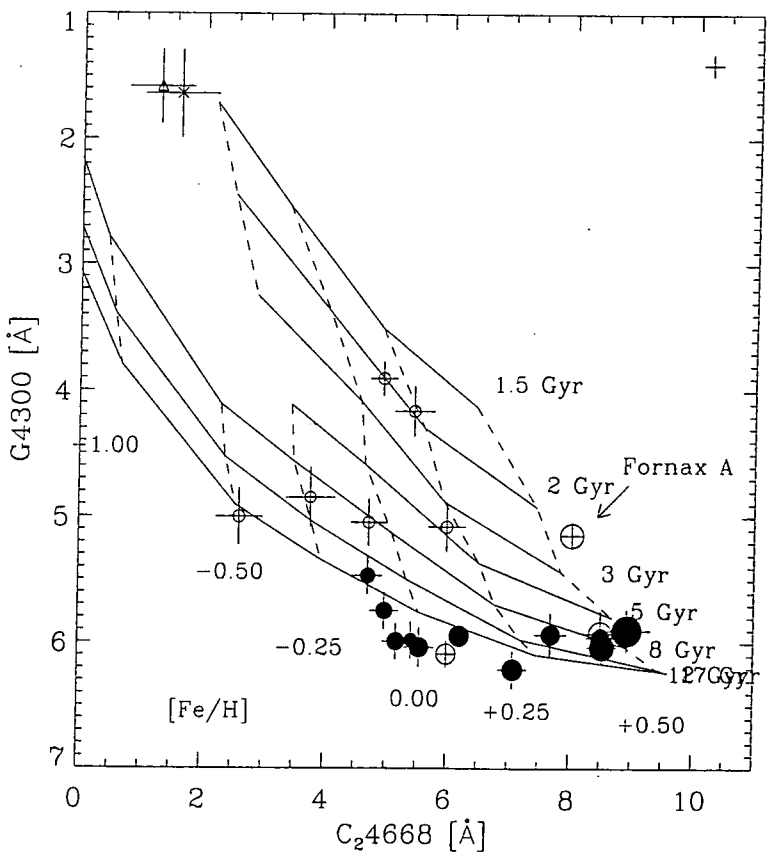

Figure 4.4: G4300 equivalent width *vs* $C_2$4668 equivalent width diagram for a complete sample of Fornax early-type galaxies. Symbol definitions as in Figure 4.2. Overplotted are models from Worthey (1994).

The fact that the relative distribution of the galaxies is consistent using $H\beta$, $H\gamma$ or G4300 suggests that the Balmer indices are a good age indicator and that to first order, concerns about a possible contamination by blue HB stars seem to be not necessary.

4.3.3 Two Post-Starburst or Starburst Galaxies

One of the most striking differences in using G4300 or $H\gamma_A$ instead of $H\beta$ is seen in the behaviour of ESO358-G25 represented by an open triangle. This galaxy moves relatively to much younger ages compared to the rest of the sample. In fact it shows emission in $H\beta$ and $H\gamma$ filling in the absorption (see Figure 4.5). It also shows among the strongest emission in [OIII]λ5007 in the sample (see Table 4.2). The arrows in Figs. 4.2 & 4.3 indicate an estimated emission correction determined by a rough subtraction of the emission features. According to the calculations of Poggianti and Barbaro (1997) **strong** Balmer absorption is created mainly at the main sequence turn off and can not originate from other evolutionary stages (at least not for metal poor systems). Hence the young ages estimated from the model predictions are reliable.

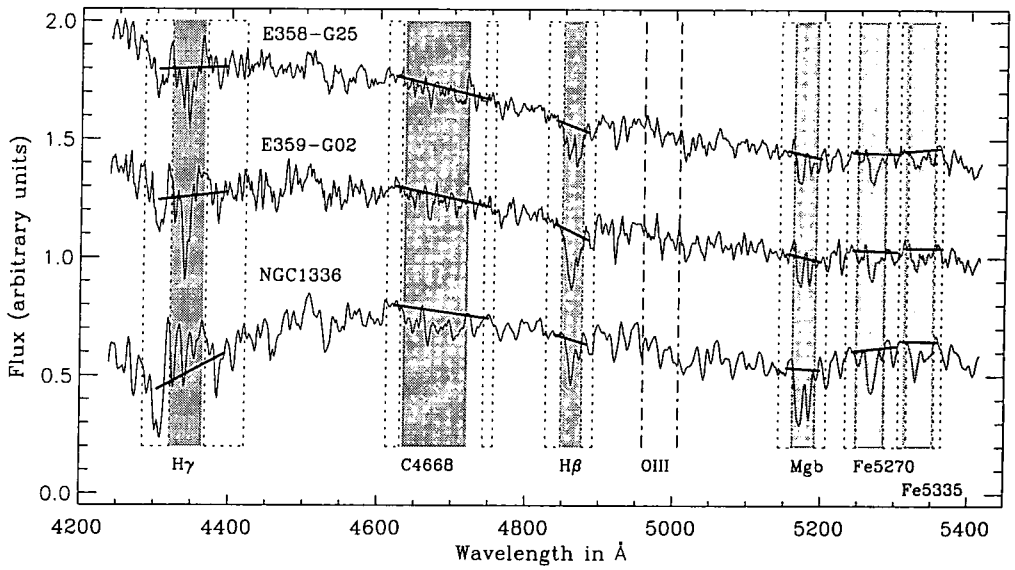

Figure 4.5: The spectra of ESO358-G25, ESO359-G02 and NGC1336 are shown. The shaded areas mark the central passbands of some relevant indices. The thick solid lines indicate the pseudo-continuum defined by two side-passbands (dashed boxes). We have also marked the position where [OIII] emission at 4959 Å & 5007 Å is expected if present. The spectra are *not* broadened to the Lick/IDS resolution in order to illustrate the different line strengths. Note the emission in $H\beta$ and $H\gamma$ for ESO358-G25 and that the spectra of both ESO-galaxies do not drop bluewards of 4500 Å but stay constant.

The two lenticular galaxies ESO358-G25 (open triangle) and ESO359-G02 (cross) have remarkable spectra for early-type galaxies, they show blue continua, strong Balmer lines, and weak metal lines. Overall they resemble the spectrum of a F6V + K0III (3:1) stellar composite very well. These galaxies are amongst the faintest in our sample and are $\sim$3° away from the centre of the cluster. They are reminiscent of the high $H\delta$ galaxies in the Coma cluster found by Caldwell et al. (1993) or the galaxies in redshift z=0.3

clusters identified by Couch and Sharples (1987) and by Barger et al. (1996) as being in the post-starburst phase (ESO359-G02) or starburst phase (ESO358-G25).

4.3.4 Emission in Early-Type Galaxies

Optical emission-lines in extragalactic objects always originates from warm ionized gas but there are several excitation mechanisms: (a) photoionization by O and B stars, (b) planetary nebulae (PN), (c) photoionization by old post-AGB stars (after the PN around the central star has dissipated), (d) photoionization by a power-law continuum source, and (e) shock-wave heating (Baldwin et al., 1981; Binette et al., 1994).

Elliptical galaxies normally contain much less ionized gas than do spirals. In fact, for a long time they were regarded as dust and gas free. However, spectroscopic surveys of large samples of early-type galaxies revealed that about 50-60% of the galaxies show weak optical emission lines (Phillips et al., 1986; Caldwell, 1984). Typically the reported strength of emission lines such as [OII]λ3727, [Hα] and [NII] λ6584 indicates the presence of only $10^3 - 10^5 M_\odot$ of warm ionized gas in the centre. A more recent study of 56 bright elliptical galaxies by Goudfrooij et al. (1994a) detected ionized gas in 57% of their sample and confirms the amount of ionized gas present. Macchetto et al. (1996) detected in their imaging survey of 73 luminous elliptical and lenticular galaxies a fraction of $\sim$ 80% with ionized gas. Interestingly the detected dust and ionized gas show a wide variety of distributions and is not only concentrated in the centre.

The origin of the gaseous component in ellipticals is not yet settled. It could be either of external origin, resulting, for example from a cooling flow or from a merger with a small gas rich galaxy. Or it could be of internal origin, resulting from stellar mass loss. A determination of the composition of the gas could give clues about its origin, but the chemical composition can only be determined if the ionization mechanism is well understood. The emission-line spectra of giant elliptical galaxies are usually similar to those of LINERs (Low-Ionization Nuclear Emission Regions), where the ionization is provided by an energetic radiation from the nucleus, usually in the form of a power law. Emission lines are generally weak. However, Binette et al. (1994) showed that post-AGB stars from the old stellar population of an early-type galaxy can also provide sufficient ionizing radiation to account for the observed Hα luminosity and equivalent width.

In general it is possible to analyse the relative strength of emission lines and draw some conclusions about the excitation mechanisms but this relies on accurate measurements of the strength of often weak emission lines. In early-type galaxies many of the emission lines are also present in absorption in the parent galaxy and therefore it is difficult to measure or even detect the emission.

More important for this study is that stellar absorption line-strength measurements can be severely affected if there is emission present in the galaxy which weakens the

stellar absorption. For example nebular Hβ emission on top of the integrated stellar Hβ absorption weakens the Hβ index and leads therefore to wrong (i.e., too old) age estimates (see Figure 4.2). González (1993) detected in several of his galaxies [OIII]λ5007 emission and corrected his Hβ index according to ΔHβ = 0.7 $\times$ [OIII]λ5007. Unfortunately this turns out to be a very insecure correction because the emission spectra of H II regions are strong in H I recombination lines, but the strength of [OIII]λ4959 and [OIII]λ5007 lines can differ greatly (Osterbrock, 1989; Carrasco et al., 1996). Note however, that *on average* González's corrections are correct.

Emission can also occur in one of the side-bands of the Lick/IDS indices and raise the continuum which in turn gives larger index values. In the literature there is a nice example of [NI]λ5199 emission which affects one of the continuum side-bands of the Mgb index (Goudfrooij and Emsellem, 1996). Table 4.2 summarizes all significant emission lines in the optical and also denotes the Lick indices affected.

Table 4.2: Nebular Emission Lines

Line	λ_0 [Å]	affected Lick/IDS index	Line	λ_0 [Å]	affected Lick/IDS index
[OII]	3727	-	HeI	5876	Na_D
[NeIII]	3869	-	[OI]	6300	-
[SII]	4073	Hδ	[OI]	6364	-
Hδ	4102	Hδ	[NII]	6548	-
Hγ	4341	Hγ	Hα	6563	-
[OIII]	4363	Hγ, Fe4383	[NII]	6583	-
HeII	4686	C4668	HeI	6678	-
Hβ	4861	Hβ	[SII]	6716	-
[OIII]	4959	Fe5015, Mg1, Mg2	[SII]	6731	-
[OIII]	5007	Fe5015	[ArIII]	7136	-
[NI]	5199	Mgb , Mg2	[OII]	7325	-
FeII	5270	Fe5270	[SIII]	9069	-
[FeVII]	5721	-	[SIII]	9532	-
[NII]	5755	-			

Emission in Fornax Early-Type Galaxies

The spectral range covered by the observations in **AAT96** allows to check for emission in [OIII]. Measuring the amount of emission directly in the spectra prooved to be not very successful, as variations in continuum shape and strong absorption lines confuse the results. Therefore a stellar model of each galaxy was created by broadening G9III-K4III stars to the respective velocity dispersion and combining the resulting frames to an average galaxy-model-spectrum. This model, which has been corrected to match the continuum of the galaxy, was then subtracted from the galaxy. The resulting spectrum has on average zero counts and shows the differences between the emission free model and the galaxy in question. For most of the wavelength range there are no features visible. Exceptions are

the regions of Mgb , Hβ and Hγ_A because the model spectrum cannot reproduce the line strength observed in some of the galaxies. However, this does not affect the measurement of [OIII], because in this wavelength range the subtraction works very well and emission is readily visible if present. In Figure 4.6 normalized "emission" spectra of all Fornax galaxies and NGC3379 are presented. Note that some of the fainter galaxies (e.g., ESO numbers) have lower S/N which is reflected in somewhat noisier "emission" spectra.

The equivalent width of [OIII] emission was interactively measured on the normalized 'emission' spectra with the IRAF task `splot`. Figure 4.7 shows [OIII]λ5007 emission in equivalent width plotted against the velocity dispersion of the galaxies. Five S0s and two Es of the Fornax sample show clear emission in [OIII]λ5007 ranging from 0.1 Å to 0.7 Å in equivalent width. This is very weak even for LINERS (see Ho et al., 1993) and suggests that there is very little Hβ emission present in these objects. Whether emission can be detected or not is dependent on the strength of the emission, the S/N of the data and the velocity dispersion of the galaxy. Here the three factors combined, result in a detection limit of $\sim 0.1 - 0.2$ Å for bright galaxies and somewhat less for the fainter ones. All galaxies with zero emission in Figure 4.7 could exhibit extremely weak emission which is below our detection limit. Note that the calibration galaxy NGC3379 (filled triangle) also shows weak emission consistent with other observations (e.g., González, 1993).

[OIII]λ4959 emission was detected in only three of the emission galaxies, where the ratio [OIII]λ5007 / [OIII]λ4959 $\simeq$ 5. However, the [OIII]λ4959 emission is usually very close to the detection limit. Comparing with the work of Ho et al. (1993) one should expect a ratio [OIII]λ5007 / [OIII]λ4959 $\simeq$ 3 which is exactly what the theoretical transition probabilities for the two energy levels would predict (Osterbrock, 1989).

The [OIII]λ5007 emission measurements show clearly that some of the galaxies, mainly S0s contain warm ionized gas. But most of the elliptical galaxies do not show any signs of emission. The relation between the strength of [OIII]- and Balmer emission strength is highly dependent on the temperature of the excitation mechanism. For example ESO358-G25 which shows clear Balmer emission in the spectra exhibits roughly the same amount of [OIII]λ5007 emission as ESO359-G02 which seems to be free of Balmer emission. Therefore [OIII]λ5007 measurements cannot be used to correct Balmer absorption indices for emission without knowledge of the ionization origin. However they can give a fairly secure indication whether there is any emission at all, i.e., whether warm ionized gas is present. Overall most of the galaxies in the Fornax sample do not show any emission in [OIII]λ5007 [6] and therefore it was safe to use the Balmer indices as age indicator for these galaxies. Note that any Balmer-emission would weaken the Hβ absorption and therefore the galaxies would appear to be older. As the S0s are on average younger and most of the ellipticals do not show any signs of [OIII] emission our conclusions from Section 4.3 still hold.

[6] Also Phillips et al. (1986) found that Fornax galaxies show less than average nuclear [NII]λ6584 emission.

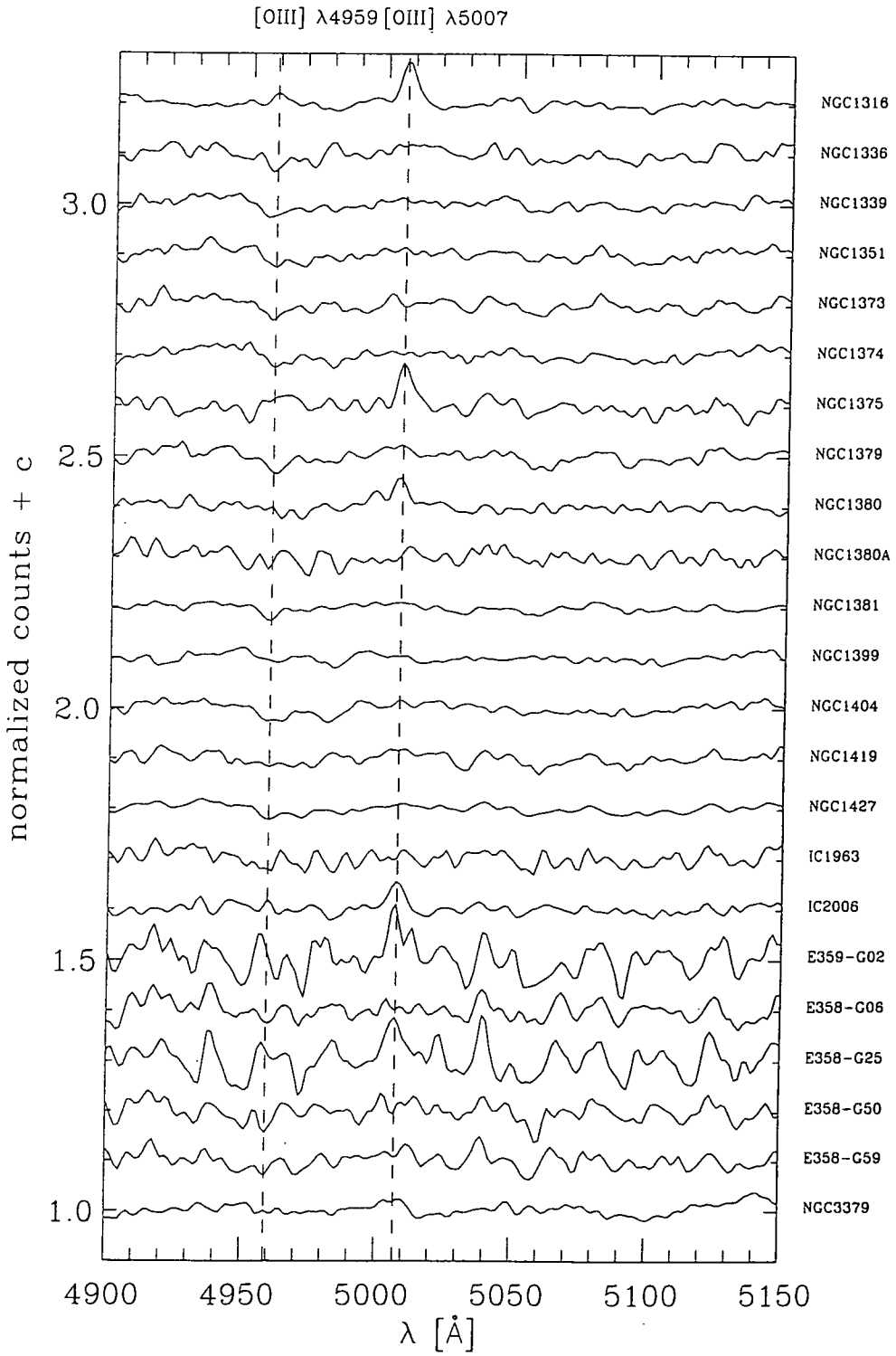

Figure 4.6: Normalized residual "emission" spectra after the subtraction of the stellar continuum. The galaxy names are indicated to the right of each spectrum. The central wavelengths of [OIII]λ4959 and [OIII]λ5007 emission are indicated by dashed lines. Some spectra show clear [OIII]λ5007 emission (see text for details).

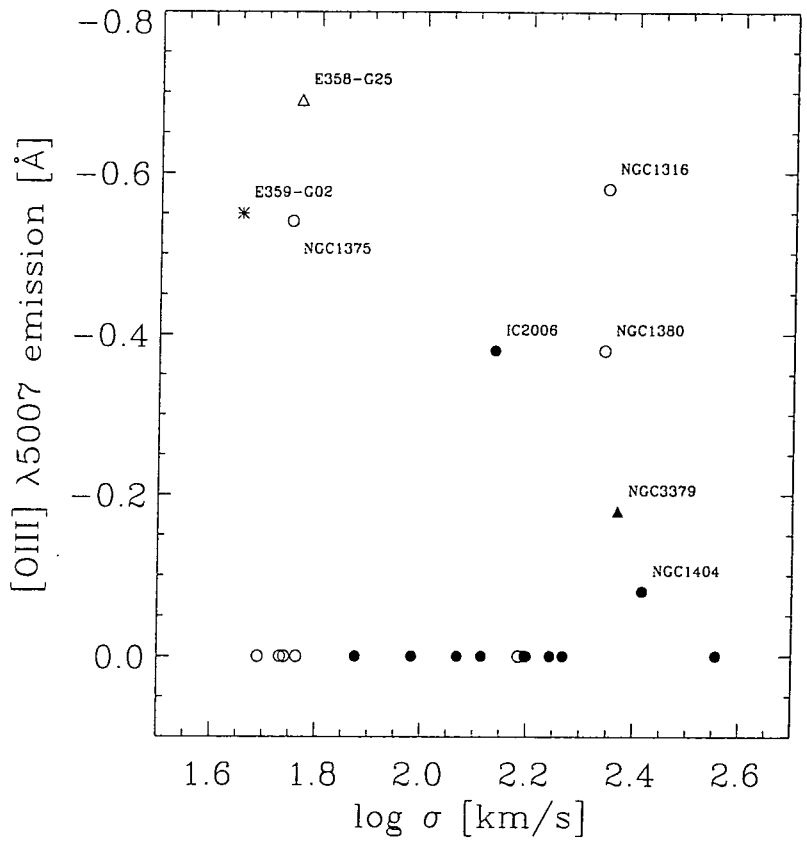

Figure 4.7: [OIII]λ5007 emission in Fornax galaxies. Filled and open circles represent Es and S0s respectively. The cross and open triangle represent post-starburst and starburst galaxies respectively and NGC3379 is represented by a filled triangle. All labeled galaxies show signs of [OIII]λ5007 emission.

As mentioned earlier on, there is a much better way to check for Balmer-emission. The relative strength of HI recombination lines in gaseous nebulae decreases rapidly with the order of the Balmer-line (Osterbrock, 1989). At the same time the stellar absorption strength stays nearly constant. See Table 4.3 for the ratios of Balmer emission. The Hγ emission is less than half as strong as for Hβ therefore the Hγ absorption is less affected by Balmer emission and should serve as a more reliable age indicator. As was shown in Section 4.3.2 this works very well for the galaxy ESO358-G25. Furthermore, none of the other galaxies move to much younger ages, indicating that emission in the Balmer lines is not jeopardising the results from Section 4.3.1. Table 4.4 summarizes all the available information on emission in Fornax early-type galaxies.

Table 4.3: HI Recombination Lines

emission lines	ratio
jHα / jHβ	3.4 - 2.7
jHβ / jHβ	1.0
jHγ / jHβ	$\sim$ 0.45
jHδ / jHβ	$\sim$ 0.25

Adapted from Osterbrock (1989) and valid for T=2,500 - 20,000° K.

Table 4.4: Emission in Fornax Early-Type Galaxies

Name	Type	[NII]λ6584 EW [Å] [a]	[OII]λ3727 EW [Å] [b]	log $\frac{M(HII)}{M_\odot}$ [c]	log $\frac{M(HII)}{M_\odot}$ [d]	IRAS detection [e]	[OIII]λ5007 EW [Å] [f]
NGC1316	S0	2.9	-	-	-	*	0.58
NGC1336	E	<0.52	-	-	-	-	-
NGC1339	E	-	-	-	-	-	-
NGC1351	E	<0.44	-	-	-	*	-
NGC1374	E	<0.40	-	-	-	-	-
NGC1375	S0	<0.55	-	-	-	-	0.54
NGC1379	E	<3.66	0.86	-	-	-	-
NGC1380	S0	2.14	-	-	-	*	0.38
NGC1381	S0	<0.64	-	-	-	-	-
NGC1399	E	<0.38	-	3.45±0.04	4.08	-	-
NGC1404	E	<0.32	-	<2.92	-	-	0.08
NGC1419	E	<0.43	-	-	-	-	-
NGC1427	E	<0.60	-	<2.78	-	-	-
IC2006	E	-	-	-	-	*	0.38
ESO359-G02	S0	-	-	-	-	.	0.55
ESO358-G06	S0	-	-	-	-	-	-
ESO358-G25	S0	-	-	-	-	.	0.69
ESO358-G59	S0	-	-	-	-	-	-

[a] from Phillips et al. (1986)
[b] from Caldwell (1984)
[c] from Goudfrooij et al. (1994a)
[d] from Macchetto et al. (1996)
[e] from Knapp et al. (1989) [*] indicates detection at 60 and 100 μm, [-] indicates no detection and [.] indicates no entry in catalogue.
[f] from this work

4.4 The Effects of Varying Metal Abundance Ratios

The prominent Mg feature in the optical wavelength region has been used for many years to determine velocity dispersions and also metallicity estimates. This feature seems to be very strong in early-type galaxies leading to metallicity estimates as large as 3 times solar for the brightest galaxies. With better S/N observations and new models it is possible to study other metal absorption lines and compare the results with Mg.

Firstly let us define precisely what we mean with "metallicity". Worthey's model predicts line-strength indices for a given age, metallicity and IMF where the metallicity is quoted in [Fe/H] [7]. Other authors quote their metallicities rather as global metallicity [M/H] = $\log(Z/Z_{\odot})$ with e.g., $Z_{\odot} = 0.02$. These different descriptions hide an important problem for all metallicity estimates: when metallicities are inferred from only one absorption line, or in other words from only those elements present in a single feature, one should actually quote the metallicity as [elements/H]. Only if the abundance ratios between these elements and others are known (a priori) then one can quote a global metallicity Z. For example, it turns out that the abundance ratios for stars in the Milky Way are not constant, but show an α-element-to-iron ratio which is larger than the solar value for stars with [Fe/H] ≤ -0.6 (e.g., Fuhrmann et al., 1995; McWilliam, 1997, α includes elements such as O, Mg, Si, Ca and Ti which are build up by synthesizing ^{4}He-particles). Stars around solar metallicity and in the solar neighborhood have solar abundance ratios. There is little knowledge about stars which are more metal rich than solar but stars of up to [Fe/H] $= 0.4 - 0.5$ have been observed in our own galaxy. Following from this it is obvious that the Lick fitting functions implicitly include any abundance-ratio variations which are present in the stars collected in the Lick/IDS stellar library i.e., the abundance ratios in the Milky Way. Namely, for metal poor models ([Fe/H] ≤ -0.6) the predictions should be α-element overabundant and model predictions around solar metallicity ([Fe/H] $= 0$) should reflect solar abundance ratios. For any further comparison of observed data and models it is assumed that Worthey's models reflect solar abundance ratios for [Fe/H] > -0.5. From a theoretical point of view it would be desirable to quote metallicity as total metallicity Z i.e., the total mass fraction of metals. From an observer's point of view, this is rather difficult because all of the Lick/IDS indices we consider in this thesis measure the abundance of one or a few specific elements – in fact they were designed to do that – but they never reflect a true measure of the total metal content. For our final metallicity estimates we will use Fe-lines and therefore we quote all metallicities in [Fe/H] rather than [M/H]. We note that for future work it would be desirable to identify index combinations which trace the total metallicity because there are indications that as long as the total metallicity is kept constant, isochrones and thus model predictions do not change very much (see e.g., Weiss et al., 1995).

[7] Note that the stellar [Fe/H] values quoted by Worthey are derived from different sources and are not necessarily based on real Fe-line measurements

For luminous elliptical galaxies many studies (e.g., Worthey et al., 1992; Worthey, 1994, 1996; Peletier, 1989; Davies et al., 1993) have shown that Mg appears to be over-abundant compared to Fe. If the objects to be compared with the models have non-solar abundance ratios then metallicity *and* age estimates will be somewhat skewed. In order to overcome these difficulties González defined the [MgFe] index (see Equation 3.5) which is of intermediate behaviour. Furthermore Worthey (1994, 1996) identified $C_2$4668 as a particularly sensitive metallicity feature that, while overabundant compared to Fe, is less overabundant than Mg. He points out however that using a different metallicity indicator does not change the relative distribution of the ages and metallicities of galaxies much but simply shifts the distribution of all galaxies together so that their relative ages should be insensitive to the choice of diagnostic.

Note also that sometimes the names of Lick/IDS indices are somewhat misleading in the sense that e.g., Fe5270 does not only measure the absorption caused by Fe at 5270 Å but also measures other elements/molecules which happen to affect the same wavelength region (Tripicco and Bell, 1995, see also Table 4.5). See Table 3.1 on page 39 for the main contributers to each Lick/IDS index; elements in round brackets affect the index in a negative sense. In the Lick/IDS system it is therefore difficult, if not impossible, to identify an index which measures pure Fe-abundance, i.e., [Fe/H]. Tripicco and Bell (1995) state that Fe4383 is the only Fe index which is more strongly affected by a doubling of the Fe abundance than a doubling in the overall metal abundance. Coming back to the previous paragraph where we elaborated on the difficulties of measuring total metallicity Z, we note that Fe-lines might be after all not such a bad choice for a total metallicity [M/H] estimate.

In the following we will explore how non-solar abundance ratios affect the age and metallicity estimates from the previous Sections. We then develop some methods to obtain unbiased measurements.

4.4.1 The Mg-Overabundance

How exactly does the Mg-overabundance manifest itself in an age/metallicity diagnostic diagram? Figure 4.8 shows a plot of $H\gamma_A$ equivalent width *vs* four different metallicity indicators: Mg*b* , $C_2$4668, <Fe> and Fe4383.

In Figure 4.8 there are several important things to note:

1. The model grids clearly show that Mg*b* is not a good choice as metal indicator because the models are almost degenerate. This reflects the fact that Mg*b* is not only dependent on metallicity but also to a high degree on age. $C_2$4668, <Fe> and Fe4383 do much better in this respect. See Worthey (1996) for a similar comparison for Lick/IDS galaxies.

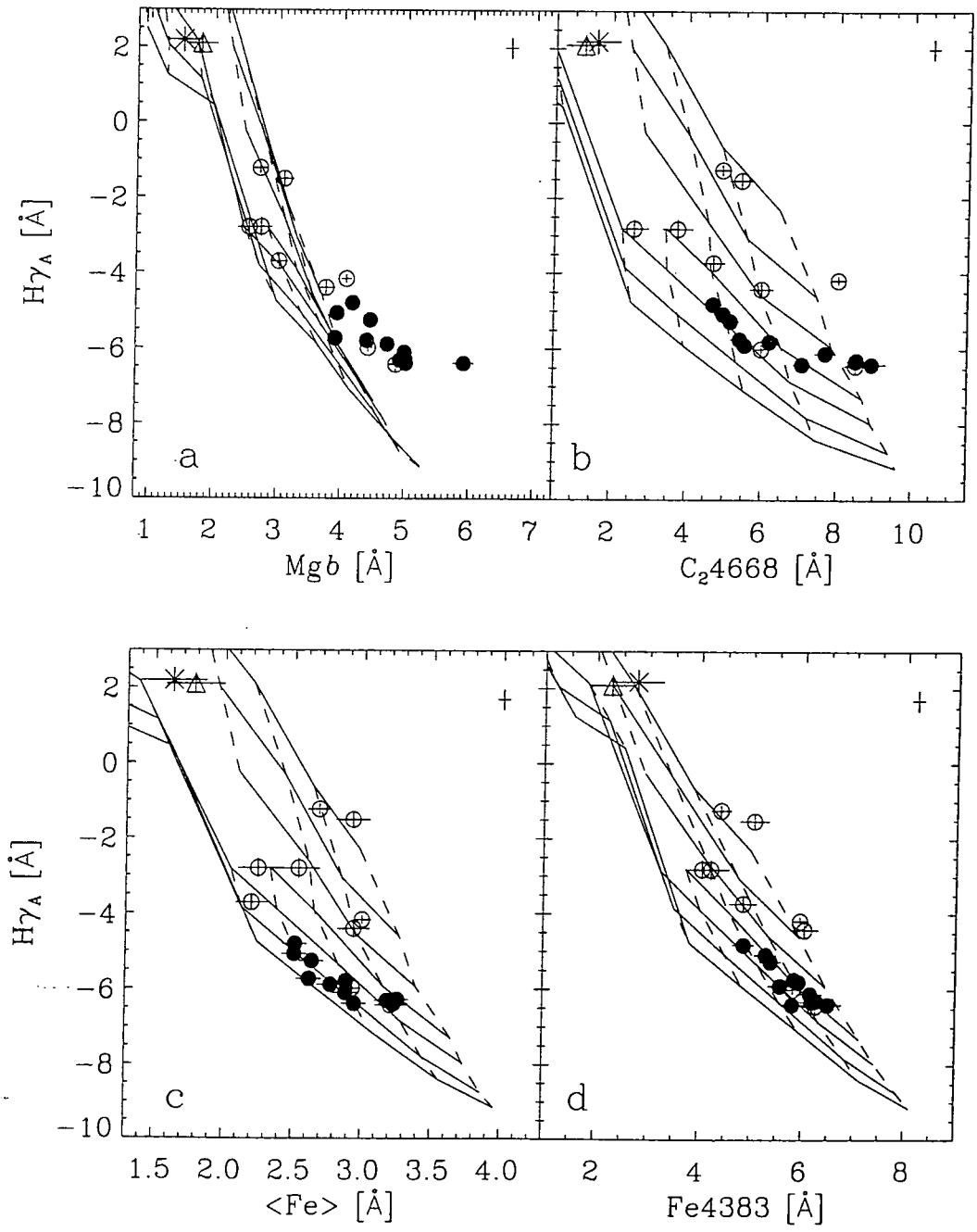

Figure 4.8: $H\gamma_A$ equivalent width *vs* Mg*b* , $C_2$4668, <Fe> and Fe4383 equivalent width diagram for the complete sample of Fornax early-type galaxies. Overplotted are models by Worthey (1994). The crosses in the right upper corner of each plot represent the rms error in the transformation to the Lick/IDS system. Symbol definitions as in Figure 4.2. Note how the metallicity distribution and hence the absolute ages change with the choice of metal indicator.

2. It is evident from panel (a) that when using Mgb as metal indicator that almost all elliptical galaxies (filled circles) are outside the model grid, giving metallicities of [Fe/H] > 0.5. In contrast the other metal indicators such as <Fe> and $C_2$4668 give metallicities [Fe/H] $\leq$ 0.5. The obvious discrepancy in the metallicity estimates is usually ascribed to different metal abundance ratios between the models ($\sim$ solar) and the galaxies in question (see e.g., Trager et al., 1998) e.g., the Mg-overabundance. Note that in all plots the younger S0s (open circles) stay roughly at the same position with respect to the model grid. This is evidence that S0s might not be affected by Mg-overabundance. Interestingly, the bulges of the two "old" S0s, NGC1380 and NGC1381, stay at the same position relative to the Es, suggesting that they had a very similar formation mechanism as the Es. For all four metal indicators the metallicity sequence of the Es is preserved.

3. The model grids do not separate the effects of age and metallicity completely. As a result, a mean shift in metallicity introduced by abundance ratio variations as seen for the Es will change the absolute age estimates as well. When the model grids are extrapolated to higher metallicities the Hγ_A *vs* Mgb plot suggests very young ages for the Es; Fe-lines such as <Fe> give evidence for a rather old population of elliptical galaxies in Fornax.

4. As suggested by Worthey the relative age distribution of the sample is preserved when a sensible metallicity indicator is used.

How can we investigate and quantify the Mg-overabundance further? To date there are only a few attempts to predict line-strength indices for varying abundance ratios (see e.g., Borges et al., 1995; Weiss et al., 1995; Greggio, 1997). Borges et al. (1995) models are based on separate fitting functions for each [Mg/Fe] bin, but the predictions for solar abundance ratios ([Mg/Fe]=0.0) do not agree with Worthey's models. Since we use mainly the well accepted models of Worthey throughout this thesis we will not compare with Borges's models. What can be done within the context of Worthey's models is to analyse plots of Fe-lines *vs* other Mg-indicators and see whether the data points are consistent with the solar abundance ratio model predictions or not.

Figure 4.9a shows a plot of Mg_2 in magnitudes *vs* Fe5270 equivalent width. In these coordinates the effects of age and metallicity degenerate almost completely. But this allows us to determine easily any differences between the model predictions and the observed data. And indeed we see again that for large Mg_2 absorption, the elliptical galaxies do not follow the model predictions, but exhibit a too large Mg absorption i.e., are Mg overabundant (or Fe underabundant). As seen in Figure 4.8 the young S0s are consistent with solar abundance ratios. Remarkably, a sample of six bright spheroidal (Sph) galaxies in the Virgo cluster observed by Gorgas et al. (1997) populate a similar location in previous plot. Worthey (1996) states that these, almost degenerate model grids would not change very much when input parameters such as age, metallicity, helium abundance, mixing

length, horizontal branch morphology or IMF are varied.

Greggio (1997) presented a simple way to estimate the [Mg/Fe] ratio on the basis of Worthey's models with assumed solar abundance ratio. For an α-element overabundance of [Mg/Fe]=0.4 the expected differences are: Mg_2 increases by $\sim$ 0.015 mag and Fe5270 decreases by $\sim$ 0.48 Å. The correction for a 17 Gyrs isoage line of the Worthey models are indicated in Figure 4.9 by arrows. Compared with the corrected models all ellipticals lie within the model predictions, which suggests Mg overabundances ranging from 0.0 to 0.4 dex. Note that the metal poor Es seem to be less overabundant, approaching solar ratios, consistent with the findings by González (1993).

Obviously the previous statements are very sensitive to the models one uses in the analysis. We will now explore a similar diagram to Figure 4.9a, but compare with model predictions by Weiss et al. (1995), which are independent of Worthey models. Figure 4.9b shows a plot of Mg_2 in magnitudes *vs* <Fe> equivalent width. Overplotted are models by Worthey and two models by Weiss et al. (1995) for [Mg/Fe]=0.00 and 0.45 (details see Figure caption). Again, in these coordinates the position of Es is outside the model predictions of Worthey, however they are consistent with the [Mg/Fe]=0.45 models from Weiss et al. (1995) confirming the result, that luminous Es are overabundant by up to 0.4 dex in Mg. We note that the [Mg/Fe]=0.0 models do not agree with Worthey models in an absolute sense, but the relative distribution of solar abundance and non solar abundance ratio models are consistent with it. In summary we conclude that there is an offset between the model predictions but both independent models give strong evidence of an overabundance of Mg compared to iron.

Some of the uncertainties in determining non-solar abundance ratios are caused by poorly determined Fe-line strength. The <Fe> index, being a combination of two Fe lines is already much better determined than either of the individual Fe lines Fe5270 and Fe5335. In order to find an index combination which breaks the age/metallicity degeneracy as well as possible and which is not affected by Mg-abundance ratio variations we will define a new Fe line index: Fe3. The new index combines three strong Fe-lines in order to maximize the sensitivity towards Fe-abundance and at the same time minimizes uncertainties due to large errors in individual lines. As mentioned before none of the Lick/IDS indices measures the absorption strength of only one element but rather the combination of all elements present in the index-region. Tripicco and Bell (1995) investigated with synthetic spectra the influence of individual elements on the total index. We summarize their results for selected indices in Table 4.5. For the new Fe3-index abundance ratio problems are somewhat reduced as some elements affect the individual indices in opposite ways, but all three indices are dominated by Fe abundance in a positive sense. Fe3 is defined as

$$\mathrm{Fe3} = (\mathrm{Fe4383} + \mathrm{Fe5270} + \mathrm{Fe5335})/3 \qquad (4.2)$$

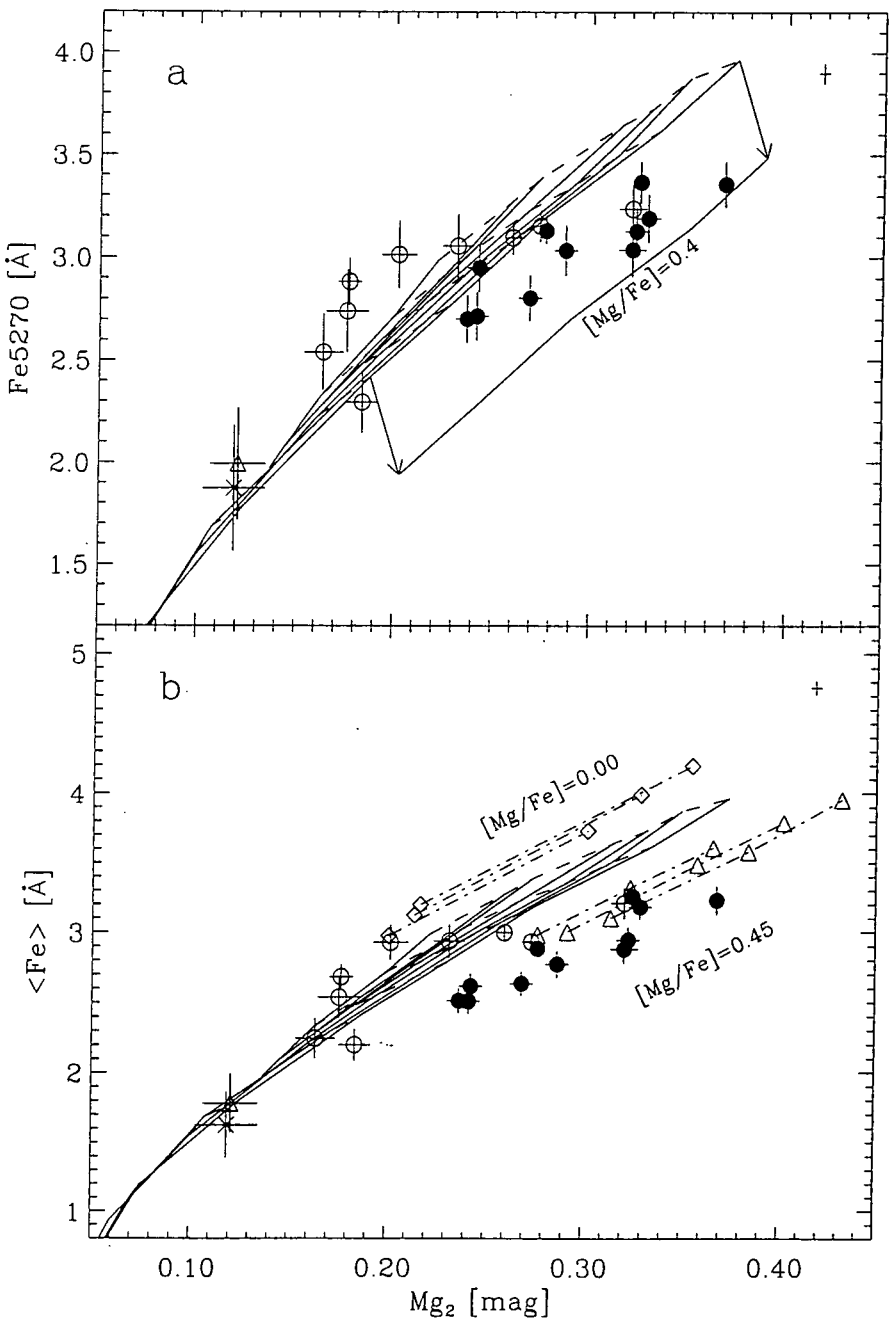

Figure 4.9: (a) Mg_2 *vs* Fe5270 equivalent width diagram for the complete sample of Fornax early-type galaxies. Overplotted are models by Worthey (1994) and a correction for [Mg/Fe]=0.4 for the 17 Gyrs isoage line (taken from Greggio, 1997). (b) Mg_2 *vs* <Fe> diagram. Overplotted are models by Worthey (1994) and two models by Weiss et al. (1995) (dot-dashed lines). The solar abundance ratio model is calculated for three ages, 12, 15 & 18 Gyrs (dot-dashed lines represent isoage lines) at Z=0.02 & 0.04 (diamonds) and a mixing length parameter of $\alpha_{MLT} = 2.5$. The [Mg/Fe]=0.45 model represents the same ages but metallicity steps of Z=0.02, 0.04 & 0.07 (triangles) and $\alpha_{MLT} = 2.0$.

Table 4.5: Spectral Index Response to Abundance Changes: Cool Giant

Index	I_0	Error	C	N	O	Mg	Fe	Ca	Na	Si	Cr	Ti	[M/H]
C4668	8.62	0.640	25.2	0.1	-4.0	-0.9	0.1	-0.1	-0.2	-1.6	-0.2	0.5	4.0
Mgb	3.65	0.230	-3.5	0.0	0.1	6.0	-1.3	-0.2	-0.4	-0.4	-2.0	0.1	1.3
Fe4383	9.02	0.530	1.1	-0.1	-0.4	-1.1	3.1	-0.4	-0.1	-0.7	-0.0	0.2	1.7
Fe5270	4.49	0.280	1.4	0.3	-0.2	-0.9	1.7	0.1	-0.1	-0.3	0.1	0.2	1.8
Fe5335	3.40	0.260	-1.0	-0.1	0.1	-0.6	2.4	0.0	-0.1	-0.2	0.5	0.2	1.9

Taken from Tripicco and Bell (1995)

Column 2 gives the computed index value, column 3 gives the (observed) standard error, columns 4-13 give the effect of the changes in units of the standard error as the element abundance is increased by 0.3 dex, and column 14 gives the effect (again in units of the standard error) for an increase in *overall* metallicity by 0.3 dex.

Although all three Fe lines do not reflect a pure Fe abundance they are among the best Fe-indicators within the Lick/IDS system. A comparison with other metallicity indicators in the Lick/IDS system shows that the new Fe3 index agrees well with the model predictions and that the model predictions are consistent. See Figure 4.10 for plots of Fe3 against various other metal lines.

How does our new Fe3 index compare with the previous Mg-overabundance estimates? Figure 4.11a & b show diagrams of Fe3 *vs* Mgb and Mg_2 respectively. Both diagrams confirm the previous results and as they combine our most sensitive Fe-indicator with the two Mg-lines we will use them in Section 5.4 on page 124 to investigate the effects of Mg-overabundance on the Mg-σ relation.

The results by Tripicco and Bell (1995) suggest that all Fe indices are affected in a *negative* sense by an increase in Mg-abundance (see Table 4.5) and therefore any Mg-overabundance makes the Fe indices not grow in a linear way with [Fe/H] but slower. This leads to the most Mg rich galaxies being even further away from the model grids. However, according to Tripicco and Bell (1995) the negative dependence on Mg-abundance is a factor of 2-3 weaker than the positive dependence on Fe-abundance.

Another interesting index diagnostic diagram in connection with the Mg-overabundance was first investigated by Fisher et al. (1995). They found a strong correlation between the central Mgb to Fe5270 ratio and the Hβ absorption for elliptical and brightest cluster galaxies. This is a surprising relation as it is much tighter than e.g., Mgb /Fe3 *vs* σ_0 (see Figure 5.10 on page 125). Mehlert (1998) has recently confirmed the Fisher et al. relation in a sample of bright Coma galaxies. Both works conclude that this diagram gives evidence that galaxies with a strong Mg overabundance are older (weaker Hβ absorption) than the ones which approach solar abundance ratios. For the Fornax cluster we present in Figure 4.12 relations between Mg_2/<Fe> and Mgb /<Fe> *vs* Hβ and Hγ_A. Overplotted are model predictions by Worthey (1994). The solid line represents a OLS Bisector fit (see Section 5.2 on page 108 for details) where all galaxies except ESO358-G25 and ESO359-G02 were included. The following equations summarize the fit results.

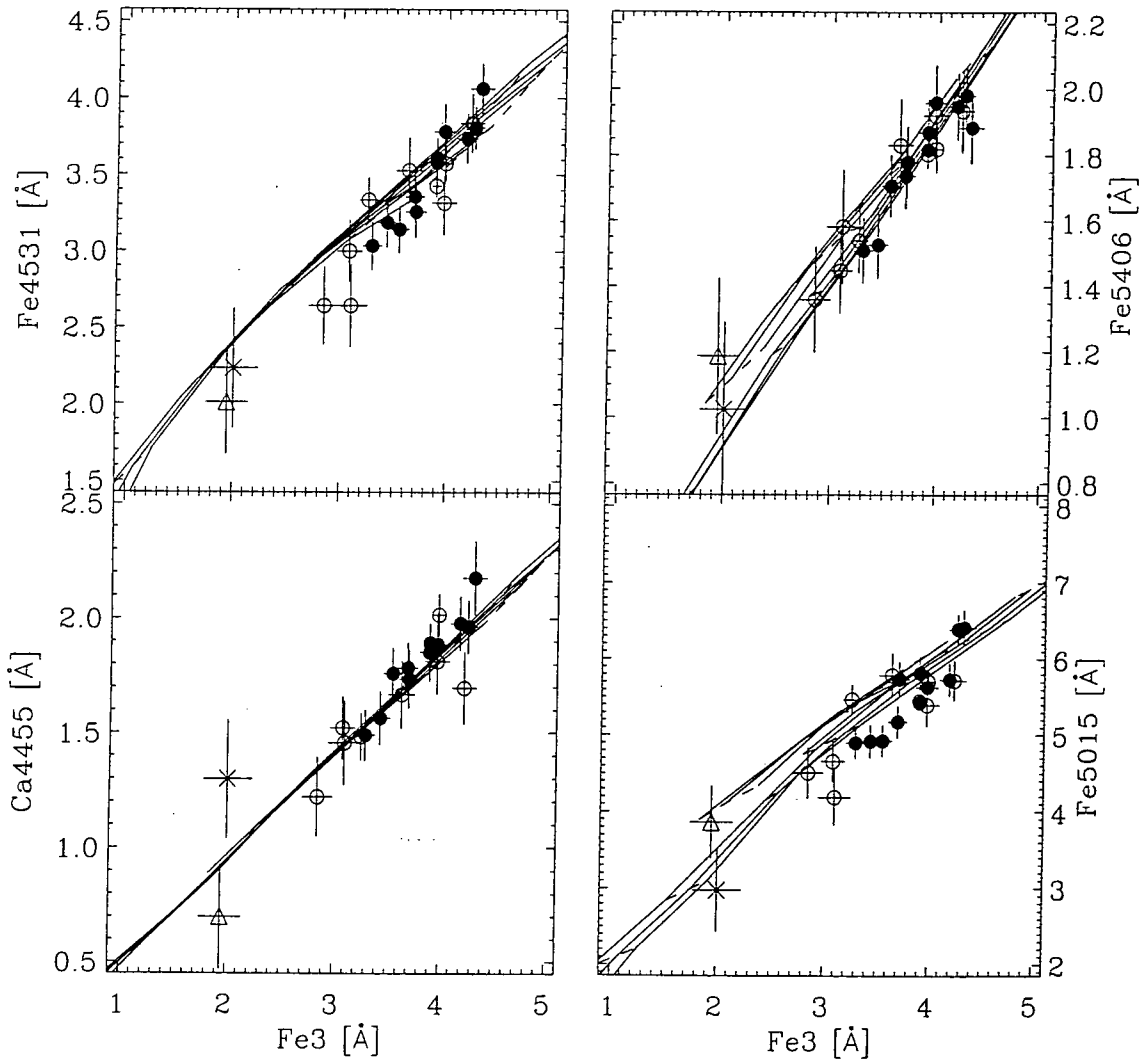

Figure 4.10: Fe3 equivalent width *vs* other metallicity indicators in the Lick/IDS system. Note how well the observed values follow the model predictions (Worthey, 1994).

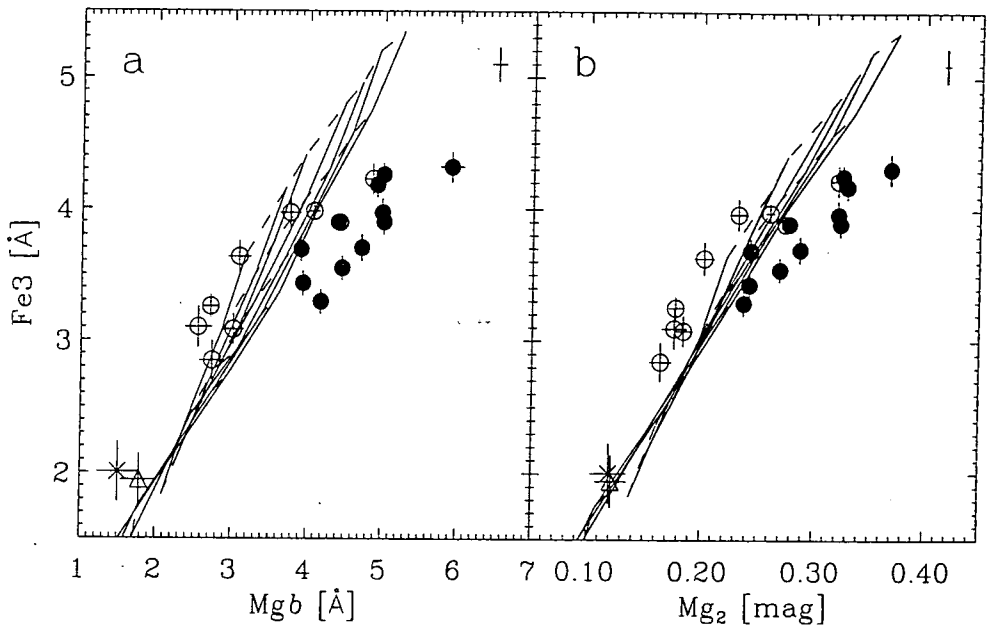

Figure 4.11: The new iron index Fe3 (see Equation 4.2) is plotted against Mgb and Mg2. The increasing Mg-overabundance for luminous ellipticals can be seen in both diagrams. The cross in the right upper corner indicates the rms uncertainty in the transformation to the Lick/IDS system.

$$\text{Mg}b\ /\langle\text{Fe}\rangle = (-0.526 \pm 0.060) \times \text{H}\beta + (2.455 \pm 0.114) \quad (4.3)$$

$$\text{Mg}b\ /\langle\text{Fe}\rangle = (-0.149 \pm 0.017) \times \text{H}\gamma_A + (0.739 \pm 0.088) \quad (4.4)$$

$$\text{Mg}_2/\langle\text{Fe}\rangle = (-0.031 \pm 0.004) \times \text{H}\beta + (0.151 \pm 0.007) \quad (4.5)$$

$$\text{Mg}_2/\langle\text{Fe}\rangle = (-0.009 \pm 0.001) \times \text{H}\gamma_A + (0.049 \pm 0.005) \quad (4.6)$$

The Fornax cluster shows a very similar result to Fisher et al. (1995) and Mehlert (1998). Remarkably the relation seems to hold even for the fainter S0s but possibly not for the two star burst galaxies. How can we explain such a tight relation where galaxies of very different age and metallicity are involved?

Usually one would expect some sort of an age/metallicity degeneracy to produce such a tight relation. The model predictions, spanning ages from 2 to 17 Gyrs and metallicities from -2.0 to +0.5, show indeed that only a very tight locus in the Mg/<Fe> *vs* Hβ or Hγ_A plane should be occupied. As Hβ and Hγ_A are very age sensitive features we conclude that Mg/<Fe> is also very age sensitive. In other words the models are degenerate in these coordinates because the effects of age and metallicity on these indices cancel each other out. However, the slope of the predicted relation is very different from the observed one.

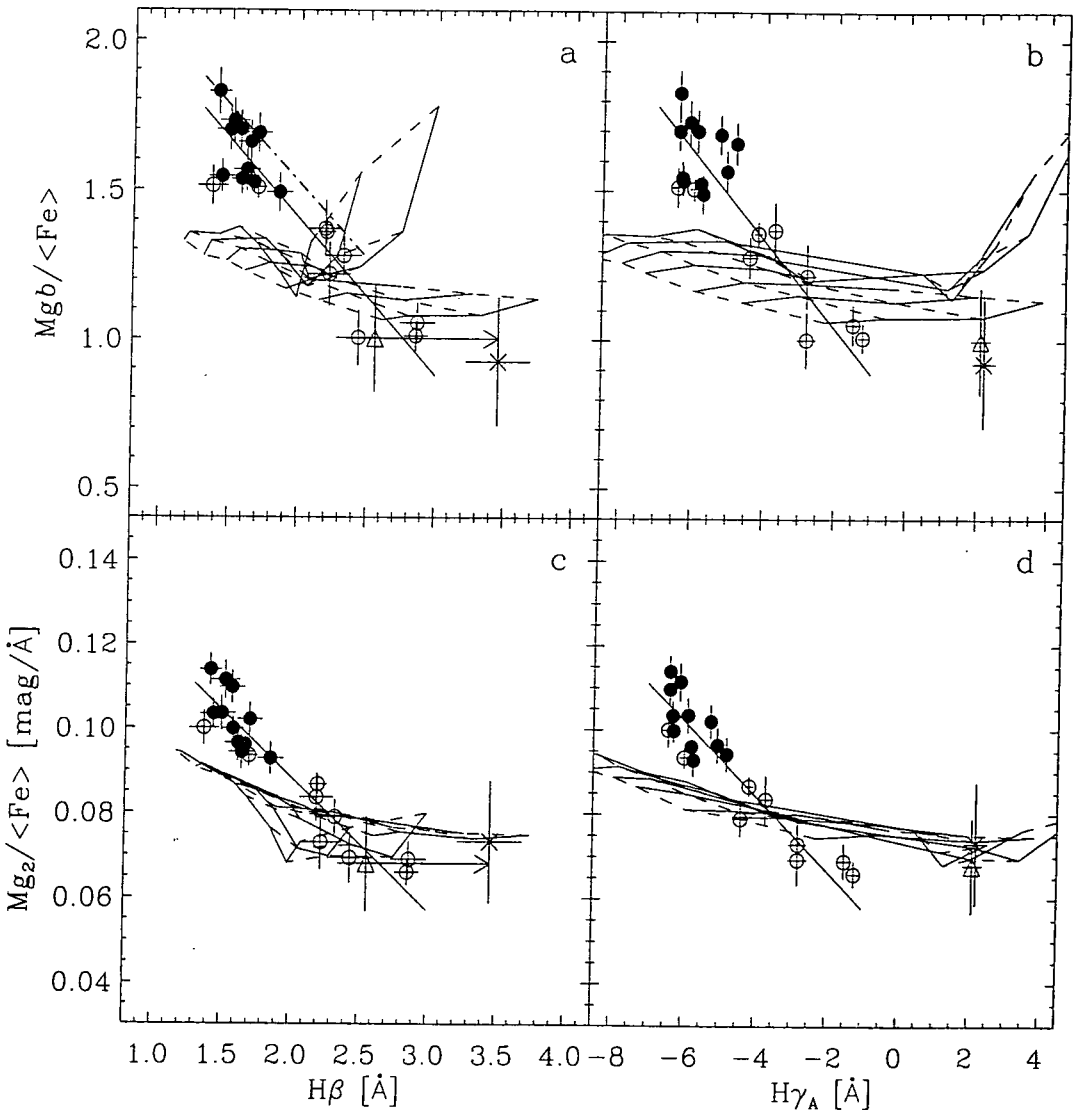

Figure 4.12: Shown are relations between Mg/<Fe> and the Balmer absorption indices Hβ and Hγ_A. Model predictions from Worthey et al. (1994) are overplotted in panel (a) to (d). In each plot the solid line represents a OLS Bisector fit to the Es and S0s (excluding the two starburst galaxies). In (a) the dot-dash line indicates the relation found by Mehlert (1998) for a sample of bright Coma galaxies.

This is unsurprising, because what we are seeing here is the result of a steady increase in Mg overabundance towards bright and large early-type galaxies. We emphasize that the change in Hβ or Hγ_A for the elliptical galaxies does not necessarily indicate a change in age because the Balmer lines do not completely break the age/metallicity degeneracy. Galaxies with the same age but *decreasing* metallicity show an *increasing* Hβ or for that matter Hγ_A index (see also Figure 4.2).

So far we have focussed on the well known Mg-overabundance in elliptical galaxies. But are there any other elements or indices which are overabundant, and even more important, what physical mechanism causes the overabundance?

The first signs of α-element enhancements were found in metal poor galactic stars in the 1960s (see review by McWilliam, 1997). There is a trend that the α-element overabundance increases with decreasing metallicity to up to [α/Fe]=$\sim$0.5. All the metals we find today have to be built up by nucleosynthesis from primordial gas. By burning nuclear fuel starting with Hydrogen, stars slowly build up metals and release them via stellar winds and supernovae (SNe) back to the inter-stellar medium (ISM). In this simple picture it is not clear how the varying abundance ratios can be accounted for. However, Tinsley (1979) proposed that SNeIa (resulting from mass accretion by a white dwarf; progenitor mass $\lesssim 10M_\odot$; time scale $\gtrsim 10^8 - 10^9$ yr) are the major producers of iron-peak elements in the Milky Way and that SNe of type II (resulting from exploding massive stars; progenitor mass $\gtrsim 10M_\odot$ time scale $\lesssim 10^6 - 10^7$ yr) produce mainly α elements. The time delay between the SNe would then account for the different abundance ratios observed in stars. Stars which formed early (i.e., metal poor stars) show an overabundance of α-elements and later star formation (i.e., metal richer) will involve more and more iron produced by SNeIa. These predictions are based on the Galaxy but already Tinsley (1979) recognized the implications it might have for elliptical galaxies: *"Therefore, by analogy with the picture of halo formation* [...] *elliptical galaxies may differ systematically in their relative abundances from the disk stars of the solar neighborhood"*. Note that asymptotic giant branch (AGB) stars can contribute as well to the metal enrichment of stellar populations (Edvardsson et al., 1993). These stars (progenitor mass $\sim 1 - 3M_\odot$) release mainly elements such as Y, Zr, Ba and Nd via stellar winds to the interstellar medium.

There are alternative explanations for an α-enhancement. The following scenarios have been proposed:

1. Selective mass loss, such that SNeIa products are lost more efficiently.
2. An Initial Mass Function (IMF) biased towards massive stars.
3. Lower rate of SNeIa compared to the Milky Way.

The plausibility and caveats of these scenarios is discussed in e.g., Thomas et al.

(1998a, and references therein). Following the results of previous authors it seems likely that most of the stars in luminous elliptical galaxies formed in a very short time, i.e., in a "fast clumpy collapse", before SNeIa could produce enough iron to significantly dilute the [Mg/Fe] ratio (see also Bender, 1996). Yet when one allows the IMF to be much flatter than the Salpeter value, the merger of two spiral-type galaxies can produce equally high [Mg/Fe] ratios (Thomas et al., 1998a). The detailed calculations of [Mg/Fe] ratios as a function of galaxy formation history are very complicated and still model dependent. Additionally the α-elements cannot be treated as a single group because the production of each element depends sensitively on stellar progenitor mass. For example Mg is only produced in significant amounts by stars with $> 35M_{\odot}$ whereas Si and S are produced by stars of $\sim 20M_{\odot}$ (Woosley and Weaver, 1995).

4.4.2 Are Other Elements Overabundant?

This leads us to the question whether other indices in the Lick/IDS system show non-solar abundance ratios. In Figure 4.13a we show a diagram of C_24668 equivalent width *vs* our best Fe-indicator Fe3. One can see that for $C_24668 < 6.0$ Å (roughly [Fe/H] $\leq +0.25$) S0s as well as Es agree with the solar ratio model predictions. For $C_24668 > 6.0$ Å the trend changes suddenly and the C_24668 absorption strength seems to be too large. This suggests that for $C_24668 < 6.0$ Å early-type galaxies in Fornax have roughly solar abundance ratios, but for $C_24668 > 6.0$ Å they seem to be overabundant in C_24668 similar to Mgb. Note that the C_24668 index is dominated by C_2 bands although many other metals are included in the index passband; in particular the Mg-abundance contributes negatively! Alternatively the Fe indices could be affected negatively and thus Fe would be under-abundant compared to C_24668. Looking at Table 4.5 the most promising candidate would be Mg but the effects are small compared to the increase in Fe and also we do not see a step in the Fe-index *vs* Mgb plots which we would expect if Mg suddenly lowers the Fe indices.

None of the other indices used in this thesis showed obvious signs of overabundance. Incidentally we must not forget that our age indicators namely the Balmer lines Hγ_A and Hβ could also be affected by non-solar abundance ratios. To our knowledge there are no detailed calculations for metal rich populations, however the work by Salaris et al. (1993) suggests that the turnoff temperature would be lowered by increasing the α-element abundance. This of course would influence the Balmer lines as they measure the turnoff temperature. As no appropriate models are available we will assume that Worthey's model predictions for Hβ & Hγ_A are correct. C_24668 is extraordinarily sensitive to metallicity and therefore it has been used as an average-metal indicator within the Lick/IDS system. We will now investigate how the overabundance influences the age/metallicity estimates by correcting the C_24668 index and re-analysing the ages and metallicities of Fornax early-type galaxies.

Using the model predictions one can attempt to correct the C_24668 index for non-solar

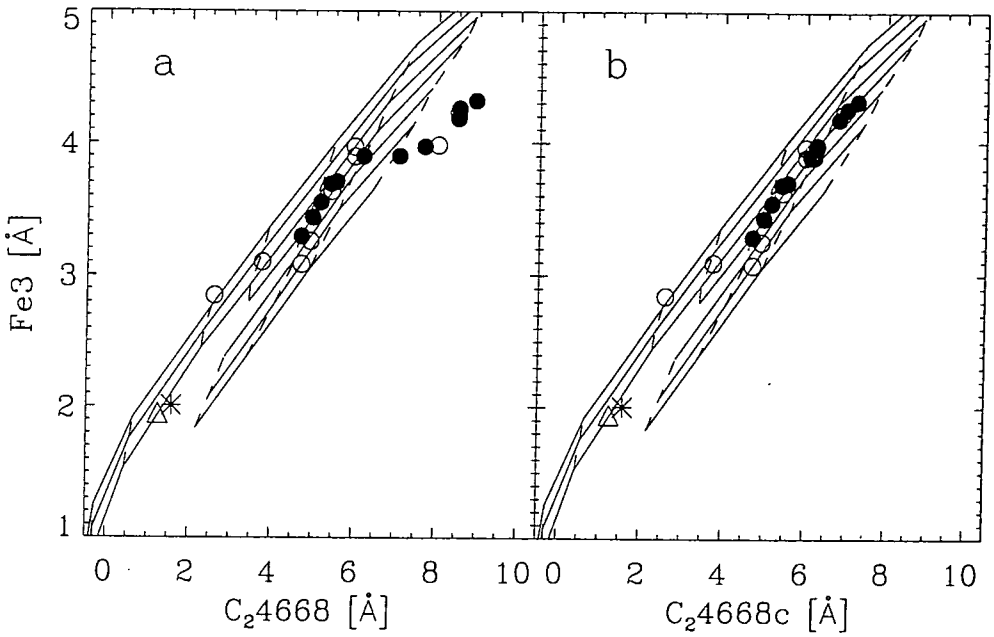

Figure 4.13: (a) Fe3 equivalent width *vs* $C_2$4668 equivalent width diagram before and (b) after correction for the non-solar abundance ratio of $C_2$4668.

abundances i.e., reduce the equivalent width of the galaxies with the strongest $C_2$4668 values so that they agree with the models. Figure 4.13b shows the relation between Fe3 and $C_2$4668 after the correction. Five ellipticals and two S0s have been shifted to lower values of $C_2$4668. From now on we use the corrected $C_2$4668 index in any line-strength analysis, indicated by the notation: $C_2$4668c. The new index values for the corrected galaxies are presented in Table 4.6. Other Fe-lines in the Lick/IDS system (e.g., Fe4531, Fe5015, Fe5406) agree very well with the new $C_2$4668c index, suggesting that the previous correction makes sense. Figure 4.14 shows $C_2$4668c against other metallicity indicators in the Lick/IDS system. Note that we could have used any other metal indicator in the Lick/IDS system to correct $C_2$4668 and we would have achieved very similar results.

Table 4.6: The $C_2$4668-Index Before and After Correction

name	$C_2$4668 [Å] before corr.	$C_2$4668c [Å] after corr.
NGC1316	8.02	6.25
NGC1339	7.69	6.25
NGC1374	7.07	6.10
NGC1380	8.50	6.90
NGC1399	8.93	7.25
NGC1404	8.52	7.00
IC2006	8.50	6.80

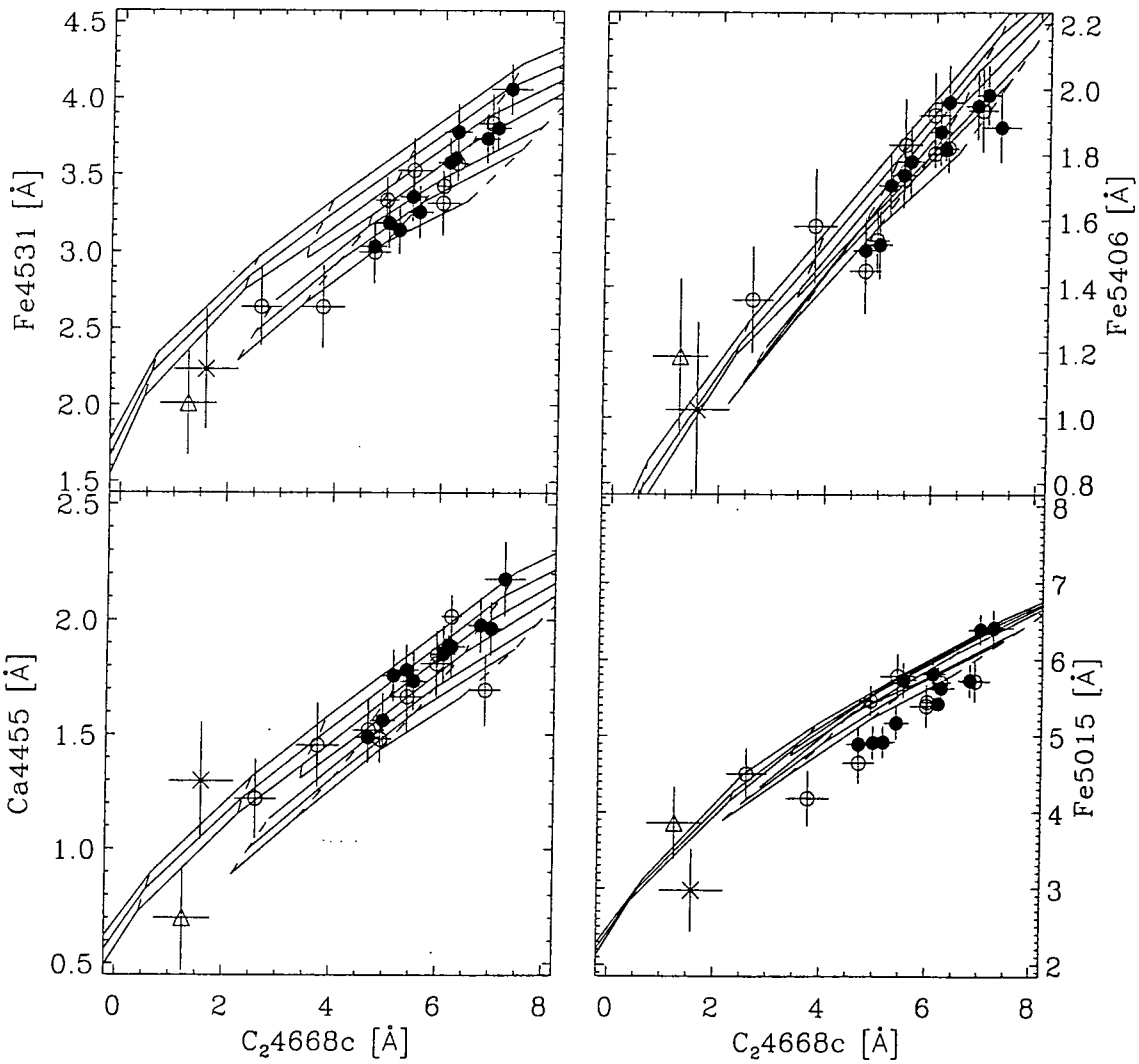

Figure 4.14: $C_2$4668c equivalent width *vs* other metallicity indicators in the Lick/IDS system. Note how well the observed values follow the model predictions (Worthey, 1994).

In the age/metallicity analysis of the previous Sections $C_2$4668 has been used as a mean metallicity indicator. For galaxies with [Fe/H] $\leq +0.25$ this is certainly a good choice. But for more metal rich galaxies this index seems to be affected by overabundance problems. This has important consequences. Generally one is interested to derive metallicities in terms of [Fe/H] or global metallicity $Z/Z_{\odot}$, rather than being biased to α-elements. Broad band colours for example are driven by [Fe/H] but the influence of [Mg/Fe] is negligible (Kurth et al., 1998). Revisiting Figure 4.3 on page 74 where a trend of decreasing age with increasing metallicity was apparent in Es, one has to conclude that this trend was mainly caused by the overabundance of these galaxies in $C_2$4668 compared to the models. With the new $C_2$4668c index the metallicity range is reduced to [Fe/H] < 0.35 and none of the galaxies are outside the model predictions (for details see Section 4.4.3 and Figure 4.15).

It is essential to realize that, as demonstrated in the example of $C_2$4668, *varying* abundance ratios can create or broaden a metallicity sequence while leaving age indicators such as Hβ, to first order, the same. As the model grids do not break the age/metallicity degeneracy completely, a shift in the metal-index always introduces a shift in age as well. *Therefore when abundance ratios vary in a given sample of galaxies, then both relative ages and metallicities will become index dependent.* As long as the effects of abundance ratios are not properly understood and implemented in the models, any age/metallicity determinations are subject of systematic errors.

However, following the previous conclusions we believe that the most unbiased metallicity estimates (in the sense [Fe/H]) within the Lick/IDS system can be drawn from the Fe indices. In particular Fe3 combining three strong Fe lines seems to be promising. But we note that velocity dispersion corrections are rather large and can lead to errors for the most luminous galaxies. Furthermore the model predictions suggest that the sensitivity towards metallicity is reduced in comparison to $C_2$4668.

4.4.3 Absolute Age and Metallicity Estimates

In this Section we seek to derive our most unbiased and accurate estimates of absolute age and metallicity for the Fornax sample. As the previous Sections have shown that this is not an easy task when one takes into account the abundance ratios. Note, the phrase absolute age or metallicity is used here in the sense of a certain luminosity weighted age and metallicity assigned to a galaxy within the Lick/IDS system.

We have defined a new metal indicator, Fe3, which we believe to be a relatively unbiased estimate of the iron-abundance of the integrated stellar populations. Furthermore we corrected $C_2$4668 for overabundance. Using these two indices in combination with our best age indicator Hγ_A we will determine absolute age and metallicity estimates of the complete sample of early-type galaxies in Fornax. These estimates are made neglecting any

non-solar abundance effects which still might influence the indices or model predictions. Note that our metallicity estimates of [Fe/H] cannot easily be converted into total metallicity Z, as the most luminous galaxies in our sample are probably Fe under abundant. So taking only the Fe-abundance one would underestimate the total metallicity Z.

Figure 4.15a shows a plot of $H\gamma_A$ *vs* Fe3. Of course, the main conclusion from previous sections, that S0s are on average younger than ellipticals, is still valid in these coordinates. The general distribution of the galaxies is very similar to those shown in the previous plots. The metallicity sequence of the Es covers the range $-0.25 < [Fe/H] < 0.35$ and the ages of the ellipticals are almost constant at ~8 Gyrs with a mild upturn for the most metal rich galaxies.

Using $C_2$4668c as metal indicator (Figure 4.15b) gives similar results, although in contrast to the Es, the S0 seems to be at slightly lower metallicities. Note that seven galaxies were corrected in $C_2$4668 using Fe3, hence $C_2$4668c is not completely independent of the Fe3 index. The ellipticals form a tight sequence in metallicity and have very similar ages. There is still a hint that the most metal rich galaxies are slightly younger. The S0s show on average very young ages, however the bulges of NGC1380 and NGC1381 are among the elliptical sequence (hardly visible in Figure 4.15).

Having identified optimal index-combinations one can now go ahead and derive *absolute* ages and metallicities from the index-index plots. We extended the model grids to a narrower spacing in age and metallicity (using the WEB based model generator by G. Worthey) so we could determine the ages and metallicities as accurately as possible. The resulting age- and metallicity-estimates for both Fe3 and $C_2$4668c *vs* $H\gamma_A$ plots are presented in Figure 4.16a, b and Table 4.7.

As expected the two index combinations show similar results. The ellipticals are old and span a range in metallicity: $-0.10 < [Fe/H] < +0.35$. Es have ages of 7-9 Gyrs where the most metal rich ellipticals seem to be slightly younger than the average. A word of caution is needed here. The independent errors of the observables from Figure 4.15, i.e., errors in Fe3, $C_2$4668c and $H\gamma_A$, translate into correlated errors in the age *vs* metallicity plane. Appropriate error bars for a galaxy of solar metallicity and 8 Gyrs age are shown in the top right corner of Figure 4.16a, b. The direction of Worthey's "3/2 rule" (i.e., the direction where the SED of galaxies does not change much) is indicated by an arrow. Note that the errors are correlated in roughly this direction. The errors are somewhat less correlated when $C_2$4668c is used as metal indicator, also the size of the errors is reduced. However this is only an average error estimate adequate for the sequence of Es and we emphasize that the exact errors depend on the position of the galaxy in the model grids. The S0s are scattered all over the age *vs* metallicity plane but are on average younger (3-4 Gyrs) than the Es. Analysing absolute ages and metallicities one sees that for the S0s the two diagrams differ substantially. This suggests that the age and metallicity estimates for the younger galaxies are subject to large uncertainties.

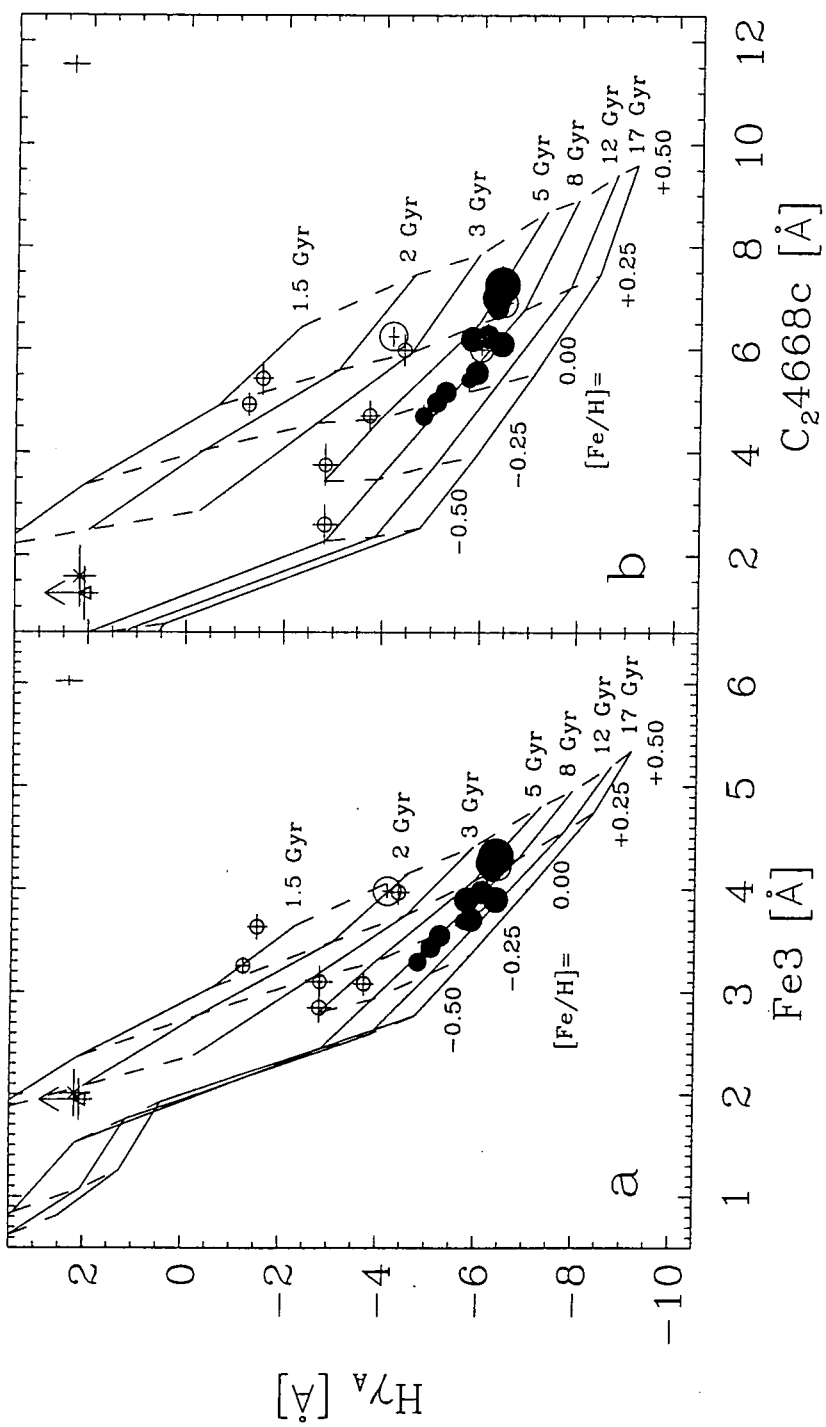

Figure 4.15: (a) Fe3 equivalent width *vs* $H\gamma_A$ equivalent width diagram. (b) C_24668c equivalent width *vs* $H\gamma_A$ equivalent width diagram. Overplotted are models by Worthey (1994). Filled circles and open circles represent ellipticals and S0s respectively. The cross and open triangle represent possible post-starburst and starburst galaxies respectively. The symbol sizes are scaled such that the area covered by the symbol is proportional to the central velocity dispersion of the galaxy. The cross in the right upper corner of each panel indicates the rms uncertainty in the transformation to the Lick/IDS system. Note that two bright S0s are hidden in the sequence of Es.

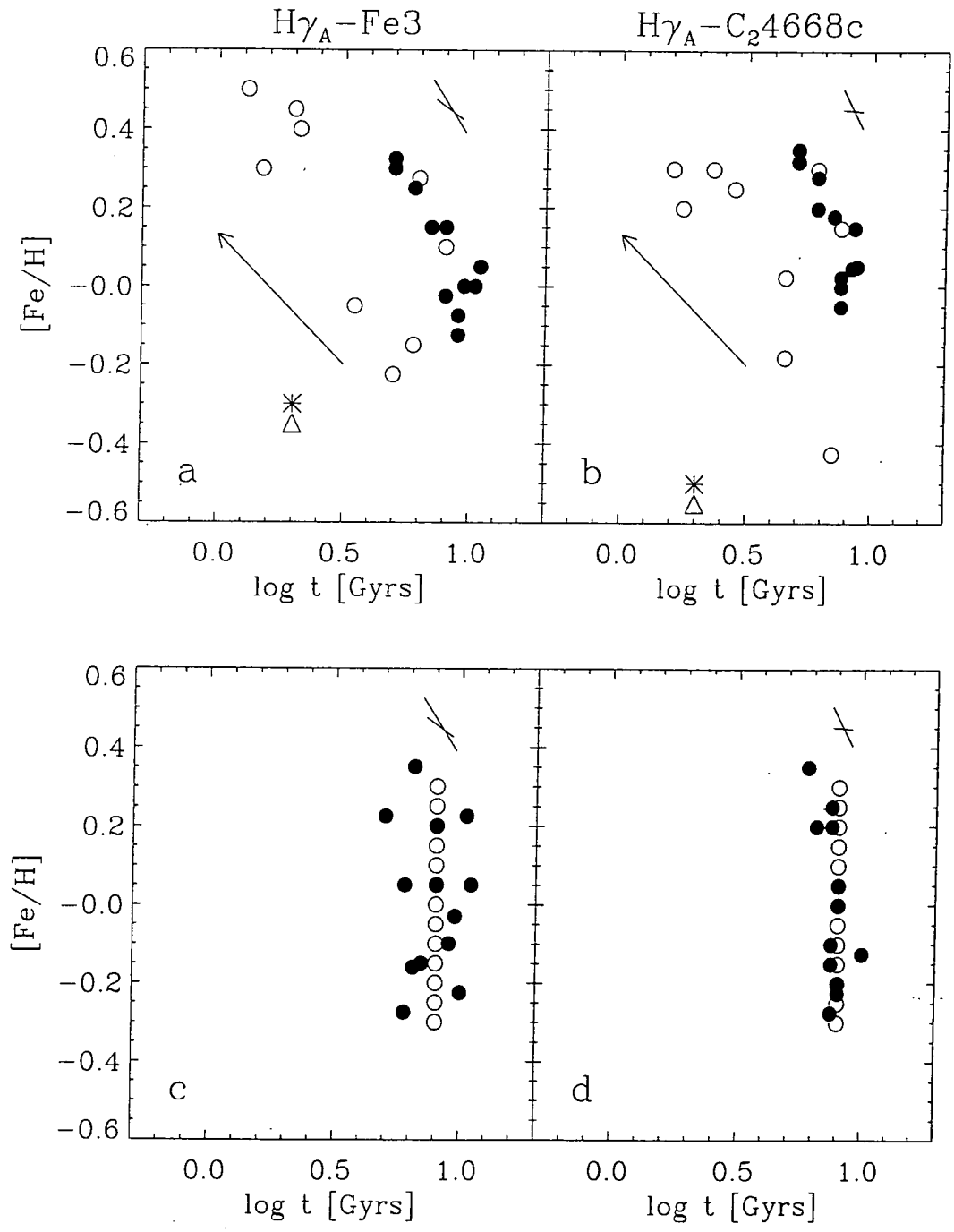

Figure 4.16: Ages and metallicities derived from index-index plots and Worthey (1994) models. (a) Ages and metallicities derived from $H\gamma_A$ *vs* Fe3 plot. (b) Ages and metallicities derived from $H\gamma_A$ *vs* C24668c plot. Panels (c) and (d) show Monte-Carlo simulations (filled circles) of an 8 Gyrs old population and a range in metallicity of -0.30 < [Fe/H] < +0.35 in steps of 0.05 dex (open circles). Mean errors in the observables were assumed to perform the simulations. For a discussion see text.

Table 4.7: The Ages and Metallicities of Fornax Early-Type Galaxies.

	from $H\gamma_A$- C_24668c		from $H\gamma_A$- Fe3	
name	age	[Fe/H]	age	[Fe/H]
NGC1316	2.3	0.300	2.0	0.450
NGC1336	7.5	-0.050	9.0	-0.125
NGC1339	7.0	0.180	8.0	0.150
NGC1351	8.7	0.052	10.5	-0.000
NGC1373	8.3	0.048	9.5	0.000
NGC1374	8.5	0.150	11.0	0.050
NGC1375	1.8	0.200	1.5	0.300
NGC1379	7.5	0.025	8.0	-0.025
NGC1380	6.0	0.300	6.3	0.275
NGC1380A	1.6	0.300	1.3	0.500
NGC1381	7.5	0.150	8.0	0.100
NGC1399	5.0	0.350	5.0	0.325
NGC1404	5.0	0.320	5.0	0.300
NGC1419	7.5	0.000	9.0	-0.075
NGC1427	6.0	0.200	7.0	0.150
IC1963	2.8	0.250	2.1	0.400
IC2006	6.0	0.280	6.0	0.250
ESO359-G02	2.0	-0.500	2.0	-0.300
ESO358-G06	7.0	-0.425	5.0	-0.225
ESO358-G25	2.0	-0.550	2.0	-0.350
ESO358-G50	4.5	-0.180	3.5	-0.050
ESO358-G59	4.5	0.025	6.0	-0.150

Ages are given in Gyrs.

In both diagrams we can see a trend such that metal rich elliptical galaxies are younger. Is it possible that correlated errors would produce such a relation? To investigate this we performed Monte Carlo simulations under the assumption that the Es form a true sequence of equal age but varying metallicity. Figure 4.16c, d show two typical Monte-Carlo simulations (filled circles) of a stellar population of constant age of 8 Gyrs and a range in metallicity from -0.30 to +0.30 (open circles). Both simulations have been performed assuming average errors in the observables. When using Fe3 as metal indicator, we find a larger spread in age due to the correlated errors than when using C_24668c. This is a direct result of the fact that the Fe3 *vs* $H\gamma_A$ diagram separates the effects of age and metallicity less effective than the $H\gamma_A$ *vs* C_24668c diagram.

In summary we find that some of the age upturn for the metal rich ellipticals may be explained by the effects of correlated errors in both diagrams but surely not all of it. This analysis does assume that the model predictions are absolutely correct. However, as can be seen from Figure 4.15, the slope (with respect to the indices) of the equal age lines changes for the last metallicity bin. This change in slope will obviously affect age

measurements in this region of the diagram, i.e., whether we find an upturn in ages for the most metal rich galaxies or not. How well is this slope-change determined? An answer to this problem is beyond the scope of this work but nevertheless an important issue.

All together, Figure 4.16 suggests that the line-strength analysis of the elliptical galaxies in the Fornax cluster is consistent with a population of approximately coeval Es (7-9 Gyrs) spanning a sequence in metallicity ($-0.10 <$ [Fe/H] $< +0.30$) where the most metal rich Es are perhaps slightly younger.

At the end of this Section we would like to relate our age and metallicity estimates with the total luminosity of each galaxy. Figure 4.17 (bottom panels) shows a plot of M_B *vs* the average log age and metallicity estimates from Figure 4.16. It seems that bright elliptical galaxies are more metal rich and younger than faint ones. A Spearman rank-order test for the Es only shows that the metallicity-luminosity relation is significant but the existence of an age-luminosity relation is doubtful. An ordinary least square fit (see Section 5.2 for fit details) gives

$$[\mathrm{Fe/H}] = -(0.08 \pm 0.02)\mathrm{M}_B - (1.60 \pm 0.39) \tag{4.7}$$

where M_B is the absolute blue luminosity.

We note that, apart from NGC1316, all young S0s are fainter than $M_B = -20$. As mentioned before, the age and metallicity estimates are model and index dependent. For that reason and because it is interesting from an observational point of view we have compared M_B directly with two age sensitive and two metallicity sensitive indices in Figure 4.17. Both metallicity indices reflect very well the range in metallicity found using the models, i.e., they show positive correlations with M_B. But the age sensitive Balmer indices on their own are not so easy to interpret. These lines show for the ellipticals a weak negative correlation which we interpret as a metallicity rather than an age effect. Note that both Balmer indices contain information from surrounding metal lines either in the central passbands or in the side band-passes. However, the existence of the young S0s, in particular NGC1316, is readily visible in the Hβ, Hγ_A *vs* M_B plot. We will not perform any more detailed analysis at this point but refer the reader to the analysis in Chapter 5 where analyse index–σ_0 relations.

4.5 Conclusions from Central Line-Strength Analysis

We have measured the central line strength indices in a complete sample of early-type galaxies brighter than $M_B = -17$ in the Fornax cluster and have applied the models of Worthey (1994) and Worthey and Ottaviani (1997) to estimate their ages and metallicities. We find that:

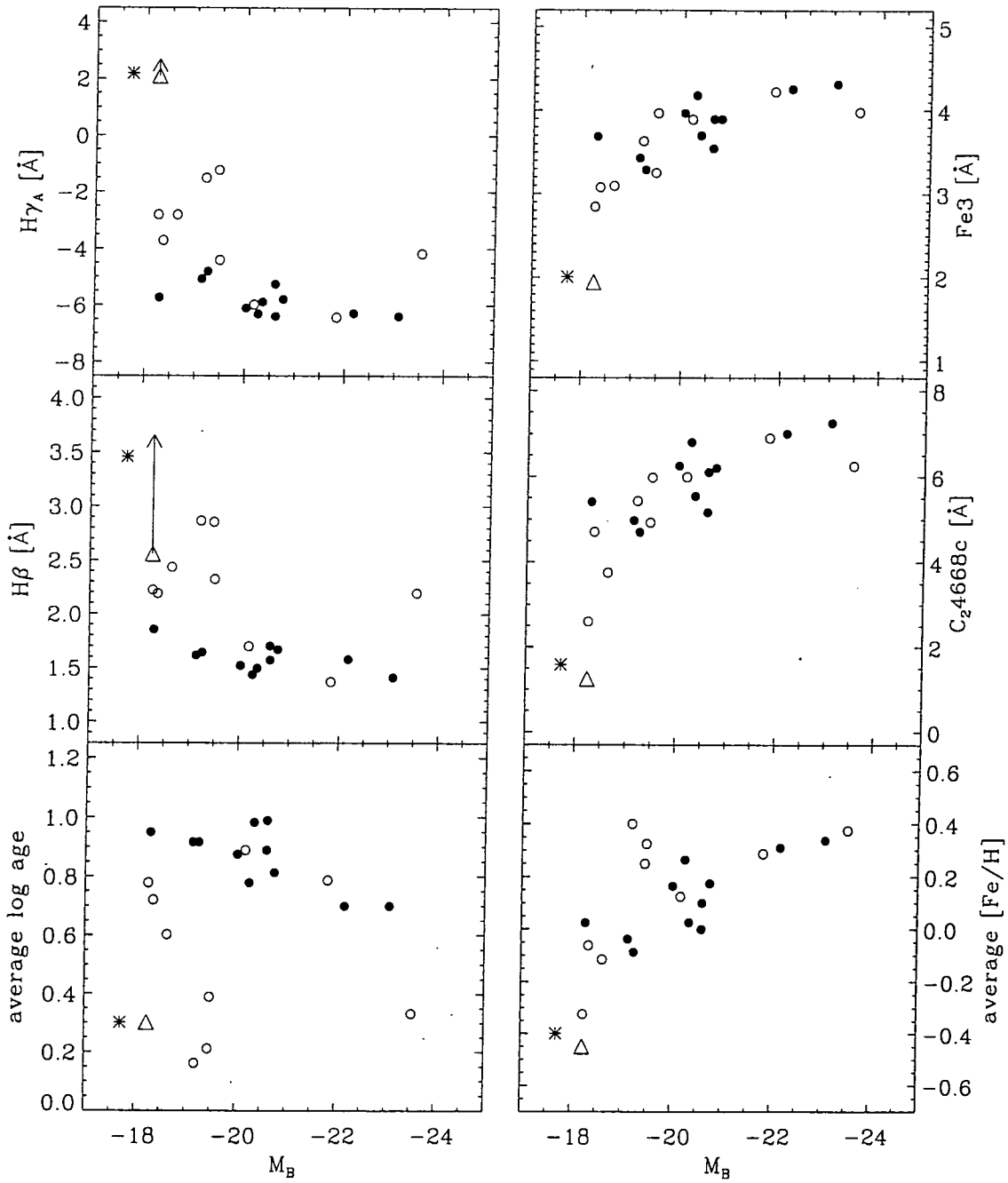

Figure 4.17: Left hand panels: Absolute blue luminosity (assuming $m-M=31.2$) plotted against age indicator $H\gamma_A$, $H\beta$ and average absolute age estimates taken from Figure 4.16. Right hand panels: Absolute blue luminosity plotted against Fe3, C_24668c and average metallicity taken from Figure 4.16. Filled circles and open circles represent ellipticals and S0s respectively. The cross and open triangle represent possible post-starburst and starburst galaxies respectively.

1. The elliptical galaxies appear to be roughly coeval with some evidence for slightly younger ages for the most metal rich ones. Using Lick/IDS indices (Hβ, Hγ_A) as well as new metallicity indicators (Fe3 and $C_2$4668c) we estimate the ages to be around 8 Gyrs. The Es form a sequence in metallicity varying roughly from -0.10 to +0.35 in [Fe/H]. This result is consistent with the conventional view of old, coeval elliptical galaxies where the metallicity scales roughly with the size of the galaxy. We note that the absolute ages and metallicities are sensitive to the detailed treatment of non-solar abundance ratios.

2. The lenticular galaxies have metallicities in the range $-0.5 <$ [Fe/H] $< +0.5$, where the estimates are not as secure as for the Es. Their *luminosity weighted ages* are on average much younger than those of the ellipticals, spanning from less than $\sim$2 Gyrs to 8 Gyrs. The bulges of the lenticular galaxies NGC1380 and NGC1381 resemble remarkably the properties of ellipticals suggesting that they experienced similar star formation histories. The peculiar S0 galaxy Fornax A (NGC1316), which is the brightest galaxy in the sample, has extremely strong Balmer lines implying a very young luminosity weighted age, yet the metallicity is equal to the most metal rich Es. We interpret this as sign of a recent (gaseous) merger which took place in this galaxy.

3. We have discovered that two of the fainter and very metal poor lenticular galaxies appear to have undergone major star-formation in the last 2 Gyrs (in one case very much more recently). These appear to be the low redshift analogues to the post-starburst or starburst galaxies seen by Couch and Sharples (1987) and recently by Barger et al. (1996) in redshift z=0.3 clusters. We note that, like Fornax A, these galaxies lie on the periphery of the cluster.

4. Not all galaxies in the Fornax cluster have solar abundance ratios. The elliptical galaxies exhibit overabundances up to 0.4 dex in Mg. There is a trend that the most metal rich galaxies are strongly overabundant whereas the metal poor ones approach solar abundance ratios. This conclusion applies also to the bulges of the large S0s NGC1381 and NGC1380. Young S0s on the other hand seem to be consistent with roughly solar abundance ratios. Furthermore we demonstrated that varying abundance ratios, which are not included in the models, can lead to a change of relative age and metallicity estimates depending on which index combination is used in the analysis.

5. Using [OIII]λ5007 as indicator, we find significant emission in only 7 out of 22 galaxies. The emission is generally weak and restricted to lenticular galaxies (with IC2006 as an exception). This result is confirmed by the use of Hγ_A as age indicator which gives the same age estimates for elliptical galaxies as Hβ although Hγ_A is much less sensitive to emission.

6. The new Fe-index Fe3, a combination of three strong individual Fe-indices, has

proved to be a reliable, sensitive and relatively unbiased (see overabundance problems) [Fe/H] indicator in the Lick/IDS system. It is superior to the previously used $C_2$4668 index because this index suffers from overabundance problems when applied to metal rich galaxies. We do not recommend the use of this (uncorrected) index, at least not for metal rich populations.

Chapter 5

Nuclear Stellar Populations and Central Velocity Dispersions

5.1 Introduction

The central velocity dispersion σ_0 of early-type galaxies is known to correlate strongly with the absorption strength of the Mg-absorption feature at 5174 Å (e.g., Burstein et al., 1988; Bender et al., 1993; Colless et al., 1998). The remarkably small scatter about this relation implies that the dynamical properties of galaxy cores are connected with their stellar populations. Analysing the Mg–σ_0 relation for a sample of 736 mostly early-type galaxies in 84 clusters, the EFAR group (Colless et al., 1998) finds the following: (i) the observed scatter about the Mg–σ_0 relation is as small as 0.020 mag in Mgb' (See Equation 5.1 for definition of Mgb') and 0.029 mag in Mg_2; the intrinsic scatter was found to be 0.013 mag in Mgb' and 0.020 mag in Mg_2. (ii) Differences between clusters are small if present at all. (iii) The Mg–σ_0 relation lacks any significant correlation with cluster velocity dispersion, X-ray luminosity or X-ray temperature. They conclude that the predominant factor which drives the Mg production is galaxy mass and not cluster mass, i.e., the amount of Mg is determined locally by the potential of the galaxy. (iv) The dispersion in M/L_R of a galaxy of a given mass is $\leq$ 41 % if the scatter in Mg–σ_0 is due to age differences only, and $\leq$ 8 % if it is due to metallicity differences only (note that these limits are dependent on the stellar population model used in the analysis). (v) Using constraints from both the Mg–σ_0 relation and the fundamental plane (FP) the following conclusion can be drawn: for reasonable correlations between age and metallicity the distributions in log *age* and $\log Z/Z_\odot$ are $\delta age/age = 15 - 32\%$ and $\delta Z/Z = 23 - 28\%$ at fixed galaxy mass.

Note that Jørgensen (1997) finds for a sample of 290 E and S0 galaxies a weak dependence of the Mg_2–σ_0 residuals with environment. Galaxies in low density regions tend to have slightly weaker Mg_2 for their velocity dispersion than galaxies in high density environments. Guzmán et al. (1992) also found a small environmental effect in the sense

that Coma galaxies in the halo of the cluster show weaker Mg_2 absorption compared to their central brethren.

The relatively tight constraints which the Mg–σ_0 relation implies for the stellar populations in a galaxy at a given σ_0 makes it a useful tool in the investigation of the star formation history of early-type galaxies as function of redshift. See Ziegler and Bender (1997) for an example of the utility of the Mg–σ_0 relation at medium redshift. However, as we will see in the course of this Chapter, the Mg-absorption feature is difficult to interpret when the effects of [Mg/Fe] variations are taken into account.

Correlations of other metal indices, such as <Fe>, with the central velocity dispersion have been expected for a long time but no convincing evidence has yet been found (e.g., Jørgensen, 1997). However, we will demonstrate that galaxies in the Fornax cluster do show a clear correlation between Fe-indices and central velocity dispersion.

This Chapter is organized as follows. In Section 5.2 we will first investigate the "classical" Mg–σ_0 relation for the Fornax cluster. Then in Section 5.3 we extend the study to other line-strength indices such as Fe3 and the Balmer lines. In Section 5.4 we explore in detail the sources of scatter in the Mg–σ_0 relation at a given σ_0 and finally we will conclude with our interpretation of the index–σ_0 relations in Section 5.5.

5.2 Mg–σ_0 Relation in the Fornax Cluster

First we will investigate the "classical" Mg–σ_0 relation for the complete sample of Fornax early-type galaxies (central $2\farcs3\times3\farcs85$ aperture). Following Baggley (1996) and Colless et al. (1998) we find it more convenient to express the "atomic" Mgb index in magnitudes like the "molecular" index Mg_2. Note that one should not use log Mgb instead because this introduces a non linear term in comparison to Mg_2. A priori it is not clear whether log Mgb or Mgb' correlates better with $\log\sigma_0$, but as the classical Mg–σ_0 relation was established with Mg_2 measured in mag we adopt this approach here for Mgb as well. The conversion between Mgb and Mgb' is

$$\mathrm{Mg}b' = -2.5\log\left(1-\frac{\mathrm{Mg}b}{\Delta\lambda}\right) \tag{5.1}$$

where $\Delta\lambda$ is the width of the index bandpass (32.5 Å for Mgb).

The Mgb' –σ_0 and Mg_2–σ_0 relations for the Fornax cluster are shown in Figures 5.1a and 5.1b, respectively. In order to fit linear relations, we performed an ordinary least square fit with Y = Mgb' as dependent variable [hereafter OLS (Y|X)] and also a fit which is the bisector of OLS regressions of Y on X and X on Y [hereafter OLS bisector]. Isobe et al. (1990) recommend the OLS (Y|X) fit for scientific problems where one variable

is clearly an effect and the other the cause. The OLS bisector is recommended when one wants to estimate the underlying functional relation between the variables. Here both methods are shown in order to illustrate how different fitting methods lead to different results. For the Mg–σ_0 relation analysis, we favour the OLS (Y|X) method for three reasons: (1) consistency with previous authors, as frequently they fit their data using the OLS (Y|X) method; (2) the Mg content of a galaxy seems to be driven by the central potential of the galaxy (see conclusions of Colless et al. (1998)) which is approximated by its central velocity dispersion σ_0 and (3) the individual errors in the observables compared to the dynamic range of the data are smaller (by a factor of two) for the velocity dispersion. In other words the central velocity dispersion is better determined than the Mg-index.

A different and perhaps more general fitting technique would be a maximum likelihood analysis. However, our sample does not have any complicated selection effects or measurement errors which are significantly not normally distributed. So we decided to employ a simple OLS (Y|X) fitting routine. The code used to derive the OLS (Y|X) fits is an IDL implementation of the Fortran code by Isobe et al. (1990). Errors are estimated by a Jack-Knife error analysis (boot strap gives similar results). Table 3.3 on page 59 lists the adopted central velocity dispersions which were used for all σ_0 - related plots. For this discussion all fits are performed for the elliptical galaxies (filled circles) only.

A fit using OLS (Y|X) gives

$$\begin{aligned} \mathrm{Mg}b' &= (0.105 \pm 0.020) \log \sigma_0 - (0.061 \pm 0.043), \\ \mathrm{Mg}_2 &= (0.191 \pm 0.023) \log \sigma_0 - (0.124 \pm 0.054). \end{aligned} \tag{5.2}$$

For the OLS bisector method the following fits were obtained:

$$\begin{aligned} \mathrm{Mg}b' &= (0.120 \pm 0.015) \log \sigma_0 - (0.093 \pm 0.034), \\ \mathrm{Mg}_2 &= (0.228 \pm 0.039) \log \sigma_0 - (0.207 \pm 0.085). \end{aligned} \tag{5.3}$$

A comparison with the literature shows that the fits found in this work compare well with previous studies. The EFAR group (Colless et al., 1998) give the following fits (simple regressions): $\mathrm{Mg}b' = (0.113 \pm 0.011) \log \sigma_0 - (0.093 \pm 0.027)$ and $\mathrm{Mg}_2 = (0.202 \pm 0.017) \log \sigma_0 - (0.181 \pm 0.041)$, while Jørgensen (1997) quotes $\mathrm{Mg}_2 = 0.196 \log \sigma_0 - (0.155 \pm 0.009)$.

For both indices the Fornax ellipticals show a correlation with the central velocity dispersion. Remarkably, both bulges of the luminous S0s, NGC1380 and NGC1381, follow the general relation set by the elliptical galaxies. Yet the peculiar S0 NGC1316 shows a Mg-absorption which is too low by 0.040 and 0.064 mag for $\mathrm{Mg}b'$ and Mg_2 respectively. This

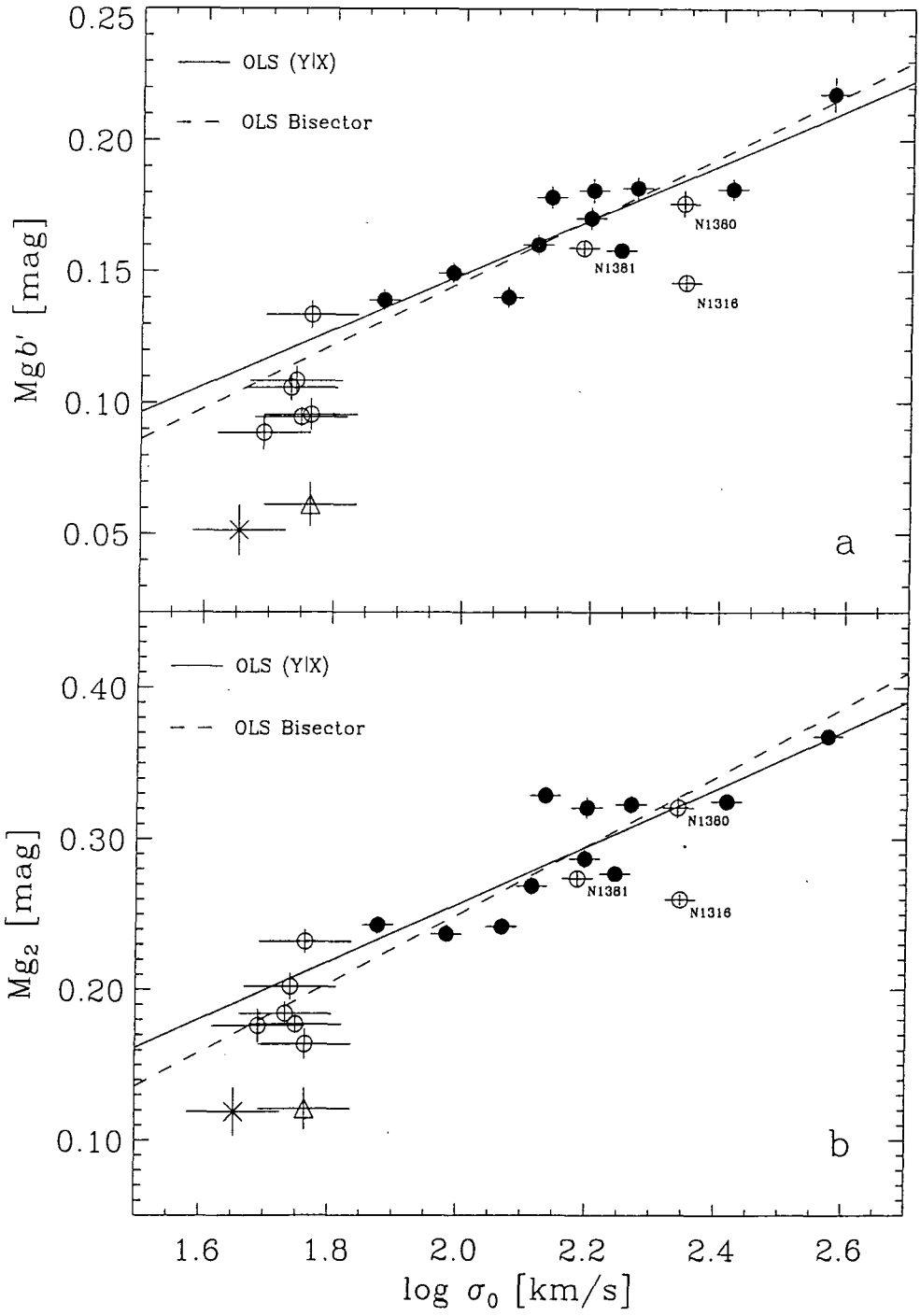

Figure 5.1: The Mgb' & Mg$_2$–log σ_0 relation for Fornax early-type galaxies. Two fits are shown: a normal ordinary least square fit with Mg as dependent variable (OLS (Y|X), solid line) and the ordinary least square bisector method (OLS Bisector, dashed line). The fit was performed on ellipticals (filled circles) only.

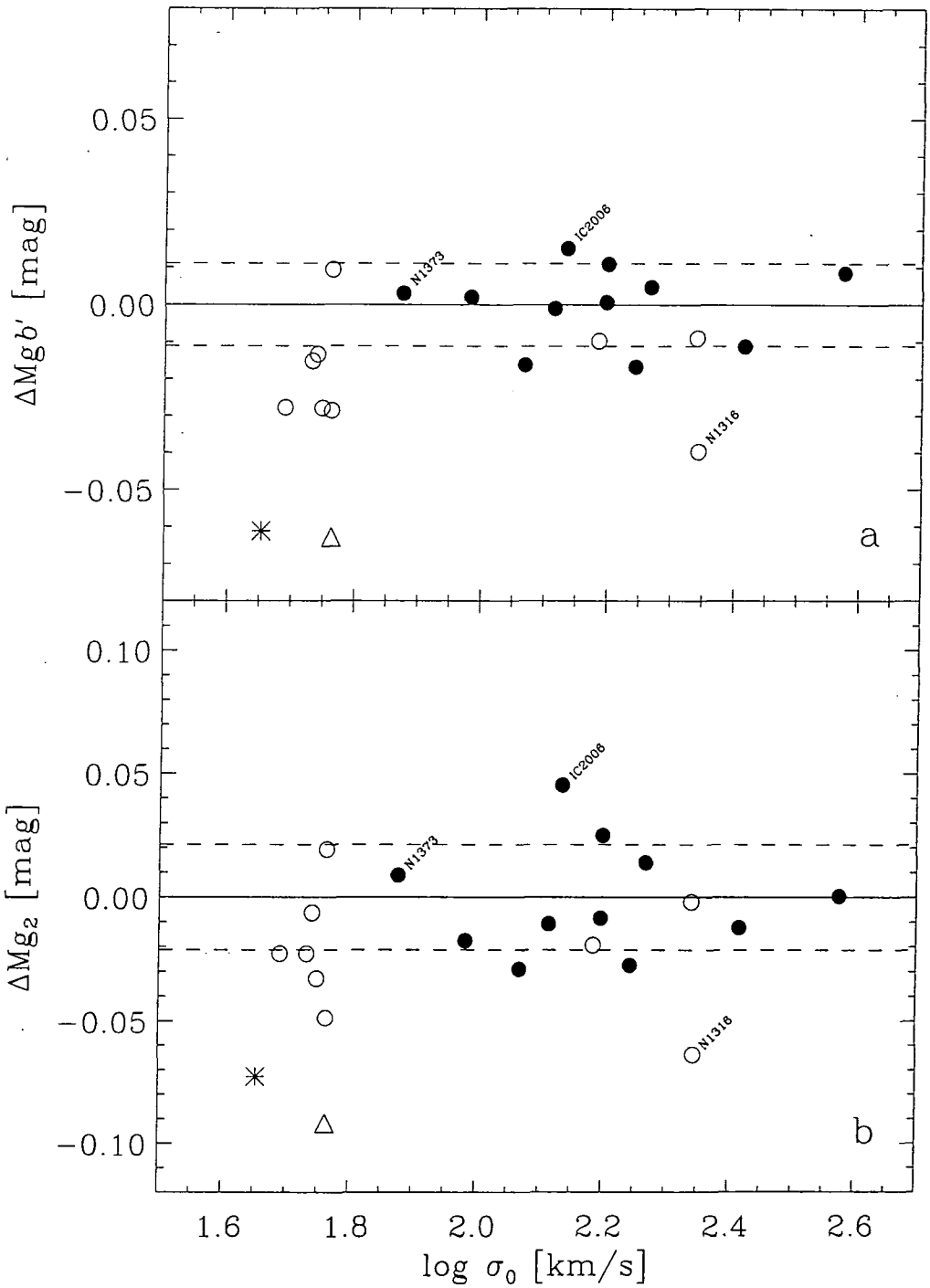

Figure 5.2: Residuals of the Mgb' & Mg_2–log σ_0 relation (Figure 5.1; OLS (Y|X) fit). The dashed lines indicate roughly the 1 σ scatter in the residuals.

is not surprising as we have shown in Section 4.4.3 that this galaxy has an extraordinary young (luminosity weighted) central stellar population for an early-type galaxy of its brightness and velocity dispersion. This is surely an extreme case, presumably the result of a recent merger, but it demonstrates nicely how the Mg–σ_0 relation can be influenced by young stellar populations in the centre of the galaxy. Some examples of anomalously low Mg values were previously identified by Jørgensen (1997).

The general trend that the presence of young stellar populations moves galaxies to lower Mg-absorption strength is also shown by the fainter young S0s. Except for IC1963 all of them are below the mean relation set by the Es. The extremely young starburst galaxies (open triangle and cross) are the furthest away from the relation with offsets of $\sim$0.07 and $\sim$0.10 mag in Mgb' and Mg_2 respectively. We note that the bulk of the young galaxies in Fornax have small velocity dispersions with $\sigma_0 \approx 50 - 70$ kms^{-1}.

Colless et al. (1998) find that the cD galaxies in their sample have on average 0.014 mag higher values in Mgb' and 0.012 mag higher in Mg_2 than the other early-type galaxies. The only cD galaxy in our sample is NGC1399 which does not show any significant offset. The EFAR group also does not find any difference between E and E/S0 galaxies for the Mg–σ_0 relation implying that the centres (=bulges) of E/S0 galaxies are created in a similar way to their elliptical brethren. Excluding all galaxies below $\sim$100 kms^{-1}, thus matching the Colless et al. sample, the two bright S0s in the Fornax sample give further evidence that E and E/S0 galaxies follow the same Mg–σ_0 relation.

Figure 5.2 shows the residuals from the Mg–σ_0 fits [OLS (Y|X)] in Figure 5.1. The sample is too small to perform a proper analysis on the scatter in the relation. However to get a rough estimate of the scatter, the dashed lines indicate the area in which 7 galaxies out of 11 (=64%) are enclosed which is roughly equal to the 1 σ scatter assuming a Gaussian distribution; that is $\pm$0.011 and $\pm$0.021 mag for Mgb' and Mg_2 respectively. These values are almost identical with the intrinsic scatter in the relations because the measurement errors for the indices are small compared to the scatter. For a detailed analysis of the sources of scatter at a given σ_0 the reader is referred to Section 5.4.

In summary the Mg–σ_0 relation for Fornax suggests that the cluster harbours a normal population of old early-type galaxies ($\sigma_0 \gtrsim 70$ kms^{-1}) consistent with other nearby clusters of different richness. The peculiar S0 galaxy NGC1316 is the only bright galaxy which deviates from the mean relation. However, there is a substantial population of faint ($\sigma_0 \lesssim 70$ kms^{-1}) and youthful S0s which show a large spread towards low Mg-absorption.

5.3 Other Indices *vs* σ_0

Do other line-strength indices in the Lick/IDS system correlate with the central velocity dispersion? Starting from the tight Mg–σ_0 relation one may expect equally good correla-

tions for Fe-indices. However Jørgensen (1997), for example, found only a weak correlation of <Fe> with σ_0 where the relation was driven by the smallest and the largest galaxies. For large galaxy samples the errors in the Fe-indices are usually rather large, hence these uncertainties may have weakened any real correlation in previous studies. Figure 5.3 shows a plot of our "best" Fe indicator Fe3′*vs* $\log \sigma_0$ for the Fornax cluster. Here Fe3′ is measured in magnitudes and defined as follows.

$$\mathrm{Fe3}' = (\mathrm{Fe4383}' + \mathrm{Fe5270}' + \mathrm{Fe5335}')/3 \tag{5.4}$$

where the individual indices, Fe4383′, Fe5270′, Fe5335′ are measured in magnitudes and are defined in a similar way as Mgb' (see Equation 5.1; note that $\delta\lambda$ is dependent on the index).

For the Fornax ellipticals Fe3′ is clearly correlated with the central velocity dispersion in the sense that greater velocity dispersions lead to stronger absorption in Fe3′. Similar to the Mg–σ_0 relation most of the galaxies follow a linear trend in this log-log plot. There are two remarkable exceptions: NGC1373 and IC2006. These galaxies show too large Fe3′ absorption for their central velocity dispersions. IC2006 also shows strong Mg-absorption compared to the mean relation. Yet their estimated ages and metallicities (see Figure 4.16 and Table 4.7) do not seem to be special. Remarkably, NGC1316 which showed very low Mg values in the previous plots is consistent with the mean Fe3′–σ_0 relation. Also the other two bright S0s are consistent with the relation of the Es. The OLS(Y|X) fit shown in Figure 5.3 was performed on Es only *excluding* NGC1373 and IC2006. A Spearman rank-order test yields a correlation coefficient of 0.95 with a probability of <0.1% that the parameters are not correlated. Including NGC1373 and IC2006 in the fit reduces the correlation coefficient to 0.83 (significance level of 0.2%). The best fit OLS (Y|X) is

$$\mathrm{Fe3}' = (0.050 \pm 0.012) \log \sigma_0 - (0.015 \pm 0.025). \tag{5.5}$$

Including NGC1373 and IC2006 yields a OLS (Y|X) fit of

$$\mathrm{Fe3}' = (0.036 \pm 0.011) \log \sigma_0 - (0.018 \pm 0.025). \tag{5.6}$$

The slopes of these fits are much shallower than the Mg–σ_0 relation. This may be a reason why previous samples of early-type galaxies did not show a clear correlation of Fe-indices with central velocity dispersion. Alternatively, if outliers like NGC1373 and IC2006 are a common phenomenon, then they would in combination with larger measurement errors destroy any tight correlation with the central velocity dispersion σ_0.

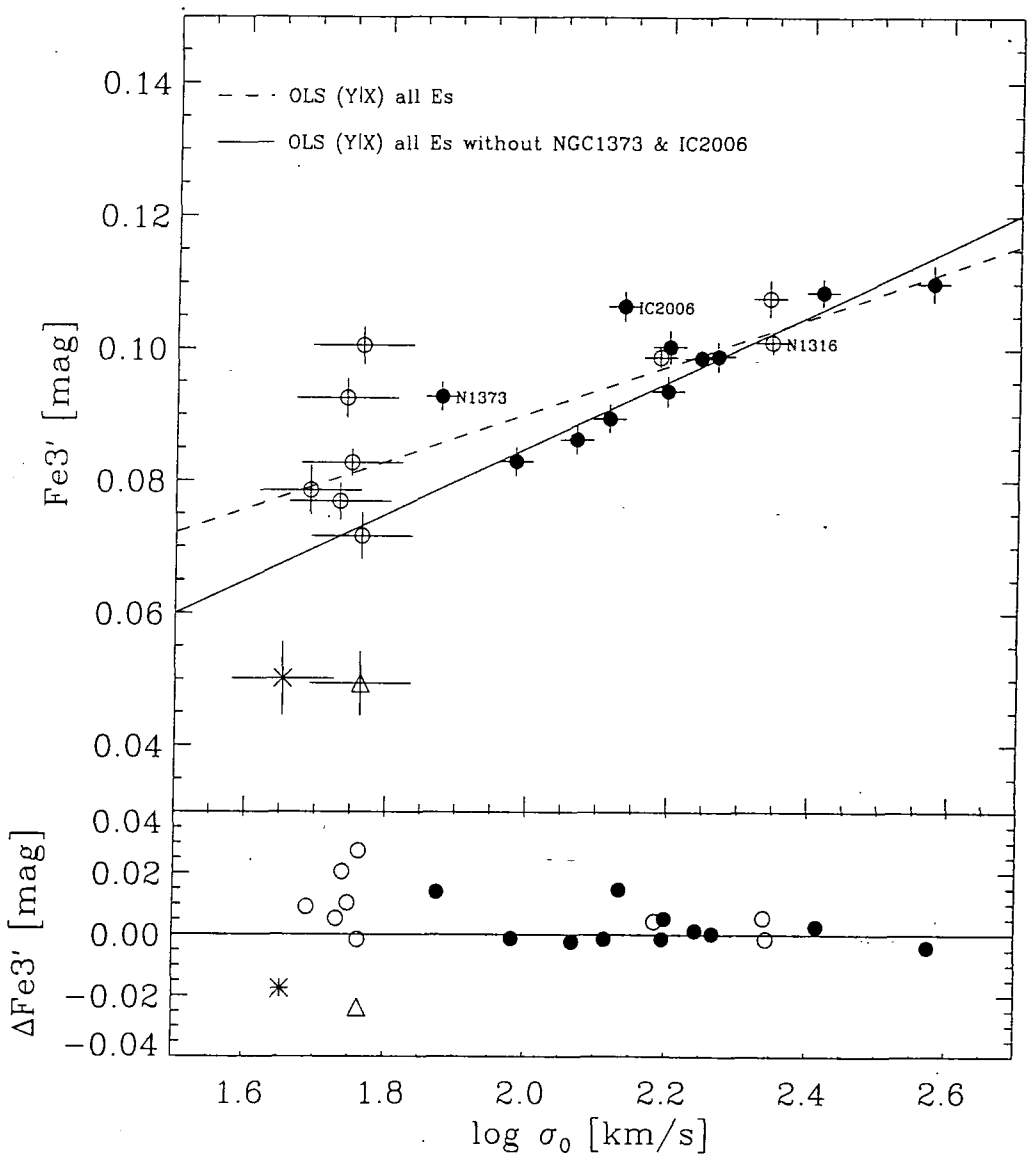

Figure 5.3: The Fe3′–log σ_0 relation (upper panel). Note that most of the young S0s show surprisingly strong absorption in Fe3′. The residuals, shown in the lower panel, are calculated with respect to the solid line i.e., the fit excluding NGC1373 and IC2006.

The behaviour of the young S0s is in remarkable contrast to the Mg–σ_0 relation. Most of them show stronger Fe3′ absorption than one would expect from the mean relation for Es; whereas Mg is very weak in those galaxies. Some of the faint S0s even show as much Fe3′ absorption as a medium sized elliptical. The two starburst galaxies show very weak Fe3′ absorption, consistent with them being extremely young.

This leads us to the question of whether other Fe-indices, or metal-indices in general, show a similar correlation with the central velocity dispersion of the galaxy? In Figure 5.4 a collection of 10 important metal index *vs* $\log\sigma_0$ relations is presented. For consistency all OLS (Y|X) fits (solid lines) have been performed on Es only, excluding IC2006 & NGC1373. In each panel the slope of the fit (± Jack-Knife error) and the correlation coefficient of a Spearman rank-order test (confidence level in brackets) are shown.

First it should be stressed that all metal-indices are positively correlated with the central velocity dispersion. Also all Fe-indices, Ca4455 and $C_2$4668c are consistent with a relation of slope 0.05 as was found for the Fe3′ index. To guide the eye the dot-dashed lines in each panel in Figure 5.4 represent a slope of 0.05 centred on $\log\sigma_0 = 2.2$. The relatively strong absorption in Fe3′ for the young S0s is mirrored by all Fe-indices. The galaxies IC2006 & NGC1373 show equal or stronger than average absorption for all 10 metal indices (see also Figure 5.5 for residual plots). However, NGC1316 deviates from the main relation only in the two Mg–σ_0 plots. Finally, as pointed out previously, the Mg–σ_0 relations are significantly steeper than the average Fe-index–σ_0 relation.

So far we have considered only metal lines. Figure 5.6 presents the relation between the Balmer lines Hβ' and Hγ_A′*vs* σ_0. Note that both indices are also measured in magnitudes following the definition in Equation 5.1. The best fit OLS (Y|X) to Es excluding IC2006 & NGC1373 gives:

$$\begin{aligned} \mathrm{H}\beta' &= (-0.013 \pm 0.007)\log\sigma_0 + (0.091 \pm 0.014), \quad \text{and} \\ \mathrm{H}\gamma_A' &= (-0.063 \pm 0.026)\log\sigma_0 + (0.006 \pm 0.056). \end{aligned} \tag{5.7}$$

Both indices show negative correlations with the central velocity dispersion σ_0. Elliptical galaxies and the bulges of NGC1380 and NGC1381 show little spread around the mean relation whereas the younger galaxies, most remarkably NGC1316, tend to have significantly stronger Balmer absorption at a given σ_0. We emphasize here that the slope in the relation of the coeval (!) ellipticals is mainly caused by a metallicity effect (metal poorer galaxies have stronger Balmer absorption) and has little to do with age differences. This is also reflected in the behaviour of Hγ_A′ as the "Fe-rich" galaxies IC2006 and NGC1373 are deviant from the main relation in the sense of lower Hγ_A line strengths. Because the side-bands of the Hγ_A index are located on metal lines we argue that strong metal absorption lowers the pseudo-continuum and thus weakens the Hγ_A index. This is

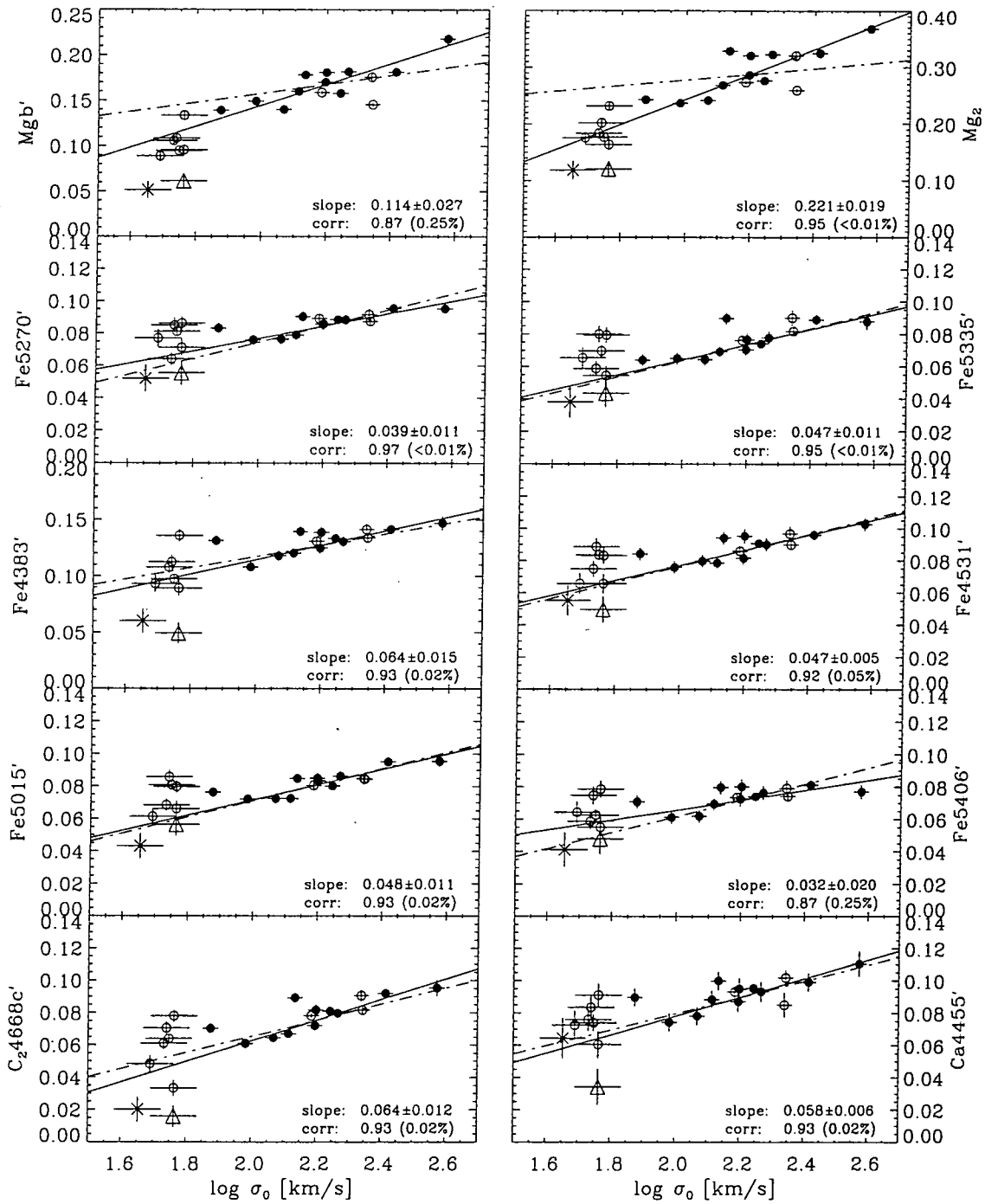

Figure 5.4: Important metal absorption indices plotted against $\log \sigma_0$. All indices are measured in magnitudes following the conversion from Equation 5.1 on page 108. Note that all indices show a positive correlation and the Fe-indices show very similar slopes. The dot-dashed line indicates a slope of 0.05 centred at $\log \sigma_0 = 2.2$. Note that the Mg indices exhibit a much steeper slope. The slope from a OLS (Y|X) fit (Jack-Knife error analysis) is shown in the lower right corner of each panel. The Spearman rank-order correlation coefficient for each dataset is also shown with the significance level in brackets. Note that only Es excluding IC2006 and NGC1373 were included in the fit; for further details see text. All indices in this plot are measured in magnitudes.

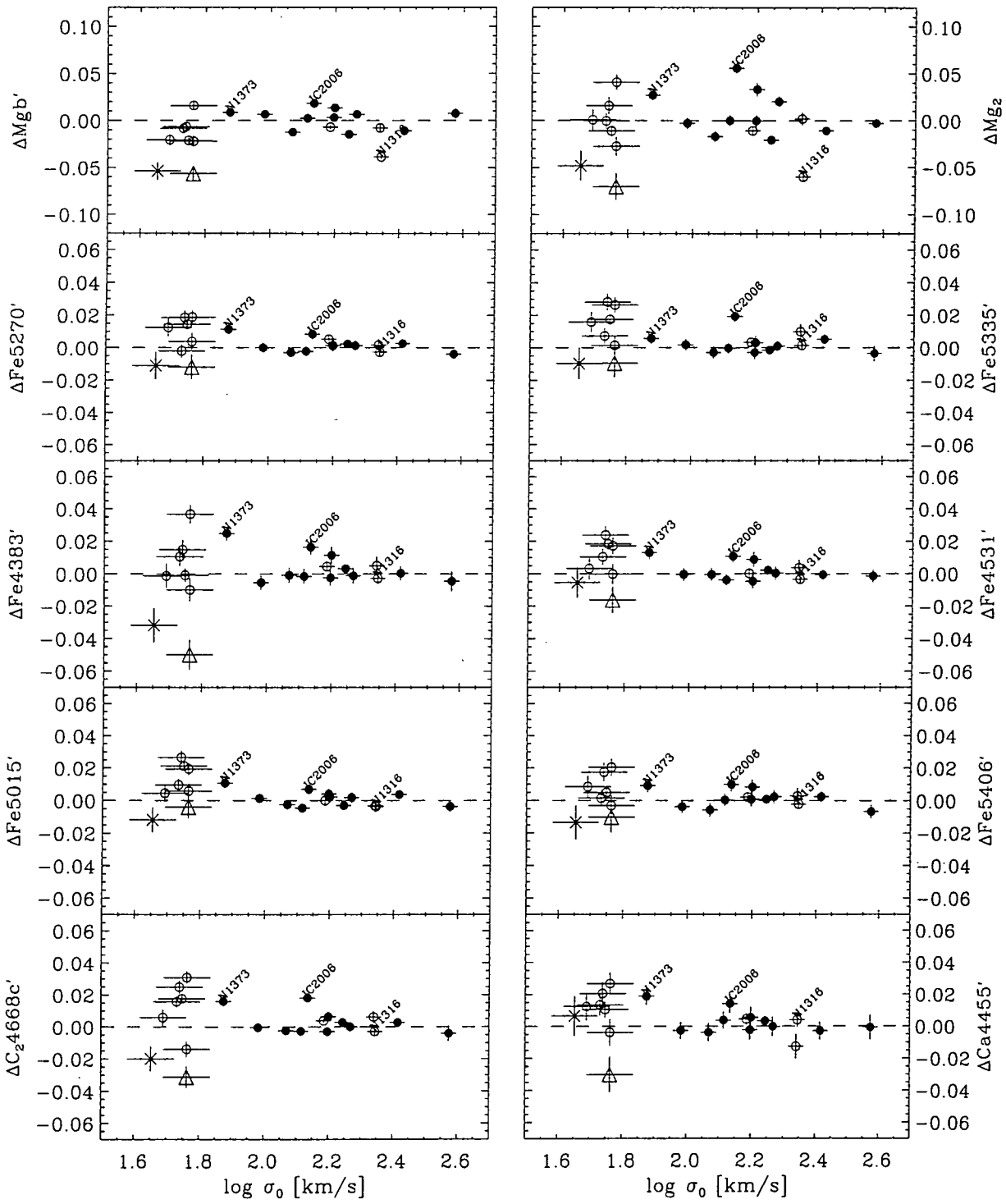

Figure 5.5: Residuals of the index - $\log\sigma_0$ relations from Figure 5.4. All indices are measured in magnitudes.

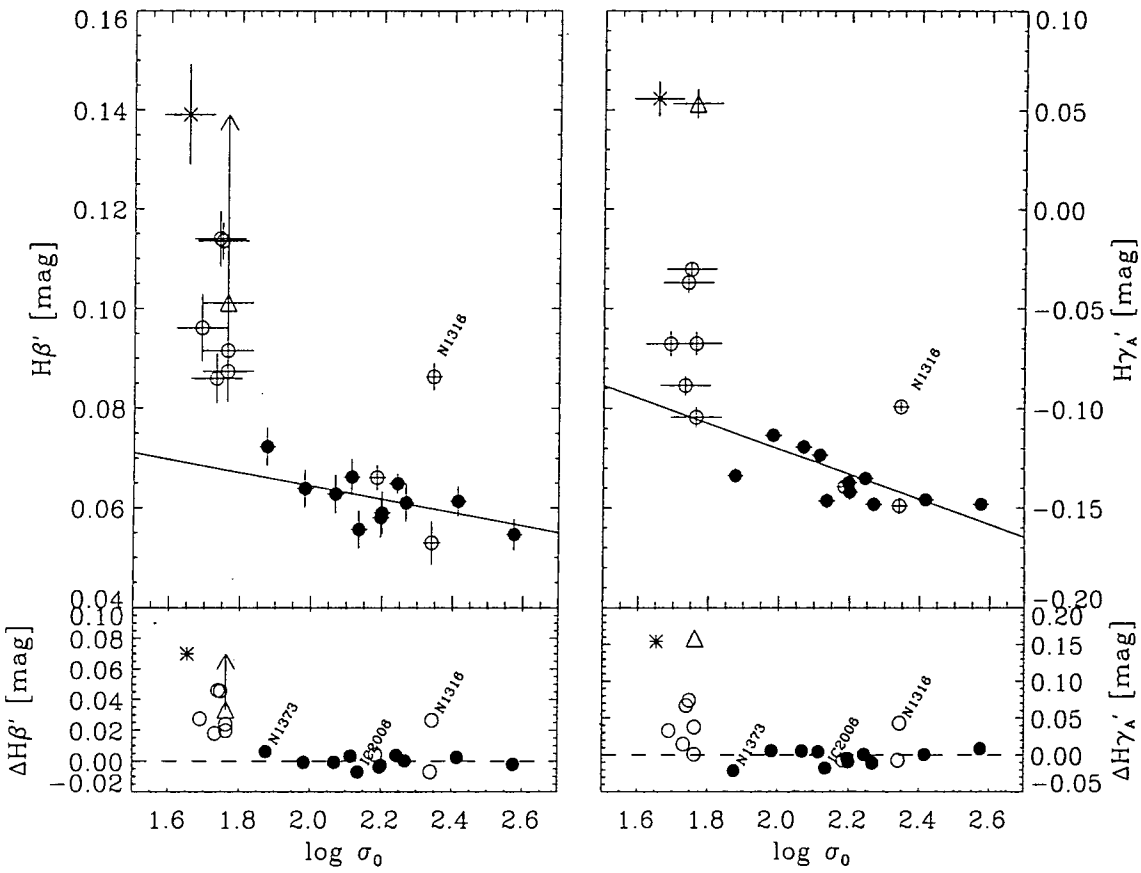

Figure 5.6: Hβ' and Hγ_A' *vs* $\log \sigma_0$ diagram. Note that ESO358-G25 (open triangle) is affected by Hβ emission as indicated by the arrows.

again an example that even our best age indicators do not fully break the age/metallicity degeneracy.

Summary and Discussion of Index–σ_0 Relations

What now follows is a summary and interpretation of the previous index–σ_0 relations. All the indices presented in the previous plots show correlations[1] with the central velocity dispersion for galaxies with old central stellar populations, indicating the existence of a homogeneous population of early-type galaxies. For our sample, we include all elliptical galaxies together with the bulges of the bright S0s NGC1380 and NGC1381. All metal indicators show positive correlations where the Fe-lines and Ca4455 show remarkably similar slopes but the Mg-lines follow a steeper relation. This steeper slope can be understood in terms of an increasing overabundance of Mg over Fe with galaxy mass. This was previously seen in Figure 4.9 and will receive further support in Section 5.4. On the contrary, the

[1] Hβ' is perhaps an exception in the sense that the correlation in Figure 5.6 is not statistically significant.

Balmer lines Hβ' and H$\gamma_A{}'$ show a negative correlation with central velocity dispersion. The peculiar S0 galaxy NGC1316 which was shown to harbour a significant fraction of young stars deviates from the Mg–σ_0 relation such that its Mg index is too weak. Interestingly this behaviour is not seen in any of the other metal indicators, but obviously the galaxy shows strong Balmer lines. This leads us to the role young (and small) S0s play in index–σ_0 relations. On the one hand the majority of the younger S0s show weak Mg absorption at a given σ_0 but on the other they have Fe-lines that are strong compared to the mean relation. The two starburst galaxies are an exception such that they have in general the weakest metal lines in the sample but the strongest Balmer absorption.

Two of the galaxies with old stellar populations, NGC1373 and IC2006, deserve further attention. These galaxies roughly follow the mean relation but they consistently show too strong metal-line absorption for their central velocity dispersion. How can we interpret this in the context of their stellar populations?

First of all let us try to understand what drives any of the index–σ_0 relations. We know from our analysis of the central stellar populations that the ellipticals are old and coeval but vary substantially in metallicity. Considering the metal lines in particular it seems natural to interpret the positive correlation with σ_0 as a consequence of increasing metallicity (see also e.g., Bender et al., 1993), similar to the colour magnitude diagram (e.g., Bower et al., 1992; Kodama and Arimoto, 1997). The fact that the Fornax Es are coeval would suggest that age in general does not drive the index–σ_0 relations. Note, if age would contribute in other clusters to the relation we would expect to find a different slope of the Mg–σ_0 relation to that found here for Fornax. However, it is not clear at all whether other parameters, such as the Mg-overabundance, contribute also to the relation.

To investigate the hypothesis that metallicity is the main driver in index–σ_0 relations we employ the models by Worthey and translate the index–σ_0 relations into physically more meaningful relations of metallicity and age *vs* σ_0. In Figure 5.7 we present our estimates of the average metallicity ([Fe/H]) and average log age *vs* log σ_0. The average ages and metallicities of the galaxies are taken from Table 4.7 on page 102 where we took the mean of both age/metallicity estimates.

Not surprisingly we find a positive correlation between metallicity and central velocity dispersion. A OLS(Y|X) fit to all Es excluding NGC1373 and IC2006 gives

$$[\mathrm{Fe/H}] = (0.79 \pm 0.14) \log \sigma_0 - (1.66 \pm 0.30). \tag{5.8}$$

A Spearman rank-order test shows that the relation between average age and central velocity dispersion is not significant[2]. Of course, this just reflects the fact that the galaxies

[2]The Spearman rank-order correlation coefficient is -0.54 with a significance level of 13.5%.

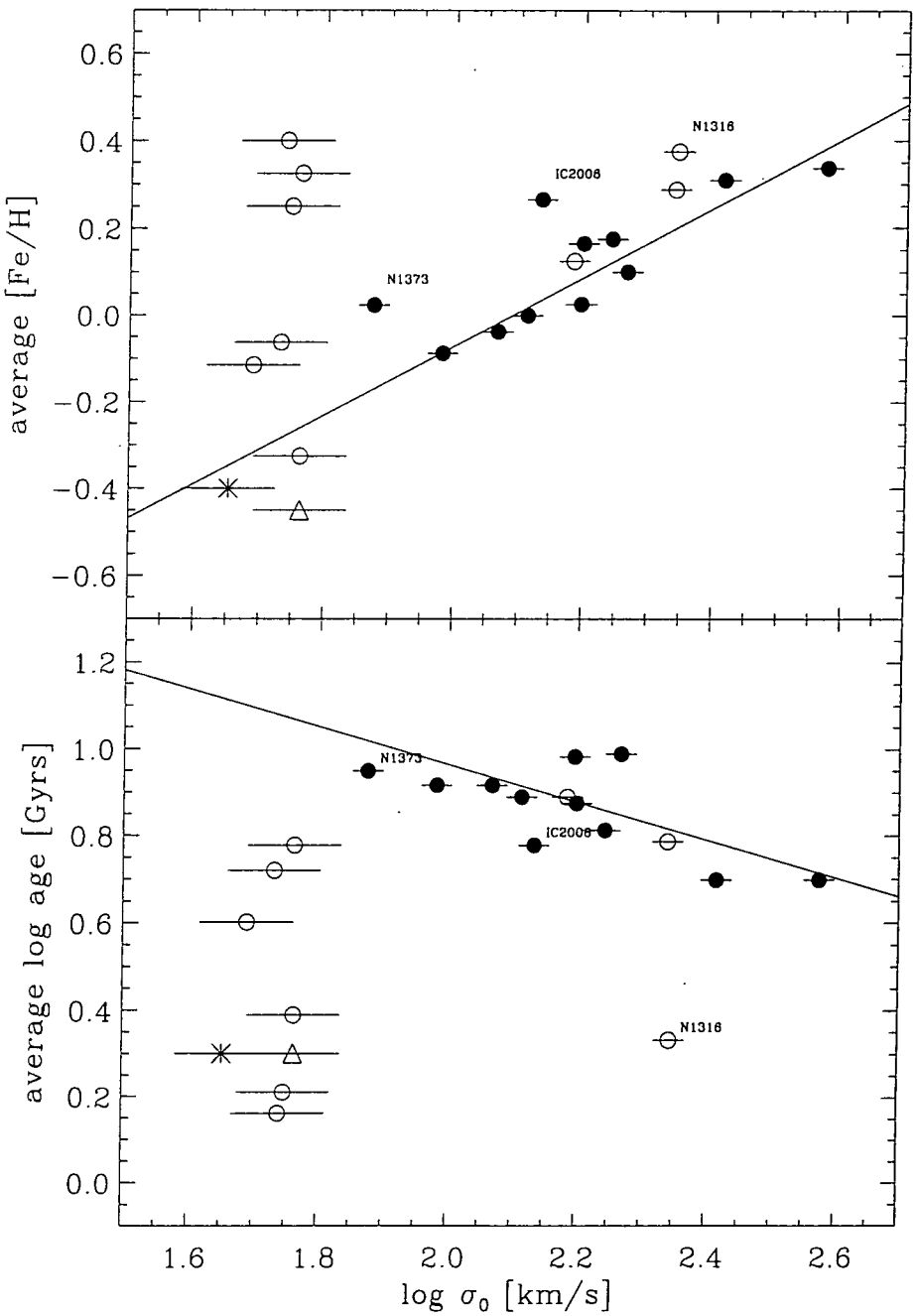

Figure 5.7: Average metallicity and average age plotted against $\log \sigma_0$. The average values are derived by taking the mean estimate from both age/metallicity diagnostic diagrams in Section 4.4.3 on page 98; see also Table 4.7 on page 102.

with old central stellar populations are roughly coeval. We would like to emphasize at this point that the relations shown in Figure 5.7 are model dependent and in particular the derived slope and intercept are sensitive to the treatment of non-solar abundance ratios. Nevertheless it is clear that there is a tight relation between the metallicity of the galaxy and its central velocity dispersion. NGC1373 and IC2006 are again offset from the main relation – which is the reason why we excluded them from the fit. The younger S0s span a large range in metallicity. However, we note that for the young S0s, due to their younger luminosity weighted ages and probably composite stellar populations, the assigned metallicities are quite insecure. If our hypothesis that the index–σ_0 relations are driven by metallicity is true, how can we explain the residuals of both NGC1373 and IC2006?

IC2006 has been studied in detail by Schweizer et al. (1989). They found a large counter-rotating ring of neutral hydrogen (HI) associated with faint optical features. van Gorkom and de Zeeuw (1994) re-analysed the optical photometry of Schweizer et al. taking into account the inclination of the galaxy and concluded that it probably has a large disk in the outer parts which is seen almost face on and therefore difficult to detect. They suggest that it should be classified as E/S0 rather than a bona fide elliptical. Schweizer et al. also detected emission lines indicating a central mass of ionized gas (see also Section 4.3.4 on page 79). The gas is counter-rotating with respect to the stars and is highly turbulent ($\sigma_0 = 190$ kms^{-1}). Schweizer et al. also suggest that the HI ring may have formed during a merger which created IC2006.

All this goes to show that IC2006 is not a "normal" elliptical but is likely to have suffered from a (late?) major merger involving significant amounts of gas. We suggest that in IC2006, contrary to the formation of "normal" Es, the star formation continued for a longer time (or a secondary starburst occurred) yielding a high Fe-content, produced via SNe of type Ia (see also discussion at the end of Section 4.4.1). This would explain why we find strong Fe3 absorption for IC2006 compared to its velocity dispersion. A similar line of argument can be employed to explain the relatively high Fe- and low Mg-content seen in the younger S0s.

There is little known about the galaxy NGC1373; perhaps the best explanation why this (elliptical) galaxy is somewhat off the mean relation is to regard it as a transition galaxy between Es and the faint S0s.

Recently Trager (1997) suggested that the centres of elliptical galaxies seem to populate a plane in age-metallicity–σ_0 space. Trager's relation implies that at fixed σ_0 more metal rich galaxies are younger. Can we confirm this with the data from the Fornax cluster? First of all in the Fornax cluster we do not find a large spread in age for elliptical galaxies hence the correlation with either σ_0 or [Fe/H] is weak, if at all present. The correlation between σ_0 and metallicity is by far the strongest. To investigate any evidence for a plane we follow Trager and plot in Figure 5.8 the residuals from a fit to average

log age *vs* average [Fe/H] against log σ_0. Examining Figure 5.8, there is little evidence for any correlation for the ellipticals. In summary, the Fornax data does not support the existence of a t-Z-σ_0 "plane" for elliptical galaxies. However we note that (as can be seen from Figure 5.7) some S0s and IC2006 give evidence for a connection between age and metallicity such that at fixed σ_0 more metal rich galaxies have younger luminosity weighted ages indicating extended star-formation. This behaviour could explain some of the effect Trager found when analysing González's sample.

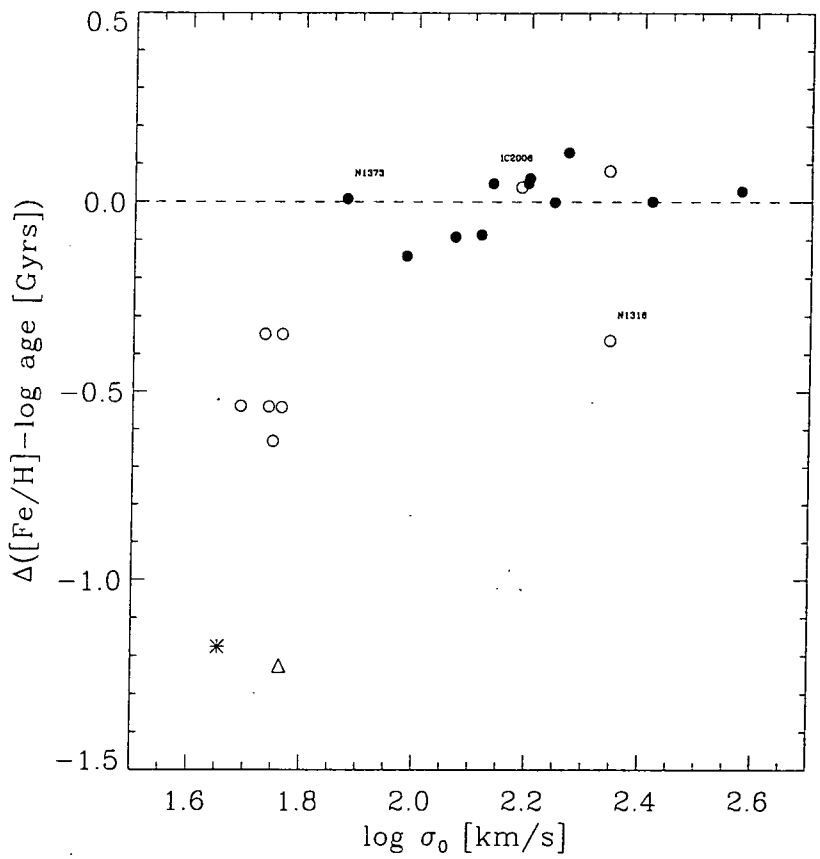

Figure 5.8: Plotted are the residuals from an OLS (Y|X) fit to the average log age *vs* [Fe/H] relation (see also Figure 4.16) against log σ_0.

Before we investigate the scatter about the mean Mg–σ_0 relation we would like to demonstrate what kind of index–σ_0 relations are predicted by the models. The problem here is that the models predict only the strength of a given index for a given age and metallicity. However, with the help of Equation 5.8 on page 119 we can relate the metallicities to the central velocity dispersion log σ_0. If we then assume a mean age for all galaxies we can predict any index–σ_0 relation in the Lick/IDS system. In Figure 5.9 we show three examples of such model index–σ_0 relations.

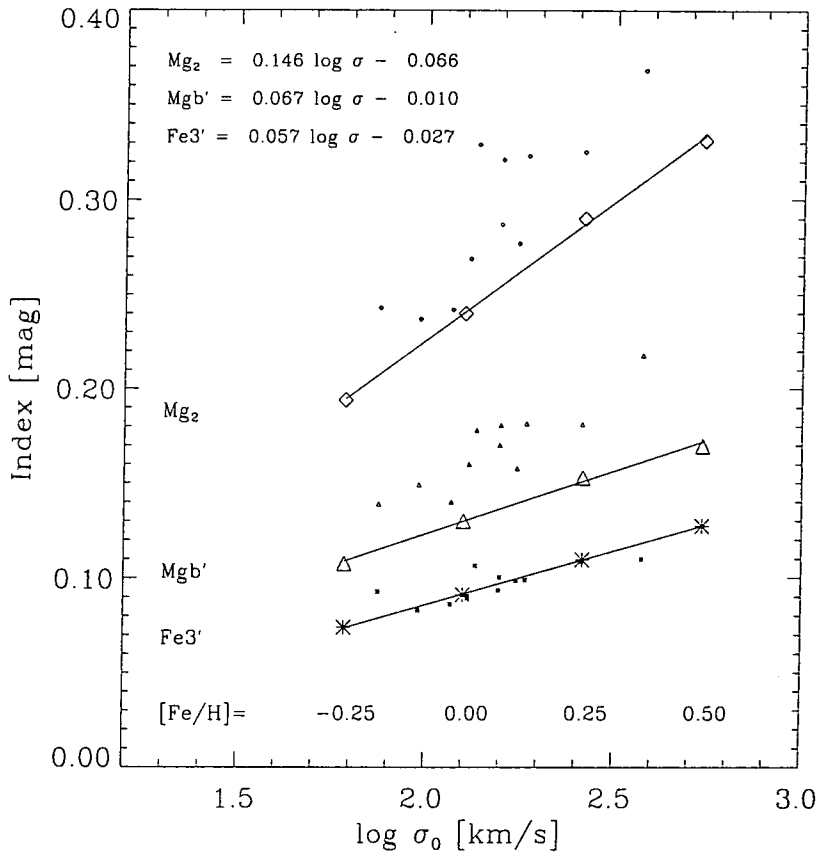

Figure 5.9: Model predictions of Mg_2, Mgb' and Fe3'–σ_0 relations (large symbols). Metallicities are transformed into $\log \sigma_0$ with Equation 5.8. A mean luminosity weighted age of 8 Gyrs was assumed. The fits for the three model relations (solid lines) are given in the left upper corner. The small symbols represent the measured central index values of the Fornax ellipticals. Note that the slope predicted by the models is not consistent with the observations for Mg_2 and Mgb' .

The first thing to notice is that the slopes are different. For Mg_2 the models predict the steepest relation. However, comparing the predicted slopes with our measurements (small symbols) we see that only the Fe3' model slope is consistent with the observations. This is not surprising because our metallicity estimates and therefore the model calibrations are based on Fe indices. It is important to notice that the Mg slopes are predicted to be steeper than the Fe slope but the slopes do not reach the values which are observed, i.e., 0.191 and 0.105 for Mg_2 and Mgb' respectively. We suggest that this is further evidence for an increasing [Mg/Fe] ratio with central velocity dispersion.

5.4 What Causes the Spread in the Mg–σ_0 Relation?

We investigated several index–σ_0 relations finding generally tight correlations for galaxies with old stellar populations. Nevertheless there is still some scatter left which is clearly larger than the observational errors, e.g., for Mgb and Mg_2. The Mg–σ_0 relation has been investigated by many authors, but perhaps the best paper on this topic is by Bender et al. (1993). They conclude that if the spread in the Mg–σ_0 relation at a given σ_0 is due to age only then the rms spread in age is only 15% for bright dynamically hot galaxies (DHGs). Alternatively, if the spread is only due to metallicity then they infer a rms spread of about 15% in metallicity. A similar analysis by Colless et al. (1998) using up-to-date model predictions and constraints from the FP find slightly larger numbers (see also the introduction to this Chapter). The tightness of these relationships is often used to emphasize the homogeneity of early-type galaxies, which is supported by the findings for the Fornax cluster. The detailed stellar population analysis we performed for the Fornax cluster allows us now to investigate the cause of the scatter in the Mg–σ_0 relation at a given σ_0.

Two obvious potential sources of scatter in the Mg–σ_0 relation are age and metallicity variations. But there may well be other effects responsible for the scatter, such as variations of the Mg-overabundance at a given σ_0. Previous authors did not allow for this effect; however if there is a spread introduced by [Mg/Fe] variations this would *only reduce* the previously inferred spread in age and metallicity (this assumes that the two effects are not strongly anti-correlated). In this Section we will investigate the effects that age, metallicity and [Mg/Fe] variations have on the scatter in the Mg–σ_0 relation at a given σ_0 for the Fornax cluster. Note that there may well be other parameters influencing the relation which we do not consider in this work.

We have already derived central age and metallicity estimates for our sample. However, in order to examine any dependence on [Mg/Fe] ratios, we first have to establish how we can measure them. We decided to take two approaches:

1. **Model independent:** We assume that the quantities Mgb/Fe3 and Mg_2/Fe3 give a good indication of the [Mg/Fe] ratio. Results are presented in Figure 5.10a and b.

2. **Model dependent:** We estimate [Mg/Fe] using a plot of Mgb , Mg_2 *vs* Fe3 (similar to Figure 4.9 on page 89). Assuming that the Es span roughly a range in [Mg/Fe] = 0.0 to 0.4 we assigned each galaxy a value by measuring the (perpendicular) distance between the solar-ratio models (Worthey, 1994) and the position of the galaxy in the diagram. See Figure 5.10c and d for results.

Both methods have some caveats which we will discuss now. The simple ratio of Mgb/Fe3 or Mg_2/Fe3 has been used by some authors (e.g., Mehlert, 1998) in order to measure the overabundance of Mg. As long as the galaxies in question have approximately

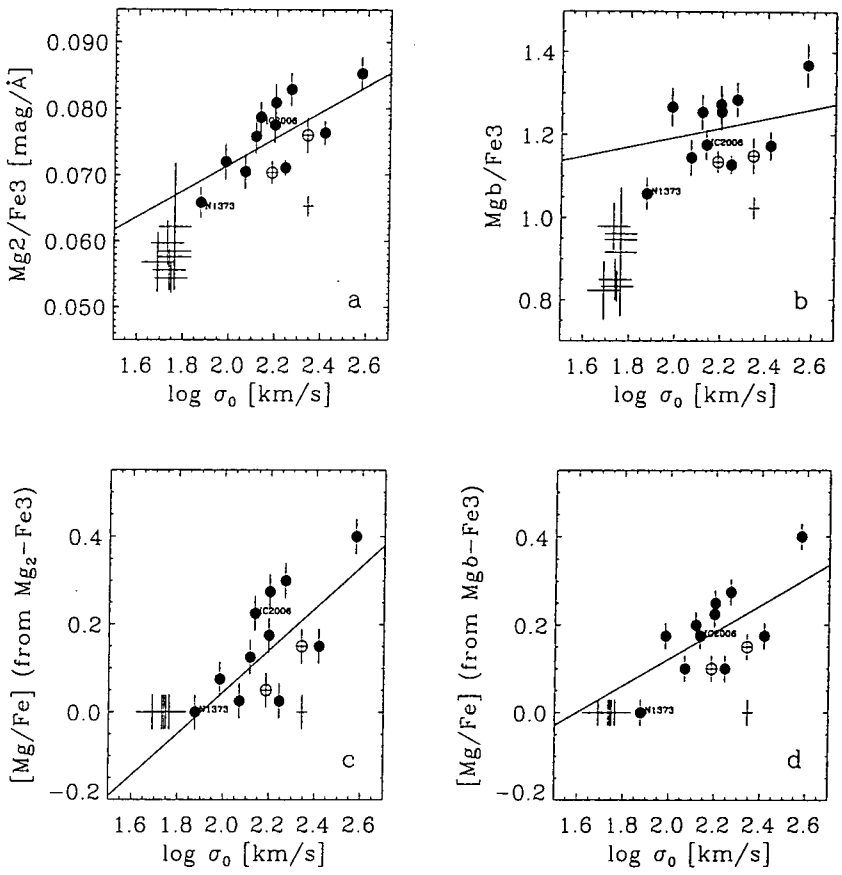

Figure 5.10: Panels (a) and (b) show the ratio of Mg_2/Fe3 and Mgb/Fe3 plotted against central velocity dispersion respectively. Panels (c) and (d) show the [Mg/Fe] ratios as estimated from a comparison of Mg_2 and Mgb plotted against Fe3 and model predictions (see also Figure 4.9 on page 89). Filled circles represent Es and the two open circles represent the old S0s NGC1380 and NGC1381, all other galaxies are indicated by their error bars but not included in the OLS (Y|X) fits (solid line). See text for details.

the same age, this is certainly a good choice. However, as we demonstrated in Figure 4.12 on page 93, Mg/<Fe> is sensitive to age thus not necessarily measuring only [Mg/Fe]. Indeed, the young S0s span a large range in Mg/Fe3 (see Figure 5.10, panels (a) & (b)) that is more naturally explained by age variations than by any variations in [Mg/Fe]. This is consistent with the results of the second (model dependent) method where all young S0s have roughly solar abundance ratios and have therefore been set to [Mg/Fe]=0 (see Figure 5.10, panels (c) & (d)). The error bars in Figure 5.10 (c) & (d) indicate a simple estimate of the average errors. Analysing Figure 4.9 on page 89 we concluded that there is a trend of more metal rich galaxies having greater [Mg/Fe] ratios. This is now confirmed in a more quantitative way in Figure 5.10 (c) & (d). We note that this trend is extremely sensitive to the slope of the models and therefore model dependent. However, using the models of Worthey (1994) there is substantial spread in [Mg/Fe] at a given σ_0. Examining

Figure 5.10 (a) & (b) one cannot safely conclude that the previously discussed trend in [Mg/Fe] is as prominent. But there is clearly a substantial spread in Mg/Fe3 at a given σ_0. In summary, both methods indicate a spread in [Mg/Fe] at a given σ_0, regardless of any trend of [Mg/Fe] with σ_0.

We aim to explore the sources of scatter in the Mg–σ_0 relation by investigating possible correlations between deviations in the Mg–σ_0 relation and deviations in log age – σ_0, [Fe/H] – σ_0 and [Mg/Fe] – σ_0 relations. We note that for some of the relations, e.g., Mgb/Fe3–σ_0 one cannot speak of a real correlation but rather that the fit divides "high" and "low" values of the quantity at a given σ_0. However, for the following δ-δ analysis this will serve our purposes.

We present in Figure 5.11 several plots of residuals from a given (parameter–σ_0) relation against the residuals from the Mgb–σ_0 relation (left hand panels) and Mg_2–σ_0 relation (right hand panels).

The three parameters in question: age, metallicity and [Mg/Fe] ratio are represented both by using models and by plotting a model independent quantity which is closely related to the parameter in question; e.g., age is presented as average age estimate in Gyrs and also by using $H\gamma_A{}'$ as an age indicator [Δ(log age – σ_0) and $\Delta(H\gamma_A{}'-\sigma_0)$ plots respectively]. When analysing age, metallicity and [Mg/Fe] effects we emphasize that only the *combination* of the four diagrams concerning the parameter in question should be considered. If there is a correlation in only one of the diagrams then this is likely to be a statistical fluctuation.

The residuals were derived from OLS (Y|X) fits to the (parameter–σ_0) relations. We chose to include in the fits only galaxies with "normal" old stellar populations; i.e., we included all ellipticals and the S0s NGC1380 and NGC1381 but excluded NGC1373 and IC2006 (in total 11 galaxies). Note that none of the following discussion would change if we include IC2006 & NGC1373 or exclude the bright S0s, and that all types of galaxies are plotted in Figure 5.11.

Results:

None of the plots show a good correlation at first glance. However, the residuals from the $(H\gamma_A{}'-\sigma_0)$ relation and the residuals from the (log age – σ_0) relation do suggest that younger galaxies have weaker Mg-absorption (top four panels in Figure 5.11). This confirms our findings from Section 5.2 where we already pointed out that young galaxies deviate from the Mg–σ_0 relation. One of the best example for this effect is NGC1316 which is labelled in Figure 5.11. Note that both model dependent and model independent quantities give similar results and it is only the young S0s which give a correlation.

The middle four panels in Figure 5.11 investigate the dependence on metallicity. Note

that the metallicities of the young S0s are subject of large errors because they are likely to have composite stellar populations and it is difficult to estimate the true mean metallicity. We do not find any obvious correlation, maybe with the exception of the $\Delta(\mathrm{Fe3}' - \sigma_0)$ *vs* $\Delta(\mathrm{Mg}_2 - \sigma_0)$ plot, so one has to conclude, that for our sample metallicity variations at a given σ_0 are rather unimportant.

Finally we explore the dependence on [Mg/Fe] (bottom four panels). Here we do find a weak correlation. However, the correlation seems to be mainly driven by elliptical galaxies.

To investigate the latter finding we focus in Figure 5.12 on galaxies with old stellar populations only, i.e., the galaxies which generally show only small deviations from the main Mg–σ_0 relation. We find a positive correlation – for model independent, as well as model dependent estimates of [Mg/Fe] – with the residuals from the Mg–σ_0 relation. Note that one would expect a correlation just due to correlated noise in these coordinates. The arrows in Figure 5.12 (lower four panels) indicate the direction and strength of the correlation if only correlated noise was present (based on Monte Carlo simulations). The actually observed correlation is significantly stronger.

So early-type galaxies in Fornax with old stellar populations show more than average Mg absorption at a given σ_0 when their stellar populations show greater than average [Mg/Fe] ratios at a given σ_0 and vice versa. This implies that galaxies with the same central velocity dispersion can experience different star-formation histories which lead to varying [Mg/Fe] ratios. One can think of a whole variety of scenarios to explain this finding. However we suggest two extreme scenarios: (1) all ellipticals are created in an initial stellar burst but they experience somewhat different star-formation histories, e.g., the initial stellar burst varies slightly in length thus yielding different [Mg/Fe] values; (2) some elliptical galaxies are created in dissipational mergers of two spiral-like galaxies. In this case it is not clear that the central velocity dispersion of the merger product is connected to the central metallicity in the same way as in scenario (1). So rather then changing the Mg content we suggest that the central velocity dispersion varies for a given Mg content. Of course, any combination of (1) and (2) is plausible as well.

The galaxies NGC1373 and IC2006, previously identified as having peculiar stellar populations, seem not to follow the trend very well. In summary when considering only galaxies with old stellar populations (Figure 5.12), the strongest, in fact the only clear correlation with the residuals from the Mg–σ_0 relation is due to [Mg/Fe] ratio variations. Note that changing the fitting parameters, such as including NGC1373 & IC2006 or measuring the Mg overabundance using <Fe> rather than Fe3 does not change the overall result.

At this point it would be desirable to see exactly how much of the spread can be attributed to the [Mg/Fe] ratio variation. In order to do this one would have to correct the individual galaxies to solar abundance ratios and re-analyse the scatter. This is not

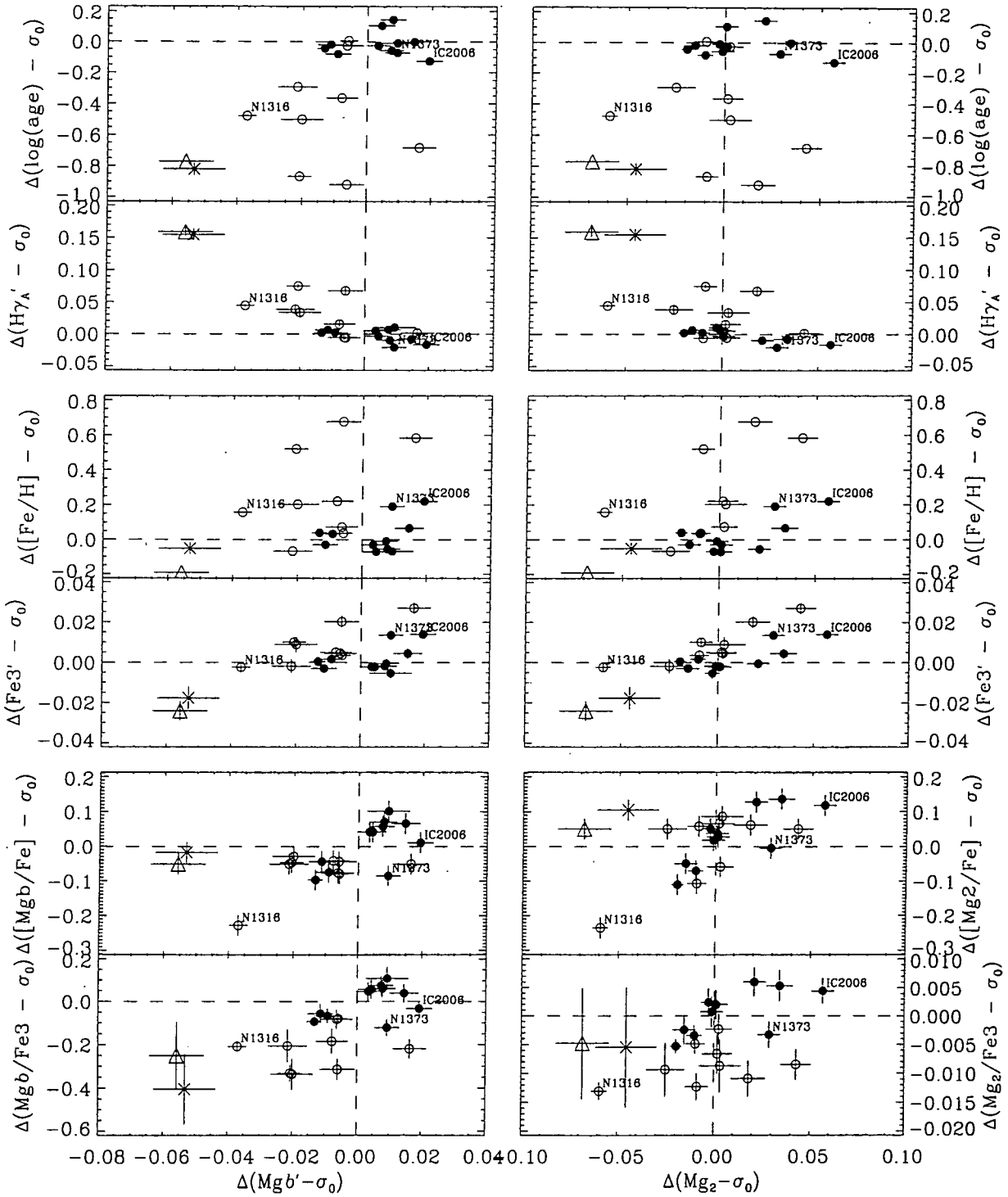

Figure 5.11: The residuals of six parameter–σ_0 relations against the residuals from the Mgb –σ_0 relation (left hand panels) and Mg_2–σ_0 relations (right hand panels). Investigated are (from the top) age, metallicity and [Mg/Fe]-ratio variations. The residuals are derived from OLS (Y|X) fits including the bulges of NGC1380 & NGC1381 and all Es but excluding NGC1373 and IC2006. See text for details. Filled circles and open circles represent ellipticals and S0s respectively. The cross and open triangle represent possible post-starburst and starburst galaxies respectively.

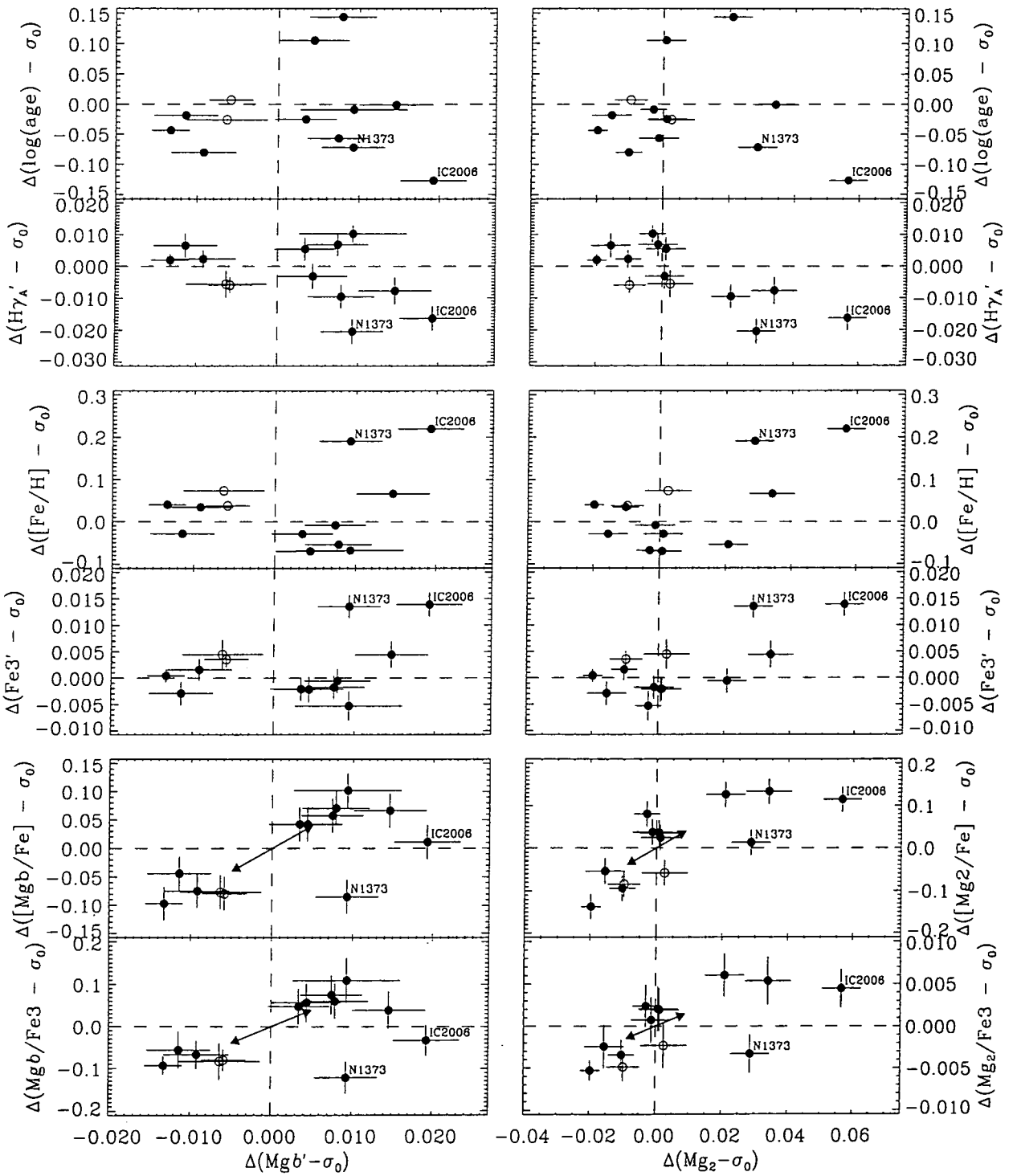

Figure 5.12: Same as Figure 5.11 but only galaxies with old central stellar populations are shown. See text for details.

a trivial task and would rely heavily on model predictions for Mg-overabundant stellar populations. We have not attempted such an analysis because we feel that the current stellar model predictions are not yet secure enough in this respect.

5.5 Conclusions from Index–σ_0 Relations

1. Early-type galaxies with $\sigma_0 \gtrsim 70$ kms^{-1} in the Fornax cluster follow a Mg–σ_0 relation consistent with the relation in other nearby clusters. Additionally we find a sizeable fraction of young (luminosity weighted) S0s with velocity dispersions $\lesssim 70$ kms^{-1}. Their central Mg-absorption strength is generally weaker than suggested by the mean relation of Es. The bright peculiar galaxy NGC1316 (Fornax A), likely to be the product of a recent merger and shown to have a young stellar population, also shows extremely weak Mg absorption for its σ_0.

2. For the first time it is shown that non Mg metallicity indicators in the Lick/IDS system such as Fe5270 and Fe5335 follow also a clear positive correlation with central velocity dispersion. However, the slope of the Fe–σ_0 relations (slope: ~ 0.05) is shallower than that for Mg_2. Two galaxies, NGC1373 and IC2006, deviate from the main relation, showing strong Fe absorption lines for their central velocity dispersions. It is suggested that IC2006 is the product of a gaseous merger which is responsible for the high Fe content.

3. We argue that the main driver in any of the index–σ_0 relations is the increasing metallicity with galaxy mass. Age effects play only a minor role in the general trend of the relations. However, we emphasize that in the case of Mg-indices the slope is steeper compared to the Fe-lines. We ascribe this to an increasing [Mg/Fe]-ratio with galaxy mass for old early-type galaxies.

4. We investigated the sources of scatter in the Mg–σ_0 relation by using our estimates of age, metallicity and [Mg/Fe] ratio. The Fornax data suggests that the presence of young stellar populations introduces significant deviations from the mean relation as seen in the case of NGC1316 and the faint S0s. Metallicity variations at a given σ_0 seem not to contribute significantly to the observed spread. However, the majority of the remaining, relatively small, scatter among the old and roughly coeval galaxies can be ascribed to variations in [Mg/Fe] ratios. As a result of this, and assuming that the Fornax result is true in general, any previous estimates of age or metallicity spread at a given σ_0 are *overestimated* (see e.g., Colless et al., 1998). The latter assumes that age and [Mg/Fe] are not strongly anti-correlated.

5. The existence of [Mg/Fe] ratio variations at a given central velocity dispersion is interesting in itself. It implies that the star-formation history of old galaxies at a given σ_0 is not entirely homogeneous. This can be explained by (1) slightly different star-formation histories, i.e., different time-scales for the initial stellar burst or

(2) a different galaxy-formation history. For example, a merger scenario where the resulting central velocity dispersion shows a relation with central metallicity different from the one for Es created in an initial stellar burst. Any combination of (1) or (2) is of course possible.

6. As a final point we would like to note that [Mg/Fe] variations can influence index, and in particular Mg-index relations, but they are unlikely to affect global quantities such as effective radius and effective surface brightness. As demonstrated in this Chapter the Mg-index tracks in a complicated way the behaviour of age, metallicity and [Mg/Fe] ratio. So when using a Mg-index as an indicator of the stellar populations in global scaling relations, one has to be extremely careful about what causes the changes in Mg.

Chapter 6

Velocity Dispersion Profiles & Rotation Curves

6.1 Introduction

In this Chapter we present our measurements of velocity dispersion and rotational velocity as a function of radius for those galaxies where exposures showed sufficient S/N. This includes also data from both of the NTT runs. In this thesis we are not primarily interested in the velocity dispersion profiles itself but they are required for the velocity dispersion corrections for the line-strength gradients presented in Chapter 7. Most of the line-strength indices show a relatively weak dependence on velocity dispersion so the velocity dispersion profiles do not have to be extremely accurate. Therefore we restrict ourselves to a brief presentation of the basic kinematic results. The data are reduced as described in Section 2.4.3, where the spectra obtained at the AAT did not require any focus corrections. The analysis was performed with the `fxcor` task in IRAF rather than with FCQ (see Section 3.5 on page 48) because the former program allows one to measure velocity dispersions and recession velocities at much lower S/N and therefore at greater distance from the galaxy centre.

This chapter is organized as follows. In Section 6.2 we compare our measurements between runs and with the literature and in Section 6.3 we present the rotation curves and velocity dispersion profiles for all exposures where we were able to extract useful profiles.

6.2 Literature Comparison

To our knowledge there are only two major kinematical studies of Fornax early-type galaxies besides this work: D'Onofrio et al. (1995) and Graham et al. (1998). The data of the latter was not publicly available at the time of writing so we can only compare with

D'Onofrio et al. and observations from other authors of luminous Es in Fornax and NGC3379. We present comparisons for NGC1427, NGC1404 and NGC3379.

The rotation curves in the following plots are obtained by subtracting the median recession velocity and reflecting all radial measurements with r<0 about the r- and v-axes. In all plots, the different sides of a galaxy are represented by triangles pointing up and down respectively if not stated otherwise in the Figure caption. The error for the recession velocities are given by the `fxcor` program (calculated as suggested by Tonry and Davis (1979)) where the values presented here are the error weighted average of a set of cross-correlations with different stars (e.g., 12 different templates for the AAT96 run). The FWHM of the correlation peaks are averaged in the same way i.e., using the errors from the recession velocity estimates which are also a good indicator of the error in the FWHM. However the final error on the derived velocity dispersions takes into account the error in the correlation peak width itself and the error in the calibration curve (see also Section 3.5.1). For most of the galaxies the uncertainties in the calibration curve is the major contributor to the total error.

To demonstrate the reliability of our kinematic measurements we compared three galaxies with data from the literature. Figure 6.1 shows a comparison of our major axis kinematical measurements of NGC1427 (NTT93- and AAT96-run) – a galaxy with a peculiar core – with data from D'Onofrio et al.. The agreement between all three measurements is excellent, in particular the peculiar core kinematics of NGC1427 (major axis) are confirmed in all three observations.

Figure 6.2 shows a comparison for NGC1404. The data were obtained in the AAT96 run and the results are compared with the measurements by Franx et al. (1989b). .Our measurements are derived from a combined frame of two 5min exposures. Although these short exposures were originally not intended to be used for extended kinematics and line-strength analysis it turned out that we can measure gradients. This is also true for the other exposures from the same observing run. In order to get a reasonable number of independent spectra along the radial profile of a galaxy, we used a S/N binning of 20-30 per Å. Note that the central extractions will still have a higher S/N because the smallest unit we can extract is one pixel row and in the centre of a galaxy the number of counts is high. In summary Figure 6.2 shows that we are able to recover the velocity dispersion as a function of radius reasonably well even for low S/N binning. The rotational velocity for this galaxy is consistent with zero.

Another much used galaxy for literature comparison is the "bona fide" elliptical galaxy NGC3379. In Figure 6.3 we compare our data, extracted from a single exposure of 5min and a S/N binning of 30 per Å with data from Franx et al. (1989b), González (1993) and Bender et al. (1994). Here both, velocity dispersion and rotation, are in excellent agreement again.

In conclusion all three comparisons have shown that we are able to recover the velocity

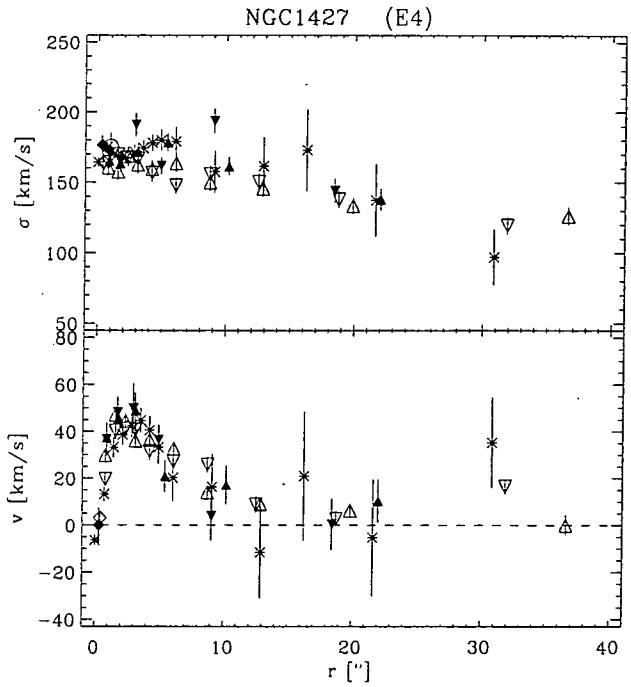

Figure 6.1: NGC1427: comparison of our major axis kinematical measurements from the AAT96 run (open triangles) with our measurements from the NTT93 run (filled triangles) and with D'Onofrio et al. (1995) major axis measurements (stars). Our adopted central velocity dispersion is indicated by an open circle.

dispersion profiles and the rotation curves to a high accuracy even at low S/N binning. Measurements from different observing runs show consistent results. The use of a simple, but stable program such as `fxcor` has allowed us to work at low S/N and therefore probe the outer regions of galaxies in our sample as well as possible. This overlaps well with the area that we can extract line-strength gradients from and therefore need velocity-dispersion corrections.

6.3 Results

The following Figures (6.4 - 6.6) present velocity dispersion profiles and rotation curves for all exposures where we were able to extract them[1]. At the top of each mini plot we give the galaxy name, morphological type and observed as well as major axis position angle (PA). In the upper right corner of each panel the observing run is indicated with the usual abbreviations. Open diamonds, open triangles pointing up and down represent the centre and different sides of a galaxy respectively. The adopted central velocity dispersion

[1]Note that some data obtained at the NTT could not be used. The second night of the NTT93 run showed a reduced spectral resolution probably caused by a wider slit. As no standard stars were taken for the second night we were unable to estimate velocity dispersions.

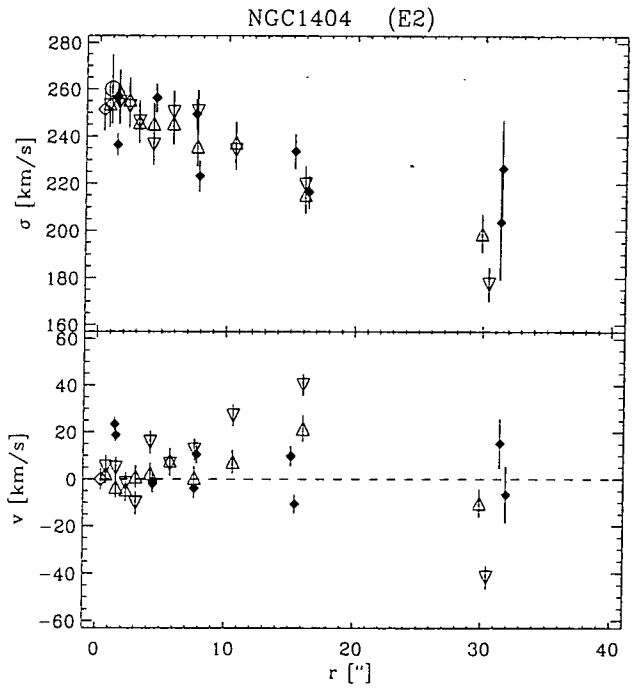

Figure 6.2: NGC1404: comparison of our kinematical measurements from the AAT96 run (PA=90°; combined exposure from night 2&3; binning: S/N=28 per Å; open triangles) with Franx et al. (1989b) (PA=74°; filled diamonds). Our adopted central velocity dispersion is indicated by an open circle.

from Tab 3.3 on page 59 is indicated by a filled circle. Tables of velocity dispersion and rotational velocity can be obtained from the author if requested.

One important thing to note is that many galaxies show significant rotation although most exposures are taken at a fixed, i.e., 90°, position angle. This gives further evidence to the conclusion by D'Onofrio et al. (1995) and Graham et al. (1998) that most of the Fornax ellipticals are consistent with being supported by rotation and isotropic velocity dispersion. A more detailed analysis is beyond the scope of this thesis. However we will finish with some remarks on individual galaxies.

Comments on individual galaxies

- **NGC1339:** Observations from two different observing runs are available, NTT92 and AAT96 (Figure 6.4; middle panels). The NTT92 data show a steep rise of the velocity dispersion in the centre whereas the AAT96 data do not. We note that the AAT96 data are convolved with bad seeing. It was the first observation of a galaxy after the sky cleared during the second night of the observing run.

- **NGC1316:** This galaxy, observed at intermediate PA, shows a central dip ($r \lesssim 3''$) in the velocity dispersion profile but further out up to r=30″ it seems to have a

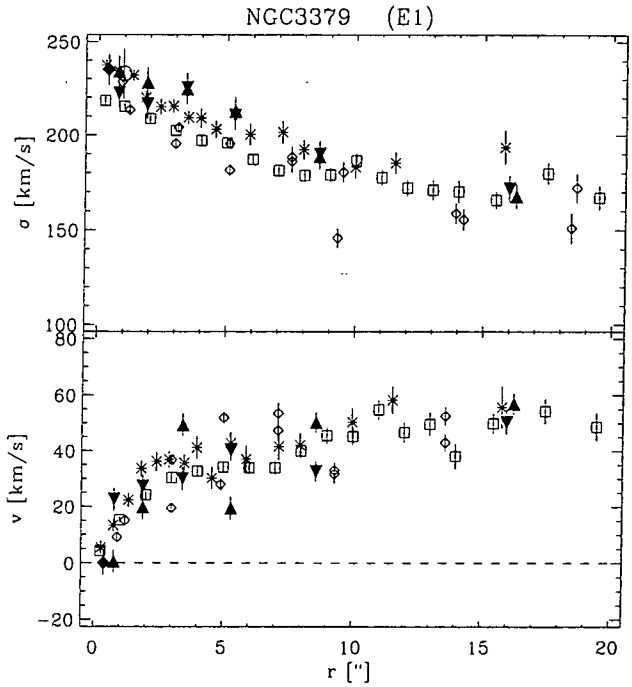

Figure 6.3: NGC3379: comparison of our kinematical measurements from the AAT96 run (PA=90°; binning: S/N=30 per Å; filled triangles) with Bender et al. (1994) (PA=72°; stars), Franx et al. (1989b) (PA=68°; open diamonds) and González (1993) (PA=74°; open squares). Our adopted central velocity dispersion is indicated by an open circle. Note that some data points from the literature at radii >20″ are not shown.

constant $\sigma = 240$ kms^{-1} (Figure 6.4; top left panel). Young stellar populations and patchy dust in the centre of this galaxy lead to the conclusion that it harbours young stellar populations and was probably created in a recent merger. The rotation curve shows a asymmetric rotation. This might be a sign of the merger which happened in this galaxy.

- **NGC1381:** The minor axis shows a curious rotation curve (Figure 6.5; middle right panel). We do not regard this feature as real but rather a result of technical problems (e.g., slit not exactly centred on nucleus of the galaxy).

  For one exposure of this galaxy the slit was offset parallel from the minor axis by roughly 8″ such that the slit crossed a bright star close to NGC1381. The rotation curve shown was determined by subtracting the mean recession velocity of the galaxy (Figure 6.5; bottom left panel).

- **NGC1399:** Both major and minor axis show evidence of slow rotation (Figure 6.6; top panels).

- **NGC1427:** The major axis features a peculiar core with a maximum rotation of ~ 50 kms^{-1} at 3″ and zero rotation from 15″ onwards (Figure 6.1). This kinematical signature is consistent with the findings by Carollo et al. (1997). Their analysis of HST-WFPC2 images suggests a stellar disk between 0.″3 and 3″.

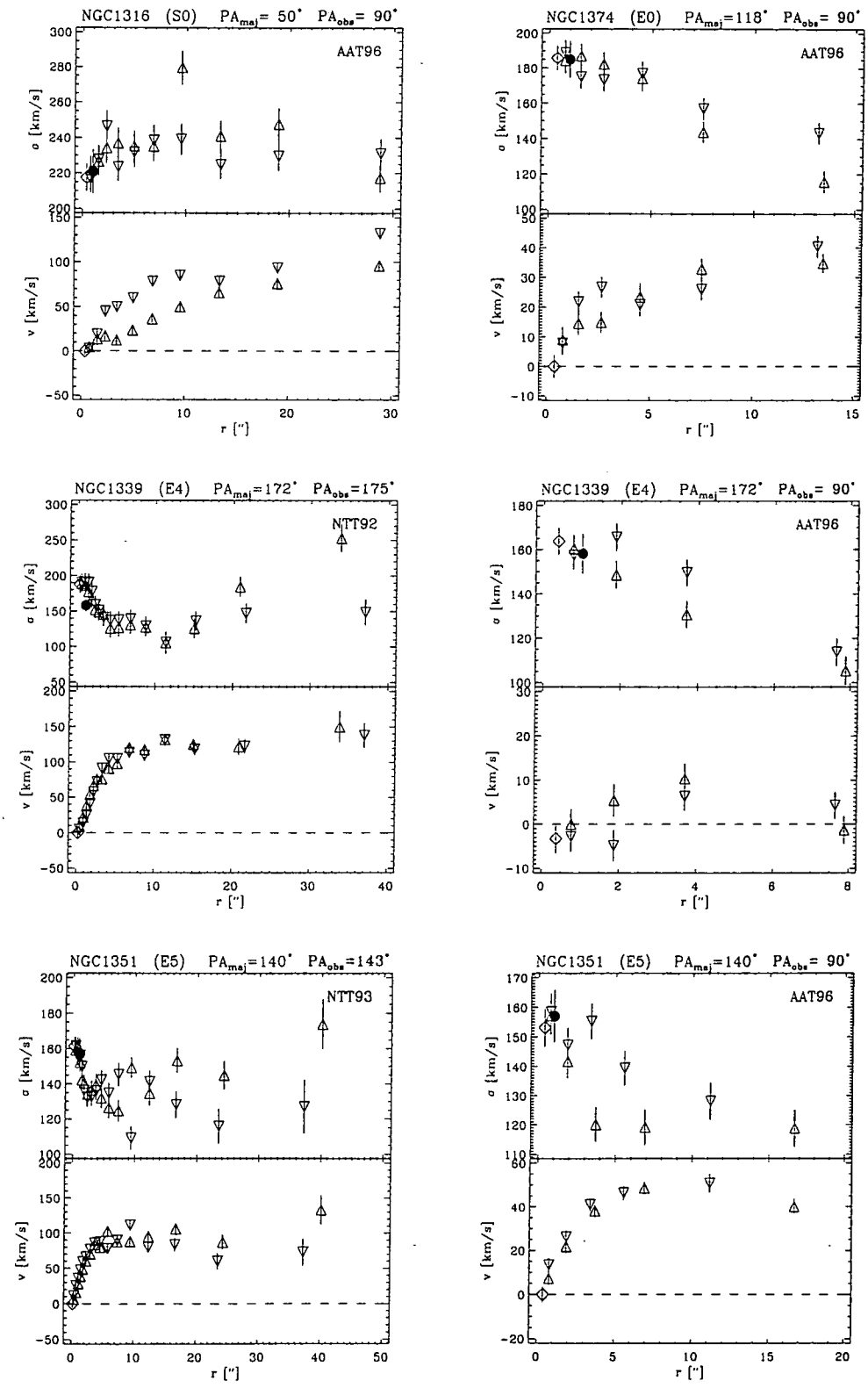

Figure 6.4: Velocity dispersion profiles and rotation curves. Open diamonds, open triangles pointing up and down represent the centre and different sides of a galaxy respectively. The adopted central velocity dispersion is indicated by a filled circle. The galaxy name, morphological type as well as the PA of the major axis and the **observed** axis are given in the title of each panel.

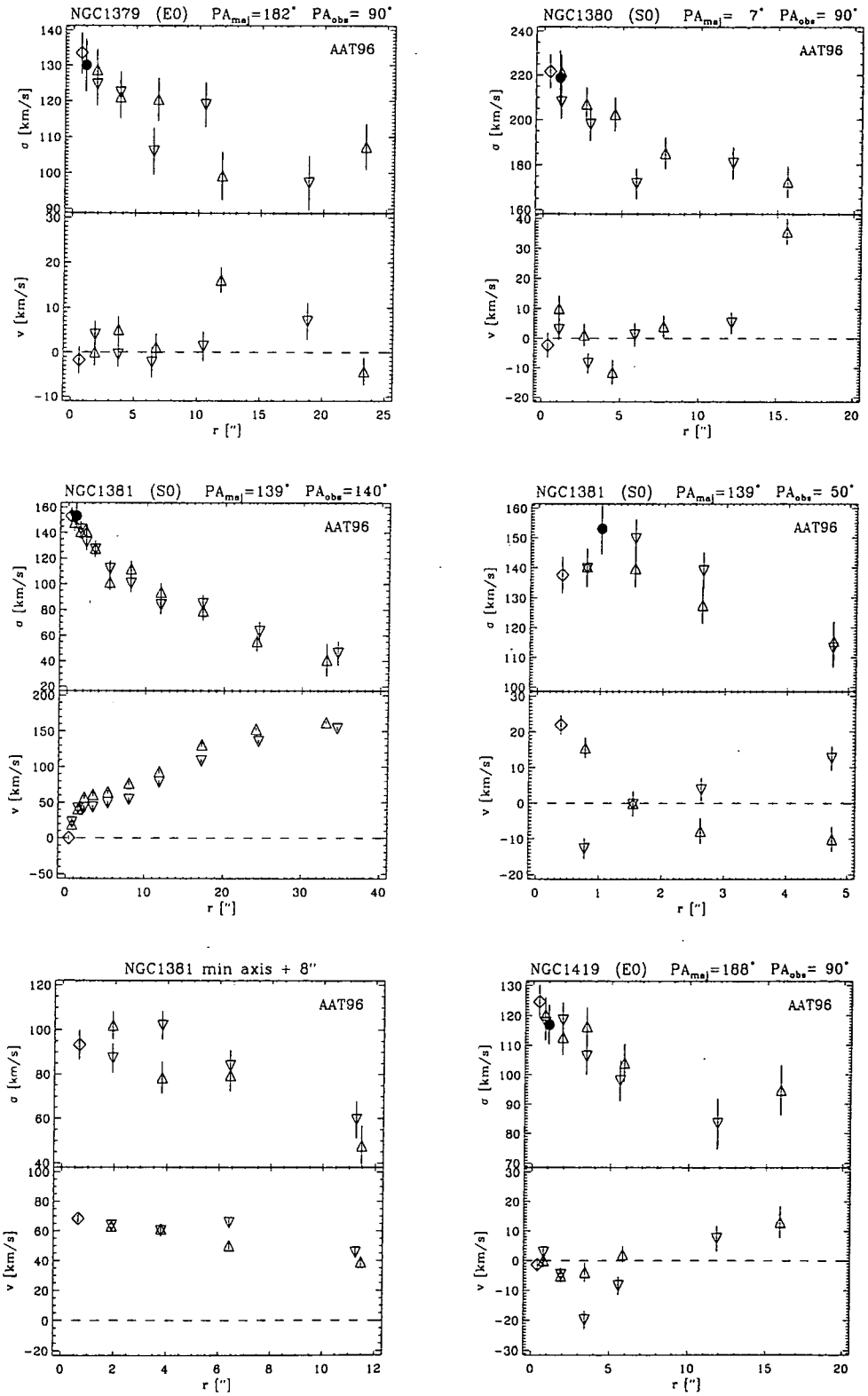

Figure 6.5: Velocity dispersion profiles and rotation curves. Open diamonds, open triangles pointing up and down represent the centre and different sides of a galaxy respectively. The adopted central velocity dispersion is indicated by a filled circle. The galaxy name, morphological type as well as the PA of the major axis and the **observed** axis are given in the title of each panel.

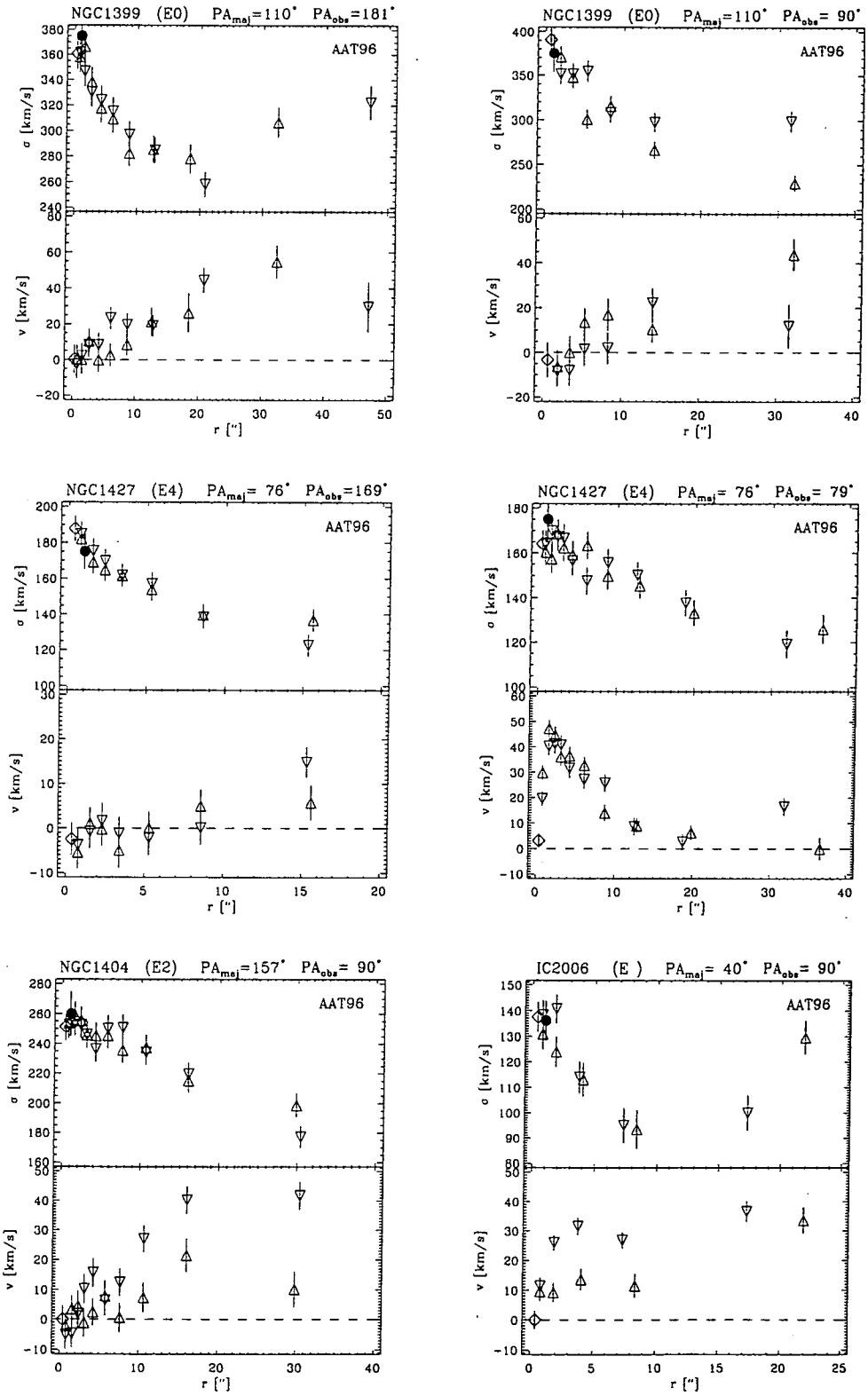

Figure 6.6: Velocity dispersion profiles and rotation curves. Open diamonds, open triangles pointing up and down represent the centre and different sides of a galaxy respectively. The adopted central velocity dispersion is indicated by a filled circle. The galaxy name, morphological type as well as the PA of the major axis and the **observed** axis are given in the title of each panel.

Chapter 7

Line Strength Gradients in Early-Type Galaxies

So far all of our line-strength analysis concentrated on the nuclear regions of early-type galaxies. But how do quantities such as age, metallicity and [Mg/Fe] ratio vary with radius in a given galaxy? Is the centre of a galaxy a good indicator of its global stellar populations? These and similar questions will be addressed in this Chapter.

7.1 Introduction

It has been known for more than 30 years from colour gradients that the properties of stellar populations in a galaxy vary with radius, e.g., de Vaucouleurs (1961) measured bluer colours when he observed a galaxy with larger apertures. Later observations (e.g., Spinrad et al., 1971) showed that the colour trend is evident in decreasing line-strength with radius for many absorption features. The results from these early works are now well established and line-strength profiles for large samples have been published, mostly using the Lick/IDS system (Efstathiou and Gorgas, 1985; Gorgas et al., 1990; Carollo et al., 1993; Davies et al., 1993; Fisher et al., 1995; Mehlert, 1998). However, measuring line-strength gradients still remains a challenge because gradients are generally not strong and measuring accurate absorption strength (on a standard system!) of weak Fe-lines at large radii is difficult. Despite the vast amount of available data it is not at all clear how, for example, Mg-gradients compare with Fe-line gradients, or whether, as suggested by some authors, the centres of Es are populated by slightly younger stellar populations than those present further out. This uncertainty is partly caused by inhomogeneous data samples and uncertain calibration to a standard system.

With the availability of stellar population models some groups have started to translate the index-gradients into more physical age, metallicity and abundance ratio gradients.

Early results by González (1993) suggested that abundance ratios stay constant within a given elliptical galaxy. His analysis of the age/metallicity gradients showed a variety of gradients with no obvious trend. His work was continued by Fisher et al. (1995) analysing a sample of ellipticals and brightest cluster members. They confirmed previous abundance ratio results and found that the Hβ absorption is roughly constant with radius. Using Worthey's models this translates into a shallow negative age gradient where galaxy centres are younger. Most recently Mehlert (1998) supported this picture with her analysis of bright Coma early-type galaxies. We note however, that these results are based on Hβ measurements which can be severely affected by nebular emission (see also Section 4.3.4).

Even without the help of models, the "pure" index gradients can tell us something about the formation history of early-type galaxies perhaps even how much dissipation was involved. For example, early evidence that the slope of the Mg_2 gradient is related to the central Mg_2 absorption strength (Gorgas et al., 1990; Davidge, 1992) has recently been confirmed by González and Gorgas (1996) and Mehlert (1998). Galaxies with high central Mg absorption have steeper gradients than Mg-weak galaxies. Mehlert (1998) found this also to be true for <Fe>. However, all these correlations are rather weak and seem to be driven by galaxies with the weakest and strongest central index strength.

This Chapter is organized as follows. In Section 7.2 and 7.3 we describe the Lick/IDS calibration and extraction of line-strength gradients. A inter-run and literature comparison for the gradients is presented in Section 7.4. The results and analysis is presented in Section 7.5 where we first investigate the raw gradients and then transform them with the help of stellar population models into age, metallicity and [Mg/Fe] gradients. Finally, we conclude in Section 7.6.

7.2 Establishing the Lick/IDS offset for NTT Data

For this analysis we will make use for the first time of the NTT line-strength data. Before we can analyse the line-strength gradients we have to make sure that we measure the "same" indices in all three observing runs. That means we have to carefully calibrate the data to the standard Lick/IDS system. Our general calibration procedure (using stars to establish offsets) cannot be used for the NTT observing runs because there were not enough standard stars observed in common with the Lick/IDS stellar library. As mentioned before, the AAT96 run (which is already calibrated to the Lick/IDS system) was designed to serve as our standard for all three runs, so we compared the indices measured on the central parts of galaxies (NTT runs) with the AAT96 data. In detail we extracted from each galaxy observation at a given position angle (sometimes two exposures combined) a central spectrum matching the AAT96 standard aperture ($2\farcs3 \times 3\farcs85$, see also Section 2.4.2). Furthermore the spectra were focus-corrected, continuum-corrected and broadened to the Lick/IDS resolution. Finally velocity dispersion corrections were

applied to the central line-strength measurements. Note that by matching the nuclear line-strength measurements we intrinsically assume that we also match the line-strength measurements further out in a galaxy. At this point this is an ad-hoc assumption but we will show in Section 7.4 that this is reasonable. The established Lick/IDS offsets and the corresponding diagrams can be found in Table 7.1 and Figures 7.1 to 7.4 respectively. The galaxies used in the offset evaluation are noted in the Figure captions with their respective symbols.

Generally we find very good agreement between the observing runs resulting in small offsets. Table 7.1 states the offset (column 2 & 5) and the error in the transformation to the AAT96 system (column 3 & 6), column 4 & 7 state the total error in the Lick/IDS offset, that is the offset error of the NTT and AAT96 runs summed in quadrature. For indices such as $H\gamma_A$ and G4300 the spread around the mean offset is much smaller than when we compared the AAT96 stars with the Lick/IDS stellar library as presented in Figure 3.3 on page 44[1]. We attribute this to the high quality and careful reduction of our data. The two Fe-lines Fe5270 and Fe5335 are perhaps an exception in this respect. The reason for this is that the CCDs in the NTT observing runs exhibited bad columns in the region where former Fe-lines were recorded on the chip. We interpolated (linearly) over these bad columns but of course some information is always lost and this can lead to slightly wrong estimates of the true absorption. In general the quality of the NTT observations is poorer than the AAT96 data. One of the likely causes here are the unstable bias patterns for the NTT92 run and that both CCDs mounted at the red beam of the NTT exhibited many bad columns. Some indices (e.g., $C_2$4668) in the blue part of the red beam from the NTT runs are heavily affected by the transmission function of the beam splitter. As a result the continuum shape is extremely difficult to correct for. We have taken great care to remove the response function of the CCD and the beam splitter. However, we recognize that indices in the turnover region are still affected. For the latter reason we will not use the $C_2$4668-index measurements obtained at the NTT telescope in any further analysis.

7.3 Extracting Line-Strength Gradients

Now, that we have established accurate Lick/IDS offsets for all three observing runs we can derive line-strength gradients for the galaxies. The extraction procedure of calibrated 1-d spectra at different position in a galaxy is described in Sections 2.4.3 and 2.4.4. These 1-d extractions can then be treated in the same way as our central spectra. We measure line-strength indices and correct them for the velocity dispersion at the respective radius. The velocity dispersion at a given radius is taken from the velocity dispersion profiles presented in Chapter 6. For most of the indices the velocity dispersion corrections are a shallow function of the velocity dispersion (see Figure 3.13 on page 61), hence any small

[1] Please note that the y-range in each panel of Figures 7.1 and 7.3 matches the one of Figure 3.3 on page 44, so a direct comparison is possible.

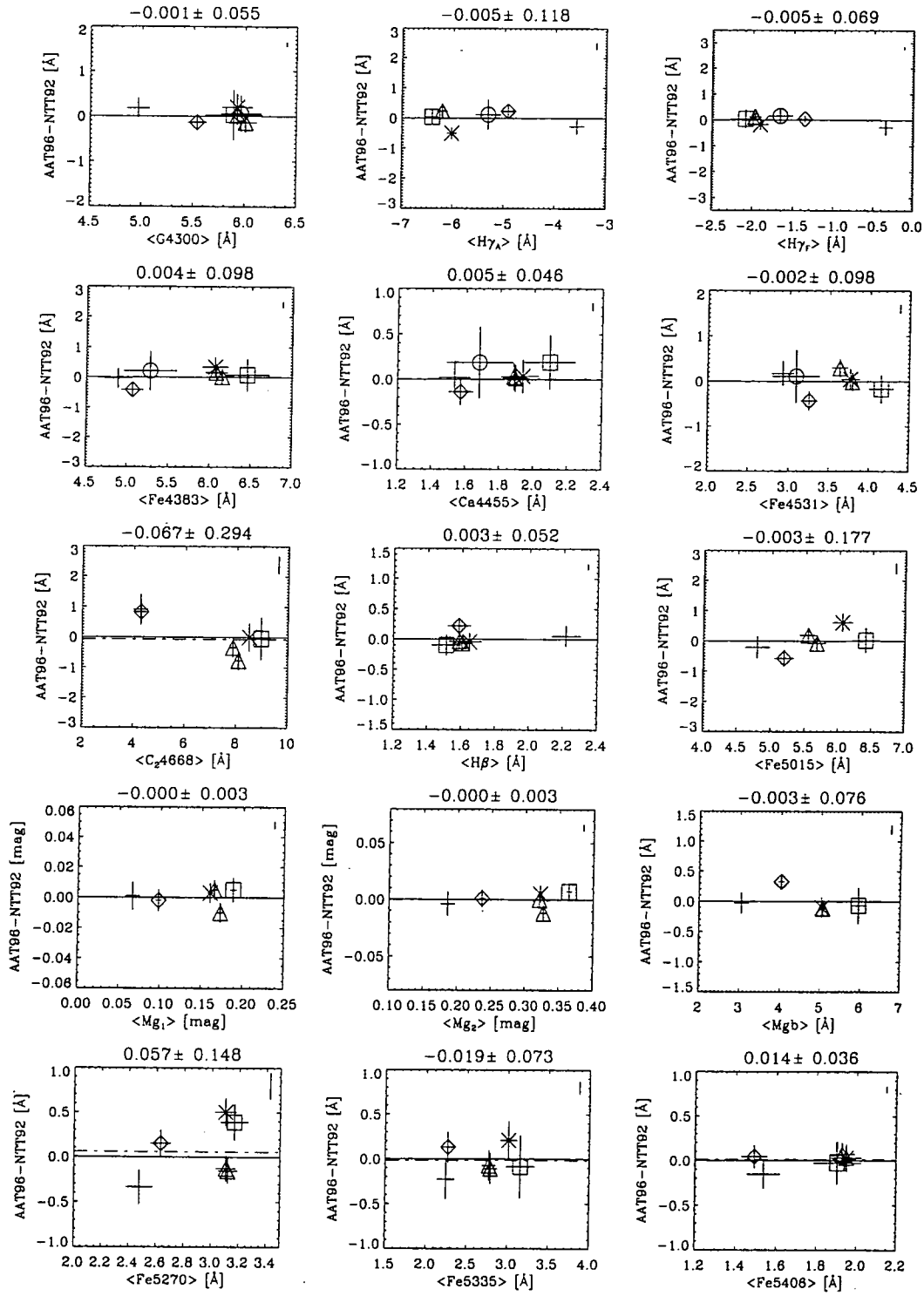

Figure 7.1: Lick/IDS offset for NTT92 determined by comparison with calibrated AAT96 data. The following galaxies were observed in common with the AAT96 run: ESO358-G59 (plus), NGC1336 (diamond), NGC1339 (triangle), NGC1379 (circle, only blue CCD), NGC1399 (square) and NGC1404 (cross). Note that for NGC1339 major and minor axis are represented by the same symbol. The error bar in the upper right corner of each panel indicates the size of the offset error.

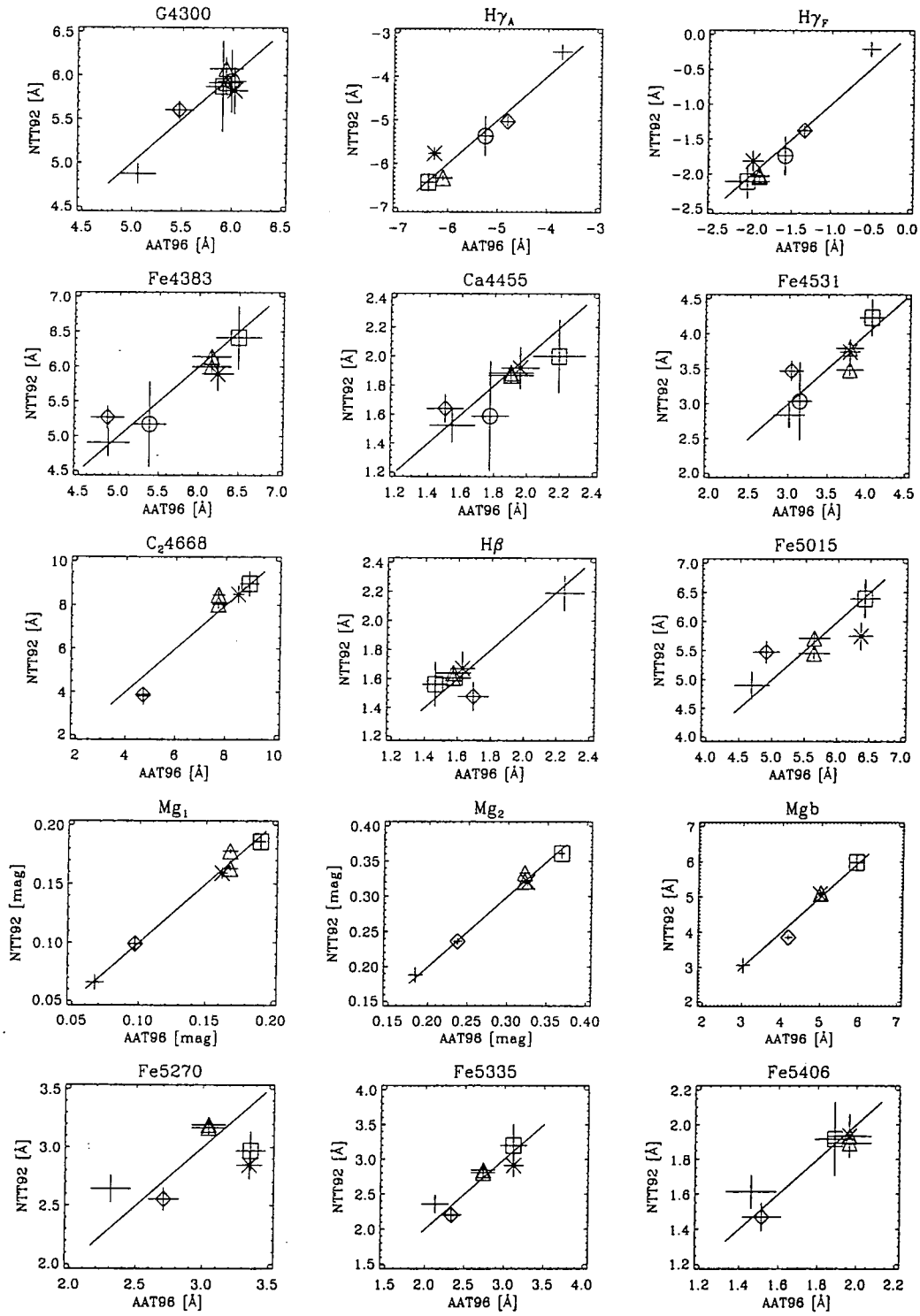

Figure 7.2: Lick/IDS offset NTT92: *linear comparison.* Symbol definitions see Figure 7.1.

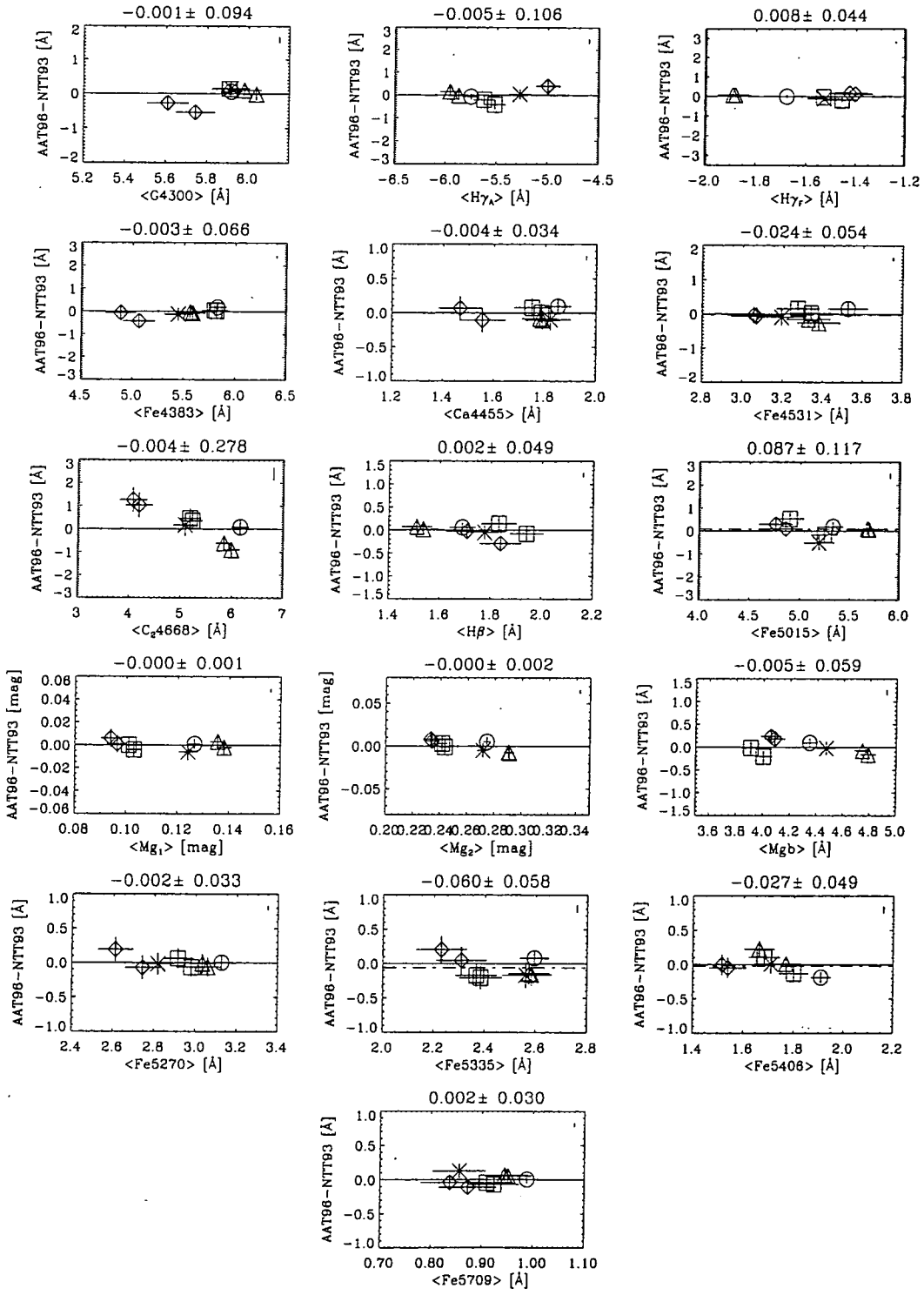

Figure 7.3: Lick/IDS offset for NTT93 determined by comparison with calibrated AAT96 data. The following galaxies were observed in common with the AAT96 run: NGC1336 (diamond), NGC1351 (triangle), NGC1373 (square), NGC1379 (cross) and NGC1427 (circle). Note that for NGC1336, NGC1351 and NGC1373 major and minor axis are represented by the same symbol. The error bar in the upper right corner of each panel indicates the size of the Lick/IDS offset error.

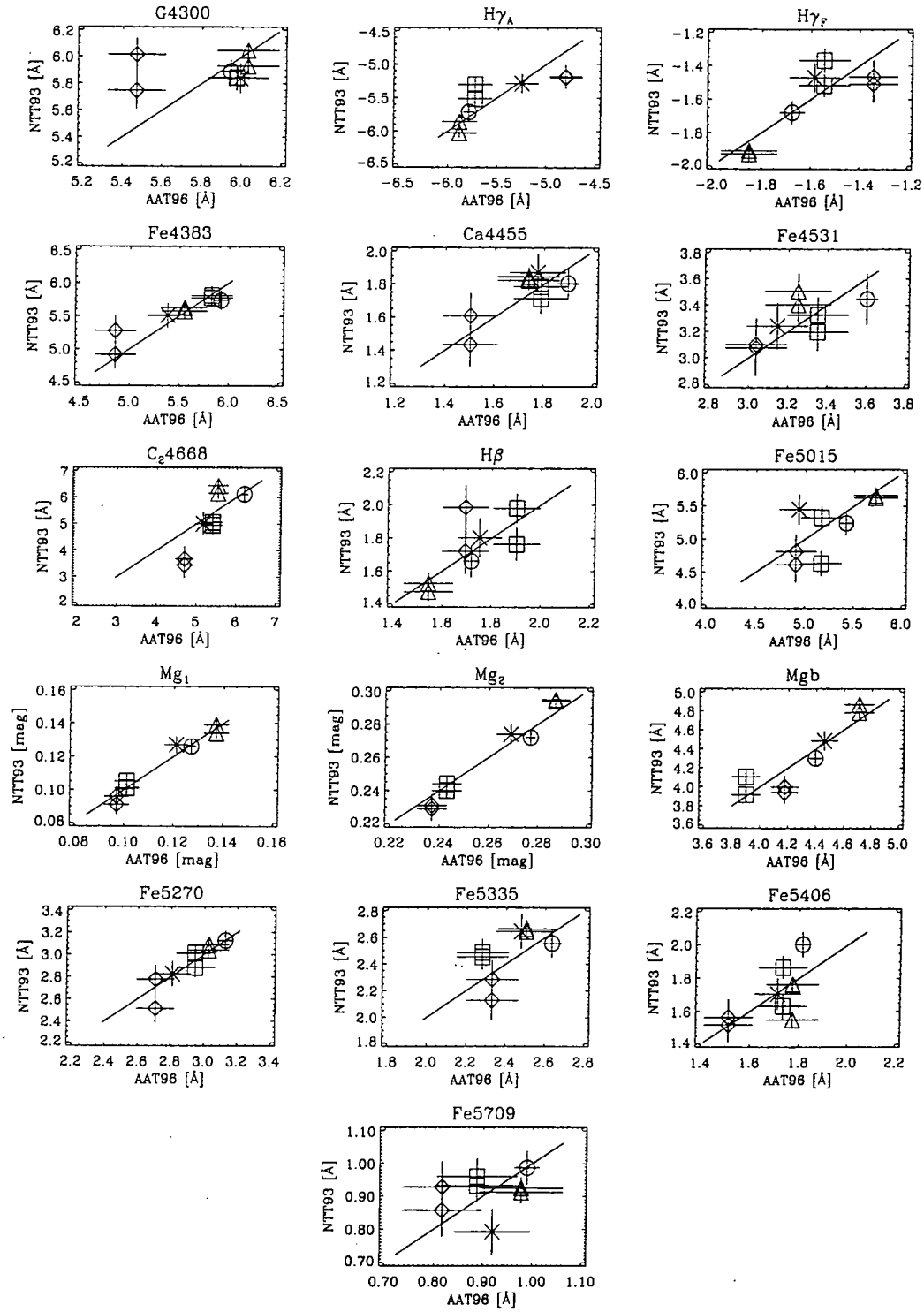

Figure 7.4: Lick/IDS offset NTT93: *linear comparison.* Symbol definitions see Figure 7.3.

Table 7.1: Adopted Lick/IDS Offsets for NTT92 and NTT93

	NTT92			NTT93		
Index	offset	±AAT	±Lick/IDS	offset	±AAT	±Lick/IDS
(1)	(2)	(3)	(4)	(5)	(6)	(7)
G4300	+0.33 Å	0.06 Å	0.11 Å	+0.39 Å	0.09 Å	0.13 Å
Fe4383	−0.47 Å	0.10 Å	0.16 Å	−0.52 Å	0.07 Å	0.15 Å
Ca4455	+0.49 Å	0.05 Å	0.08 Å	+0.48 Å	0.03 Å	0.07 Å
Fe4531	+0.25 Å	0.10 Å	0.14 Å	+0.00 Å	0.05 Å	0.11 Å
$C_2$4668	+0.00 Å	0.29 Å	0.34 Å	−0.35 Å	0.28 Å	0.33 Å
Hβ	+0.05 Å	0.05 Å	0.06 Å	+0.00 Å	0.05 Å	0.06 Å
Fe5015	+0.31 Å	0.18 Å	0.20 Å	+0.00 Å	0.12 Å	0.15 Å
Mg_1	+0.004 mag	0.003 mag	0.004 mag	+0.003 mag	0.001 mag	0.003 mag
Mg_2	+0.022 mag	0.003 mag	0.004 mag	+0.022 mag	0.002 mag	0.004 mag
Mg *b*	+0.11 Å	0.08 Å	0.13 Å	+0.16 Å	0.06 Å	0.12 Å
Fe5270	+0.00 Å	0.15 Å	0.16 Å	+0.11 Å	0.03 Å	0.06 Å
Fe5335	+0.00 Å	0.07 Å	0.11 Å	+0.00 Å	0.06 Å	0.10 Å
Fe5406	+0.00 Å	0.04 Å	0.06 Å	+0.00 Å	0.05 Å	0.06 Å
Fe5709	...	...	...	+0.00 Å	0.03	0.07
Hγ_A	+0.96 Å	0.12 Å	0.30 Å	+1.21 Å	0.11 Å	0.30 Å
Hγ_F	+0.36 Å	0.07 Å	0.16 Å	+0.44 Å	0.04 Å	0.15 Å

The values in column 2 & 5 represent AAT96 - NTT

errors in σ do not translate into significant errors for the line-strength indices. However, before the correction was applied we carefully smoothed the velocity dispersion profiles in such a way that the two sides of a galaxy were averaged and sometimes obvious "outliers" were excluded. When line-strength profiles exceeded the range of useful σ-estimates we used the σ from the last reasonable data point. When we were not able to extract any useful velocity dispersion profiles at all, as in the case of faint S0s, we applied a constant σ correction using the adopted central velocity dispersion (see Table 3.3 on page 59). This procedure probably overestimates the correction as most of the galaxies show decreasing σ-profiles, however usually the corrections in this velocity dispersion range are very small. The correction factors for the velocity dispersion correction where derived in the same way as for the AAT96 run (see Section 3.5 on page 48) and the results are very similar (not shown).

7.4 Literature and Run-to-Run Comparison

In order to demonstrate that we calibrated all three observing runs to the same, standard Lick/IDS system we will compare first our data between different observing runs and then compare with literature data.

In Figure 7.5 the data for NGC1427 (major axis) from three exposures and two different observing runs are presented. See Figure caption for observational details. Shown are index *vs* log (r/r_e) relations for 10 important line-strength indices in the Lick/IDS system, where r_e denotes the effective radius scaled to the position angle of the observation. Note that for the NTT observing runs spectra are recorded on two different CCDs, i.e., the blue and red beam of the spectrograph. Hence the radial sampling is different for indices recorded on different CCDs. At the top of the plot the name of the galaxy, the type, the effective radius in arcsec and the position angle of the major axis are given.

The data are in excellent agreement for all 10 indices presented. The classical indices such as Mg_2 and Mgb can be recovered in an extremely consistent way. The "new" indices such as $H\gamma_A$ are also in very good agreement. Note that $H\beta$ is constant with radius but shows substantial spread consistent with the error bars.

Figure 7.6 presents data for NGC1404 (AAT96 and NTT92, observational details see Figure caption). The error bars are somewhat bigger for these shorter exposures but still the two observations are in excellent agreement. The central drop in <Fe> for the NTT92 data is probably caused by a combination of focus variations and incomplete removal of bad columns.

Finally in Figure 7.7 we compare our data with the literature. There is not much high quality data available for the Fornax cluster but we can compare data for NGC3379: Among others there are observations by Davies et al. (1993), González (1993) and Vazdekis et al. (1997).

The overall agreement is not as good as one may have hoped although we do agree with Davies et al. and González very well for the indices in common. There are substantial offsets to the calibration adopted by Vazdekis et al.; additionally there is a significant difference for Mg_2 which increases with radius. However when we take the error in the Lick/IDS-system offset into account (see error bars in the lower left corner of each panel) then our central index measurements are consistent with the original Lick/IDS measurements (filled circles). We recognize that this is also true for the Vazdekis et al. data when compared to the Lick/IDS data.

In summary we have shown that our line-strength gradients are very well calibrated within our system. We emphasize that although we performed our offset corrections only for the central parts of the galaxies, the agreement at larger radii is excellent. The literature comparison has shown that our measurements are consistent with the results of other authors. However, due to the rather large systematic error in the Lick/IDS offset for individual indices one has to be aware of these errors when making comparisons to model predictions.

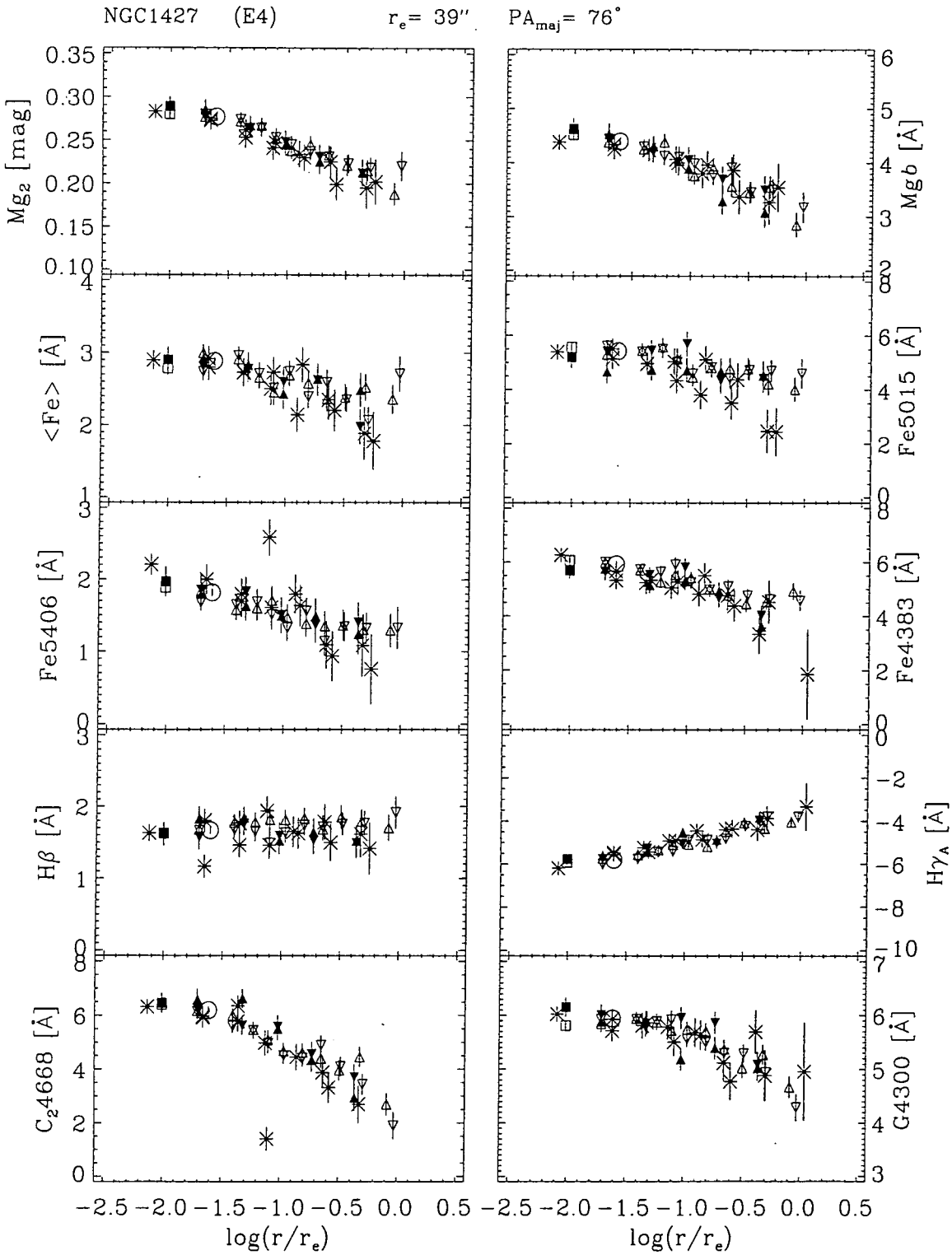

Figure 7.5: NGC1427: Shown are data from three different observations. AAT96, 30min exposure, PA=79° (open triangles); AAT96, 10min exposure, PA=90° (filled triangles) and NTT93, 30min exposure, PA=80° (stars). The adopted central line-strengths from Chapter 4 is indicated by an open circle.

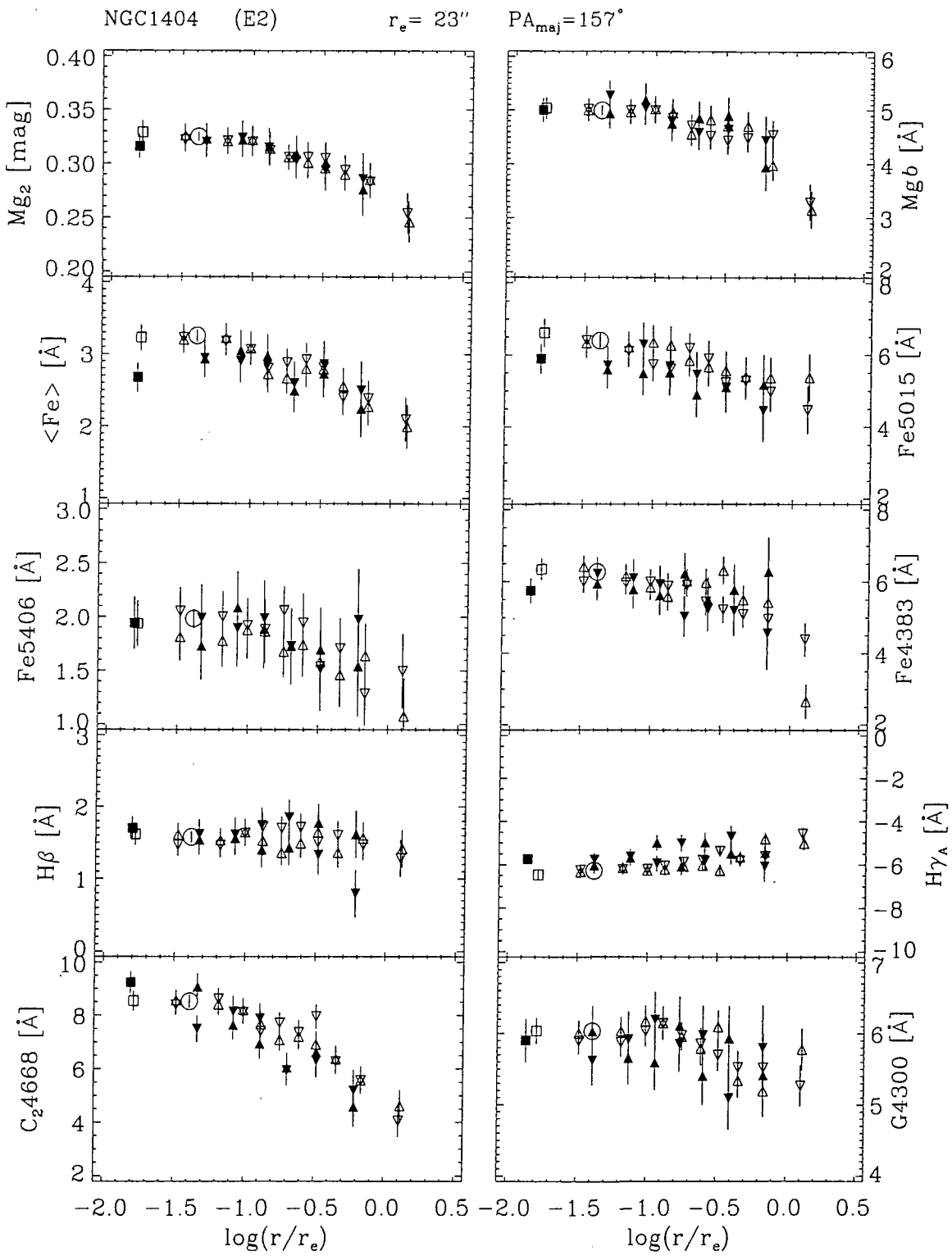

Figure 7.6: NGC1404: two observations are shown. AAT96, combined 2×5min exposure, PA=90° (open triangles) and NTT92, 20min exposure, PA=110° (filled triangles).

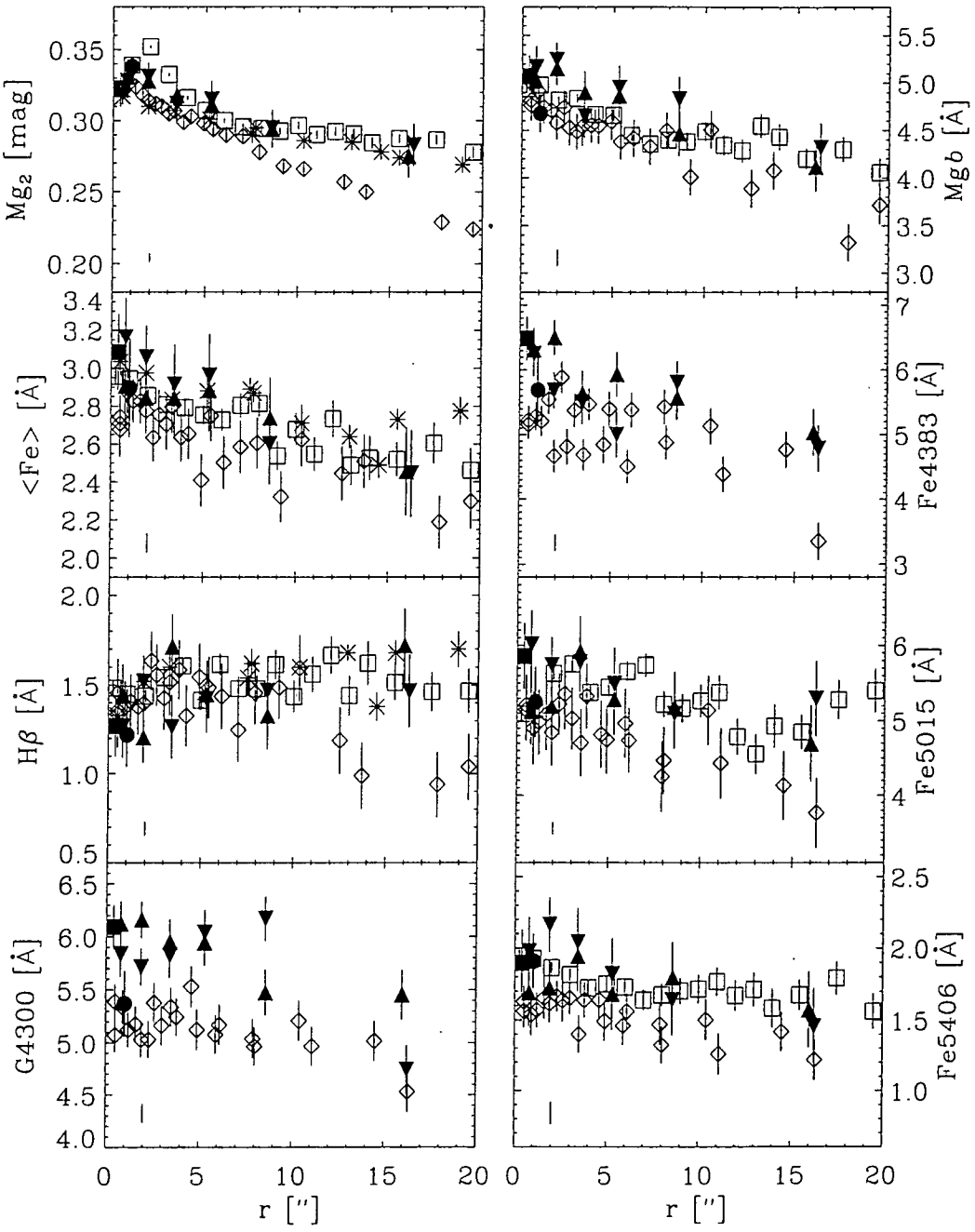

Figure 7.7: A literature comparison for NGC3379: Filled triangles and filled square (centre of the galaxy) represent our data (5min exposure at PA=90°); the stars represent the data from Davies et al. (1993) (plotted at intermediate PA, i.e., averaged position angles); the open diamonds represent data from Vazdekis et al. (1997) (PA=70°). The open squares represent data from González (1993) (PA=74°). The filled circles denote the central line-strength given by the original Lick/IDS measurement (Trager, 1997). The error bar in the lower left corner of each panel indicates the rms uncertainty in the transformation to the Lick/IDS system for our data.

7.5 Results

In this Section we present fully calibrated (Lick/IDS system) line-strength gradients for a complete sample of early-type galaxies in the Fornax cluster. Firstly in Section 7.5.1 we will consider only the "pure" index-gradients and investigate their utility in stellar population analysis. In Section 7.5.2 we will transfer former gradients into more physical age, metallicity and [Mg/Fe] gradients with the help of stellar population model predictions.

7.5.1 Index-Gradients

In Chapter 5 where we analysed the correlations between central stellar populations and central velocity dispersion we presented all indices as measured in magnitudes, i.e., in the way Mg_2 is defined. This has the advantage that one can directly compare the slopes and also indices with negative values, such as $H\gamma_A$, are naturally included in the definition (note that a simple logarithm of a negative value is not defined). Here we will follow the same methodology. We fit a linear function to the data such that gradients are defined as

$$\text{grad } Index = \frac{\Delta Index \text{ [mag]}}{\Delta log(r/r_e)} \tag{7.1}$$

where the *Index* is measured in magnitudes and r_e is the effective radius. Hereafter the magnitude definition of otherwise atomic indices is indicated by a prime [′] after the index name, e.g., < Fe′ > or Fe4383′.

An example of the fits can be seen in Figure 7.8. The fits are least squares fits (IDL program `svdfit`) with error weighting (weights=$1/err^2$) of data points from both sides of a galaxy. Points at radii less than 1″ were excluded from the fits, as they may be affected by seeing (see dashed line in plots). A priori it is not clear that a linear fit to the data is a valid approach to describe all of the index-gradients. And in fact there is clear evidence for some indices and galaxies that they do not follow a linear trend in a log-log plot. Nevertheless a linear fit is a simple and easy approach to take, it has also been used exclusively in the literature. Furthermore we regard a gradient as characteristic for a galaxy when it is measured over approximately one effective radius or more.

Plots of index-gradients and fits for all galaxies can be found in Appendix B[2]. Note that the outermost data points for some galaxies are beyond 1 r_e but for other galaxies they extend only to ∼0.3 r_e. Note that for NTT observations we substituted the $C_2$4668

[2]Not all data from the NTT runs could be used to derive line-strength gradients. The second night of the NTT93 run showed a reduced spectral resolution probably due to a wider slit which was not recorded during observing. As there were no standard stars taken for the second night we could not calibrate the line-strength indices and measure gradients. Furthermore the observations of NGC1339 (minor axis) suffered badly from focus variations which could not be removed, thus we discarded these exposures.

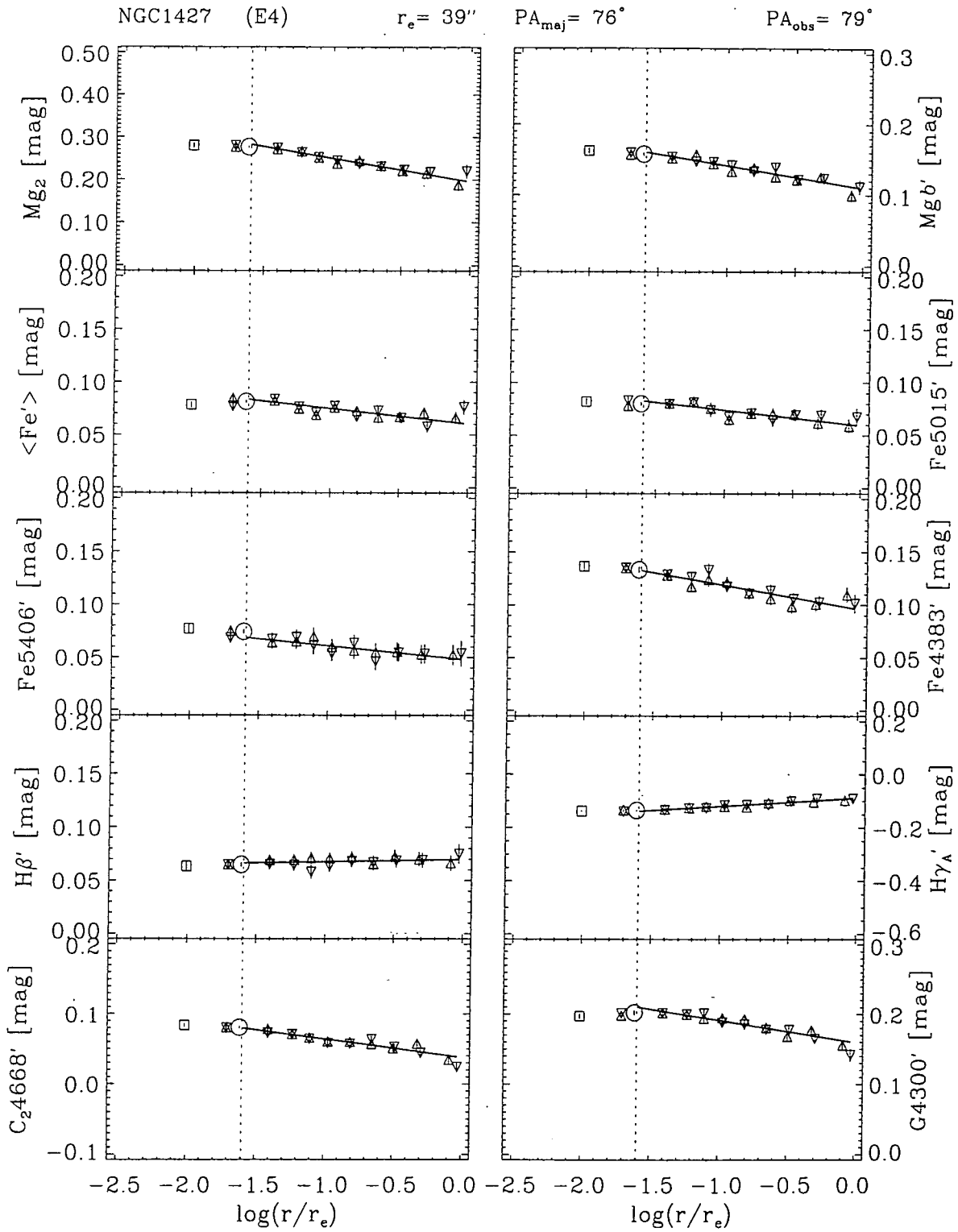

Figure 7.8: An example for fitting a linear function (solid line) to index-gradients. Plotted are indices measured in magnitudes *vs* log (r/r_e). The open square and triangles facing up and down represent the centre and different sides of the galaxy respectively. The galaxy used in this example is NGC1427 (AAT96 run). The vertical dashed line indicates the central 1″ radial range which is excluded from the fits because of seeing effects.

gradients with the more interesting $H\delta_A$ gradients. For some of the fainter galaxies we could extract only three independent data pairs in a region $>1''$. A fit to these data points can lead to an inaccurate description of the true gradients and we decided not to show a fit for the noisier cases.

In general all galaxies with high quality data show smooth gradients. Two indices, $H\beta$ and Fe5406, show consistently a larger spread and sometimes no obvious correlation at all. We ascribe this to measurement errors, because these indices are very weak with absorption strengths around 0.5 to 1.5 Å equivalent width or 0.05 to 0.10 mag. Furthermore $H\beta$ does not generally show a steep gradient and is consistent with no gradient at all for most of the galaxies. All the metal lines show generally decreasing absorption strength with radius. However, the higher order Balmer lines $H\gamma_A$ and $H\delta_A$ generally exhibit positive gradients, in fact these are among the strongest gradients found in our sample. Note that this is mostly caused by a metallicity effect as we will see in Section 7.5.2.

Although we excluded the seeing affected central regions from the fit, the gradients are still subject to various errors. First of all, the data extends to different radii for different galaxies, which introduces great uncertainty when only a fraction of the effective radius is covered. There is no correction we can make for this. Then there are uncertainties introduced by sky-subtraction errors which we will investigate in the next paragraph. The formal errors from the fit to the data are generally very small and not significant in comparison to other error sources. Finally there may be systematic errors such as problems with the Lick/IDS calibration.

To investigate the effects of sky-subtraction errors on the line-strength gradients we performed tests on two galaxies: NGC1427 & NGC1373. For the first, relatively bright, galaxy we examined a 30min exposure of the major axis whereas for the second, relatively faint galaxy, we used a 20min exposure at PA=90°. For both galaxies we artificially added (subtracted) 5% of the previously subtracted sky-spectrum to (from) the CCD-data and then re-run our line-strength program (`ls2d2`) on it. The results are presented in Figure 7.9 & 7.10. The normal data-reduction and the two sky-treated data-reductions are indicated by different symbols (see Figure caption). Note that we have taken out the mean line-strength gradient (= fit to the original data) for each index and plot only the deviations from the fit. In this way one can check the quality of the fit and any changes due to sky-subtraction errors are readily visible.

The first thing to note is that the central $1''$ region, which was excluded from the fit, substantially deviates from the otherwise linear trend of absorption lines-strength with radius. Whether all of this is caused by seeing or the inner core regions do show a special behaviour cannot be investigated without proper seeing treatment. However, we recognize that for NGC1427 (see Figure 7.9) one can see a weak feature in the gradients for Mg_2 and C_24668 at $\sim 4''$ $[\log(r/r_e) \approx -0.1]$ which may be connected to the peculiar core kinematic of the galaxy (peak of the rotation curve at $\sim 3''$, see also Chapter 6). The

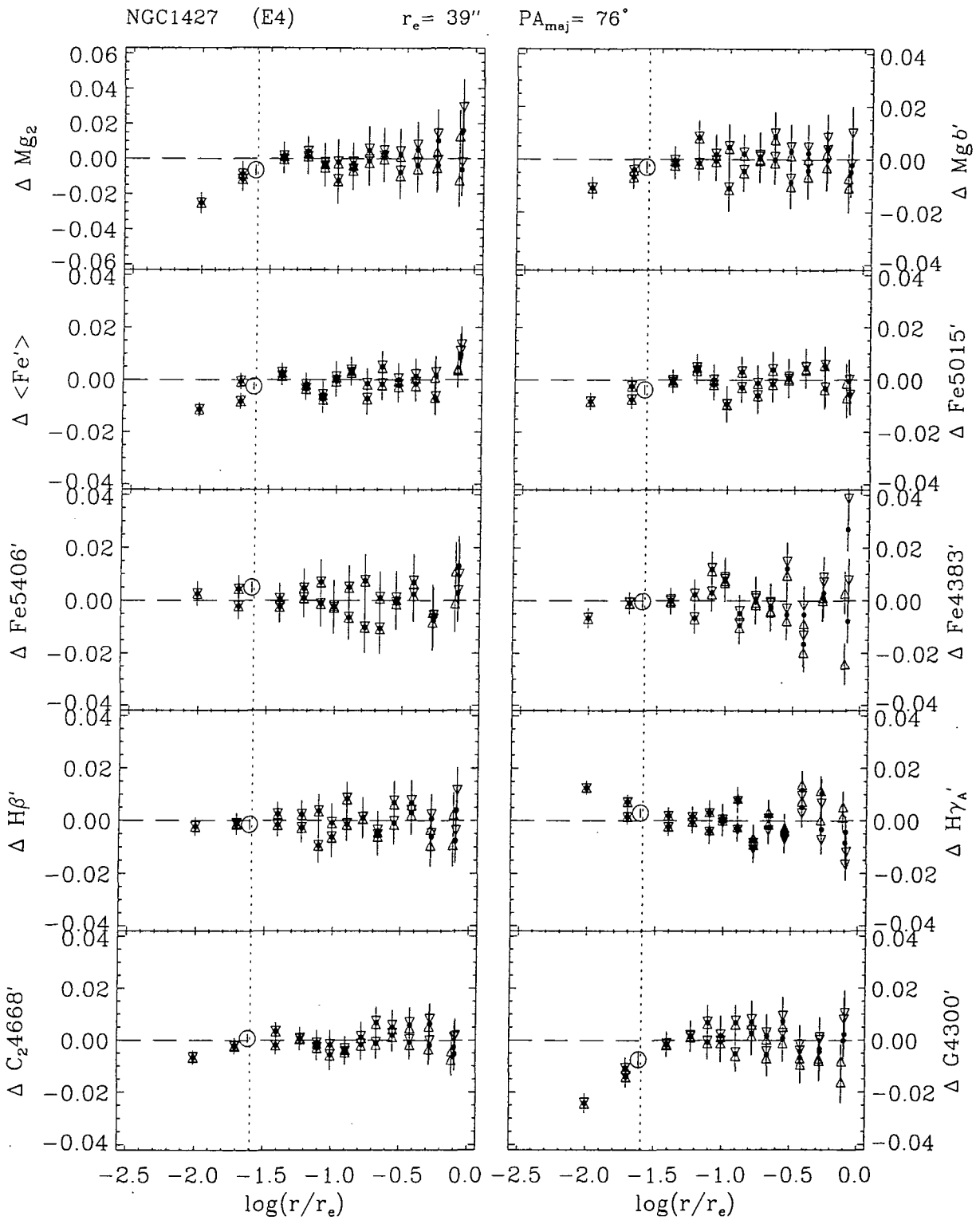

Figure 7.9: Sky subtraction errors for NGC1427: Plotted are the deviations from a fit to a normal data reduction (small filled circles), a data-reduction where we added 5% sky (triangles pointing up) and where we subtracted 5% sky (triangles pointing down). The open circle represents the adopted central index-measurement. All indices are measured in magnitudes.

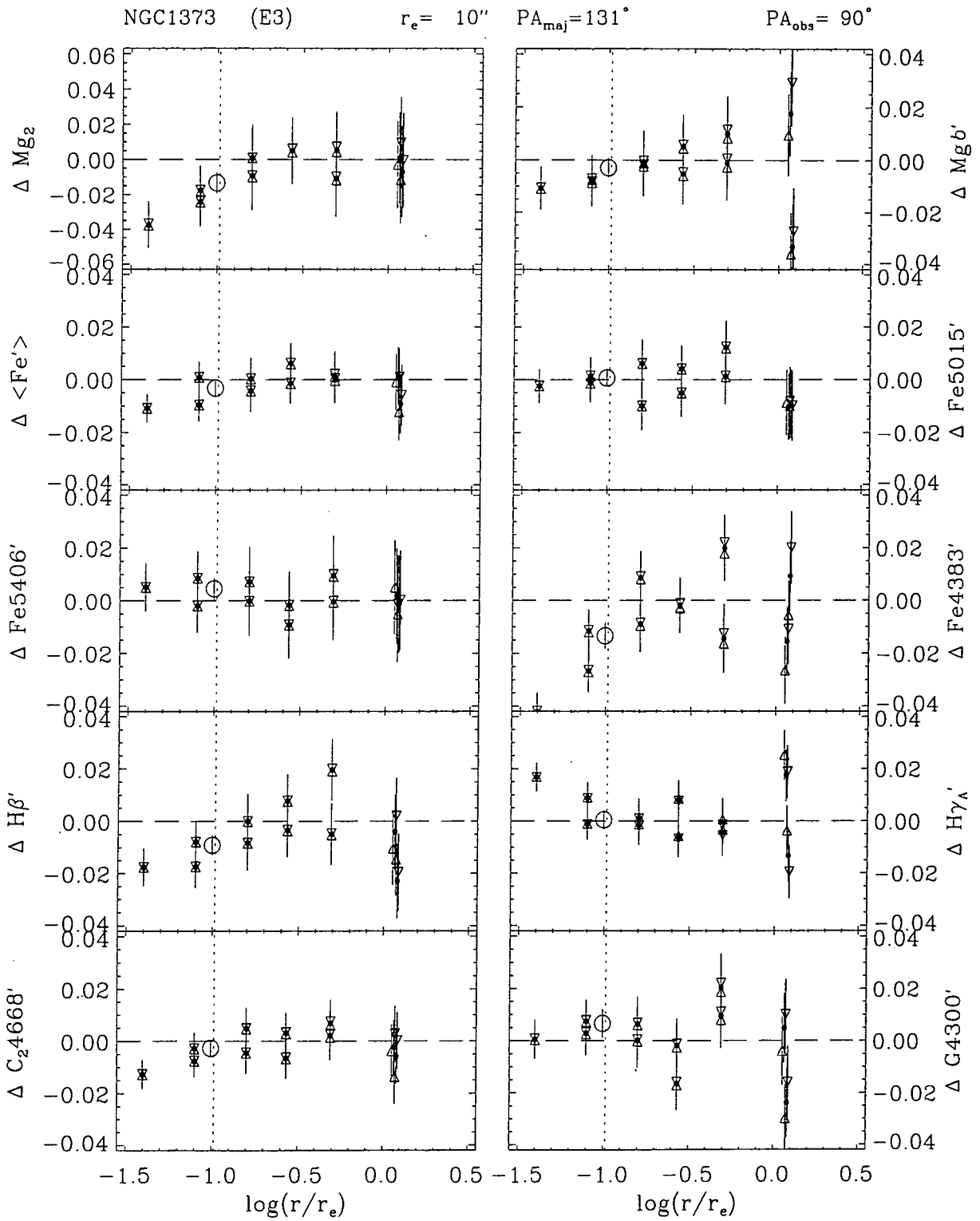

Figure 7.10: Sky subtraction errors for NGC1373: Plotted are the deviations from a fit to a normal data reduction (small filled circles), a data-reduction where we added 5% sky (triangles pointing up) and where we subtracted 5% sky (triangles pointing down). The open circle represents the adopted central index-measurement. All indices are measured in magnitudes.

other indices do not show any obvious signs connected to the kinematically decoupled core (KDC). Overall, perhaps surprisingly, the KDC in NGC1427 is only weakly reflected in the line-strengths measurements indicating that the stellar populations of the KDC and the rest of the galaxy are very similar.

Sky-subtraction errors are only significant in the outer regions and here they still account only for a small fraction of the quoted error bars for each data point. Only the last data bin perhaps shows significant deviations. Overall we conclude that the derived line-strength gradients are only slightly affected by sky-subtraction errors and the leading error in our line-strength gradient analysis will be the varying radial coverage for different galaxies. The associated errors cannot be estimated so we decided to indicate the quality of any derived gradient by symbol size in any further gradient analysis.

To investigate the gradients in more detail we will concentrate on five important indices common to all observing runs[3]: Mg_2, Mgb , <Fe>, $H\beta$ and $H\gamma_A$. For galaxies with multiple exposures we fit a linear function to the *combined* data in much the same way as described earlier on. Note that data taken at different position angles (PA) was scaled to the effective radius at this PA. This approach has been used before for elliptical galaxies (see e.g., Davies et al., 1993) and was found to be useful. For S0s it is somewhat more complicated due to the possible effect of disks. However, as we have observed most of our galaxies at fixed PA, we effectively observe a random slit orientation with respect to the major axis of the galaxy. Hence, we decided to derive an average gradient for S0s as well. In Table 7.2 we present a summary of the derived line-strength gradients.

There is a distinct difference between the gradients for S0s and Es. The metal line gradients (Mg_2, Mgb' , $< Fe' >$) are quite shallow for S0s (see also Table 7.3 for average gradients) whereas the Es show substantial negative gradients. When considering the Es only it is evident that the Mg_2 gradient is stronger than the Mgb' gradient and the $< Fe' >$ gradient. Note that our average Mg_2-gradient for Es (grad $Mg_2 = 0.067 \pm 0.019$) compares well with the mean gradient found by Davies et al. (1993, grad $Mg_2 = 0.059 \pm 0.021$).

For $H\beta'$ the situation is less clear. Both, Es and S0s do not show strong gradients on average. The $H\gamma_A{}'$ index exhibits a completely different behaviour. For Es, $H\gamma_A{}'$ shows a positive gradient whereas the S0s exhibit on average no gradient. However, three galaxies seem to be special: ESO359-G02, ESO358-G25 and NGC1380A. These galaxies have strong *negative* $H\beta'$ gradients, which is even more outstanding when one considers the $H\gamma_A{}'$ index. These three galaxies also show the strongest central Balmer absorption in our sample indicating very young *luminosity weighted* ages. Together with their weak metal line gradients this suggests that these galaxies exhibit a substantial age gradient. We will come back to this in detail in Section 7.5.2 where we analyse age and metallicity gradients.

[3]Here we decided not use Fe3 as metal indicator because for the NTT runs the three individual Fe indices which give the Fe3 index are recorded on different CCDs with distinct spatial pixel sampling.

Table 7.2: Line-Strength Gradients

Name	type	grad Mg_2	grad Mgb'	grad $<Fe'>$	grad $H\beta'$	grad $H\gamma_A'$
N1316	S0	-0.014	-0.013	-0.009	-0.008	0.002
N1375	S0	-0.007	0.002	-0.004	-0.016	-0.016
N1380	S0	-0.054	-0.025	-0.018	0.014	0.029
N1380A	S0	-0.029	-0.007	-0.016	-0.058	-0.076
N1381	S0	-0.021	-0.017	-0.004	0.002	0.011
IC1963	S0	0.007	0.005	0.004	-0.006	0.000
E359-G02	S0	0.003	0.002	-0.006	-0.065	-0.084
E358-G06	S0	0.012	-0.003	-0.004	-0.016	-0.007
E358-G25	S0	0.031	0.023	0.001	-0.028	-0.064
E358-G50	S0	-0.037	-0.006	-0.020	-0.022	0.004
E358-G59	S0	-0.009	-0.020	-0.002	0.003	0.021
N1336	E4	-0.072	-0.067	-0.019	0.003	0.037
N1339	E4	-0.103	-0.061	-0.023	-0.006	0.036
N1351	E5	-0.076	-0.053	-0.015	0.001	0.038
N1373	E3	-0.063	-0.045	-0.026	-0.010	0.057
N1374	E0	-0.091	-0.056	-0.014	0.011	0.033
N1379	E0	-0.053	-0.032	-0.007	0.004	0.029
N1399	E0	-0.046	-0.045	-0.013	0.001	0.025
N1404	E2	-0.039	-0.034	-0.020	-0.003	0.016
N1419	E0	-0.074	-0.054	-0.033	-0.007	0.052
N1427	E4	-0.056	-0.036	-0.017	-0.000	0.032
IC2006	E	-0.066	-0.025	-0.028	-0.004	0.028
N3379	E1	-0.052	-0.036	-0.014	0.007	0.027

The gradients are measured as $\Delta Index$ [mag]/$\Delta log(r/r_e)$.

Table 7.3: Average Line-Strength Gradients

Name	grad Mg_2	grad Mgb'	grad $<Fe'>$	grad $H\beta'$	grad $H\gamma_A'$
Es	-0.067 ± 0.019	-0.046 ± 0.013	-0.020 ± 0.007	-0.001 ± 0.006	$+0.035 \pm 0.012$
S0s	-0.017 ± 0.021	-0.009 ± 0.010	-0.008 ± 0.008	-0.012 ± 0.021	-0.003 ± 0.031

The gradients are measured as $\Delta Index$ [mag]/$\Delta log(r/r_e)$.
Es : all Fornax ellipticals
S0s: all Fornax S0s except E359-G02 & E358-G25

As already mentioned in the introduction to this Chapter there is evidence for a weak correlation of the gradient in Mg-absorption and central Mg-absorption strength in elliptical galaxies (e.g., González and Gorgas, 1996). Such a correlation of line-strength gradients with central parameters can be a useful constraint for galaxy formation scenarios. In Figure 7.11 (column 1) we present a plot of five index-gradients *vs* central line-strengths. Columns 2 & 3 show gradient *vs* gradient relations for our five indices.

In order to decide whether there is a significant correlation present or not we employed a Spearman rank-order test. The adopted null hypothesis is "no correlation". For all correlations with a two-sided significance level of $\leqq 0.01$ we show the Spearman rank correlation coefficient in the title. Two different samples have been considered: (1) all elliptical galaxies and S0s excluding the starburst galaxies (denoted as rs_{all}) and (2) only Es (denoted as rs_{Es}). The symbol size in Figure 7.11 indicates the fraction of the effective radius covered by our data. Small symbols indicate less extended radial coverage and therefore less reliable gradients.

The correlations between the Mg gradients and their central Mg absorption strength are significant but weak and only apparent for the whole sample. We emphasize that the Es on their own would not give evidence for a correlation. Both correlations are consistent with previous work of González and Mehlert. For the $< Fe' >$ index we find no evidence for a correlation. The two Balmer lines show weak correlations which are mainly driven by young galaxies with a central starburst.

Let us now investigate the gradient-gradient relations in columns 2 & 3. First it is reassuring for the quality of our gradients that there is a strong correlation between grad Mg_2 and grad Mgb'. The diagrams in column 2 & 3 are plotted in such a way that the x-axis covers the same range as the y-axis. So one can see that although grad Mg_2 and grad Mgb' correlate well, Mgb' gradients are shallower. This is even more obvious for the $< Fe' >$ gradients when compared to grad Mg_2. We note that the scatter in the grad Mgb' *vs* grad $< Fe' >$ plot is quite large although a significant relation is present.

There is a high degree of correlation between other, perhaps surprising, relations. For example grad Mgb' *vs* grad $H\gamma_A'$. This is a result of the age/metallicity degeneration or in other words, that both indices are influenced by age as well as metallicity. For example if Mgb' shows a steep gradient caused by metallicity, then the $H\gamma_A$ index, which is also sensitive to metallicity, has to show a gradient as well[4]. This works of course only when there are no significant age gradients present. If there are substantial age gradients (as in fact there are for the three star bursting galaxies) then the correlation breaks down. Examining the grad Mgb' *vs* grad $H\gamma_A'$ plot we can identify the three star burst galaxies as being distinct from the general trend. The remaining correlations seen in the gradient-gradient plots can be explained in a similar way.

[4] $H\gamma_A$ is negatively correlated with metallicity, i.e., when metallicity decreases, the value of the $H\gamma_A$ index increases.

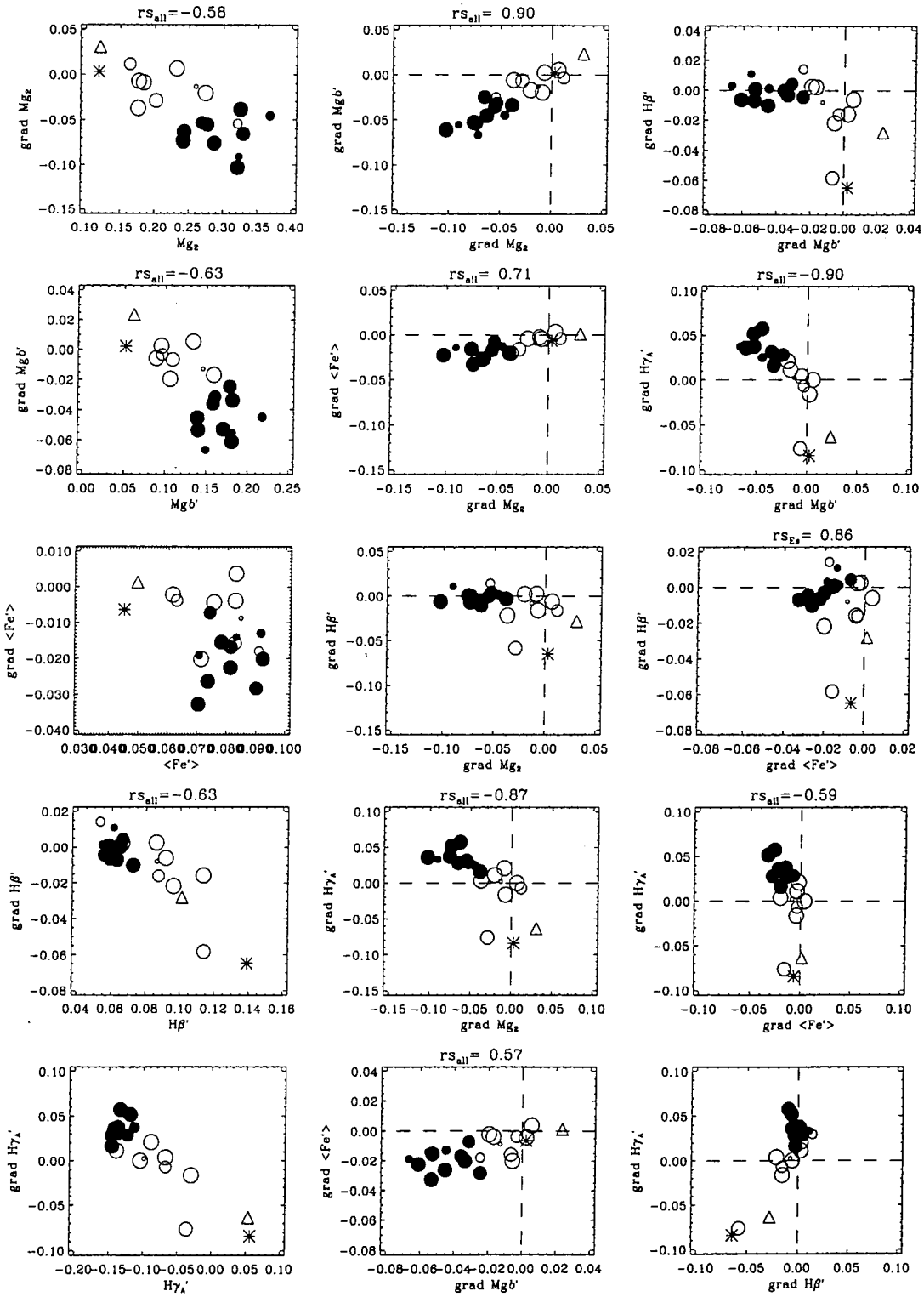

Figure 7.11: Plots of five index gradients *vs* central index-strengths (column 1), and gradient *vs* gradient plots (columns 2 & 3).

In summary, analysing the "pure" line-strength gradients for the Fornax early-type galaxies, the following points should be stressed.

1. We generally find negative metal line-strengths gradients where the S0s have on average shallower gradients. The Hβ' measurements are consistent with no gradient for the majority of the sample. However, the H$\gamma_A{}'$ index shows substantial positive gradients caused by metallicity effects.

2. We identify at least three faint S0-type galaxies with a central starburst on top of an older underlying stellar population.

3. The previously proposed correlation of central Mg-absorption strength with Mg-gradient is also found in the Fornax cluster. We note that this relation is only significant when one examines the whole sample. The Es on their own do not suggest such a correlation.

4. The gradient-gradient plots, such as grad Mgb' *vs* Mg_2, show consistent relations. However, the metal gradients are of different strength. In decreasing order: grad Mg_2, grad Mgb' and grad $< Fe' >$.

7.5.2 Age and Metallicity Gradients

In the previous Section we investigated the "pure" index-gradients, now we aim to transform index-gradients into more physical age and metallicity gradients with the help of model predictions. This is done in much the same way as discussed in Chapter 4 for the central index measurements. In fact we can use all the results from the central line-strength analysis and apply them to the gradients. In the following plots we present the radial line-strength measurements of each galaxy in a separate index-index diagram and overplot model predictions by Worthey (1994). In order to increase the S/N ratio we average the measurements of both sides of a galaxy at similar radius; different observing runs are overplotted rather than averaged.

Several index combinations seem to be interesting but for presentation purposes we have restricted ourselves to three combinations: (1) [MgFe] *vs* Hβ, (2) Fe3 *vs* Hγ_A and (3) Mgb *vs* Fe3. Note that for the Fe3-index from the NTT runs we had to average three Fe indices recorded on different CCDs with different pixel sampling. The average was taken at similar radius which is sufficient for the following analysis. The diagrams allow us to investigate the age/metallicity distribution in the way used by González , i.e., Hβ *vs* [MgFe] and with our new indicators Hγ_A and Fe3. Finally we can look into the radial dependence of the Mg-overabundance with the help of the last index-combination. For each index combination we present the Fornax S0s on one page and the Fornax ellipticals and NGC3379 on the following page.

In Figure 7.12 we present the data for our S0s in the first age/metallicity diagnostic diagram ([MgFe] *vs* Hβ). Note that the symbol size indicates the distance from the centre of a galaxy: the smaller the symbol the further away from the centre.

In Chapter 4 we concluded that the S0 galaxies NGC1380 and NGC1381 have old central stellar populations whereas the other S0s showed on average much younger luminosity weighted ages in the centre. Analysing Figure 7.12 we see that for NGC1380 and NGC1381 not only do the centres harbour an old stellar populations but also the regions further out are consistent with an old stellar population. Remarkably, the range in metallicity covered by NGC1381 is very narrow, yet the data covers more than one effective radius. We ascribe this to the fact that we present here the major axis line-strength measurements of NGC1381. Note that we will analyse NGC1381 in more detail in Section 7.5.3. In contrast, NGC1380 spans a substantial range in metallicity. For this exposure the slit was roughly aligned with the minor axis, so effectively we present line-strength measurements of the bulge component of NGC1380.

For NGC1316 the line-strength gradients suggest that the age stays roughly constant with radius whereas the metallicity decreases. However, we note that the radial extent of our data is small and we cannot draw any secure conclusions. The galaxy ESO358-G59 shows relatively strong Hβ absorption which is roughly constant with radius. However, as already pointed out in the previous Section some S0s show a totally different behaviour. The galaxies with the strongest central Hβ absorption, i.e., the youngest stellar populations, show steep gradients in age and almost no gradient in metallicity. We interpret this as strong evidence that these galaxies experienced only a *central* starburst but have an underlying, older stellar population.

To give the reader an impression of the morphology of these galaxies we present in Figure 7.16 DSS-images (size: $2' \times 2'$) of the 11 S0 galaxies in our sample. Note that IC1963, NGC1380A and NGC1381 have quite extended disks whereas the other galaxies show only a spheroidal[5] structure.

The young, spheroidal S0s in our sample (NGC1375, ESO359-G02 and ESO358-G25) fit in remarkably with the predictions of galaxy harassment in clusters (Moore et al., 1998; Lake et al., 1998). In this scenario medium sized disk galaxies (Sc-type) fall into a cluster environment and get "harassed" by high speed encounters with cluster galaxies. The end-products are spheroidal galaxies where some gas of the disk is driven into the centre of the galaxy. This gas is likely to be turned into stars in a central stellar burst which would explain why our spheroidal galaxies have younger stellar populations in the centre. We note, that these young galaxies are in the periphery of the Fornax cluster indicating that they may have been "accreted" onto the cluster from the field.

Two of the young S0s which show young populations in the centre, also have extended

[5]Here the term "spheroidal" is used for S0-type galaxies which do not show a prominent disk.

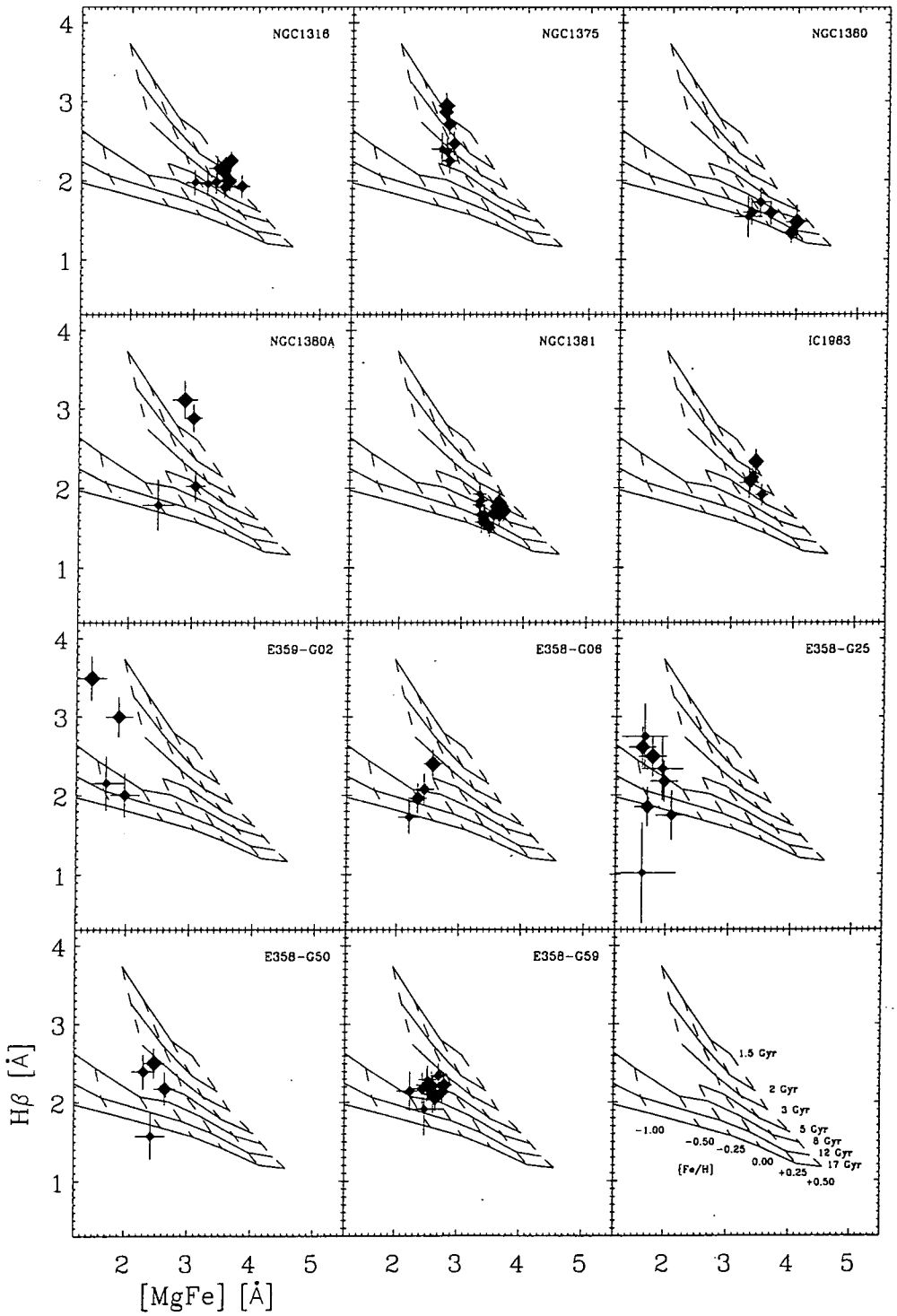

Figure 7.12: [MgFe] *vs* Hβ diagram for Fornax S0s. The size of the symbols is inversely scaled with radius. The galaxy names are given in the upper right corner of each panel. A guide plot is given in the lower right corner where lines corresponding to particular ages and metallicities are labelled. Note the large age-gradients for NGC1380A, ESO359-G02 and ESO358-G25.

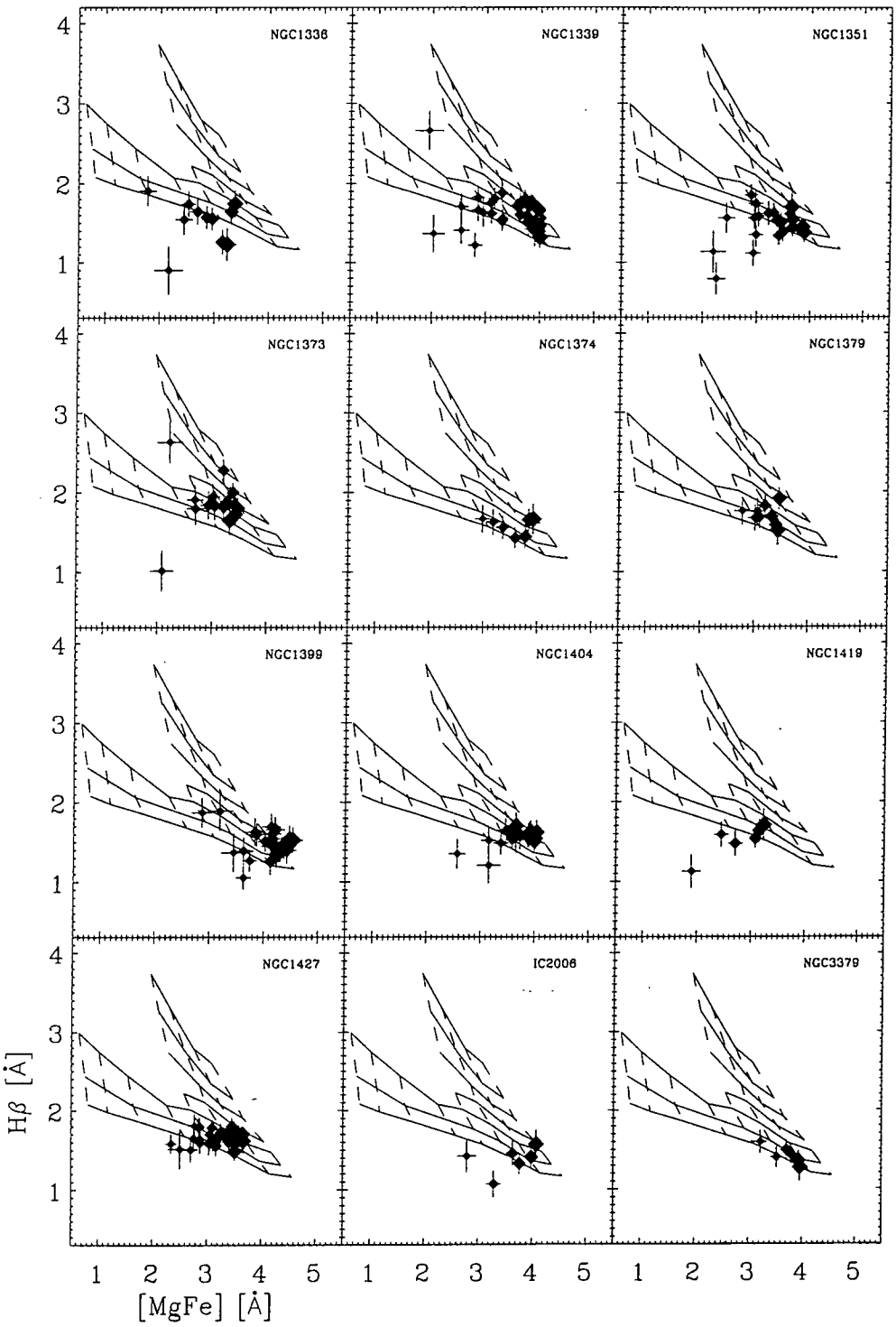

Figure 7.13: [MgFe] *vs* Hβ diagram for Fornax Es and NGC3379. The size of the symbols is inversely scaled with radius. The galaxy names are given in the upper right corner of each panel.

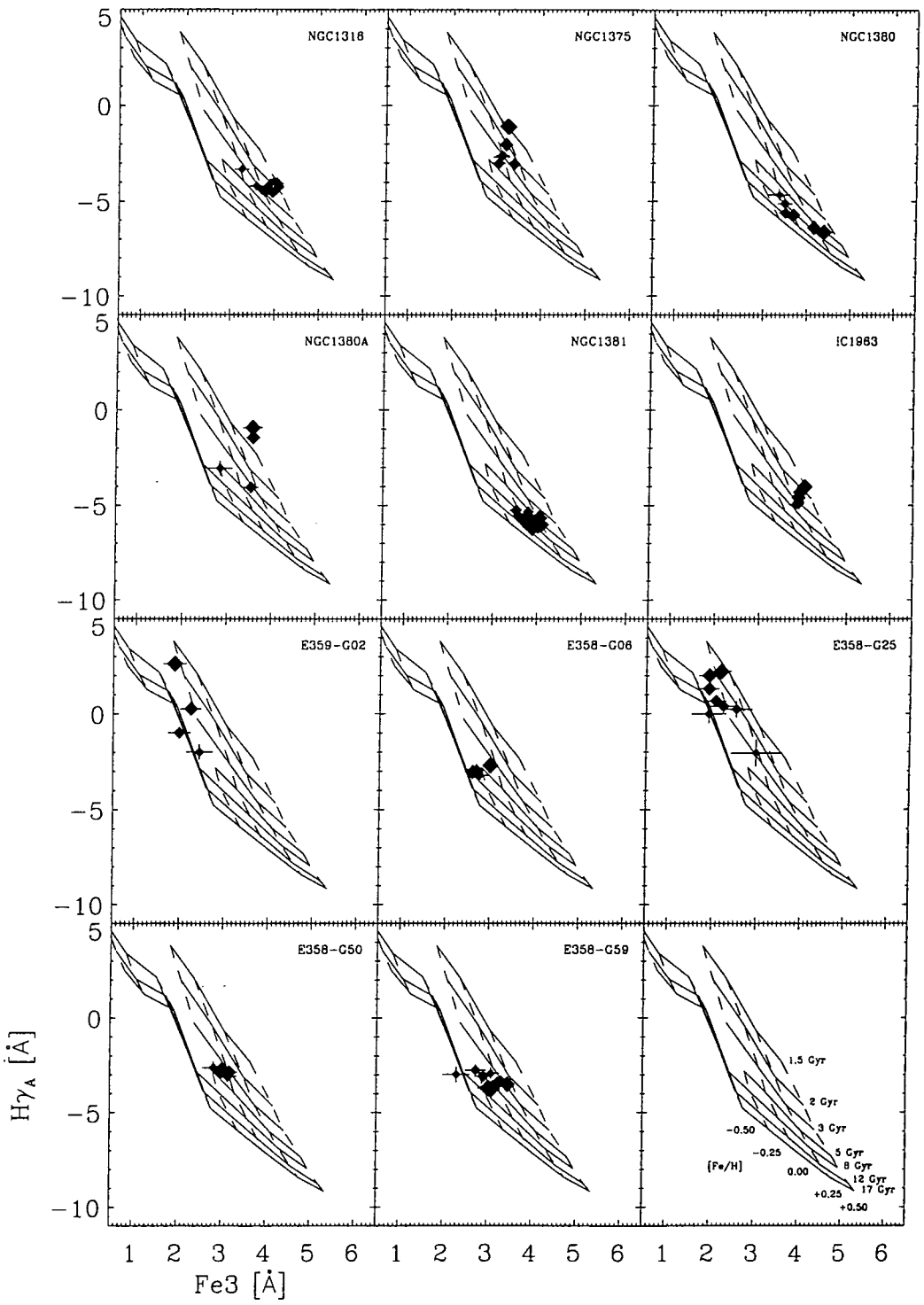

Figure 7.14: Fe3 *vs* Hγ_A diagram for Fornax S0s. The size of the symbols is inversely scaled with radius. The galaxy names are given in the upper right corner of each panel. A guide plot is given in the lower right corner where lines corresponding to particular ages and metallicities are labelled.

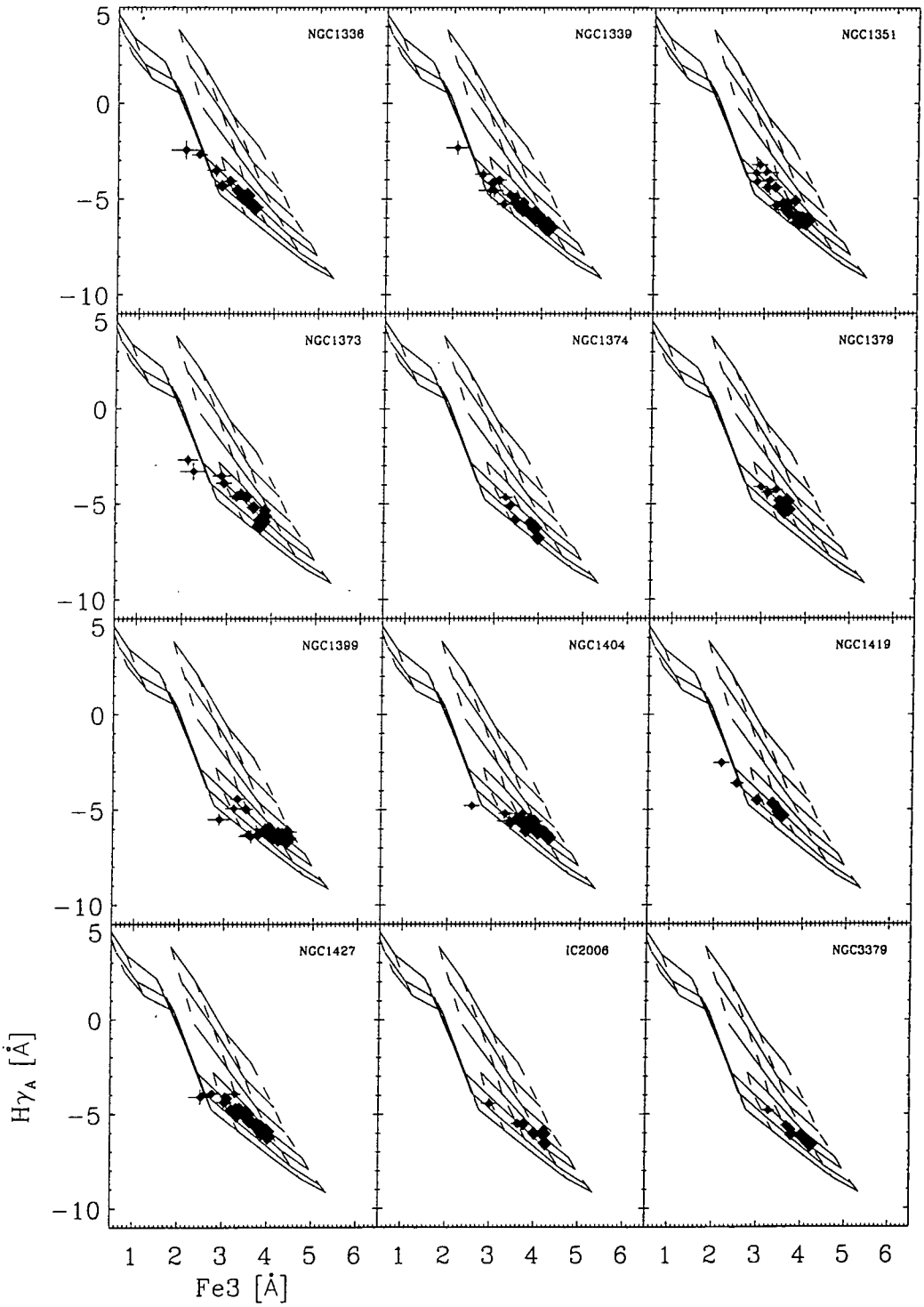

Figure 7.15: Fe3 *vs* $H\gamma_A$ diagram for Fornax Es and NGC3379. The size of the symbols is inversely scaled with radius. The galaxy names are given in the upper right corner of each panel.

disks (NGC1380A and IC1963). This seems to be in contradiction with the harassment picture. However we emphasize, that the existing harassment simulations do not include spirals with a substantial bulge component. Here the bulge is likely to stabilize the disk and the end-products may be able to keep substantial disk components (Ben Moore, private communication).

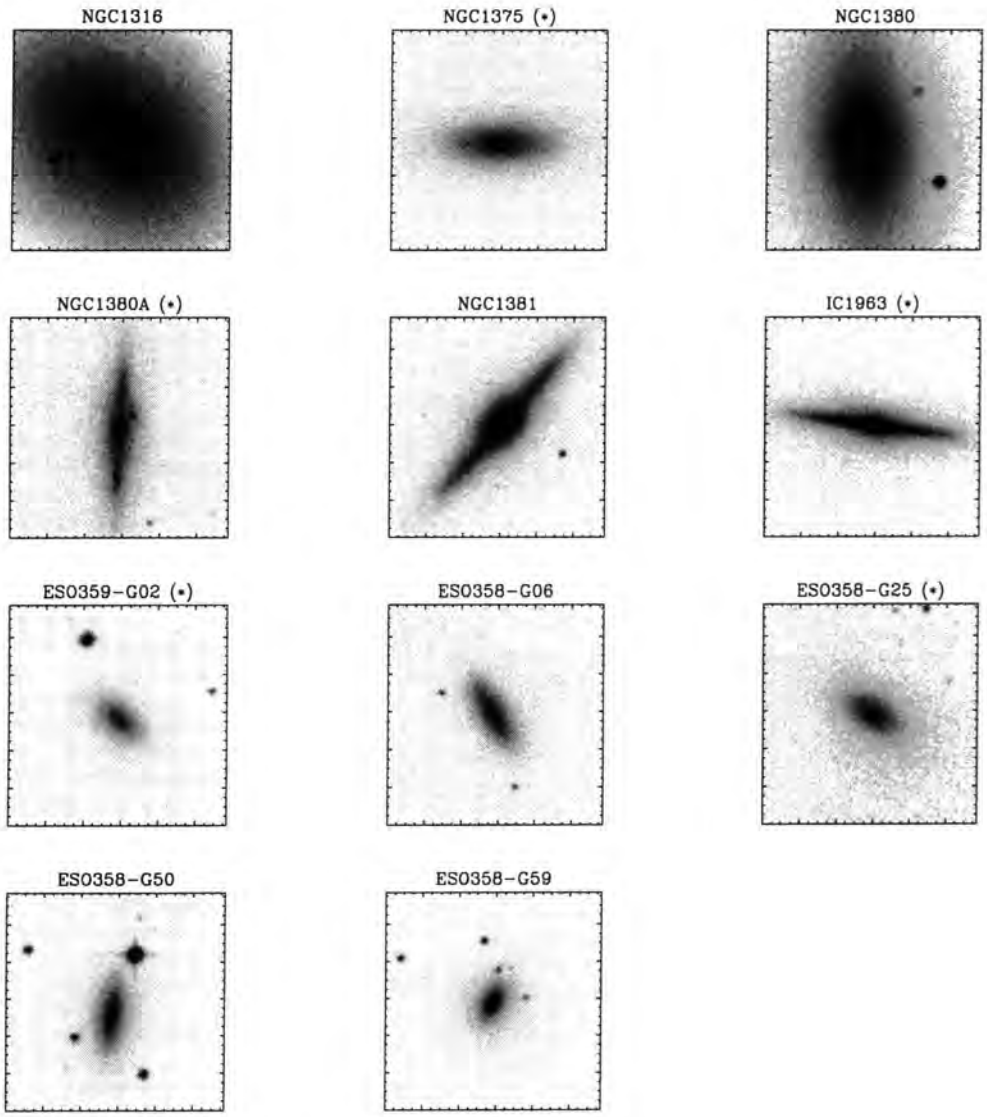

Figure 7.16: Digital Sky Survey images of the S0s in our sample. Galaxy names are noted on top of each panel. The images are $2' \times 2'$ in size, north is up and east to the left. The slit of the AAT96 run was fixed at PA = 90° which corresponds to the horizontal direction in these images. The galaxies with a star (*) behind the name show clear signs of a central starburst on top of an underlying older stellar population.

We concluded from the analysis of the central line-strength indices that none of the elliptical galaxies show signs of young central stellar populations, in fact they seem to be roughly coeval. Does this result hold when one takes the whole galaxy into account?

In Figure 7.13 we present Hβ-[MgFe] diagrams for the 11 Fornax Es and NGC3379. All of the Es show significant decreasing metallicity with radius. The scatter in Hβ is quite large so it is difficult to derive age gradients. However, some galaxies show, at least if one trusts the outermost data points, negative age gradients, i.e., galaxies are younger in the centre. This is consistent with the findings for Coma early-type galaxies analysed by Mehlert (1998) who used the same age/metallicity diagnostic diagram. Note that the data for the S0 galaxy NGC1380 (minor axis) looks rather like the data for the Es. This suggests that the bulge of NGC1380 has similar properties as the Es.

As discussed in Chapter 4, Hβ absorption can be filled in by nebular emission and is in general a weak and therefore difficult to measure absorption line. This introduces some uncertainties into the line-strengths and therefore age gradients. We have already suggested that Hγ_A is a much better age indicator in this respect and therefore we will re-analyse our sample in a second age/metallicity diagram with Hγ_A as age indicator and Fe3 as metal indicator. The plots for S0s and Es are presented in Figure 7.14 and 7.15 respectively.

In these new age/metallicity diagnostic diagrams, the scatter is reduced and age, metallicity trends are more obvious. Clearly the S0 galaxies, NGC1375, NGC1380A, IC1963, E359-G02 and ESO358-G25 show *central* young stellar population whereas the outer regions of these galaxies are older. Again metallicity gradients are not significant within those galaxies but differ substantially within the sample. Generally the new diagrams suggest similar age and metallicity gradients as seen in the Hβ-[MgFe] plots.

In the case of the elliptical galaxies, we find that all Es show decreasing metallicity gradients and are consistent with a coeval stellar population within one galaxy. Of course our sensitivity to age gradients is limited and it would be better to say that the Es show no age gradients greater than approximately $\pm$2 Gyrs for a central population of $\sim$8 Gyrs. For the outermost data points we found, for some Es, extremely low Hβ absorption, this is not reflected in the Hγ_A index. Comparing with the model predictions the two indices suggest quite different ages at large radii. However, it is possible that the Hβ index is affected by emission at these large radii.

The metallicity gradients seen in the Fe3 *vs* Hγ_A diagram seem to be quite strong, but exactly how strong are they? Can we draw any conclusions about the total metal content of Es? These questions become very important in the analysis of e.g., the Mg–σ relation, the colour magnitude diagram and the fundamental plane of elliptical galaxies. Former relations are usually tight and therefore widely used to constrain e.g., metallicity variations among Es (Colless et al., 1998). Yet they often relate global parameters, such as the effective surface brightness, with local parameters, such as the central velocity dispersion. After combining local with global parameters it is not at all clear why these relations are so tight.

In the forthcoming analysis we restrict our sample to the elliptical galaxies with old

stellar populations and assume that they have a mean luminosity weighted age of 8 Gyrs and no age gradient with radius. This means that there is a unique relation between a given index-strength and the inferred metallicity ([Fe/H]) using the models by Worthey. The thick solid lines in Figure 7.17 represent such calibrations. The filled circles on these lines show the position of the central stellar populations of Fornax ellipticals (index-values are taken from Chapter 4) when adopting the former calibration. We find a range in [Fe/H] from -0.2 dex to +0.2 dex and 0.0 dex to 0.5 dex for $< Fe' >$ and [MgFe'] , respectively. The difference in absolute terms is caused by the Mg-overabundance. Furthermore, the relative metallicity distribution is slightly more extended for the [MgFe'] calibration. This is consistent with an increasing [Mg/Fe] abundance ratio with galaxy mass.

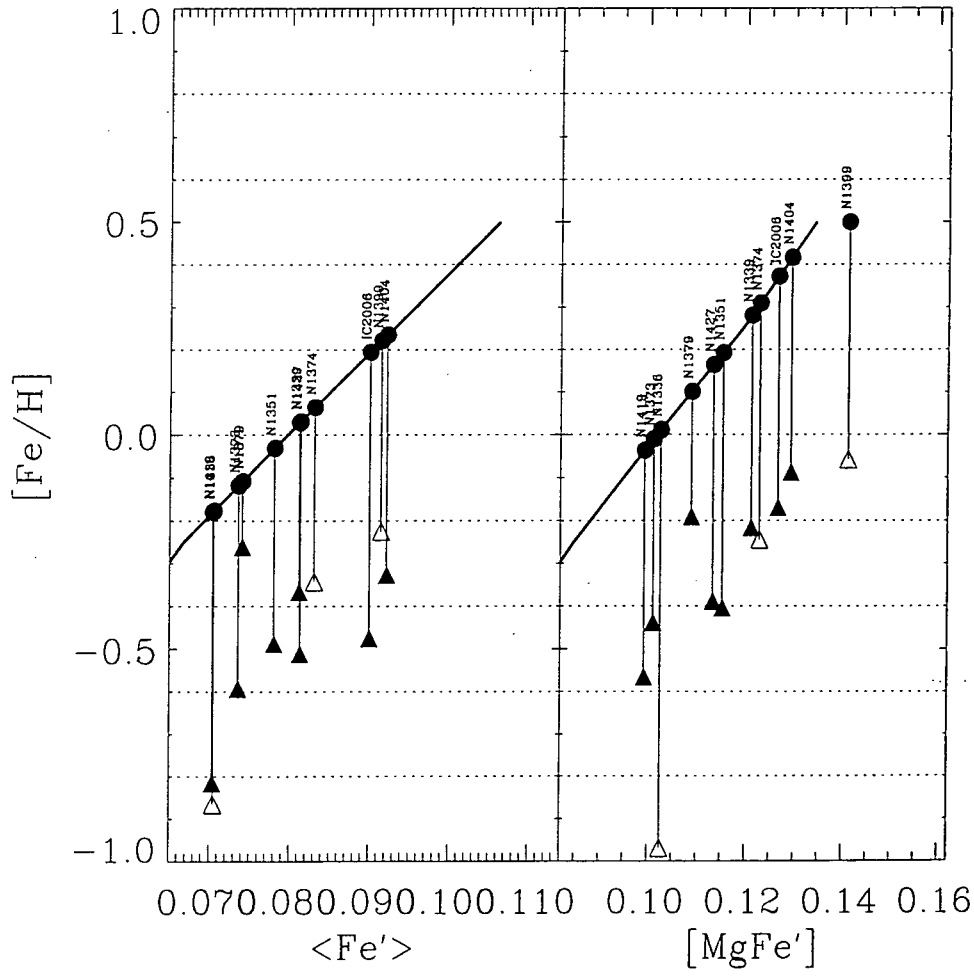

Figure 7.17: Two different metallicity calibrations are shown. The thick solid lines represent the predicted relation (Worthey, 1994) between [MgFe'] and $< Fe' >$ with [Fe/H] under the assumption that all galaxies are roughly 8 Gyrs old. The central line-strength of Es and S0s are represented by filled circles. The triangles indicate the metallicity at 1 r_e for each galaxy. The galaxy NGC1399 showed central [MgFe] values larger than the model predictions; we set it therefore equal to [Fe/H]=0.5. For a discussion of the diagram see text.

In order to show the strength of the metallicity gradient in each galaxy we take the $< Fe' >$ and [MgFe'] values at one effective radius and convert them into a [Fe/H] estimate via former calibrations. Note that for some galaxies we do not actually measure the $< Fe' >$ or [MgFe'] values at 1 r_e but we extrapolate with the help of the gradients summarized in Table 7.2. We then indicate the strength of the metallicity gradient in Figure 7.17 by drawing a vertical line such that the triangle at the end reflects the metallicity at 1 r_e. Note that the position of the triangles represents only the metallicity in terms of [Fe/H] and does not correlate with the $< Fe' >$ or [MgFe'] values shown on the x-axis. Open triangles indicate rather uncertain extrapolations.

All elliptical galaxies with the exception of NGC1379 show a 0.3-0.4 dex decrease in metallicity within 1 r_e. Arimoto et al. (1997) pointed out that there is a simple connection between the metallicity of an elliptical galaxy at 1 r_e and its total metallicity. Assuming that the surface brightness distribution of an elliptical can be described by an $r^{1/4}$–law and that the stellar mass to light ratio is constant throughout a galaxy then it follows, that the mean luminosity-weighted iron abundance of stars is to a good approximation given by the value measured at the effective radius.

Figure 7.17 shows that the metallicity sequence is still roughly preserved at an effective radius but the scatter is bigger. The *total* metallicity estimates from the previous analysis are remarkably low: [Fe/H] = -0.7 to -0.2 and -0.6 to 0.0 for $< Fe' >$ and [MgFe'] , respectively. In summary, this means that most of the *central* metallicity estimates are a good indication of the total metallicity in an elliptical galaxy when they are reduced by $\sim$ 0.4 dex. Note that there seem to be exceptions such as NGC1379 which have a much higher total metallicity than the central value would suggest.

Another method to determine metallicity gradients makes use of the measured index gradients itself and a model calibration of index gradients against predicted metallicity gradients at a given age. Here we fitted a polynomial of second order to the index–[Fe/H] relation (at 8 Gyrs) given by the models. We then used the index-gradients for each elliptical galaxy given in Table 7.2 on page 159 and determined the corresponding gradient in [Fe/H]. The analysis was performed for the following indices: Mg_2, Mgb' , $< Fe' >$ and [MgFe'] . Table 7.4 summarizes the results.

Note that although the index gradients are quite different, all indices indicate roughly the same decrease of 0.4 dex in [Fe/H]. This method uses only the predicted slope in the change of [Fe/H] with index and is therefore not very sensitive to the age calibration.

For our analysis so far we have intrinsically assumed that the [Mg/Fe] ratio is constant with radius. Indeed, previous work such as González (1993) suggested that the Mg-overabundance, although quite different from galaxy to galaxy, varies only little within a galaxy. With our last diagnostic index-diagram we will investigate now whether [Mg/Fe] ratios are constant with radius for our sample. Similar to Chapter 4 we use a Fe3 *vs* Mg*b* diagram for each galaxy to probe the [Mg/Fe] abundance ratios. See Figure 7.18 and 7.19

Table 7.4: Average [Fe/H] Gradients for Es

Index	Mg_2	Mgb'	$< Fe' >$	[MgFe']
grad	-0.38 ± 0.11	-0.52 ± 0.18	-0.43 ± 0.19	-0.48 ± 0.15

The gradients are measured as Δ[Fe/H]/$\Delta log(r/r_e)$.
The index used in the analysis is given in the first row.

for plots of S0s and Es respectively.

The S0s, with the exception of NGC1380 and NGC1381, are consistent with solar abundance ratios at all radii probed by our data. NGC1380 shows a Mg overabundance constant with radius. The situation is less clear for NGC1381, however, and we will analyse this galaxy in detail in the next section. For the elliptical galaxies we find a different picture. Some galaxies (e.g., NGC1373, NGC1427) show constant Mg to Fe ratios with radius, but others (e.g., NGC1339, NGC1351, NGC1379) seem to approach solar ratios at the largest radii ($\simeq$ 1 r_e) probed by our data. Overall the changes are rather small and show that the *central* [Mg/Fe] ratio is a good indication for the whole galaxy.

Very recently Thomas et al. (1998b) explored the formation of metal rich and Mg-overabundant stellar populations in the light of two extreme galaxy formation scenarios: (1) a fast clumpy collapse and (2) the merger of two spirals. They predict for the first formation scenario that [Mg/Fe] ratios should increase with radius, i.e., metal poorer stars are more overabundant, similar to our own galaxy. Yet for the spiral-merger scenario they predict stars with solar abundance ratios in the outer parts. None of the two scenarios is consistent with our result, i.e., roughly constant Mg-overabundance with radius. However, we note that our data does not extend to more than $\sim 1 r_e$ and it is possible that at larger radii the Mg abundance ratio approaches solar values.

The results by Thomas et al. offer a very interesting test for formation scenarios where line-strength gradients can be of help. However, the models as well as the observations involve very complicated and perhaps not yet fully understood transformations. We believe that the models as well as the observations have to be substantially improved before one can rule out certain formation scenarios.

7.5.3 The S0 Galaxy NGC1381: When and How was the Disk Formed?

In this Section we will investigate in detail the stellar populations of the S0 galaxy NGC1381 as a function of radius. This is an interesting point because the centres of our two old S0 galaxies seem to follow the relations of elliptical galaxies rather well. However, as we will show for NGC1381, if one takes the whole galaxy into account then the disk causes the galaxy to deviate from the elliptical sequence.

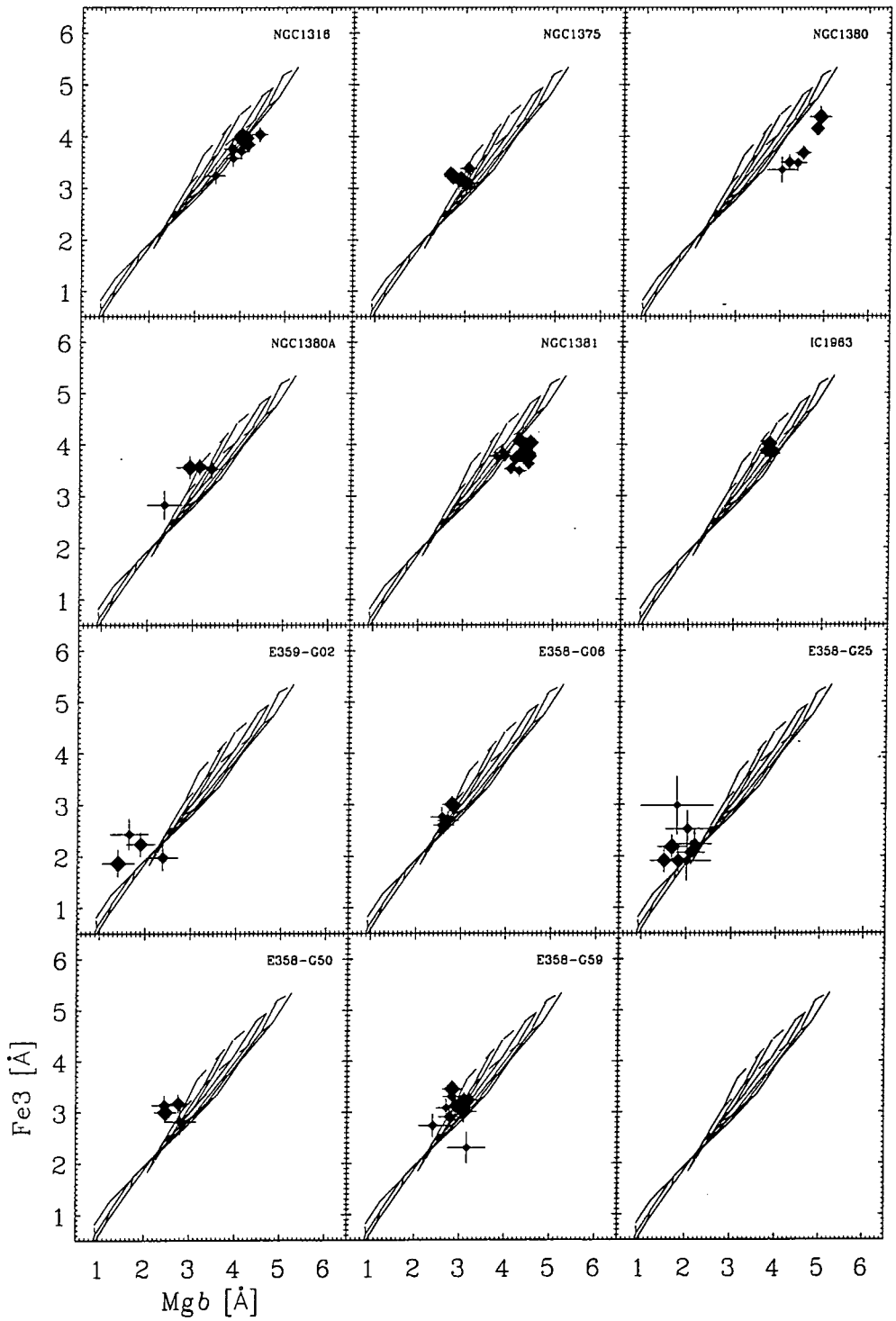

Figure 7.18: Mg*b* *vs* Fe3 diagram for Fornax S0s. The size of the symbols is inversely scaled with radius. The galaxy names are given in the upper right corner of each panel.

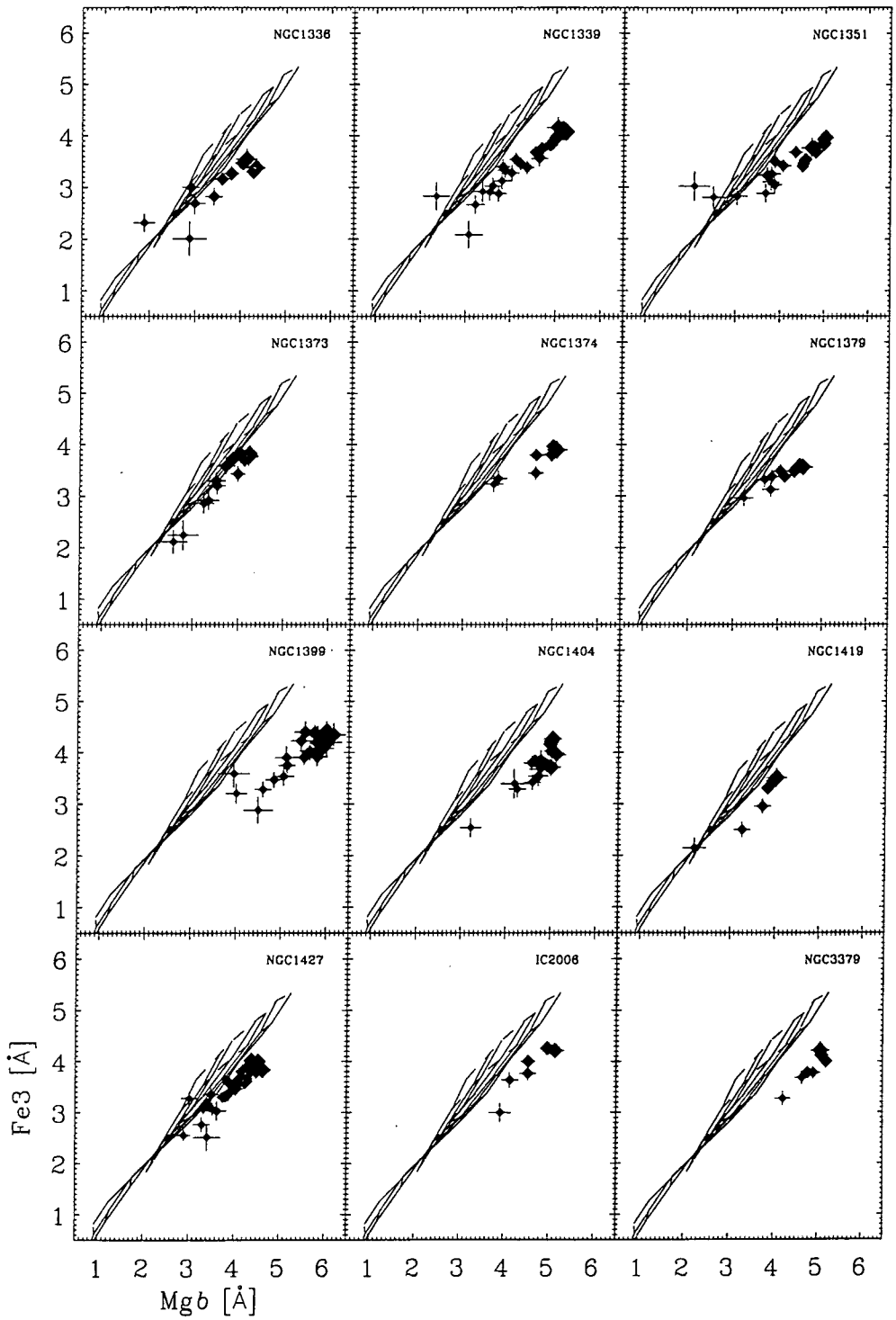

Figure 7.19: Mg*b* *vs* Fe3 diagram for Fornax Es and NGC3379. The size of the symbols is inversely scaled with radius. The galaxy names are given in the upper right corner of each panel.

For NGC1381 we obtained three deep long-slit exposures: major axis, minor axis and an exposure offset by $\sim 8''$ parallel to the minor axis so that the slit cut through the bright star to the south-west of the galaxy centre. To illustrate the morphology of NGC1381 we present a Digital Sky Survey (DSS) image in Figure 7.20. The outermost line-strength measurement of the major axis exposure is located at $32''$ from the centre which is equivalent to $1.5 \times r_e$. For the minor axis we reach $\sim 4''$ which is equivalent to $0.5\ r_e$. The offset exposure extends to about $12''$.

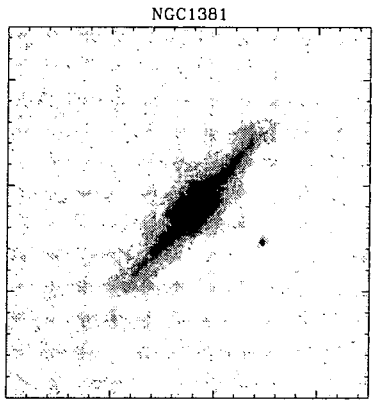

Figure 7.20: An image of NGC1381 taken from Digital Sky Survey (DSS). The size of the image is $3' \times 3'$. North is up and east is to the left.

In order to analyse the stellar populations we will employ again our age/metallicity diagnostic diagrams. First of all we present in Figure 7.21 a plot of $H\gamma_A$ *vs* Fe3 with each observed axis in a separate panel. Note that both galaxy sides have been averaged at similar radii to increase the S/N. The most striking feature is that although our major axis data covers more than one effective radius we see neither a significant age- nor a significant metallicity gradient. Yet both the minor axis and the offset exposure show metallicity gradients with no obvious age gradient. We emphasize that for the major axis the data are dominated by the bulge at small radii and by the disk at large radii and therefore the disk must have formed roughly at the same time as the bulge. The line-strength analysis of the major axis of NGC1381 is in strong contrast to the behaviour of an average elliptical galaxy, where we expect to see metal gradients in the order of 0.4 dex in [Fe/H]. As previously suggested, we believe that the disk in NGC1381 is responsible for the high metal content at large radii.

The line-strength gradients of the minor axis are consistent with the result for NGC1380 where we also found a substantial metal gradient for the bulge component. In summary we find that the whole galaxy, or at least for the parts of the galaxy where we probe the stellar content with our observations, contains an old stellar population.

How can we reconcile the high metal content in the disk of NGC1381 with our estimate

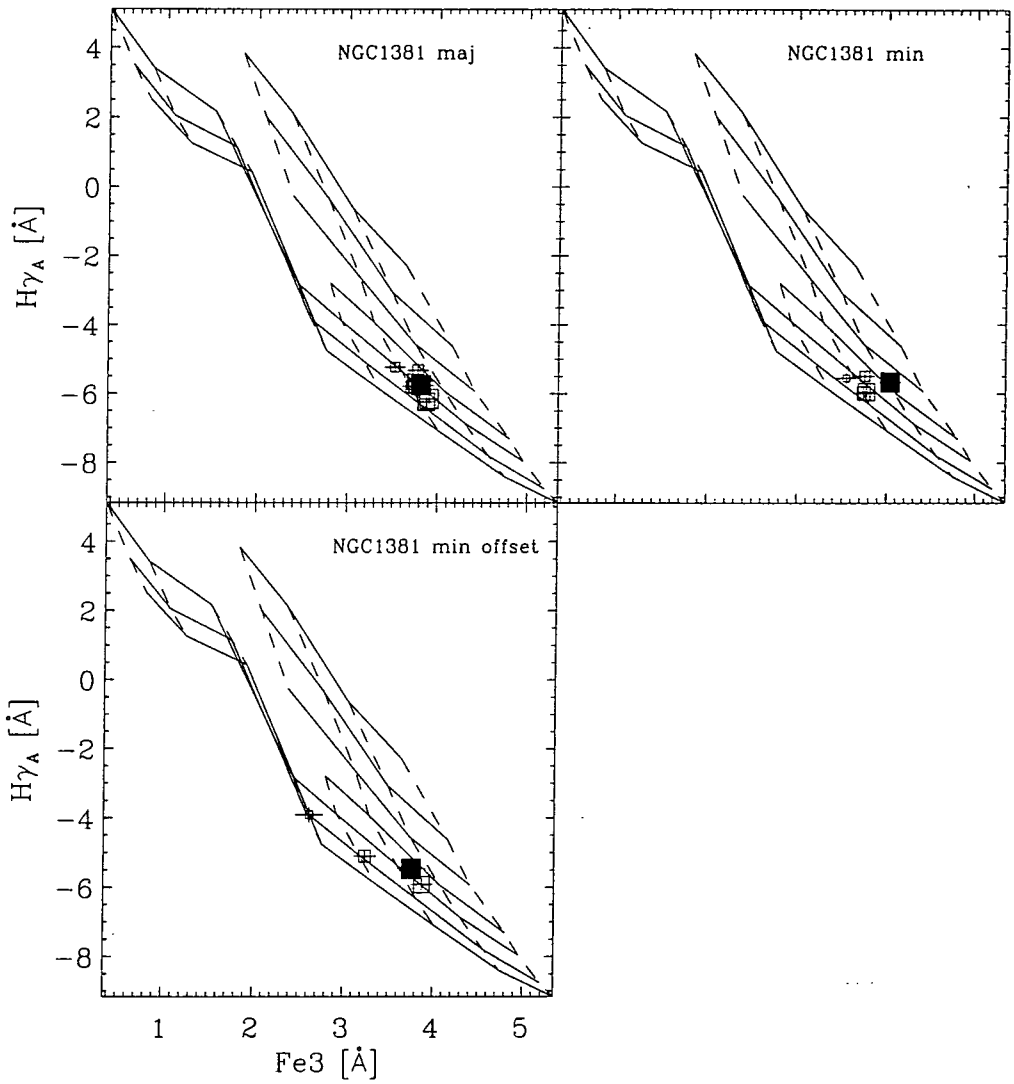

Figure 7.21: NGC1381: Line-strength gradients for three slit positions are shown in an age/metallicity diagnostic diagram. The data from the central slit position is indicated by the filled square. Note that for major and minor axis this is the galaxy centre, but for the offset axis this corresponds to a point $\sim 8''$ away from the galaxy centre along the major axis. The data from both sides of the central slit position have been averaged at similar radii (open symbols). Symbol size is inversely scaled with radius. Overplotted are models by Worthey.

of equal age for the disk and the bulge component? Before we can answer this question let us investigate another index-index diagram. Figure 7.22 shows a plot of the Mgb -index against the Fe3-index. This is our standard way to explore any [Mg/Fe] variations.

The major axis shows an extremely unusual behaviour. Although we did not find any metallicity gradient for it, we find a strong dependence of the [Mg/Fe] ratio with position along the major axis. In fact the bulge and the first part of the disk of NGC1381 seem to be overabundant by approximately 0.2 dex. However, further out the trend changes clearly towards solar abundance ratios. For the other two exposures (minor axis and offset) we see a roughly constant [Mg/Fe] ratio with radius. Note that this result is independent of the exact index combination which we use, i.e., the analysis of a Mg_2 *vs* $< Fe' >$ diagram would give the same result.

We interpret the former finding as strong evidence that the disk has experienced a somewhat more extended star-formation history of the bulge, thus building up a Fe content that approaches solar abundance ratios **and** also solar metallicity. This explains why we do not find a significant metal gradient along the major axis. The important caveat to this model is that we do not see any age upturn for the disk as the $H\gamma_A$ indicator should show if present.

We believe the solution for this inconsistency lies in the exact time scales which are involved in the star-formation process. For example if the bulge stopped forming stars $\sim$1 Gyr after the initial burst and the disk continued to form stars for only 1-2 Gyrs longer then this would be very hard to detect in the present age/metallicity diagrams. However, it would probably be long enough to account for the observed metal content.

In conclusion, we have found evidence that in the S0s galaxy NGC1381 the disk formed in a somewhat more extended fashion then the bulge and has therefore roughly solar abundance ratios and solar metallicity. The bulge component of NGC1381 resembles the properties of Es very well, that is [Mg/Fe]>0.0 and also shows a decreasing metallicity gradient. A further analysis of the exact formation process would need more careful modeling involving photometry which is beyond the scope of this thesis.

Finally we would like to present an interesting way of showing the effects of non solar abundance ratios. We concluded in the previous paragraph that NGC1381 (major axis) shows an abundance ratio which varies from [Mg/Fe] $\simeq$ 0.2 in the centre to solar abundance ratios further out. This gives us the unique possibility to show how these changes are recorded in certain indices and then compare with the (solar abundance ratio) stellar population models.

In Figure 7.23 we presents such a diagram. Here we investigate the effects of non-solar abundance ratios on Mgb and Mg_2. As can be seen from the plot, the relation set by the data substantially deviates from the model predictions in the centre of the galaxy. We conclude that even in a diagram of two Lick/IDS Mg-indices the effects of varying [Mg/Fe]

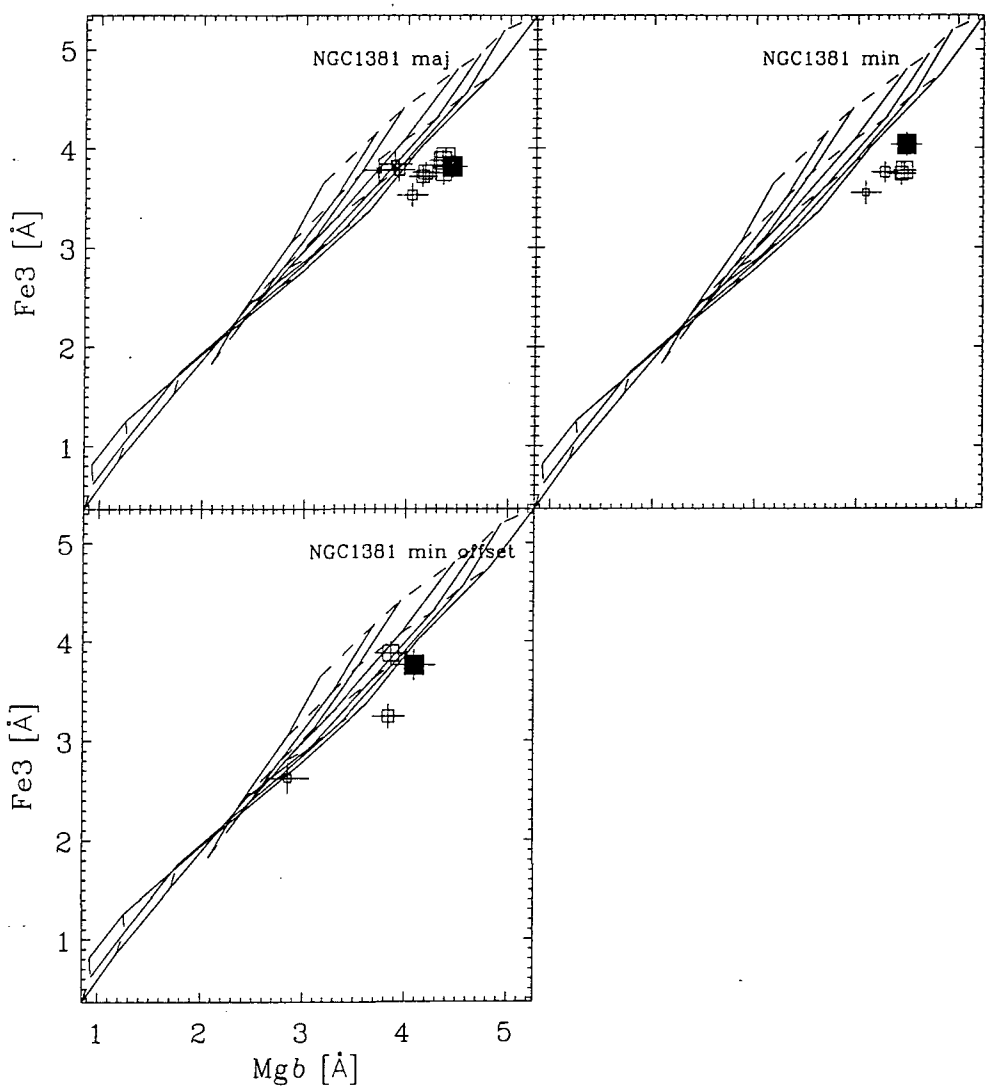

Figure 7.22: NGC1381: Line-strength gradients for three slit positions are shown in [Mg/Fe]-ratio diagnostic diagram. The centre of each extraction is indicated by the filled symbol. Both sides of the galaxy have been averaged at similar radius (open symbols). Symbol size is inversely scaled with radius. Overplotted are models by Worthey.

ratio are visible.

The reader may recognize this plot from Section 3.4 (Figure 3.6 on page 48) where we showed the central line-strength measurements for the Fornax sample in the same diagram. We can now speculate that the offset between the model predictions and the data in this diagram is caused by a Mg-overabundance in luminous Es. Note that smaller Es tend to agree with the model tracks which would then suggest that they have solar abundance ratios. This is again further evidence for a [Mg/Fe] ratio that increases with galaxy mass.

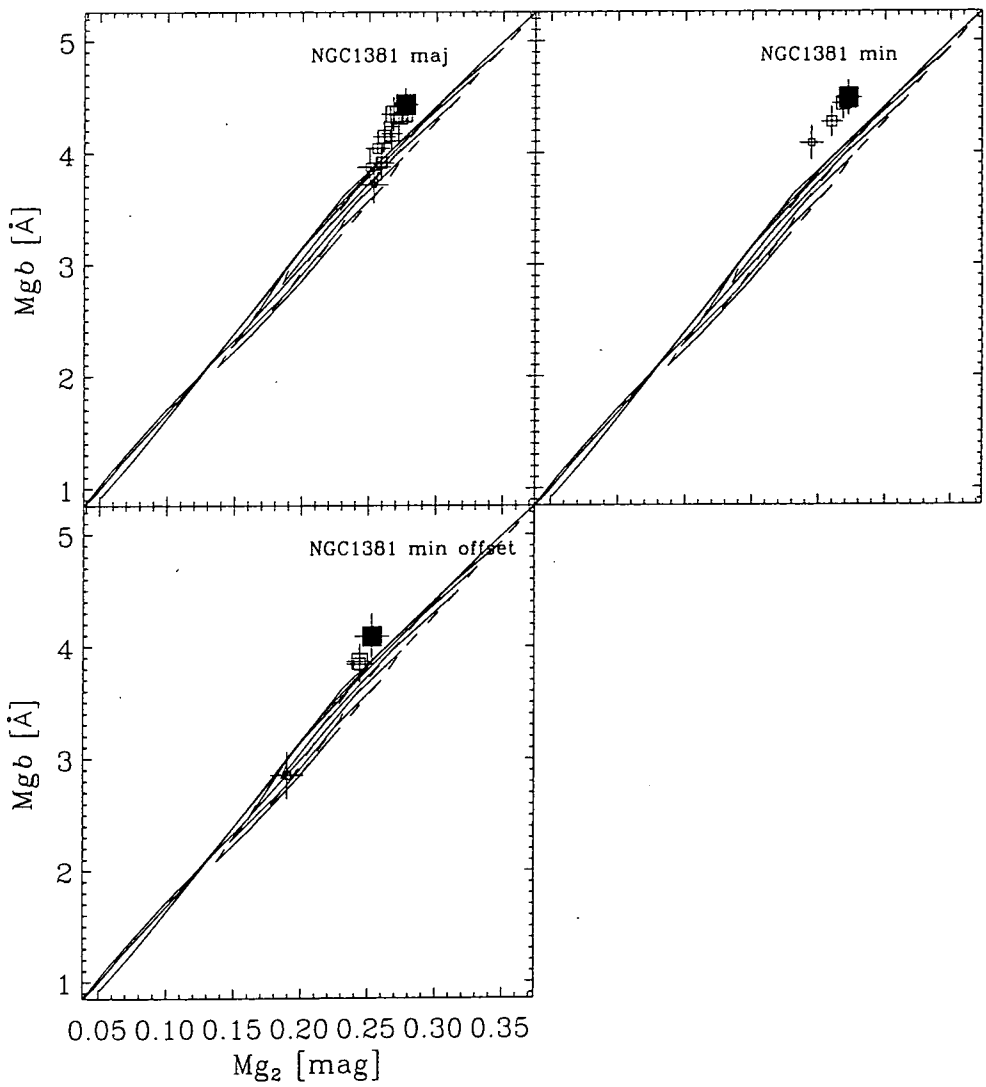

Figure 7.23: NGC1381: Line-strength gradients for three slit positions are shown in a Mg_2 *vs* Mg*b* diagram. The centre of each extraction is indicated by the filled symbol. Both sides of the galaxy have been averaged at similar radius (open symbols). Symbol size is inversely scaled with radius. Overplotted are models by Worthey.

7.6 Conclusions from Line-Strength Gradients

In Chapter 4 we concluded that the S0s show quite distinct stellar populations compared to the elliptical galaxies. This is also apparent in the line-strength gradient analysis, thus we will present our conclusions for Es and S0s separately:

Elliptical galaxies:

1. Elliptical galaxies generally exhibit smooth line-strength gradients when indices measured in magnitudes are plotted against $\log(r/r_e)$. The metal lines Mg_2, Mgb' and $< Fe' >$ show negative gradients. However, they vary in strength with Mg_2 being the strongest followed by Mgb' and $< Fe' >$. $H\beta'$ is generally constant with radius. Yet, $H\gamma_A$ shows positive gradients which are mainly caused by its sensitivity to metallicity.

2. Translating line-strength gradients into age/metallicity gradients with the help of Worthey's stellar population models we find that elliptical galaxies do not show significant age gradients but vary mostly in metallicity with radius. The difference between the central metallicity and the value at $1r_e$ is approximately [Fe/H] = -0.4 dex. Taking the value at $1r_e$ as a good indication of the total metallicity of Es (Arimoto et al., 1997) we find that our elliptical galaxies span a range of -0.7 to -0.3 in [Fe/H] (using <Fe> as metal indicator). When we use [Mg/Fe] we find values which are increased by $\sim$0.2 dex.

3. Trends of Mg overabundance with radius are generally weak indicating that the central [Mg/Fe] ratio applies to the whole galaxy or at least to the radii which are covered by our data.

S0 galaxies:

1. S0s show a less homogeneous behaviour. Gradients are on average shallower than for Es but cover a wide range. The presence of disks is an important influence on the strength of line-strength gradients.

2. The centres of the largest S0s, NGC1380 and NGC1381 harbour old stellar populations. A detailed analysis of NGC1381 shows that this galaxy consists of an old bulge with a decreasing metal gradient and a disk of roughly solar metallicity. On the major axis the combined effects of bulge and disk result in a roughly constant metallicity with radius. Furthermore, the bulge is overabundant in Mg whereas the outer disk approaches solar abundance ratios. This is evidence for a somewhat more extended star-formation history in the outer disk ($\sim 1r_e$).

3. The remaining nine S0s show all young (luminosity weighted) stellar populations in the centre. However, we identify five galaxies with a central starburst on top

of an underlying older stellar population. Two are S0s with a small bulge and a rather big disk component. The remaining 3 galaxies are dominated by the bulge component. The latter galaxies are reminiscent of the predictions of the "galaxy harassment" scheme proposed by Moore et al. (1998). Here disk galaxies (Sc-type) get stripped of their disk leaving only the bulge component, additionally the gas gets drawn into the centre where it is likely to be turned into stars. We note that the younger galaxies are in the outskirts of the Fornax cluster which may indicate that these galaxies have been "accreted" onto the cluster from the field.

Chapter 8

Conclusions

Our aim in this thesis has been to investigate the stellar populations of cluster early-type galaxies in order to understand more fully the origin of scaling relations. We obtained long-slit spectroscopy of a *complete* sample of 22 early-type galaxies in the nearby Fornax cluster. In order to study the stellar populations, we measured a series of Lick/IDS indices in the centre of our galaxies and also line-strength gradients. The data were compared with population synthesis models (Worthey, 1994) which predict the measured set of indices for a given age and metallicity of a single age stellar population.

Our analysis showed that S0-type galaxies are quite distinct from the elliptical galaxy population. Therefore we will present first our conclusions for Es and S0s separately and then discuss general results.

8.1 Elliptical Galaxies

The centres of our elliptical galaxies appear to be roughly coeval ($\sim$ 8 Gyrs, in the context of Worthey's (1994) models) with perhaps somewhat younger ages for the most luminous galaxies. The Es form a sequence in central metallicity varying from -0.2 to +0.3 in [Fe/H] when a Fe-index is used as metallicity indicator. The absolute ages and metallicities depend strongly on the index combination that is used in the analysis. This effect is caused by non solar abundance ratios which are present in early-type galaxies but not accounted for in the models. The stellar populations in our elliptical sample exhibit Mg-overabundances of up to [Mg/Fe] $\simeq$ 0.4 dex for the most luminous galaxies whereas low luminosity Es approach solar abundance ratios.

Investigating the line-strength gradients we find that elliptical galaxies do not exhibit significant age gradients within galaxies. Metal line-strength gradients are always negative and give on average ΔIndex [mag]/$\Delta \log(r/r_e) \simeq$ −0.07, −0.05 and −0.02 mag/dex for Mg_2, Mgb' and $< Fe' >$ respectively. A simple estimation of the corresponding [Fe/H]-gradients

gives Δ[Fe/H]/$\Delta \log(r/r_e) \simeq 0.4$ for all three indices. The [Mg/Fe] abundance ratio within elliptical galaxies stays generally constant, however a few galaxies show signs of a decrease in [Mg/Fe] at large radii.

8.2 S0-Type Galaxies

The centres of lenticular galaxies span a wide range in metallicity ($-0.4 <$ [Fe/H] < 0.4) and *have luminosity weighted ages that are on average much younger than those of the ellipticals*, spanning from less than $\sim$ 2 Gyrs to 8 Gyrs. The inferred difference in the age distribution between lenticular and elliptical galaxies is a robust conclusion as the models generate consistent relative ages using different age and metallicity indicators even though the absolute ages remain uncertain. The S0 population in Fornax can be roughly divided into three groups: (1) bright S0s with prominent disks and old populations, (2) bright S0s with peculiar morphology and young central stellar populations, and (3) faint and small S0s with young stellar populations in the centre.

(1) The bulges of the two bright S0s NGC1380 & NGC1381 generally follow the trend set by elliptical galaxies of a similar central velocity dispersion. For example they have stellar populations as old as the Es and exhibit similar Mg-overabundances. Also the line-strength gradients of the bulges (i.e., minor axis) are reminiscent of Es. However, metal line-strength gradients along the major axis of NGC1381, i.e., the superposition of bulge and disk, are very shallow suggesting almost no metallicity gradient. At the same time the disk seems to be as old as the bulge. In contrast to the bulge, the outer disk population (roughly at 1 r_e) shows evidence of solar abundance ratios.

(2) The second group has only one member in Fornax: NGC1316 (Fornax A). This galaxy is thought to be the product of a recent merger which is supported by the extremely young (luminosity weighted) stellar population in its centre. The young stars are consistent with having solar abundance ratios. The line-strength gradients ($r_{max} = 0.4\ r_e$) suggest a substantial decrease in metallicity while the age stays roughly constant with radius. Due to the fact that we can only measure luminosity weighted ages, it is not clear whether an underlying older stellar population exists in NGC1316 or not.

(3) The remaining 8 S0s are all relatively faint and have central velocity dispersions of $\leq$ 70 kms^{-1}. On average they are younger than the Es with five galaxies showing extremely young (luminosity weighted $\leq$ 3 Gyrs) central stellar populations. Analysing the line-strength gradients we find that the five youngest galaxies have all experienced a central starburst on top of an underlying *older* stellar population. Three out of these five galaxies show relatively strong *metal* absorption lines (NGC1375, NGC1380A and IC1963) whereas the remaining two galaxies (ESO358-G25 and ESO359-G02) show extremely weak metal absorption features. ESO358-G25 also clearly exhibits emission in [OIII]λ5007, Hγ and Hβ indicative of very recent star-formation.

Metal line-strength gradients for S0s (at intermediate PA) are in general shallower than for Es.

8.3 Discussion and General Conclusions

The previous results are based on several age/metallicity diagnostic diagrams in the Lick/IDS system comprising established indices such as [MgFe] and Hβ as well as new and more sensitive indices such as C4668, Fe3 and Hγ_A. Particularly the Hγ_A index has shown to be a good age indicator. It is better determined than Hβ and it is less sensitive to nebular emission. The inferred difference in the age distribution between lenticular and elliptical galaxies is a robust conclusion as the models generate consistent relative ages using different age and metallicity indicators even though the absolute ages remain uncertain. The absolute age uncertainty is caused by the effects of non-solar abundance ratios which are not accounted for in the stellar population models.

One of the main obstacles in this thesis has been that we can only measure luminosity weighted ages and metallicities, yet some galaxies clearly show composite stellar populations. The Lick/IDS system provides only indices in the optical wavelength range which is dominated by the light of young stellar populations if present. However, by using for example the near-IR Ca II triplet as metallicity indicator, one will be able to estimate the metallicity in a wavelength region where old stellar populations contribute most of the light and compare the result with metal lines from the optical wavelength region. Stellar population models for absorption lines in the near-IR are currently being developed (see also Section 8.4).

The difference between the abundance ratios found in bright early-type galaxies and in solar neighbourhood stars causes great uncertainty in the absolute age estimates. To overcome this problem we have used relatively unbiased metal indicators such as Fe3. However, for future work it would be desirable to define either new indices which trace the true metal abundance (total fraction of metals) or develop stellar population models which predict index-strength for a range of abundance ratios.

We have analysed one of the important scaling relations for early-type galaxies in detail, namely the Mg–σ_0 relation. We find that our sample follows a relation which is consistent with the relation in other nearby clusters such as Coma. However, the younger S0s deviate substantially from the relation set by the ellipticals. Most notably NGC1316 shows too weak Mg-absorption compared to its central velocity dispersion. At the low σ end of the relation the young S0s also exhibit generally too weak Mg-absorption.

For the first time we find a clear correlation of Fe-indices with the central velocity dispersion. The slopes of these relations are consistent with ΔIndex [mag]/$\Delta \log \sigma_0 \simeq$ 0.05 mag/dex. This is much shallower than the Mg_2 or $Mgb' - \sigma_0$ relation with a slope of

0.19 and 0.11 dex respectively. Although the models suggest a somewhat steeper slope for Mg_2 than for Fe-lines, this cannot account for the total difference between observed and predicted slopes. Therefore we conclude that this is again a sign of an increasing [Mg/Fe] ratio with galaxy mass. The young and faint S0s ($\sigma_0 < 70$ kms^{-1}) show generally large scatter around the mean index–σ_0 relation set by the ellipticals.

Two of the elliptical galaxies (NGC1373 & IC2006) show signs of enhanced Fe content with respect to galaxies of similar central velocity dispersion. In the case of IC2006 it is likely that a major merger caused secondary star-formation which "boosted" the Fe-content. However, the luminosity weighted stellar populations in this galaxy are of similar age to the other Es. The data for NGC1373 do not allow any detailed analysis.

We have analysed the sources of scatter in the Mg–σ_0 relation by investigating the influence of age, metallicity and [Mg/Fe] ratio effects. As mentioned before, on an overall scale the age variations as seen in the S0s cause most of the scatter. However, when we investigate the relatively small scatter of the old ellipticals we find the strongest correlation with [Mg/Fe] ratio variations. At a given σ_0, galaxies with a strong Mg-overabundance deviate from the mean Mg–σ_0 relation in the sense that their Mg absorption is too strong and vice versa. Perhaps surprisingly metallicity effects play only a minor role in the scatter indicating that the central velocity dispersion scales very well with the central metallicity of Es.

At least for the ellipticals in our sample, the main driver of any of the index–σ_0 relations are metallicity variations. As our ellipticals are roughly coeval we argue that there is no need for an age/metallicity conspiracy to keep the Mg–σ_0 relation or any other scaling relation tight. This of course is only shown for Fornax and has yet to be confirmed for large clusters such as Coma.

The young S0s in our sample are interesting in themselves, particularly the question of their origin. Dressler et al. (1997) found that in clusters at z = 0.5 the fraction of elliptical galaxies remains constant compared to nearby clusters but the fraction of S0 galaxies is 2–3 times lower. They suggest that a fraction of the spiral galaxy population has evolved to quiescence in the 5 Gyrs interval from z = 0.5 to the present. The harassment picture proposed by Moore et al. (1998) and Lake et al. (1998) is one of the likely mechanisms which can transform disk galaxies (Sc type) into spheroidal-type galaxies where the gas is driven into the centre of the end-products. This is consistent with our findings of small and youthful spheroidal galaxies which have experienced a central burst on top of an older stellar population. However, two of the young galaxies still have substantial disks which indicates that other mechanisms are at work as well (e.g., ram pressure stripping). We note that most of the young S0s are located in the outer regions of the Fornax cluster which may indicate that these galaxies have been accreted onto the cluster from the field.

In summary we find in the Fornax cluster a homogeneous population of old elliptical galaxies where central velocity dispersion scales well with metallicity. The S0s show a great

variety ranging from faint, youthful S0s to relatively large S0s with well established disks and mainly old stellar populations. However, when analysing individual elliptical galaxies in detail we find signs of merging such as the kinematically peculiar core in NGC1427 and the enhanced Fe-content in IC2006. Finally the peculiar S0 NGC1316 is a good example of a large galaxy assembled very recently in a merger which is reflected in a major starburst in its centre.

All together this is certainly consistent with the hierarchical merger picture where the bulk of the stars in cluster galaxies are created at high redshifts. Smaller galaxies are "accreted" onto the original cluster population with some residual ongoing star-formation.

8.4 Future Work

During the course of the last three years several projects have been started which are related to the work presented in this thesis.

- We obtained U, R imaging of our Fornax sample in order to investigate the colour magnitude relation and the FP. The data from this thesis will enable us to probe the effects of stellar populations on these scaling relations.
- We obtained deep long-slit spectra of 5 disky ellipticals in small groups and the field which also showed relatively strong absorption in Hβ. The spectra cover the optical wavelength range as well as the Ca II triplet in the near-IR. We will investigate the connections of young stellar populations and the kinematics of disks in elliptical galaxies.
- Most recently we obtained spectra of $\sim$ 50 globular clusters in M31. Due to their single age populations, results from globular clusters are intrinsically easier to interpret than those of more complex objects. The globular clusters around nearby galaxies can carry important information about the galaxy formation which is otherwise hidden in the integrated light of the parent galaxy. By comparison with the integrated light of the M31 spheroid, we plan to determine the "order of events" in the formation of M31, i.e., are globular clusters older or younger than the bulge population at the same radius?
- We have started a project which aims to obtain spectra of a well defined sample of field Es and S0s. This sample will enable us to test the predictions of the hierarchical merger picture where field galaxies are thought to be younger than the cluster population.

Bibliography

Andreon, S. (1998). *ApJ*, 501:533.

Arimoto, N., Matsushita, K., Ishimaru, Y., Ohashi, T., and Renzini, A. (1997). *ApJ*, 477:128.

Arimoto, N. and Yoshii, Y. (1987). *AA*, 173:23.

Baggley, G. (1996). *Peculiar Velocities of Clusters Determined from Early-Type Galaxies.* PhD thesis, University of Oxford.

Baldwin, J. A., Phillips, M. M., and Terlevich, R. J. (1981). *PASP*, 93:5.

Barger, A. J., Aragón-Salamanca, A., Ellis, R. S., Couch, W. J., Smail, I., and Sharples, R. M. (1996). *MNRAS*, 279:1.

Baugh, C. M., Cole, S., and Frenk, C. (1996). *MNRAS*, 283:1361.

Bender, R. (1988). *AA*, 193:7L.

Bender, R. (1990). *AA*, 229:441.

Bender, R. (1996). In Bender, R. and Davies, R. L., editors, *"New Light on Galaxy Evolution"*, volume 171 of *IAU Symp.*, page 181, Dordrecht. Kluwer.

Bender, R., Burstein, D., and Faber, S. M. (1992). *ApJ*, 399:462.

Bender, R., Burstein, D., and Faber, S. M. (1993). *ApJ*, 411:153.

Bender, R., Burstein, D., and Faber, S. M. (1997). In da Costa, L. N. and Renzini, A., editors, *"Galaxy Scaling Relations: Origins, Evolution and Applications"*, ESO Astrophysics Symposia, page 95, Berlin. Springer.

Bender, R., Saglia, R. P., and Gerhard, O. E. (1994). *MNRAS*, 269:785.

Bertola, F. and Capaccioli, M. (1975). *ApJ*, 200:439.

Bessel, M. S., Brett, J. M., Scholz, M., and Wood, P. R. (1989). *AAS*, 77:1.

Bessel, M. S., Brett, J. M., Scholz, M., and Wood, P. R. (1991). *AAS*, 89:335.

Binette, L., Magris, C. G., Stasińska, G., and Bruzual, A. G. (1994). *AA*, 292:13.

Binney, J. (1976). *MNRAS*, 177:19.

Borges, A. C., Idiart, T. P., de Freitas Pacheco, J. A., and Thevenin, F. (1995). *AJ*, 110:2408.

Bothun, G. D. and Gregg, M. D. (1990). *ApJ*, 350:73.

Bower, R. G., Kodama, T., and Terlevich, A. (1998). astro-ph/9805290.

Bower, R. G., Lucey, J. R., and Ellis, R. S. (1992). *MNRAS*, 254:601.

Bruzual, G. A. and Charlot, S. (1993). *ApJ*, 287:586.

Bureau, M., Mould, J. R., and Staveley-Smith, L. (1996). *ApJ*, 463:60.

Burkert, A. (1993). *AA*, 278:23.

Burstein, D., Davies, R. L., Dressler, A., Faber, S. M., Lynden-Bell, D., Terlevich, R. J., and Wegner, G. (1988). In Kron, R. G. and Renzini, A., editors, *Towards Understanding Galaxies at Large Redshifts*, page 17, Dordrecht. Kluwer.

Burstein, D., Faber, S. M., Gaskell, C. M., and Krumm, N. (1984). *ApJ*, 287:586.

Burstein, D., Faber, S. M., and González, J. J. (1986). *AJ*, 91:1130.

Buzzoni, A., Mantegazza, L., and Gariboldi, G. (1994). *AJ*, 107:513.

Calberg, R. G. (1984). *ApJ*, 286:403.

Caldwell, N. (1984). *PASP*, 96:287.

Caldwell, N., Rose, J. A., Sharples, R. M., Ellis, R. S., and Bower, R. G. (1993). *AJ*, 106:473.

Caon, N., Capaccioli, M., and D'Onofrio, M. (1994). *AAS*, 106:199.

Cardiel, N., Gorgas, J., Cenarro, J., and González, J. J. (1998). *AAS*, 127:597.

Carollo, C. M., Danziger, I. J., and Buson, L. (1993). *MNRAS*, 265:553.

Carollo, C. M., Franx, M., Illingworth, G. D., and Forbes, D. A. (1997). *ApJ*, 481:710.

Carrasco, L., Buzzoni, A., Salsa, M., and Recillas-Cruz, E. (1996). In Buzzoni, A., Renzini, A., and Serrano, A., editors, *Fresh Views of Elliptical Galaxies*, volume 86 of *ASP Conference Series*, page 235, San Francisco.

Carter, D. (1987). *ApJ*, 312:514.

Charlot, S., Worthey, G., and Bressan, A. (1996). *ApJ*, 457:625.

Colless, M., Burstein, D., Davies, R. L., Jr, R. K. M., Saglia, R. P., and Wegner, G. (1998). Submitted to MNRAS.

Couch, W. J. and Sharples, R. M. (1987). *MNRAS*, 229:423.

Davidge, T. J. (1992). *AJ*, 103:1512.

Davies, R. L. (1996). In Buzzoni, A., Renzini, A., and Serrano, A., editors, *Fresh Views of Elliptical Galaxies*, volume 86 of *ASP Conference Series*, page 225, San Francisco.

Davies, R. L., Efstathiou, G., Fall, S. M., Illingworth, G., and Schechter, P. L. (1983). *ApJ*, 266:41.

Davies, R. L., Sadler, E. M., and Peletier, R. F. (1993). *MNRAS*, 262:650.

de Carvalho, R. R., Djorgovski, S., and da Costa, L. N. (1991). *ApJS*, 76:1067.

de Freitas Pacheço, J. A. and Barbuy, B. (1995). *AA*, 302:718.

de Jong, R. S. and Davies, R. L. (1997). *MNRAS*, 285:1L.

de Jong, R. S., Davies, R. L., Minchin, R. F., Lucey, J. R., and Steel, J. (1998). to appear in: IAU Symposium 183. Cosmological Parameters and Evolution of the Universe. Kyoto Japan.

de Vaucouleurs, G. (1948). *Ann. d'Astrophys.*, 11:247.

de Vaucouleurs, G. (1961). *ApJS*, 5:233.

de Vaucouleurs, G., de Vaucouleurs, A., Corwin, H. G. J., Buta, R. J., Paturel, G., and Fouqué, P. (1991). *Third Reference Catalogue of Bright Galaxies.* Springer Verlag.

Djorgovski, S. and Davis, M. (1987). *ApJ*, 313:59.

D'Onofrio, M., Zaggia, S. R., Longo, G., Caon, N., and Capaccioli, M. (1995). *AA*, 296:319.

Dressler, A. (1980). *ApJ*, 236:351.

Dressler, A., Lynden-Bell, D., Burstein, D., Davies, R. L., Faber, S. M., Terlevich, R. J., and Wegner, G. (1987). *ApJ*, 313:42.

Dressler, A., Oemler, A. J., Couch, W. J., Smail, I., Ellis, R. S., Barger, A., Butcher, H., Poggianti, B. M., and Sharples, R. M. (1997). *ApJ*, 490:577.

Edvardsson, B., Anderson, J., Gustafsson, B., Lambert, D. L., Nissen, P. E., and Tomkin, J. (1993). *AA*, 275:101.

Efstathiou, G. and Gorgas, J. (1985). *MNRAS*, 215:37.

Faber, S. M., Dressler, A., Davies, R. L., Burstein, D., Lynden-Bell, D., Terlevich, R. J., and Wegner, G. (1987). In Faber, S. M., editor, *Nearly Normal Galaxies, From the Planck Time to the Present*, page 175, New York. Springer.

Faber, S. M., Friel, E. D., Burstein, D., and Gaskell, C. M. (1985). *ApJS*, 57:711.

Faber, S. M., Trager, S. C., González, J. J., and Worthey, G. (1995). In Kruit, P. C. V. D. and Gilmore, G., editors, *Stellar Populations*, volume 164 of *IAU Symp.*, page 249, Dordrecht. Kluwer.

Faber, S. M., Tremaine, S., Ajhar, E. A., Byun, Y., Dressler, A., Gebhardt, K., Grillmair, C., and Kormendy, J. (1997). *AJ*, 114:1771.

Ferguson, H. C. (1989). *AJ*, 98:367.

Ferguson, H. C. and Sandage (1988). *AJ*, 96:1520.

Fisher, D., Franx, M., and Illingworth, G. (1995). *ApJ*, 448:119.

Fisher, D., Franx, M., and Illingworth, G. (1996). *ApJ*, 459:110.

Franx, M. and Illingworth, G. (1988). *ApJ*, 327:L55.

Franx, M., Illingworth, G., and Heckman, T. (1989a). *AJ*, 98:538.

Franx, M., Illingworth, G., and Heckman, T. (1989b). *ApJ*, 344:613.

Freedman, W. L. (1992). *AJ*, 104:1349.

Fuhrmann, K., Axer, M., and Gehren, T. (1995). *AA*, 301:492.

González, J. J. (1993). *Line Strength Gradients and Kinematic Profiles in Elliptical Galaxies*. PhD thesis, University of California.

González, J. J. and Gorgas, J. (1996). In Buzzoni, A., Renzini, A., and Serrano, A., editors, *Fresh Views of Elliptical Galaxies*, volume 86 of *ASP Conference Series*, page 225, San Francisco.

Gorgas, J., Efstathiou, G., and Aragón-Salamanca, A. (1990). *MNRAS*, 245:217.

Gorgas, J., Faber, S. M., Burstein, D., González, J. J., Courteau, S., and Prosser, C. (1993). *ApJS*, 86:153.

Gorgas, J., Pedraz, S., Guzmán, R., Cardiel, N., and González, J. J. (1997). *ApJL*, 481:19.

Goudfrooij, P. and Emsellem, E. (1996). *AA*, 306:45L.

Goudfrooij, P., Hansen, L., Jørgensen, H. E., and Nørgaard-Nielsen, H. U. (1994a). *AAS*, 105:341.

Goudfrooij, P., Hansen, L., Jørgensen, H. E., Nørgaard-Nielsen, H. U., de Jong, T., and van den Hoek, L. B. (1994b). *AAS*, 104:179.

Graham, A. W., Colless, M. M., Busarello, G., Zaggia, S., and Longo, G. (1998). astro-ph/9806331.

Green, E. M., Demarque, P., and King, C. R. (1993). *The Revised Yale Isochrones and Luminosity Functions*. Yale University Obsevatory, New Haven.

Gregg, M. D. (1994). *AJ*, 108:2164.

Greggio, L. (1997). *MNRAS*, 285:151.

Gunn, J. E. and Stryker, L. L. (1983). *ApJS*, 52:121.

Guzmán, R. and Lucey, J. R. (1993). *MNRAS*, 263:47L.

Guzmán, R., Lucey, J. R., Carter, D., and Terlevich, R. J. (1992). *MNRAS*, 257:187.

Hau, G. (1998). *Elliptical Galaxy Cores*. PhD thesis, Cambridge.

Held, E. V. and Mould, J. R. (1994). *AJ*, 107:1307.

Ho, L. C., Filippenko, A. V., and Sargent, W. L. W. (1993). *ApJ*, 417:63.

Hubble, E. P. (1936). *The Realm of the Nebulae*. Yale University Press, New Haven.

Illingworth, G. D. (1977). *ApJ*, 218:43L.

Isobe, T., Feigelson, E. D., Akritas, M. G., and Babu, G. J. (1990). *ApJ*, 364:104.

Jensen, J. B., Tonry, J. L., and Luppino, G. A. (1998). *ApJ*, 505:111.

Jones, L. A. and Worthey, G. (1995). *ApJL*, 446:31.

Jørgensen, I. (1997). *MNRAS*, 288:161.

Jørgensen, I., Franx, M., and Kjærgaard, P. (1993). *ApJ*, 411:34.

Kauffmann, G. (1996). *MNRAS*, 281:475.

Kauffmann, G. and Charlot, S. (1998). *MNRAS*, 294:705.

Knapp, G. R., Guhathakurta, P., Kim, D.-W., and Jura, M. (1989). *ApJS*, 70:329.

Kodama, T. and Arimoto, N. (1997). *AA*, 320:41.

Kodama, T., Bower, R. G., and Bell, E. F. (1998). astro-ph/9810138.

Kohle, S., Kissler-Patig, M., Hilker, M., Richtler, T., Infante, L., and Quintana, H. (1996). *AA*, 309:39L.

Kormendy, J. and Bender, R. (1996). *ApJL*, 464:119.

Kormendy, J., Bender, R., Richstone, D., Ajhar, E. A., Dressler, A., Faber, S. M., Gebhardt, K., Grillmair, C., Lauer, T. R., and Tremaine, S. (1996). *ApJL*, 459:57.

Kuntschner, H. and Davies, R. L. (1998). *MNRAS*, 295:29L.

Kurth, O. M., v. Alvensleben, U. F., and Fricke, K. J. (1998). astro-ph/9803192.

Kurucz, R. L. (1992). In Barbuy, B. and Renzini, A., editors, *The Stellar Populations of Galaxies*, volume 149 of *IAU Symp.*, page 225, Dordrecht. Kluwer.

Lake, G., Katz, N., and Moore, B. (1998). *ApJ*, 495:152.

Larson, R. B. (1974). *MNRAS*, 166:585.

Larson, R. B. (1975). *MNRAS*, 173:671.

Larson, R. B. (1976). *MNRAS*, 176:31.

Larson, R. B., Tinsley, B. M., and Caldwell, C. N. (1980). *ApJ*, 237:629.

Lauer, T. R. (1985). *ApJ*, 292:104.

Macchetto, F., Pastoriza, M., Caon, N., Sparks, W. B., Giavalisco, M., Bender, R., and Capaccioli, M. (1996). *AAS*, 120:463.

Mackay, C. (1986). *Ann.Rev.AA*, 24:255.

Malin, D. F. and Carter, D. (1983). *ApJ*, 274:534.

McElroy, D. B. (1995). *AJS*, 100:105.

McMillan, R., Ciardullo, R., and Jacoby, G. H. (1993). *ApJ*, 416:62.

McWilliam, A. (1997). *ARAA*, 35:503.

Mehlert, D. (1998). *Elliptische Galaxiesn in hoher Umgebungsdichte: Der Coma Haufen.* PhD thesis, Ludwig - Maximilian - Universiät, München.

Moore, B., Lake, G., and Katz, N. (1998). *ApJ*, 495:139.

Mowlavi, N., Meynet, G., Maeder, A., Schaerer, D., and Charbonnel, C. (1998). *AA*, 335:573.

O'Connell, R. W. (1976). *ApJ*, 206:370.

O'Connell, R. W. (1980). *ApJ*, 236:430.

Oke, J. B. (1990). *AJ*, 99:1621.

Osterbrock, D. E. (1989). *Astrophysics of Gaseous Nebula and Active Galactic Nuclei.* University Science Books, Mill Valley, CA.

Pahre, M. A., de Carvalho, R. R., and Djorgovski, S. G. (1998). astro-ph/9806326.

Peletier, R. F. (1989). *Elliptical Galaxies - Structure and Stellar Content.* PhD thesis, University of Groningen, Groningen.

Peletier, R. F. and Balcells, M. (1996). *AJ*, 111:2238.

Peletier, R. F., Davies, R. L., Davis, L. E., Illingworth, G. D., and Cawson, M. (1990). *AJ*, 100:1091.

Phillips, M. M., Jenkins, C. R., Dopita, M. A., Sadler, E. M., and Binette, L. (1986). *AJ*, 91:1062.

Pickles, A. J. (1985a). *ApJS*, 59:33. Paper I.

Pickles, A. J. (1985b). *ApJ*, 296:340. Paper III.

Pickles, A. J. and Visvanathan, N. (1985). *ApJ*, 294:134. Paper II.

Poggianti, B. M. and Barbaro, G. (1997). *AA*, 325:1025.

Renzini, A. and Ciotti, L. (1993). *ApJL*, 416:49.

Rix, H. and White, S. D. M. (1990). *ApJ*, 362:52.

Robinson, L. and Wampler, E. J. (1972). *PASP*, 84:161.

Rose, J. A. (1985). *AJ*, 90:1927.

Salaris, M., Chieffi, A., and Straniero, O. (1993). *ApJ*, 414:580.

Salpeter, E. E. (1955). *ApJ*, 121:161.

Sandage, A. and Bedke, J. (1994). *The Carnegie Atlas of Galaxies.* Carnegie Institution of Washington, Washington, D.C.

Sandage, A. and Tammann, G. A. (1987). *The Revised Shapley-Ames Catalog of Bright Galaxies.* Carnegie Institution of Washington, Washington, D.C.

Sandage, A. and Visvanathan, N. (1977). *ApJ*, 216:214.

Sandage, A. and Visvanathan, N. (1978). *ApJ*, 225:742.

Sargent, W. L. W., Schechter, P. L., Boksenberg, A., and Shortridge, K. (1977). *ApJ*, 212:326.

Schweizer, F. (1998). Observational evidence for interactions and mergers. In Friedli, D., Martinet, L., and Pfenniger, D., editors, *Galaxies: Interactions and Induced Star Formation*, volume 26 of *Saas-Fee Advanced Course*, page 105. Springer, Berlin.

Schweizer, F., Seitzer, P., Faber, S. M., Burstein, D., Ore, C. M. D., and González, J. J. (1990). *ApJL*, 364:33.

Schweizer, F., van Gorkom, J. H., and Seitzer, P. (1989). *ApJ*, 338:770.

Scorza, C. and Bender, R. (1995). *AA*, 293:20.

Silbermann, N. A., Hardig, P., Ferrarese, L., and et al (1998). astro-ph/9806017.

Smith, R. J. (1998). Private communication.

Spinrad, H., Gunn, J. E., Taylor, B. J., McClure, R. D., and Young, J. W. (1971). *ApJ*, 164:11.

Stanford, S. A., Eisenhardt, P. R., and Dickinson, M. (1997). *ApJ*, 492:461.

Terlevich, A. (1998). *Probing the Star Formation History of Early-Type Galaxies in Clusters.* PhD thesis, University of Durham.

Thomas, D., Greggio, L., and Bender, R. (1998a). astro-ph/9809261.

Thomas, D., Greggio, L., and Bender, R. (1998b). *MNRAS*, 296:119.

Tinsley, B. (1979). *ApJ*, 229:1046.

Tonry, J. and Davis, M. (1979). *AJ*, 84:1511.

Toomre, A. (1977). In Tinsley, B. M. and Larson, R. B., editors, *Evolution of Galaxies and Stellar Populations*, page 401, New Haven. Yale University Press.

Trager, S. C. (1997). *The Stellar Population Histories of Elliptical Galaxies.* PhD thesis, University of California.

Trager, S. C., Worthey, G., Faber, S. M., Burstein, D., and González, J. J. (1998). *ApJS*, 116:1. Paper VI.

Tripicco, M. J. and Bell, R. A. (1995). *AJ*, 110:3035.

van Dokkum, P. G., Franx, M., Kelson, D. D., and Illingworth, G. D. (1998a). *ApJL*, 504:17.

van Dokkum, P. G., Franx, M., Kelson, D. D., Illingworth, G. D., Fisher, D., and Fabricant, D. (1998b). *ApJ*, 500:714.

van Gorkom, M. F. J. H. and de Zeeuw, T. (1994). *ApJ*, 436:642.

VandenBerg, D. A. (1985). *ApJS*, 58:711.

VandenBerg, D. A. and Bell, R. A. (1985). *ApJS*, 58:561.

VandenBerg, D. A. and Laskarides, P. G. (1987). *ApJS*, 64:103.

Vazdekis, A., Casuso, E., Peletier, R. F., and Beckman, J. E. (1996). *ApJS*, 106:307.

Vazdekis, A., Peletier, R. F., Beckman, J. E., and Casuso, E. (1997). *ApJS*, 111:203.

Weiss, A., Peletier, R. F., and Matteucci, F. (1995). *AA*, 296:73.

White, S. D. M. (1997). In da Costa, L. N. and Renzini, A., editors, *"Galaxy Scaling Relations: Origins, Evolution and Applications"*, ESO Astrophysics Symposia, page 3, Berlin. Springer.

Woosley, S. E. and Weaver, T. A. (1995). *ApJS*, 101:181.

Worthey, G. (1992). *The Controlling Parameters of the Integrated Flux of a Stellar Population.* PhD thesis, University of California.

Worthey, G. (1994). *ApJS*, 95:107.

Worthey, G. (1996). In Leitherer, C., von Alvenleben, U. F., and Huchra, J., editors, *From Stars to Galaxies: Impact of Stellar Physiscs on Galaxy Evolution*, volume 98 of *ASP Conference Series*, page 467, San Francisco.

Worthey, G., Faber, S. M., and González, J. J. (1992). *ApJ*, 398:69.

Worthey, G., Faber, S. M., González, J. J., and Burstein, D. (1994). *ApJS*, 94:687.

Worthey, G. and Ottaviani, D. L. (1997). *ApJS*, 111:377.

Worthey, G., Trager, S. C., and Faber, S. M. (1996). In Buzzoni, A., Renzini, A., and Serrano, A., editors, *Fresh Views of Elliptical Galaxies*, volume 86 of *ASP Conference Series*, page 203, San Francisco.

Zabludoff, A. I., Zaritsky, D., Lin, H., Tucker, D., Hashimoto, Y., Shectman, S. A., Oemler, A., and Kirshner, R. P. (1996). *ApJ*, 466:104.

Ziegler, B. L. and Bender, R. (1997). *MNRAS*, 291:527.

Appendix A

Final Line-Strength Measurements for Stars

Here we present in Table A.1 on the next page a summary of our fully calibrated line-strength measurements for 12 Lick/IDS comparison stars and the two velocity standards obtained during the AAT96 run.

Table A.1: Final index measurements for the stars in common with the Lick/IDS library and two velocity standards

star	G4300 [Å]	Fe4383 [Å]	Ca4455 [Å]	Fe4531 [Å]	C4668 [Å]	Hβ [Å]	Fe5015 [Å]	Mg$_1$ [mag]	Mg$_2$ [mag]	Mgb [Å]	Fe5270 [Å]	Fe5335 [Å]	Fe5406 [Å]	Fe5709 [Å]	Hγ_A [Å]	Hγ_F [Å]
HD004656	6.25	8.60	2.63	4.86	7.16	0.53	6.72	0.241	0.405	4.42	4.09	4.12	2.99	1.37	-9.68	-2.99
±	0.03	0.04	0.02	0.03	0.04	0.02	0.03	0.001	0.001	0.02	0.02	0.02	0.01	0.01	0.04	0.02
HD037160	6.78	5.04	1.43	2.96	3.28	1.12	4.21	0.069	0.177	2.95	2.36	1.95	1.23	0.82	-6.71	-2.52
±	0.01	0.02	0.01	0.01	0.02	0.01	0.02	0.000	0.001	0.01	0.01	0.01	0.01	0.01	0.02	0.01
HD047205	6.42	7.64	2.00	3.60	7.82	1.46	6.06	0.116	0.275	4.26	3.70	3.26	2.19	1.21	-8.68	-3.09
±	0.02	0.03	0.01	0.02	0.03	0.01	0.03	0.001	0.001	0.01	0.01	0.02	0.01	0.01	0.03	0.02
HD050778	6.49	8.03	2.55	4.56	6.05	0.52	6.05	0.220	0.372	4.19	3.79	3.63	2.64	1.35	-9.60	-3.15
±	0.02	0.03	0.01	0.02	0.03	0.01	0.02	0.001	0.001	0.01	0.01	0.01	0.01	0.01	0.03	0.01
HD054810	6.72	5.97	1.69	3.31	4.45	1.29	5.09	0.068	0.185	2.97	2.94	2.45	1.60	1.05	-7.52	-2.62
±	0.02	0.03	0.01	0.02	0.03	0.01	0.03	0.001	0.001	0.01	0.01	0.02	0.01	0.01	0.03	0.01
HD058972	6.31	7.82	2.39	4.51	5.81	0.73	6.39	0.175	0.323	3.63	3.82	3.62	2.63	1.33	-9.05	-2.69
±	0.03	0.03	0.02	0.03	0.04	0.01	0.03	0.001	0.001	0.01	0.02	0.02	0.01	0.01	0.03	0.02
HD061935	6.84	6.49	1.83	3.52	6.05	1.53	5.94	0.067	0.183	2.80	3.24	2.72	1.77	1.18	-7.97	-2.66
±	0.01	0.02	0.01	0.01	0.02	0.01	0.02	0.000	0.001	0.01	0.01	0.01	0.01	0.01	0.02	0.01
HD066141	6.79	7.03	2.06	3.80	5.15	0.87	5.44	0.143	0.269	3.46	3.39	2.97	2.09	1.23	-8.74	-3.11
±	0.03	0.04	0.02	0.03	0.04	0.02	0.03	0.001	0.001	0.02	0.02	0.02	0.01	0.01	0.03	0.02
HD083618	6.71	8.49	2.46	4.37	6.59	0.96	6.66	0.137	0.284	3.58	3.99	3.61	2.58	1.47	-10.00	-3.12
±	0.02	0.03	0.01	0.02	0.03	0.01	0.03	0.001	0.001	0.01	0.01	0.01	0.01	0.01	0.03	0.02
HD088284	6.64	7.23	2.01	3.66	7.39	1.79	6.62	0.067	0.204	3.24	3.56	3.05	1.97	1.29	-8.23	-2.58
±	0.02	0.02	0.01	0.02	0.02	0.01	0.02	0.001	0.001	0.01	0.01	0.01	0.01	0.01	0.02	0.01
HD095272	7.11	7.08	2.02	3.76	6.76	1.42	6.20	0.085	0.209	3.04	3.47	2.96	2.00	1.30	-8.76	-3.04
±	0.02	0.03	0.01	0.02	0.03	0.01	0.03	0.001	0.001	0.01	0.01	0.02	0.01	0.01	0.03	0.02
HD219449	6.58	6.59	1.79	3.49	6.40	1.44	6.11	0.096	0.218	3.31	3.48	3.03	1.99	1.32	-7.55	-2.48
±	0.02	0.03	0.01	0.02	0.03	0.01	0.03	0.001	0.001	0.01	0.01	0.02	0.01	0.01	0.02	0.01
Velocity standards																
HD40657	7.34	6.60	2.38	3.98	3.98	0.88	5.65	0.112	0.242	3.50	3.32	2.96	1.98	1.27	-7.34	-2.68
±	0.03	0.04	0.02	0.03	0.04	0.01	0.03	0.001	0.001	0.01	0.01	0.01	0.01	0.01	0.04	0.02
HD71597	7.21	7.84	2.62	3.90	5.67	1.02	5.93	0.118	0.266	4.13	3.68	3.42	2.36	1.39	-8.11	-3.14
±	0.14	0.17	0.08	0.12	0.16	0.06	0.12	0.003	0.003	0.06	0.06	0.07	0.05	0.04	0.17	0.10

Appendix B

Line-Strength Gradients

Here we present on the following pages plots of index gradients and linear fits to the line-strength data. The indices are measured in magnitudes according to Equation 5.1 on page 108 and plotted *vs* $\log(r/r_e)$, where r_e is the effective radius scaled to the position angle (PA) of the observation. The open square and triangles facing up and down represent the centre and different sides of the galaxy respectively. The vertical dashed line indicates the central 1″ radial range which is excluded from the fits because of seeing effects. For each galaxy the name, morphological type, effective radius, PA of the major axis and the *observed* PA are given on the top of the plot. The observing run (NTT92, NTT93 or AAT96) is indicated in the Figure caption in brackets.

Tables of line-strength measurements as a function of radius can be obtained from the author if requested.

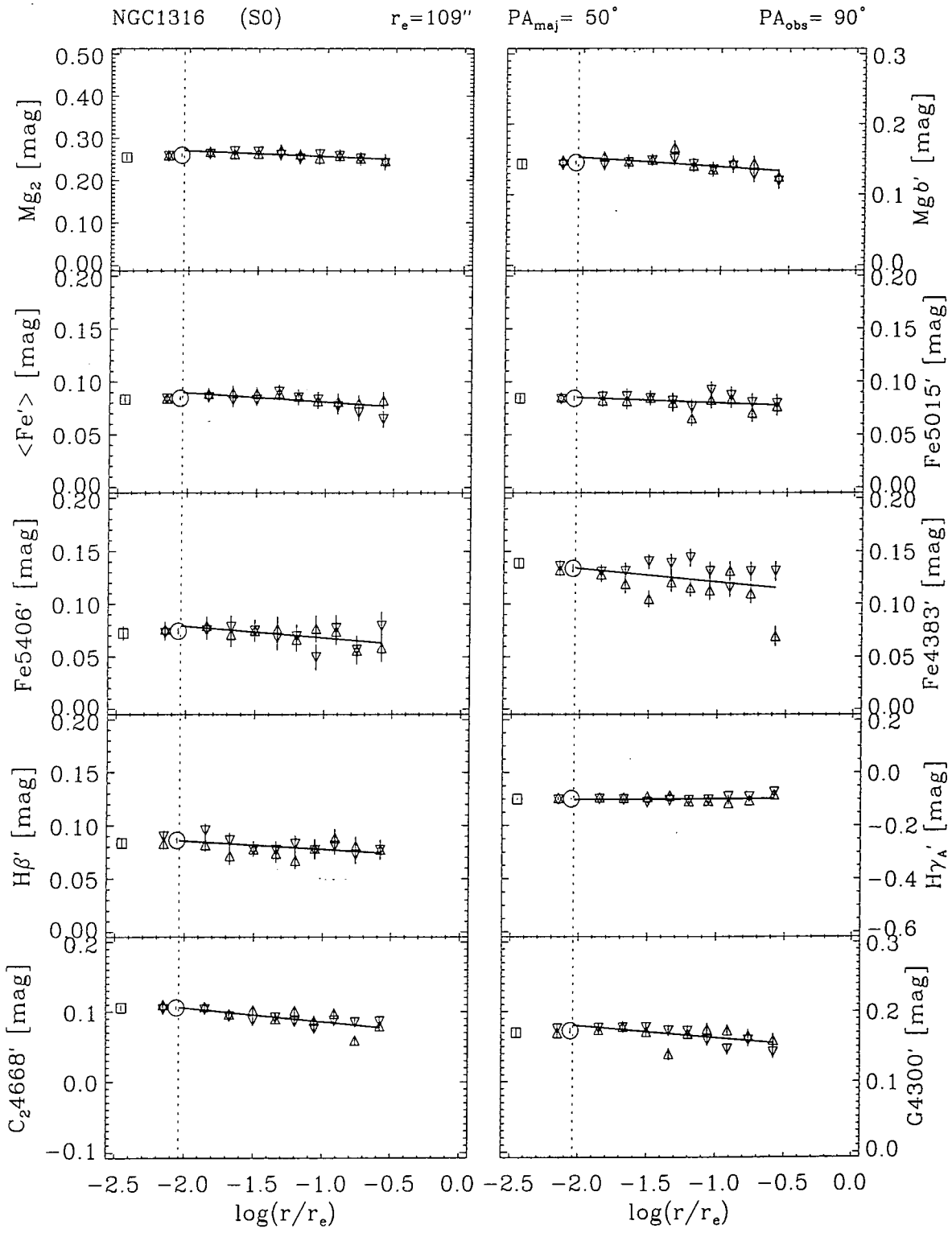

Figure B.1: Line-Strength Gradients: NGC1316 (AAT96)

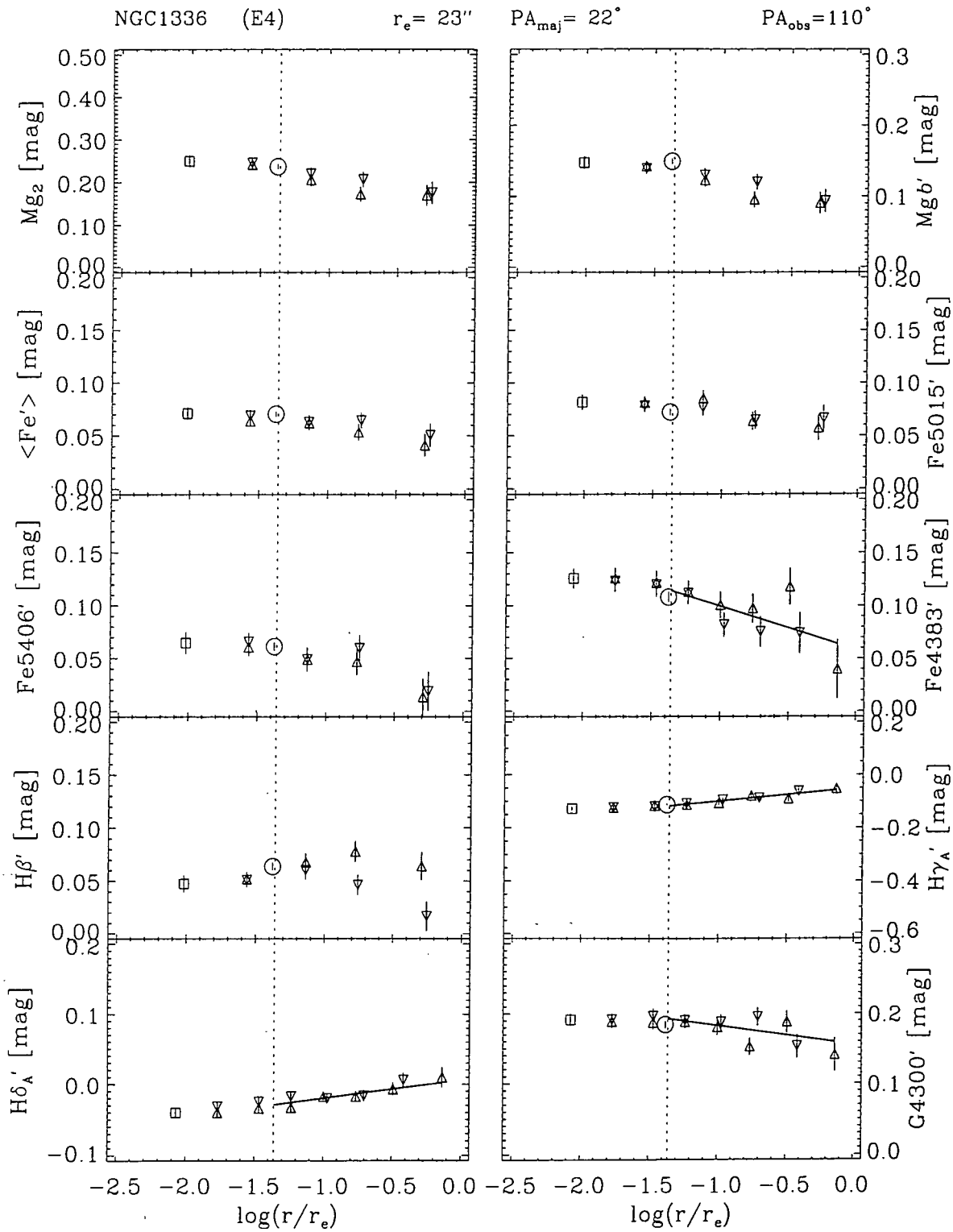

Figure B.2: Line-Strength Gradients: NGC1336 (NTT92)

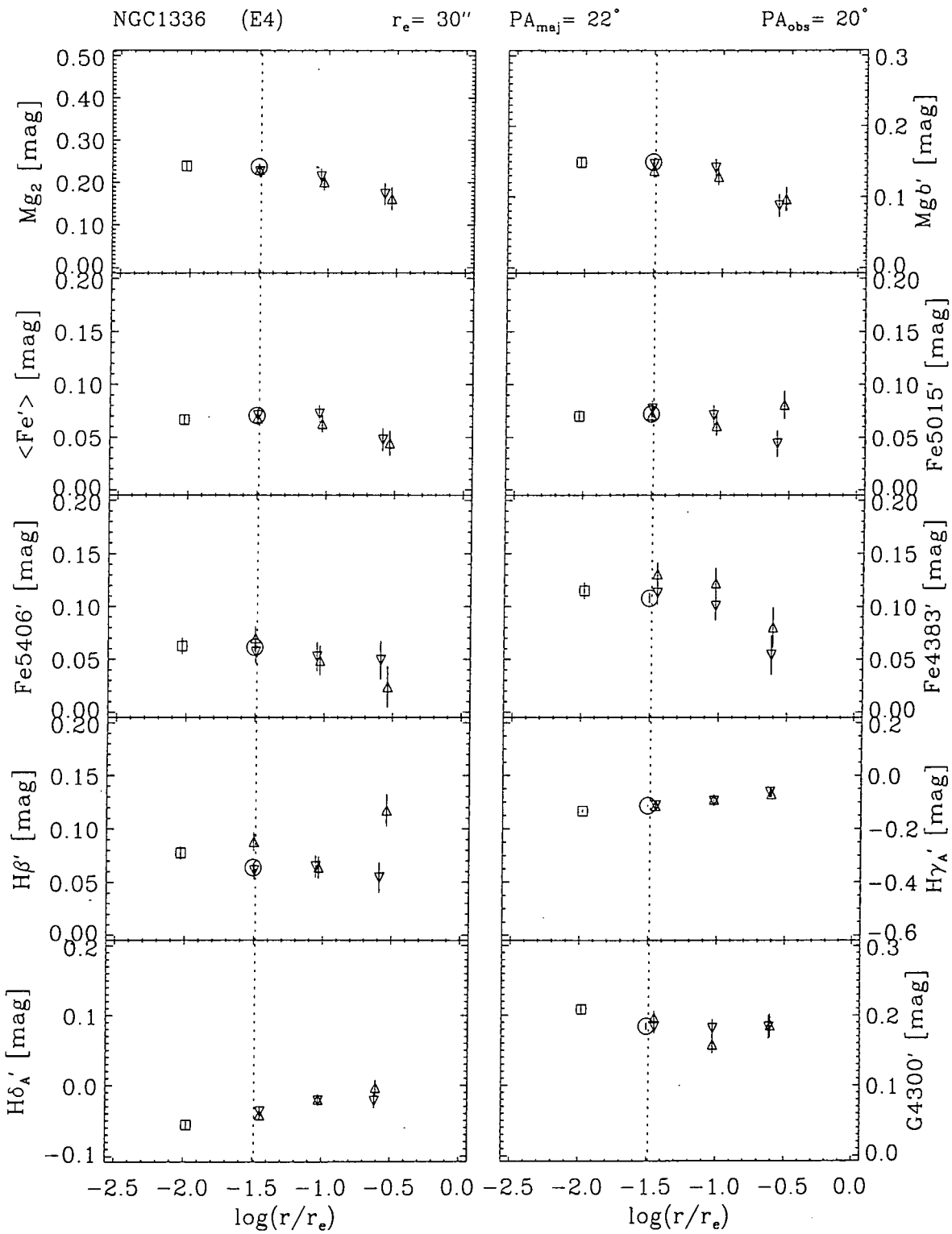

Figure B.3: Line-Strength Gradients: NGC1336 (NTT93)

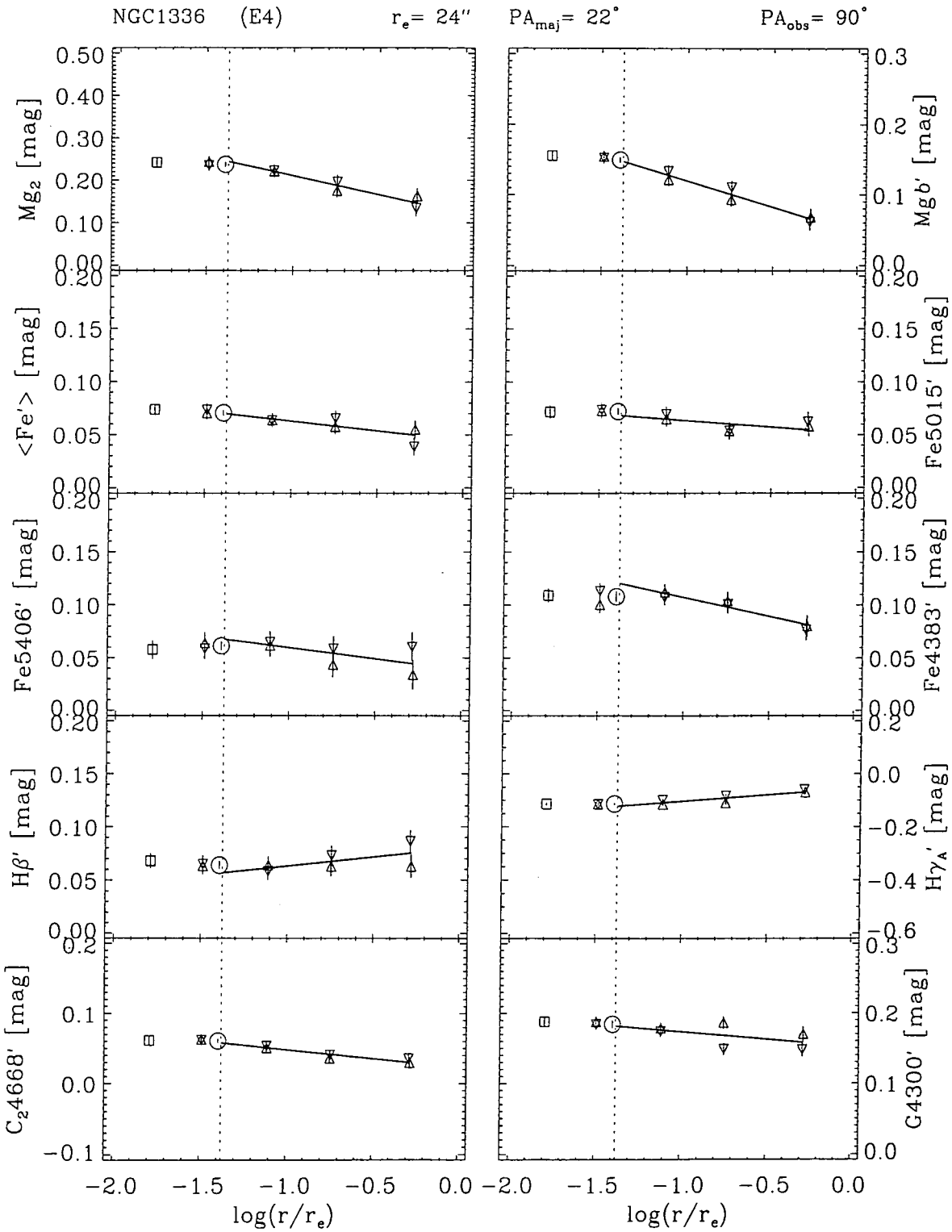

Figure B.4: Line-Strength Gradients: NGC1336 (AAT96)

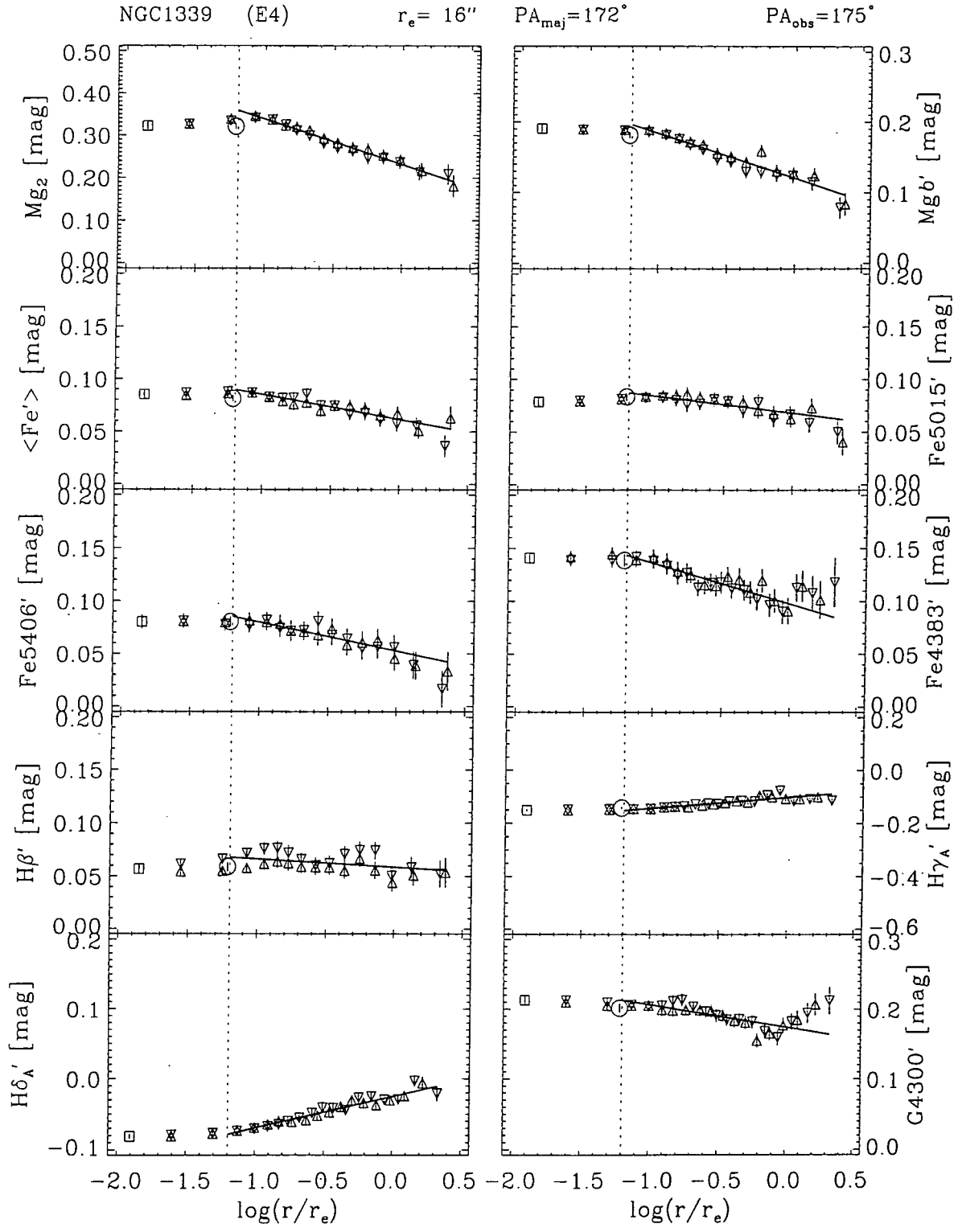

Figure B.5: Line-Strength Gradients: NGC1339 (NTT92)

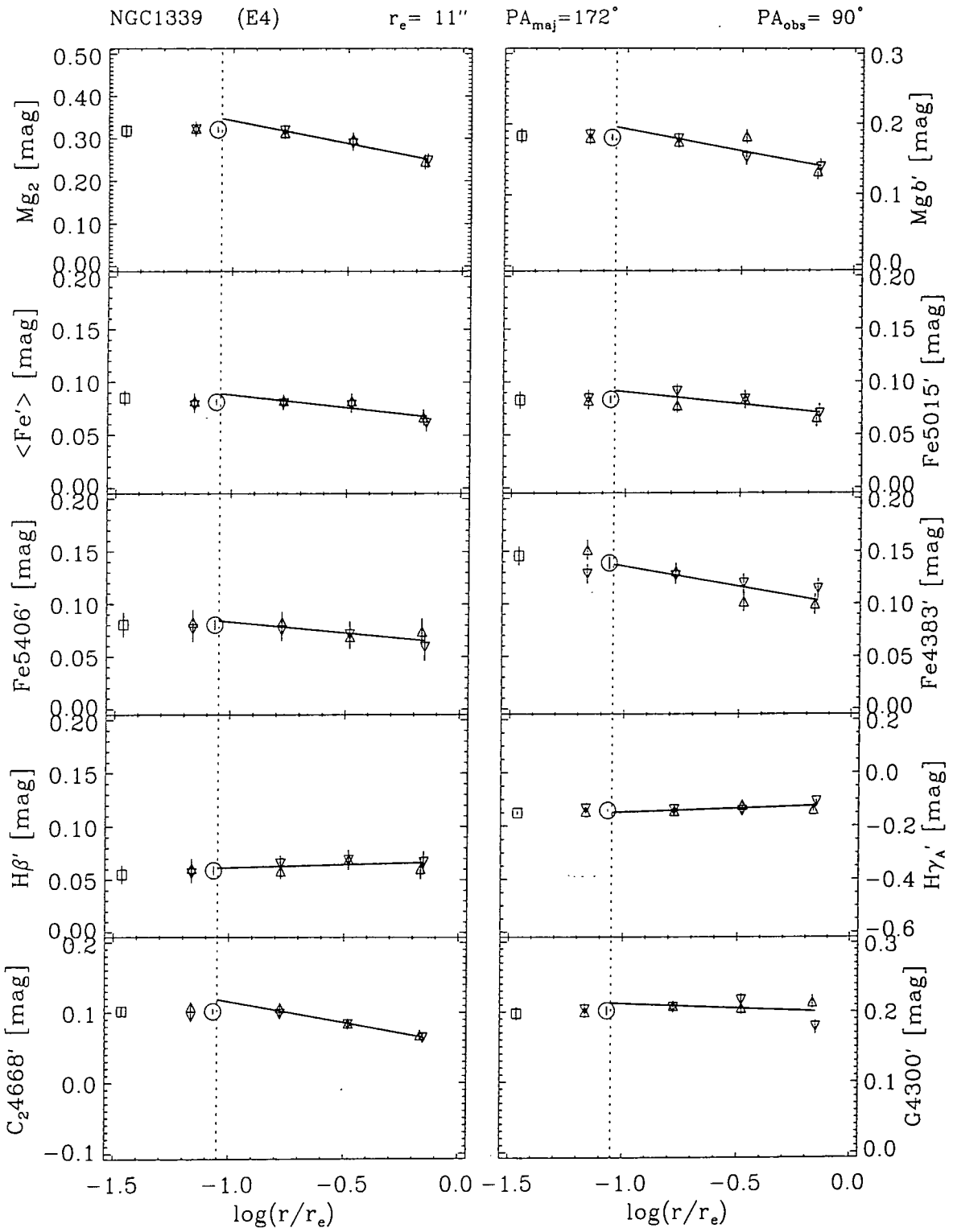

Figure B.6: Line-Strength Gradients: NGC1339 (AAT96)

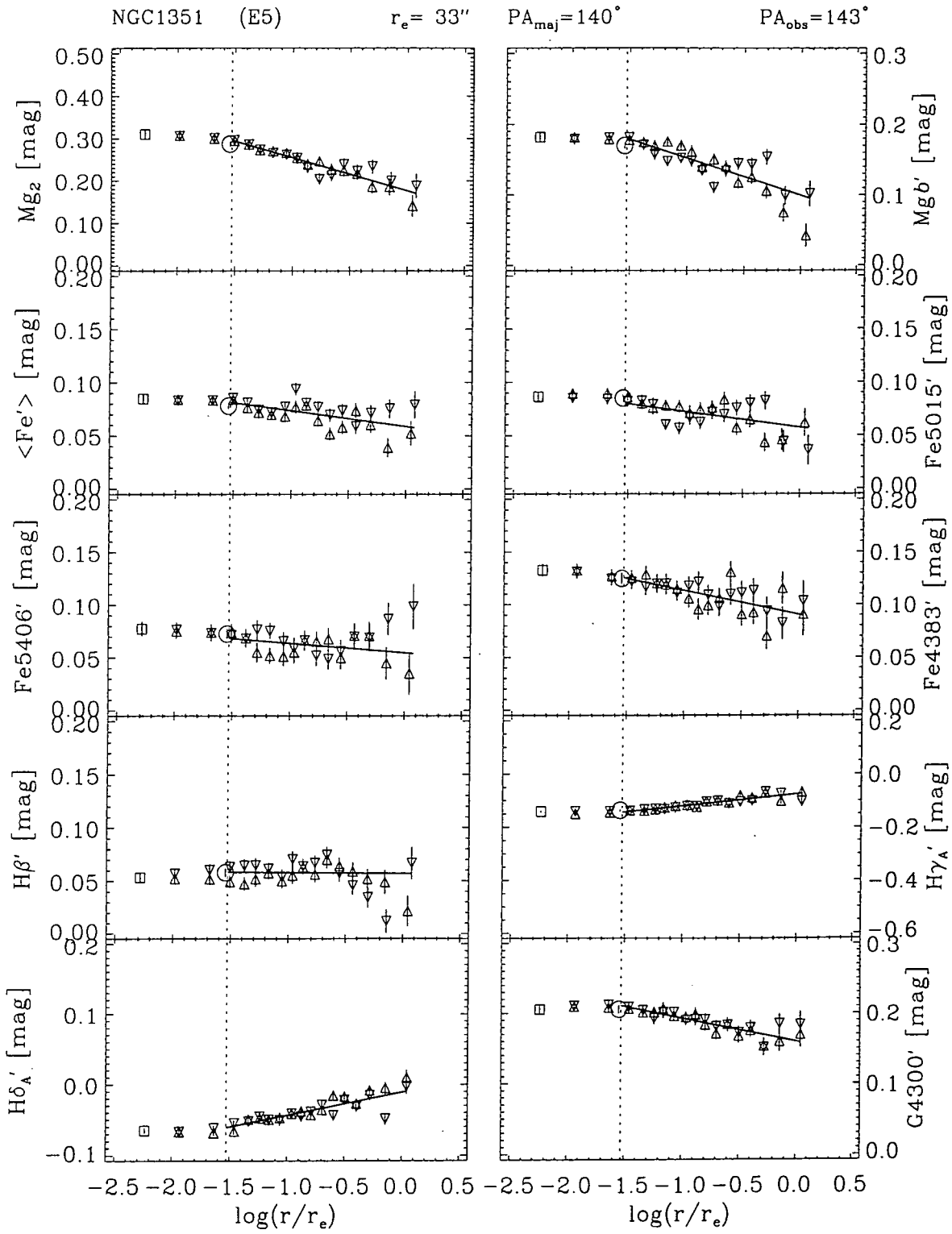

Figure B.7: Line-Strength Gradients: NGC1351 (NTT93)

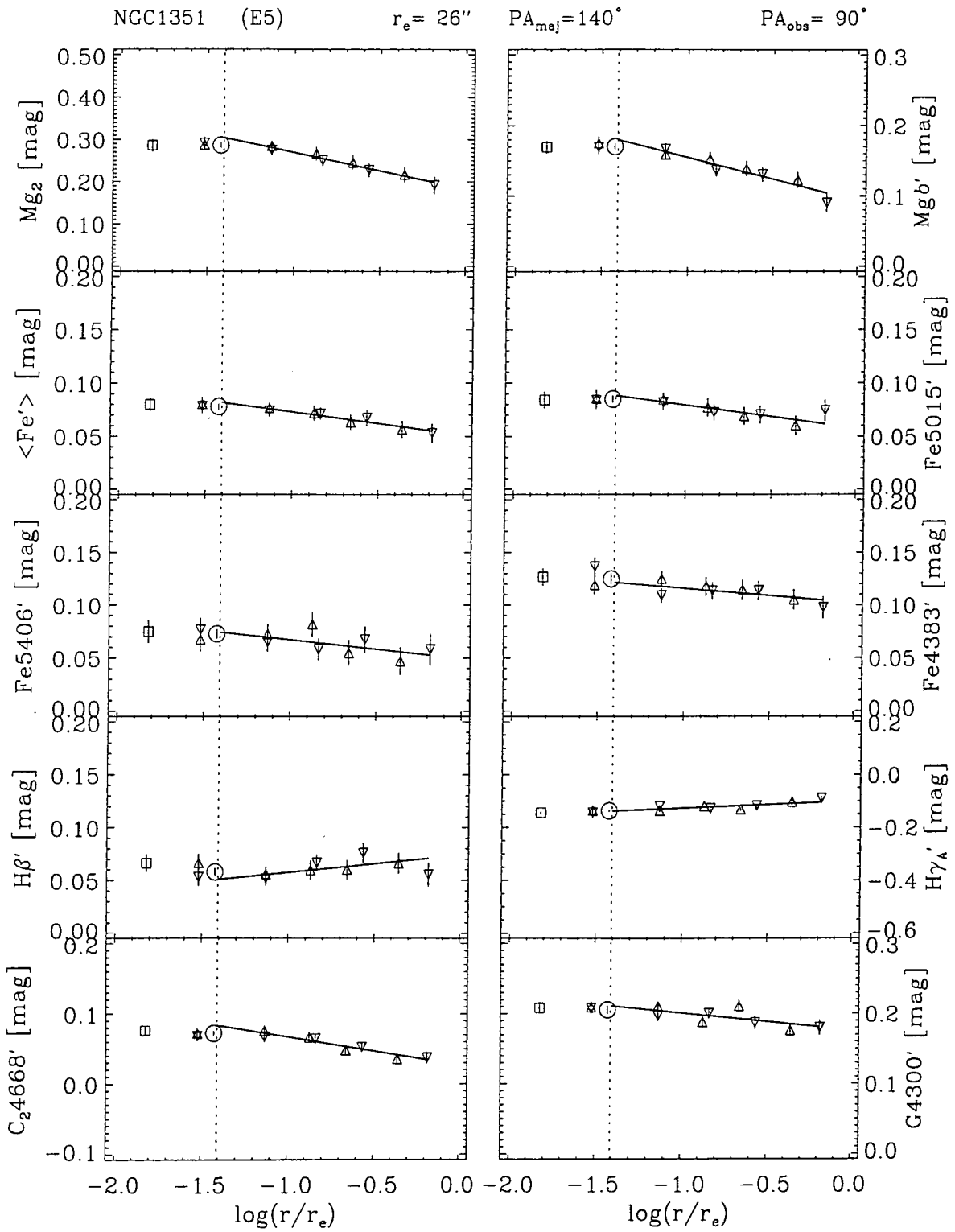

Figure B.8: Line-Strength Gradients: NGC1351 (AAT96)

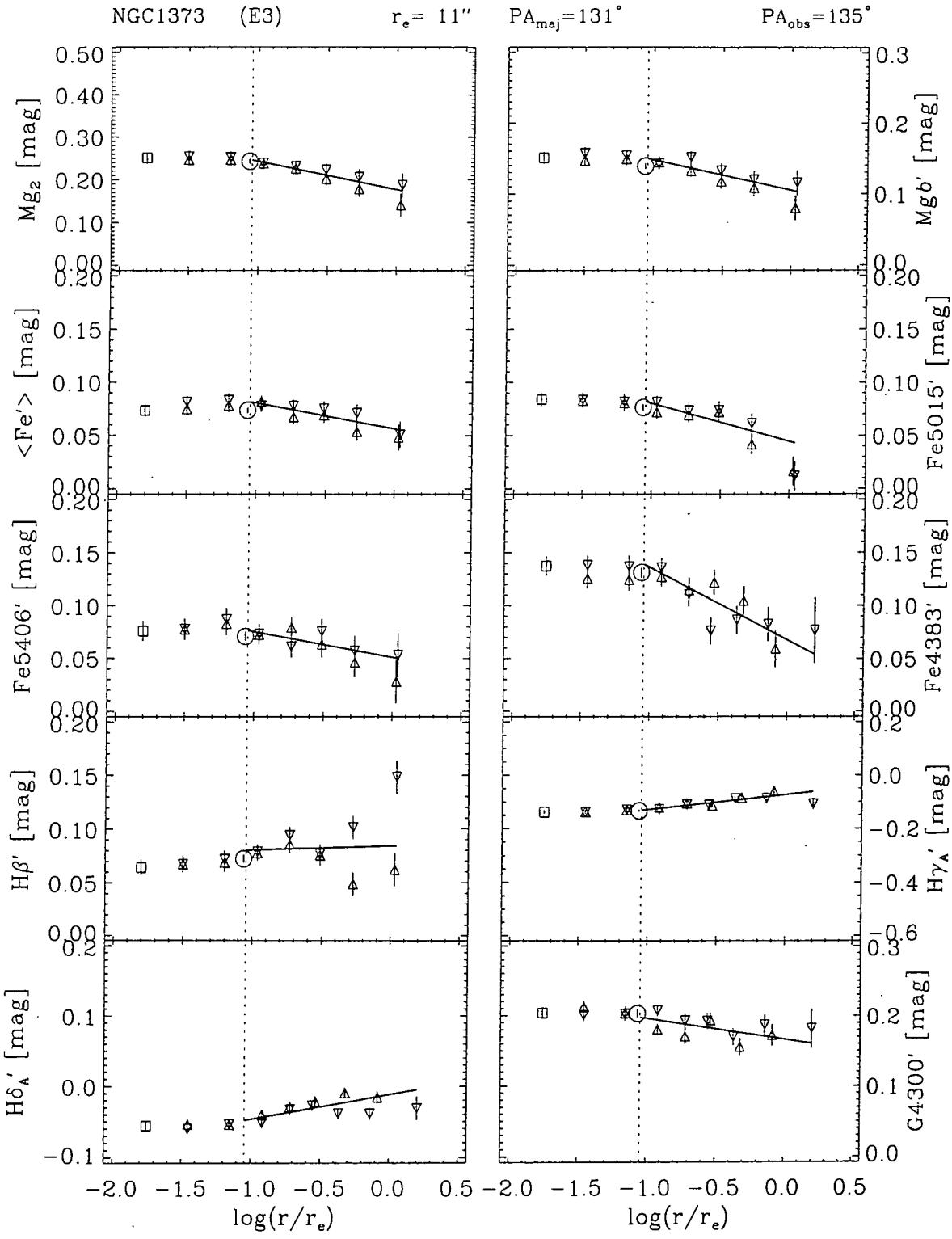

Figure B.9: Line-Strength Gradients: NGC1373 (NTT93)

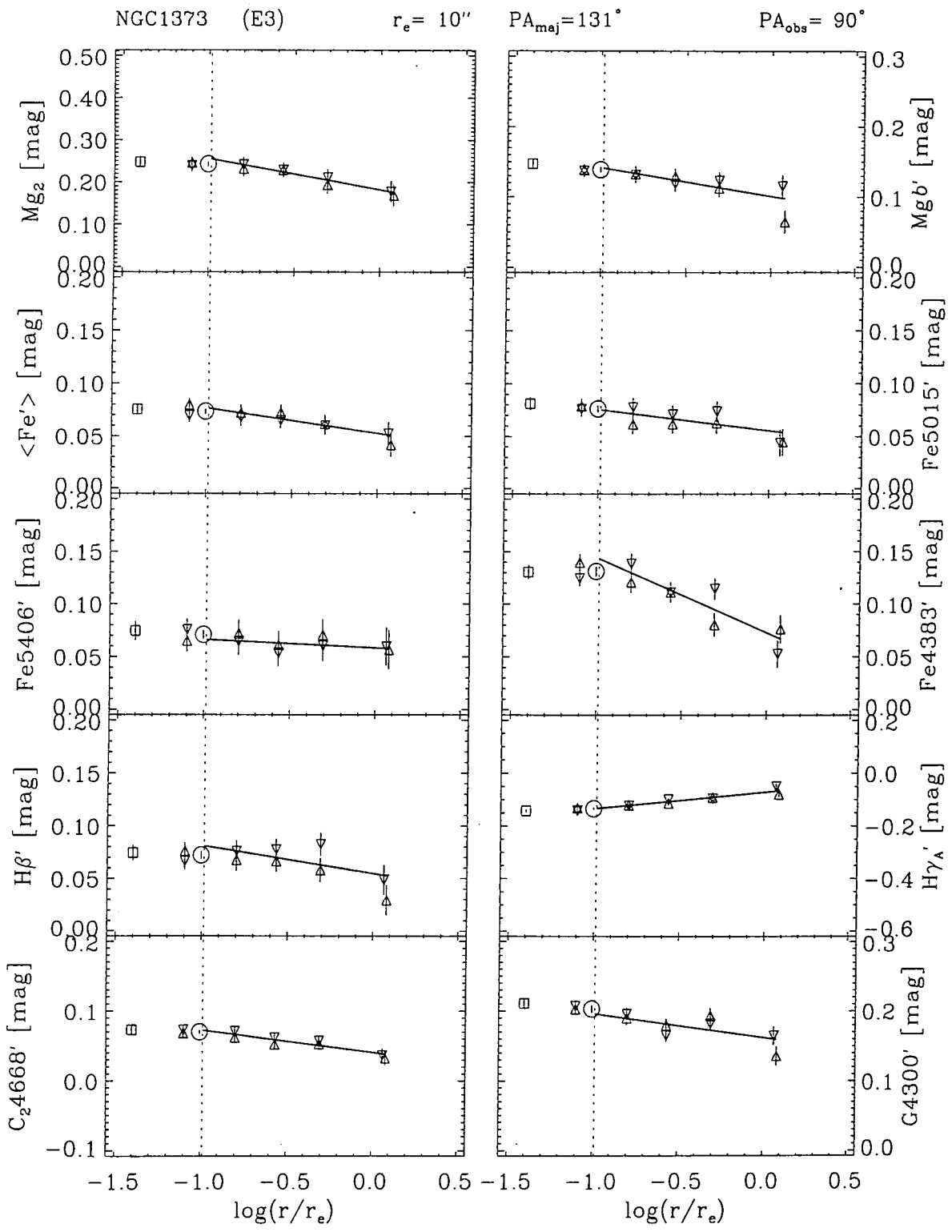

Figure B.10: Line-Strength Gradients: NGC1373 (AAT96)

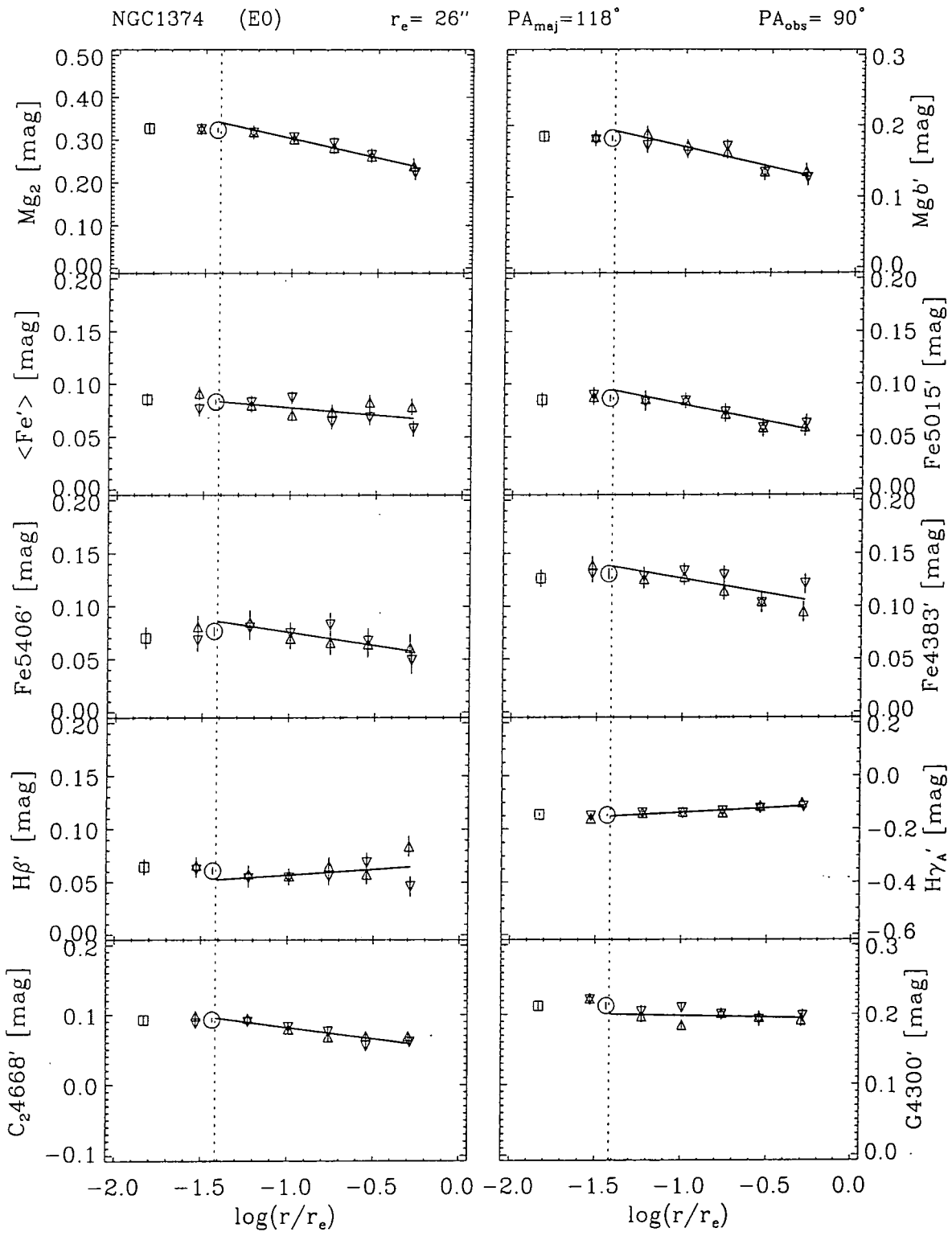

Figure B.11: Line-Strength Gradients: NGC1374 (AAT96)

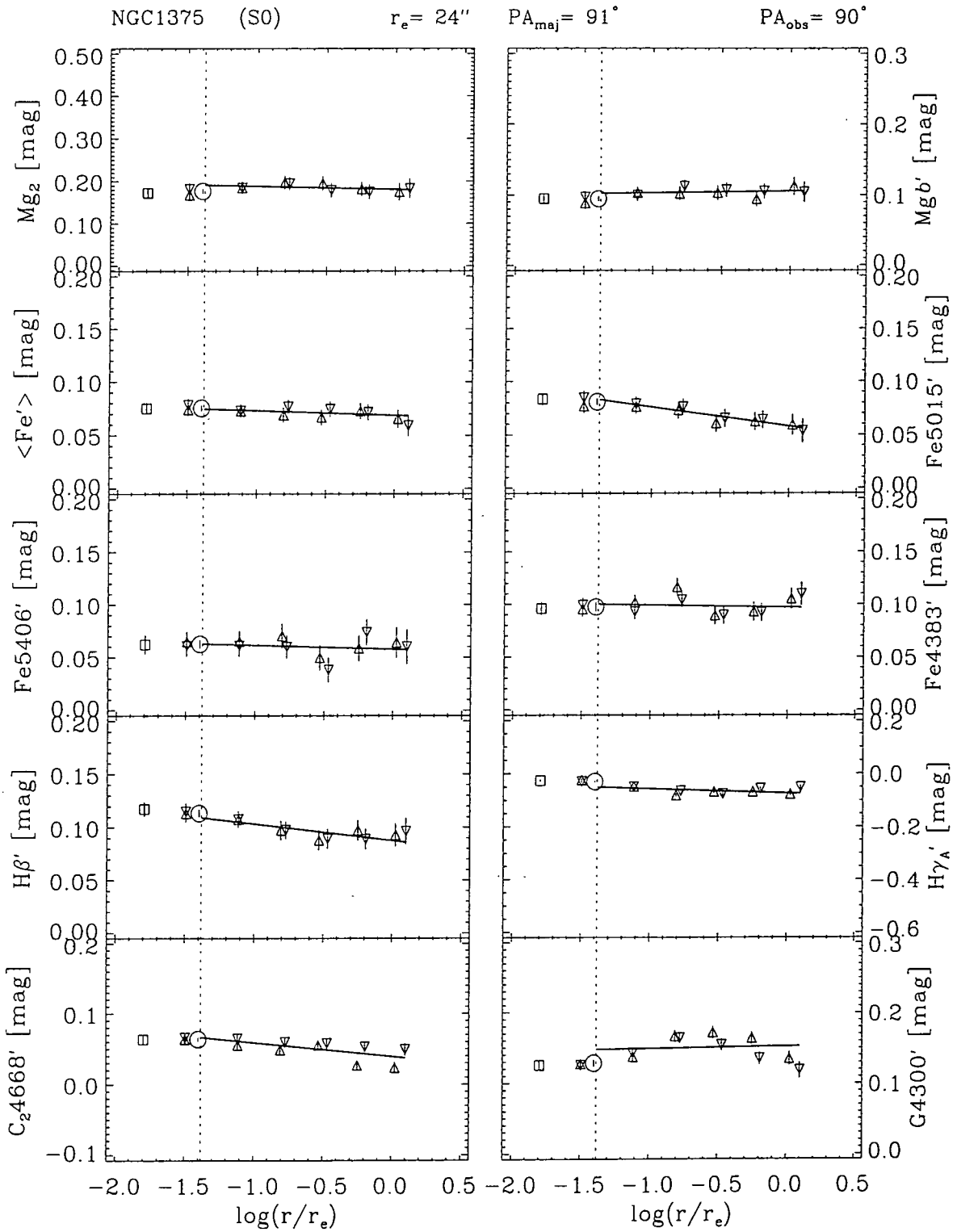

Figure B.12: Line-Strength Gradients: NGC1375 (AAT96)

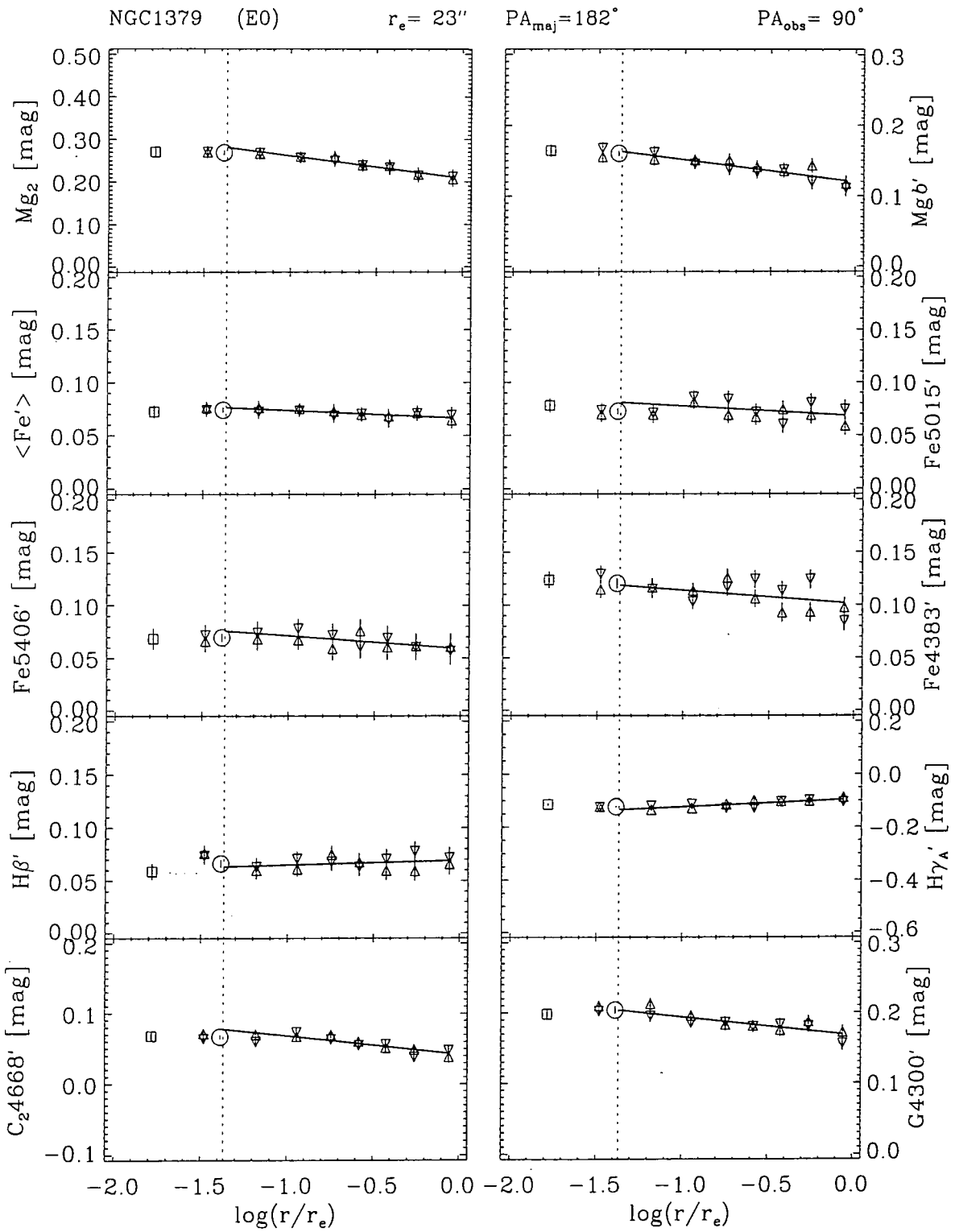

Figure B.13: Line-Strength Gradients: NGC1379 (AAT96)

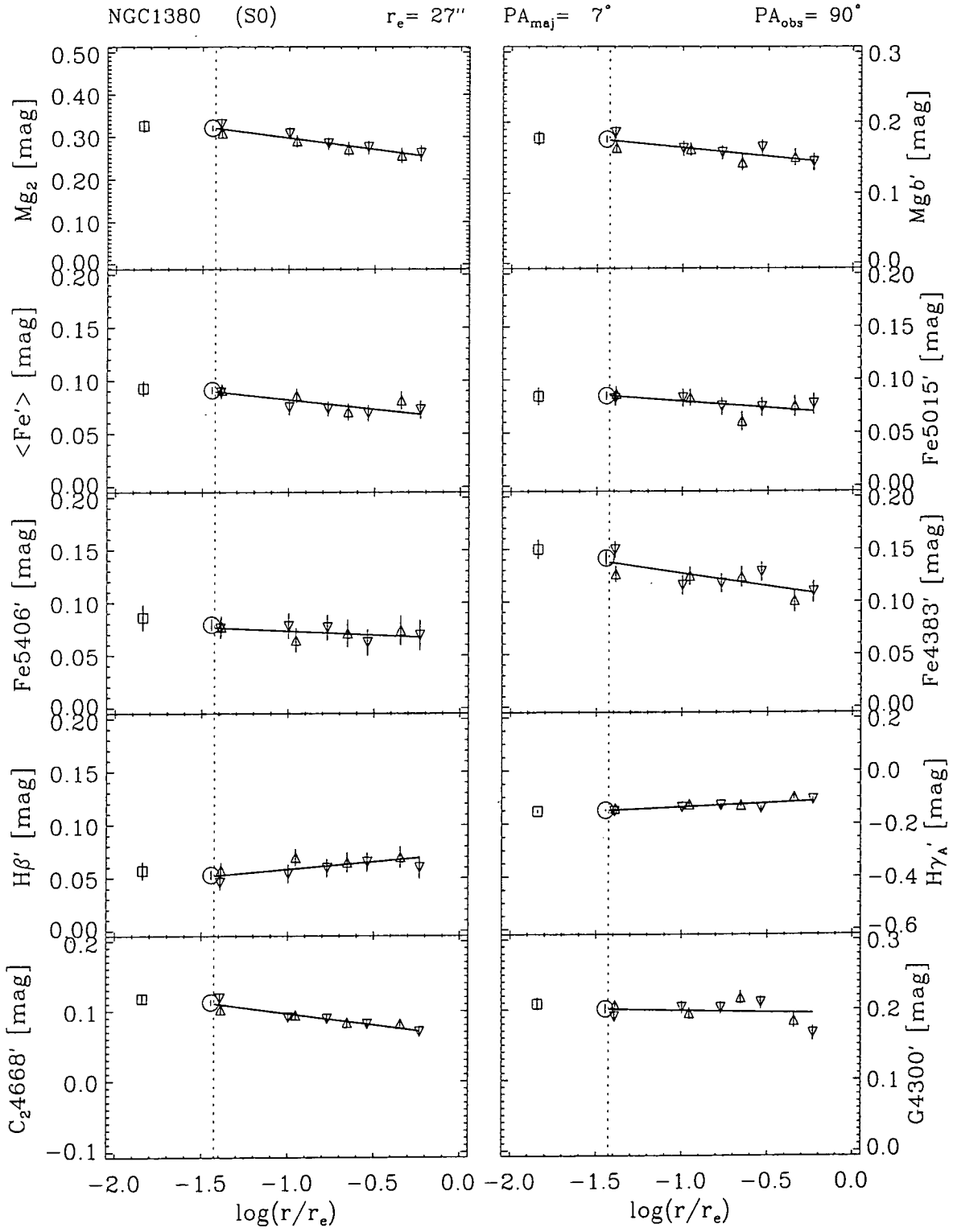

Figure B.14: Line-Strength Gradients: NGC1380 (AAT96)

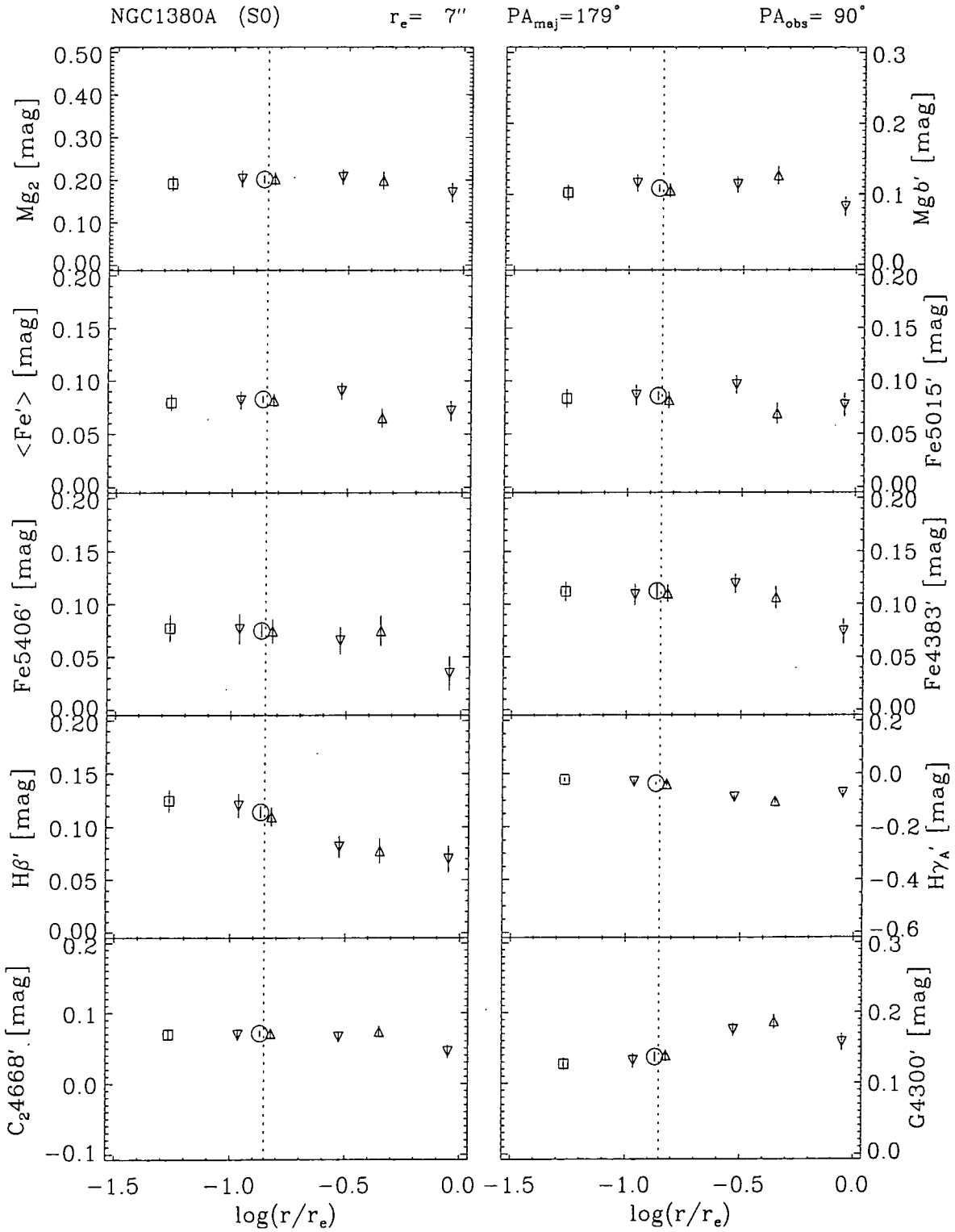

Figure B.15: Line-Strength Gradients: NGC1380A (AAT96)

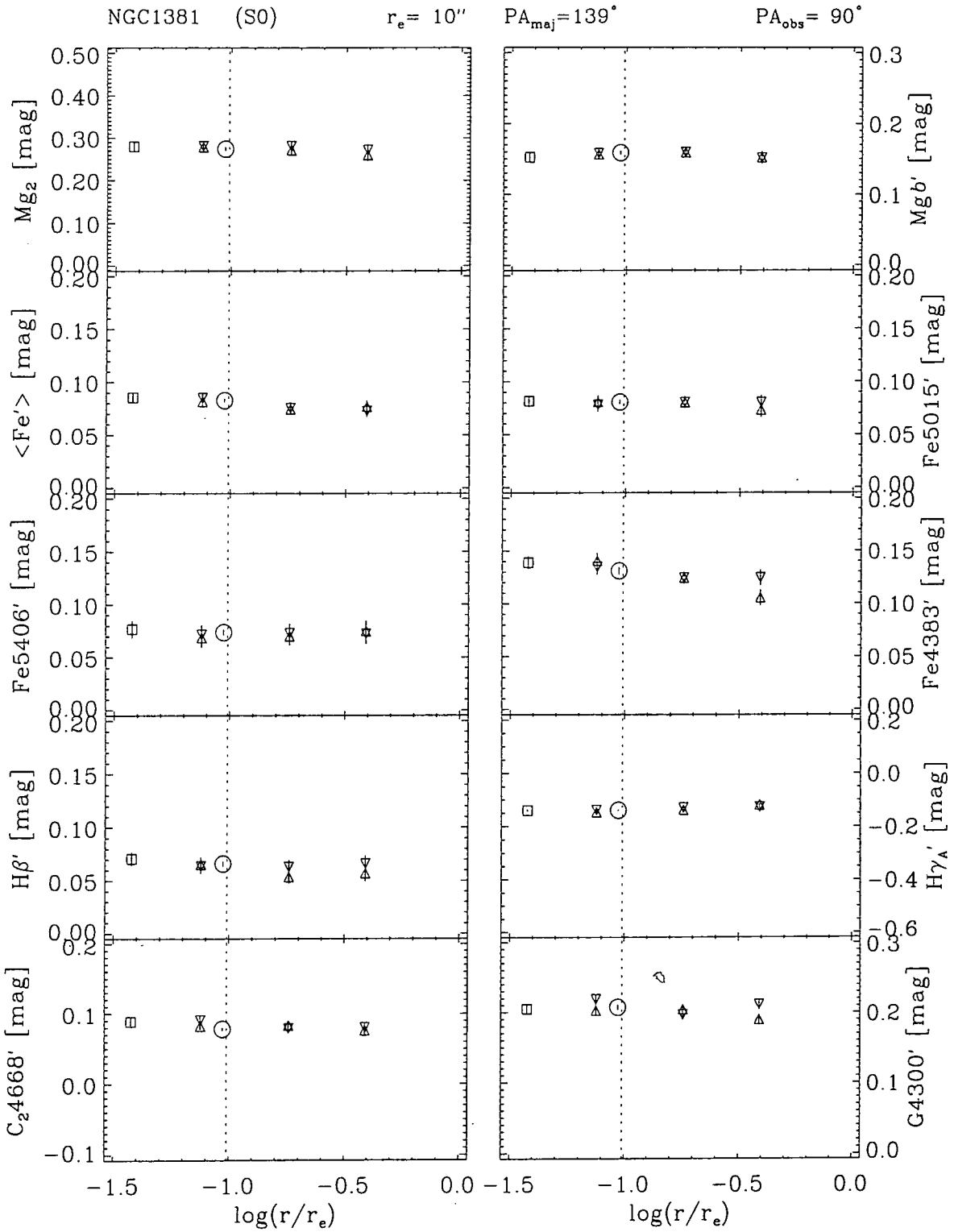

Figure B.16: Line-Strength Gradients: NGC1381 (AAT96)

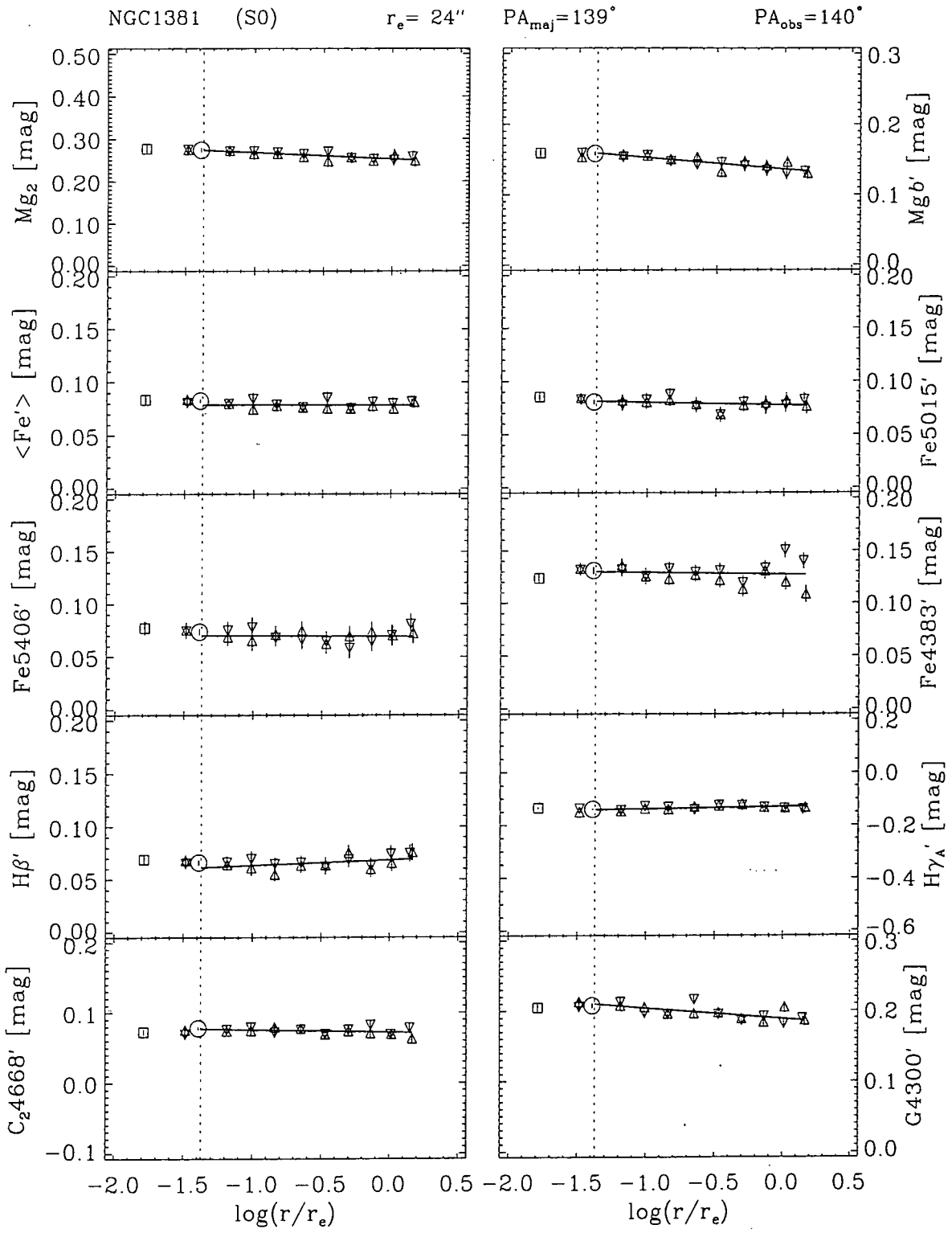

Figure B.17: Line-Strength Gradients: NGC1381 (AAT96)

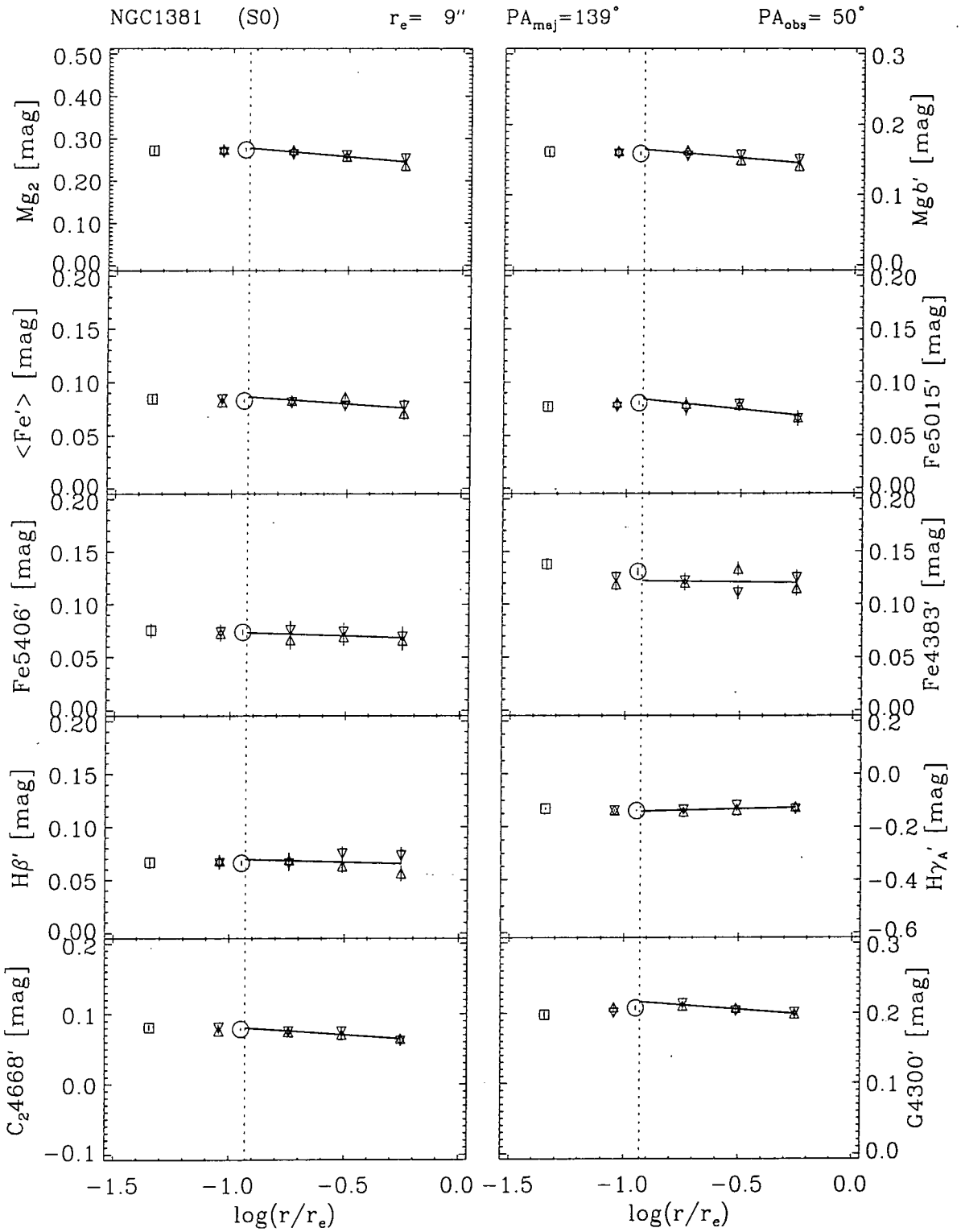

Figure B.18: Line-Strength Gradients: NGC1381 (AAT96)

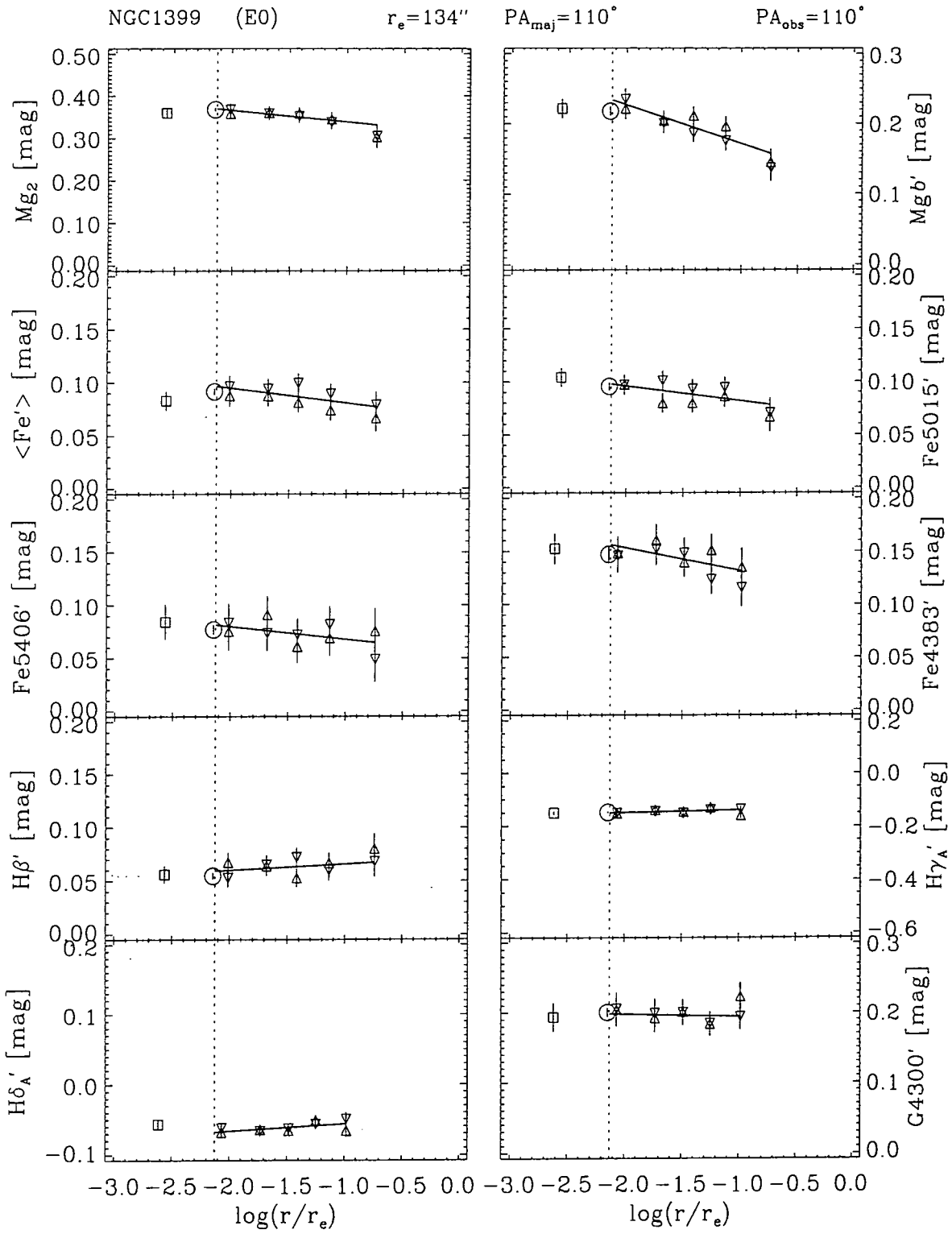

Figure B.19: Line-Strength Gradients: NGC1399 (NTT92)

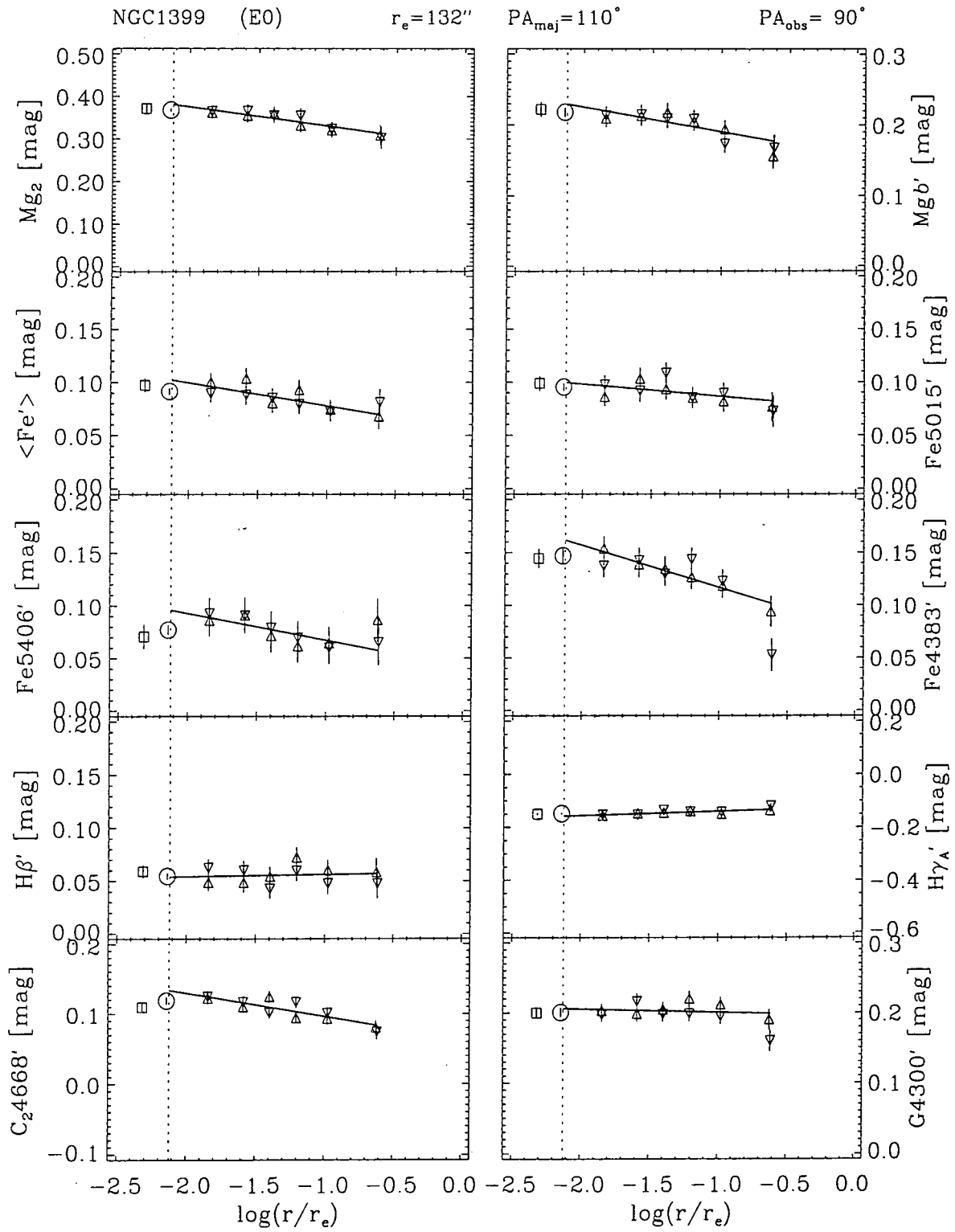

Figure B.20: Line-Strength Gradients: NGC1399 (AAT96)

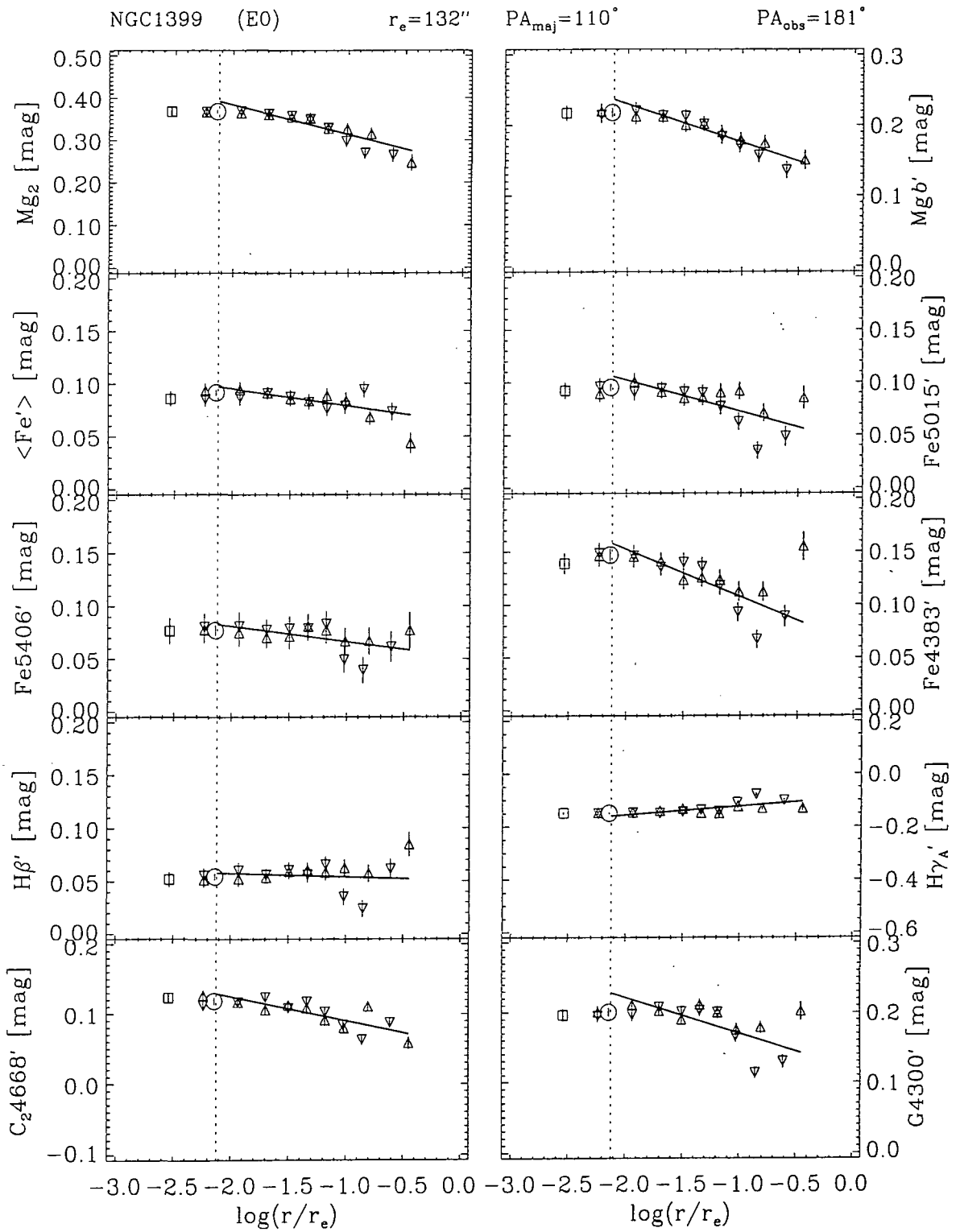

Figure B.21: Line-Strength Gradients: NGC1399 (AAT96)

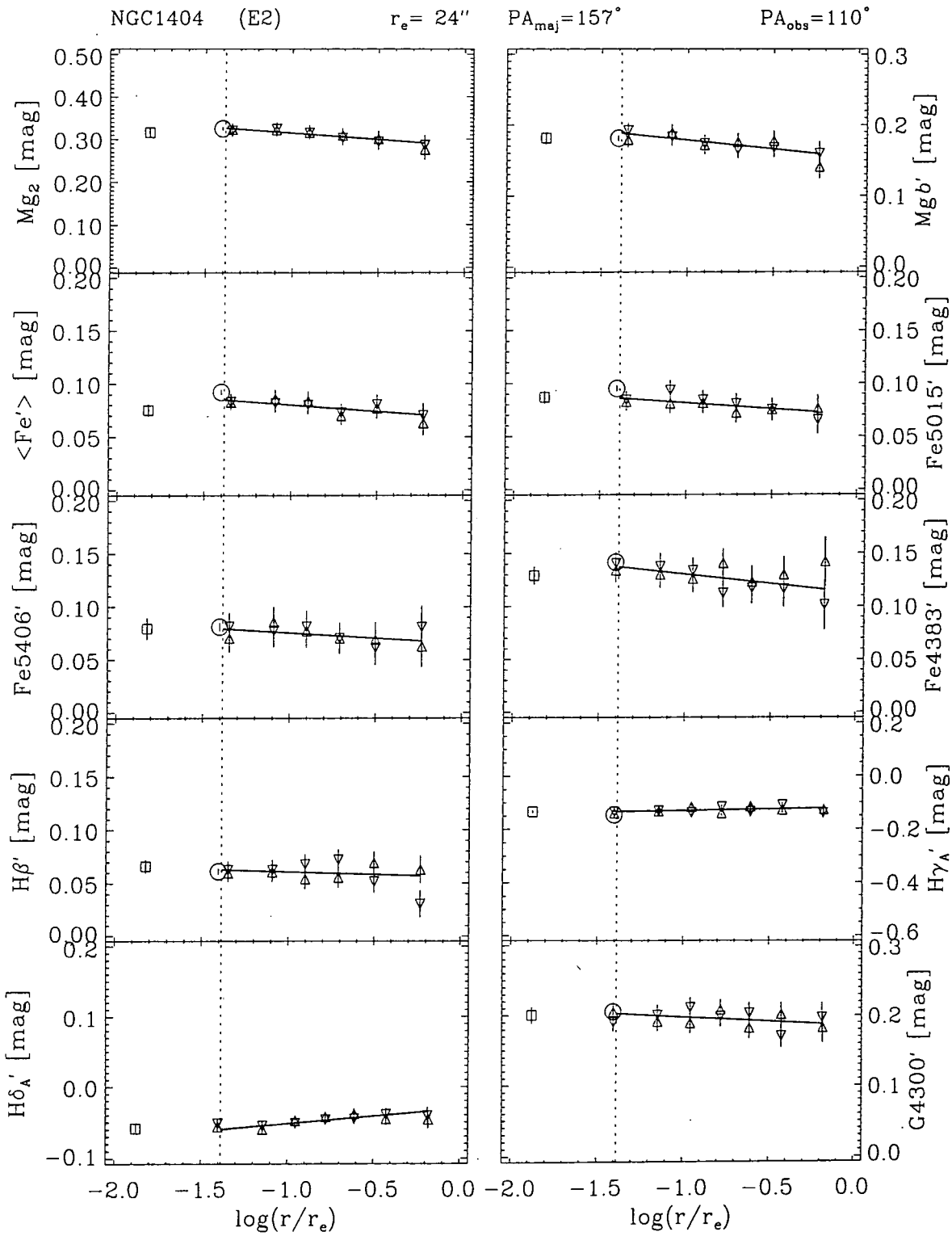

Figure B.22: Line-Strength Gradients: NGC1404 (NTT92)

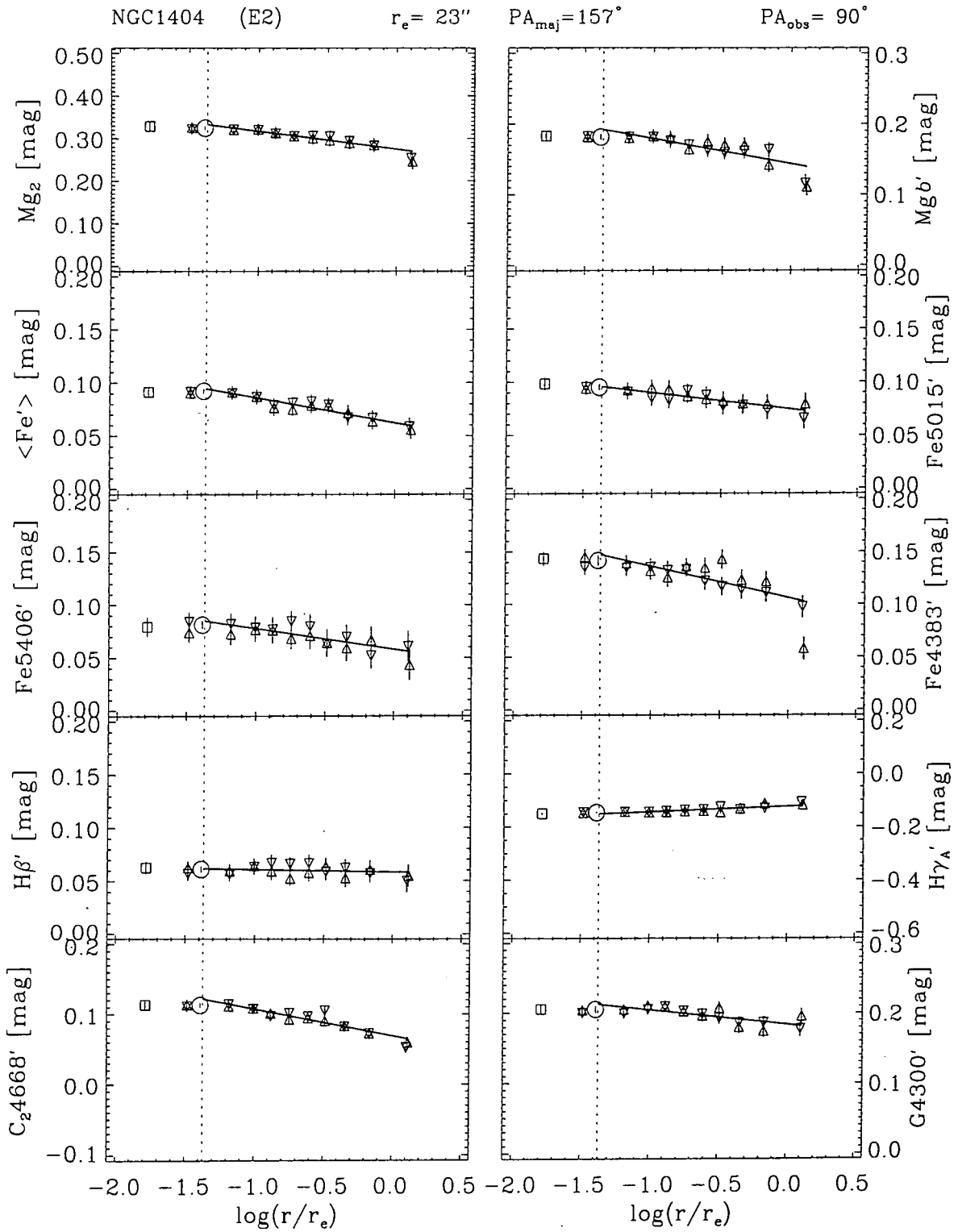

Figure B.23: Line-Strength Gradients: NGC1404 (AAT96)

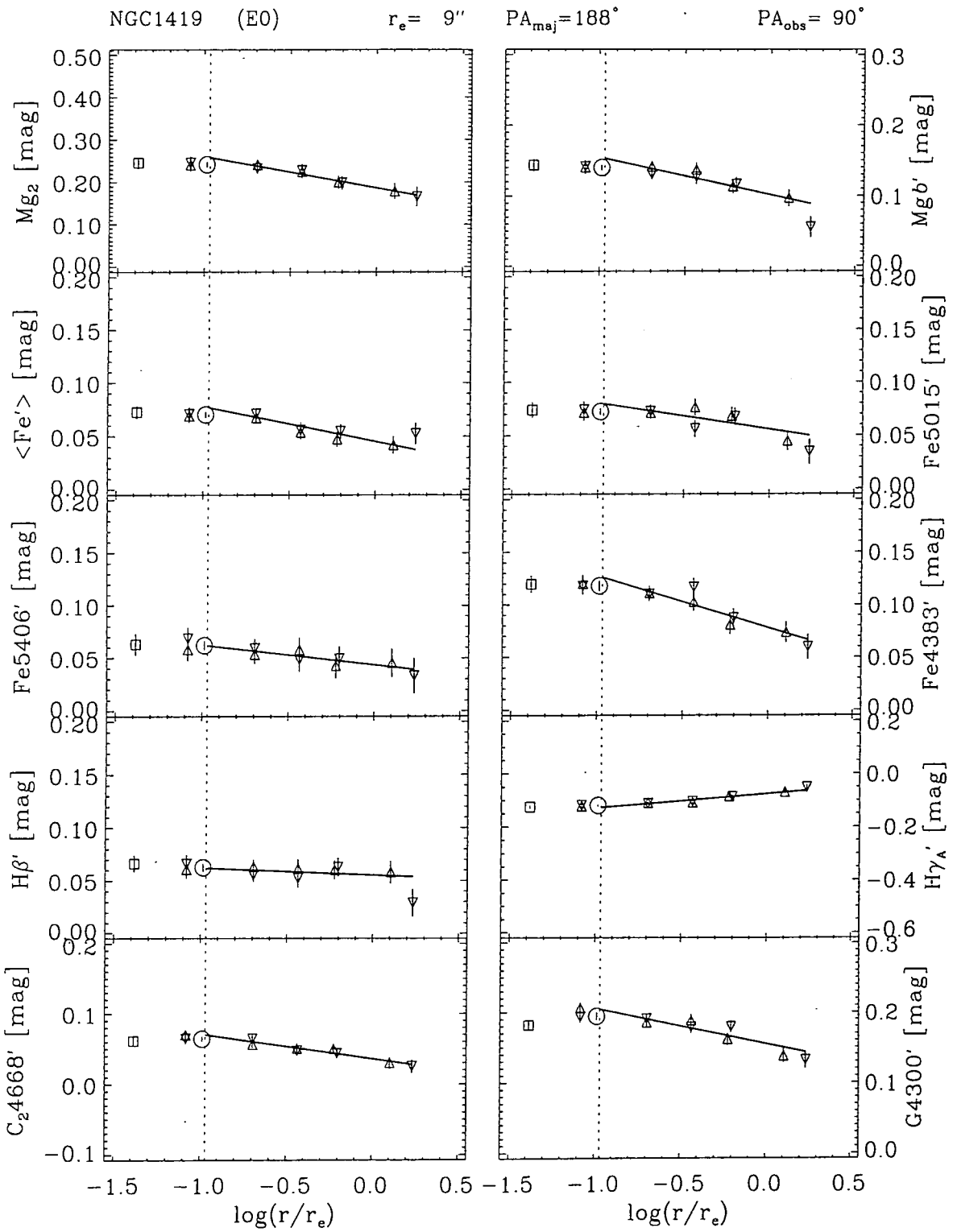

Figure B.24: Line-Strength Gradients: NGC1419 (AAT96)

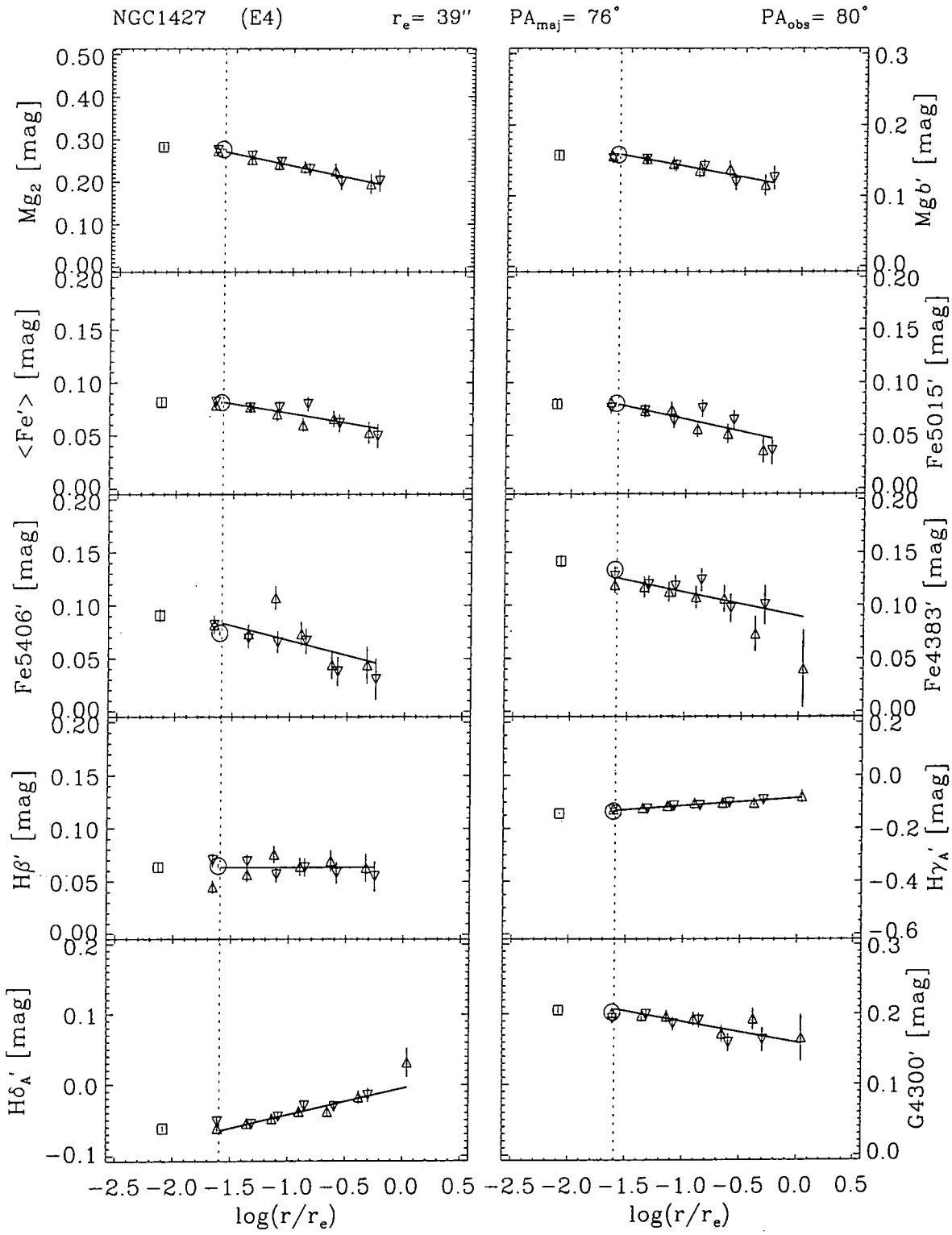

Figure B.25: Line-Strength Gradients: NGC1427 (NTT93)

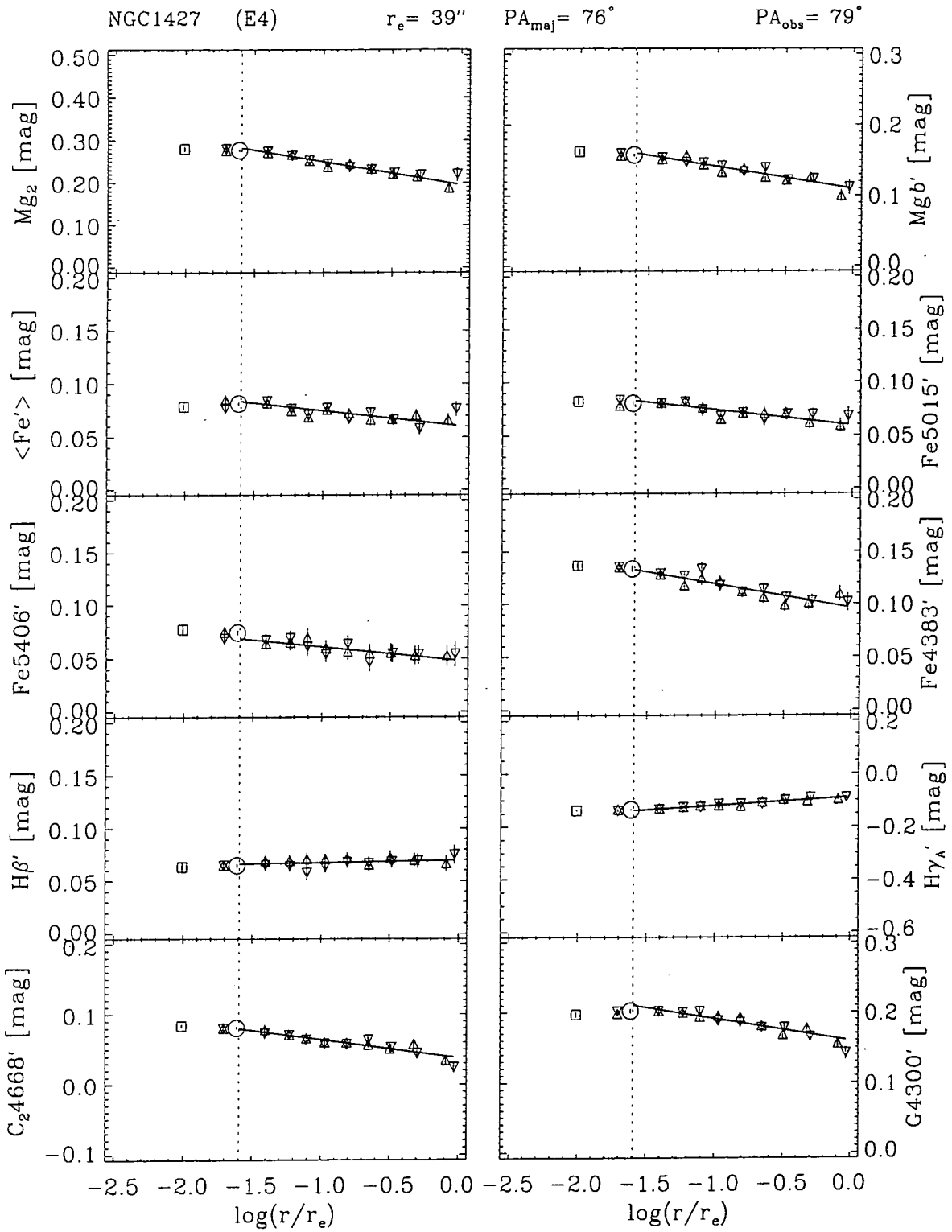

Figure B.26: Line-Strength Gradients: NGC1427 (AAT96)

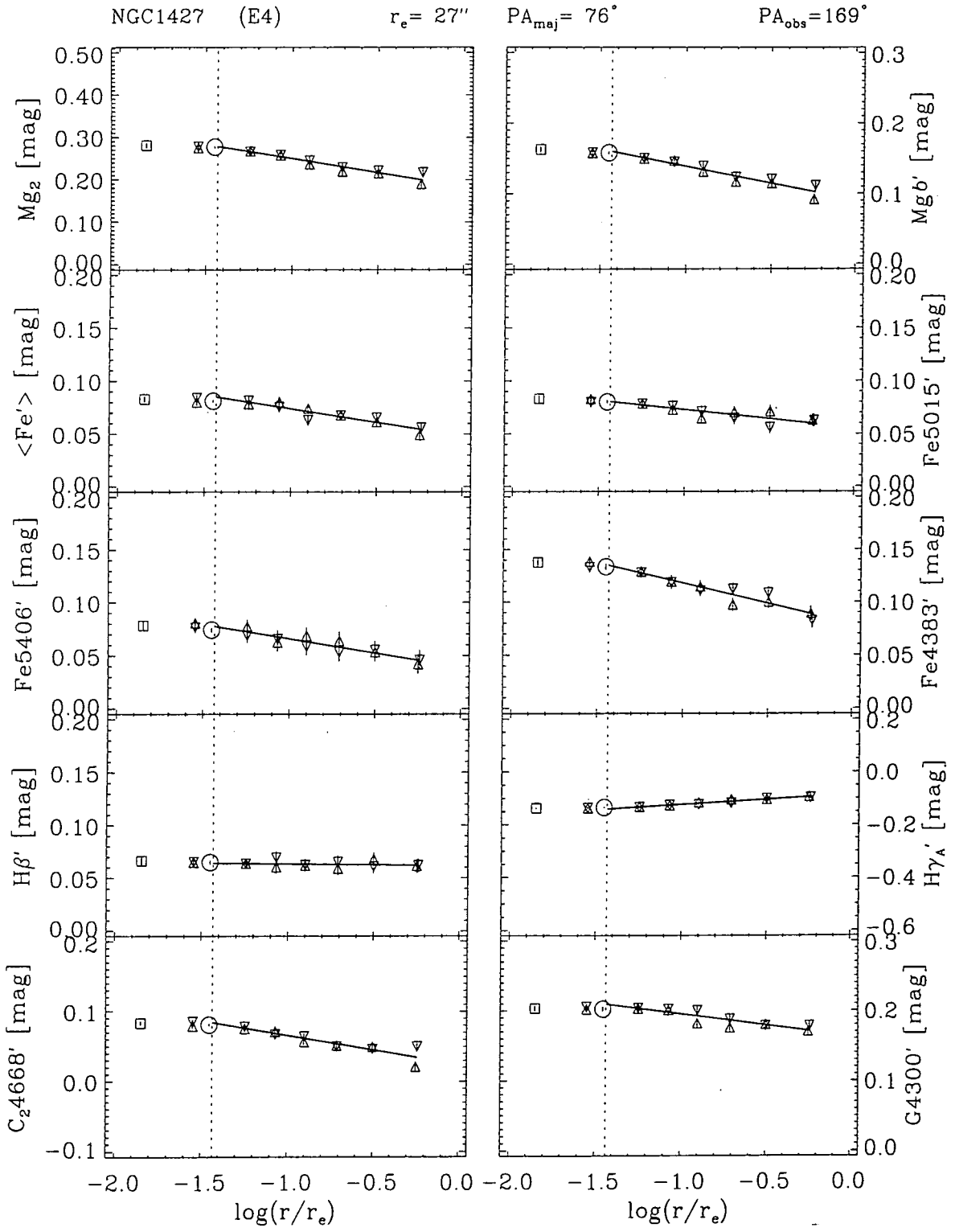

Figure B.27: Line-Strength Gradients: NGC1427 (AAT96)

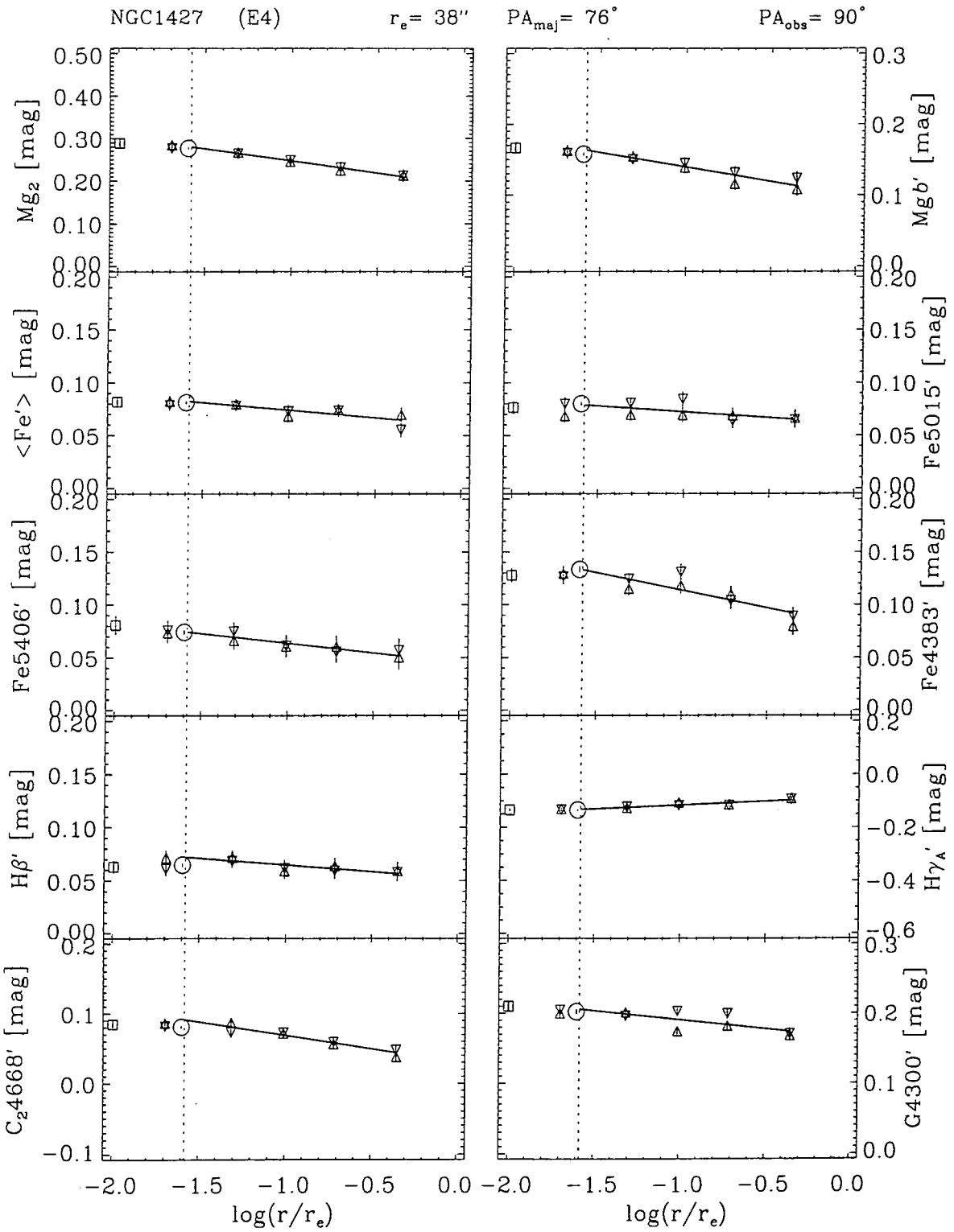

Figure B.28: Line-Strength Gradients: NGC1427 (AAT96)

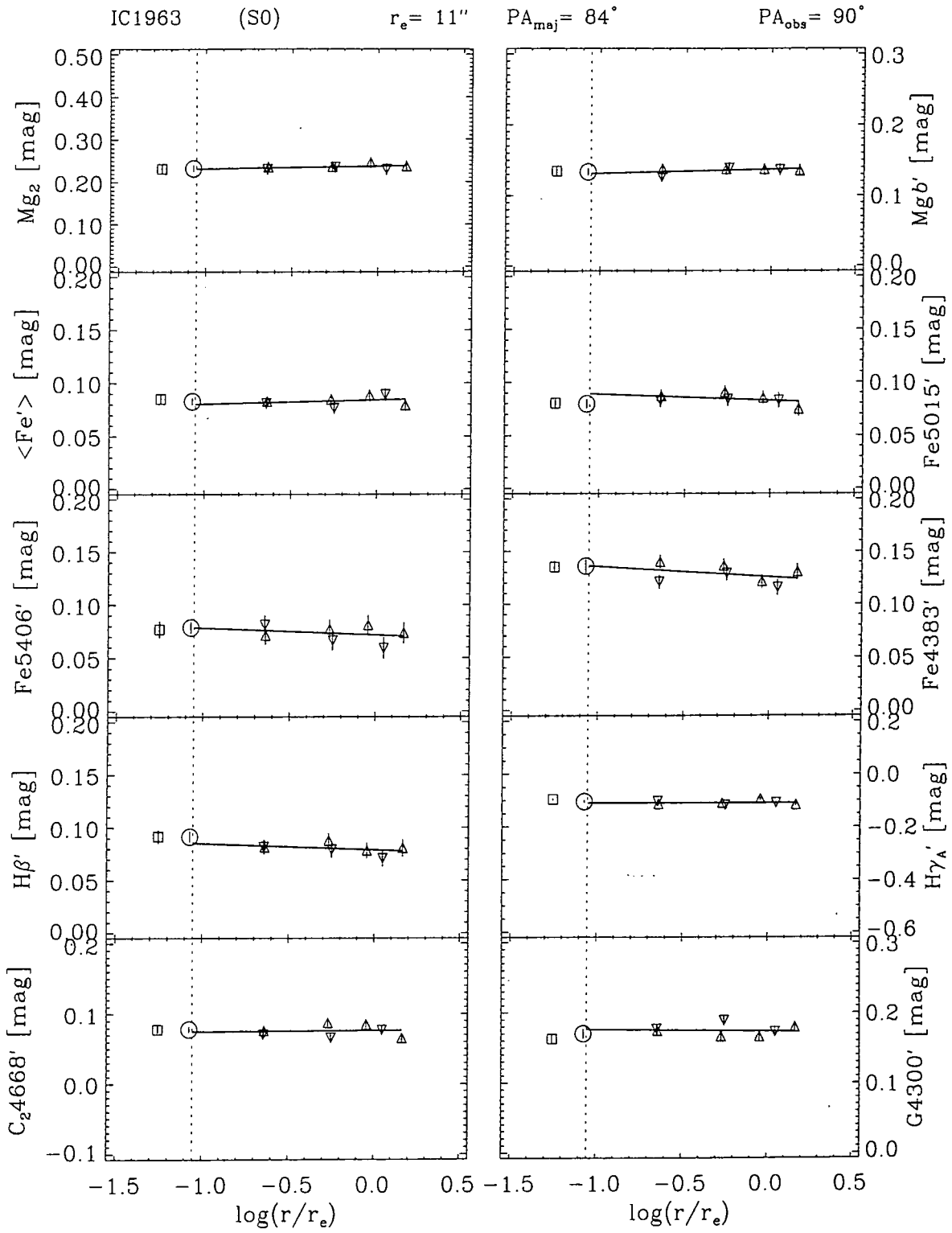

Figure B.29: Line-Strength Gradients: IC1963 (AAT96)

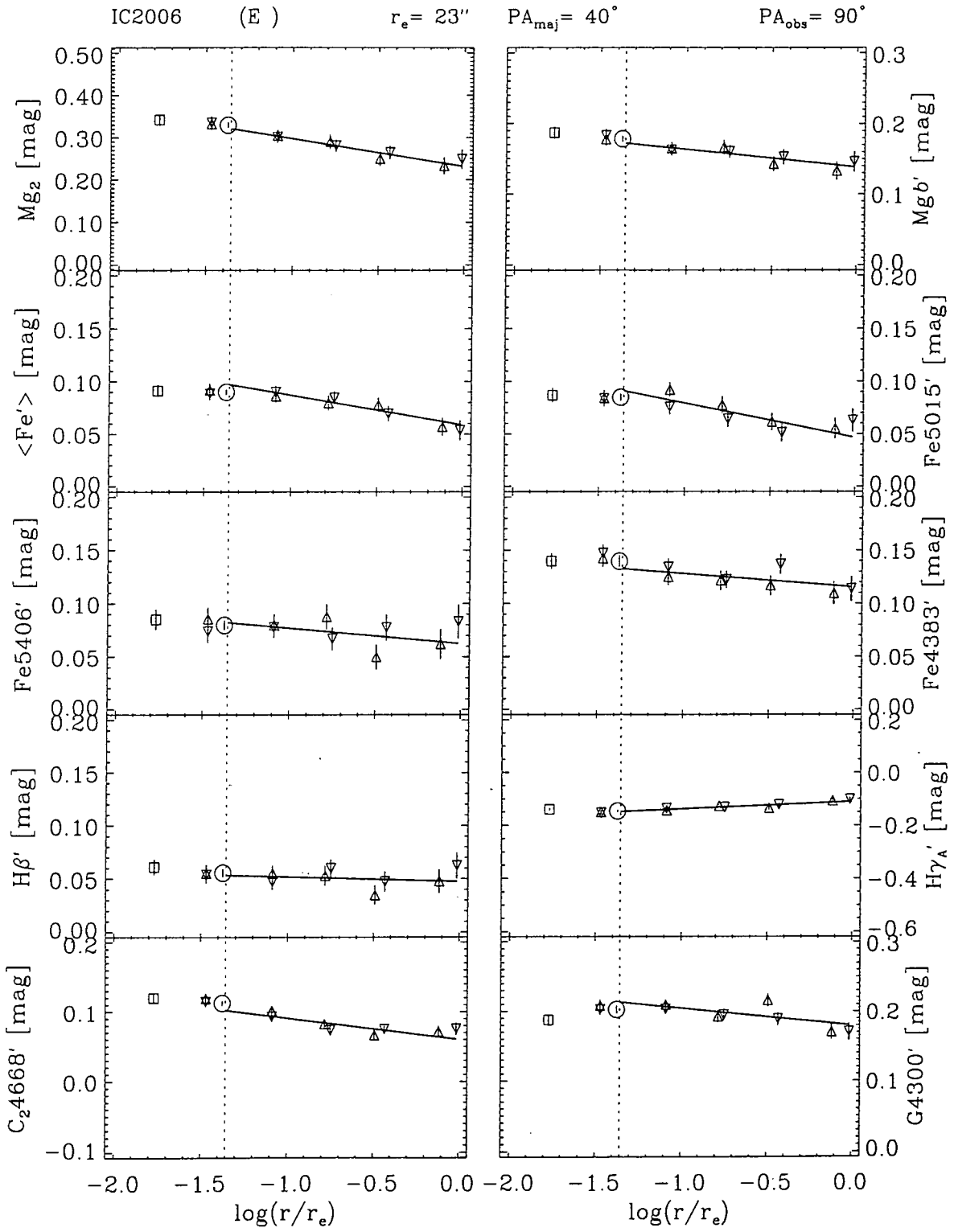

Figure B.30: Line-Strength Gradients: IC2006 (AAT96)

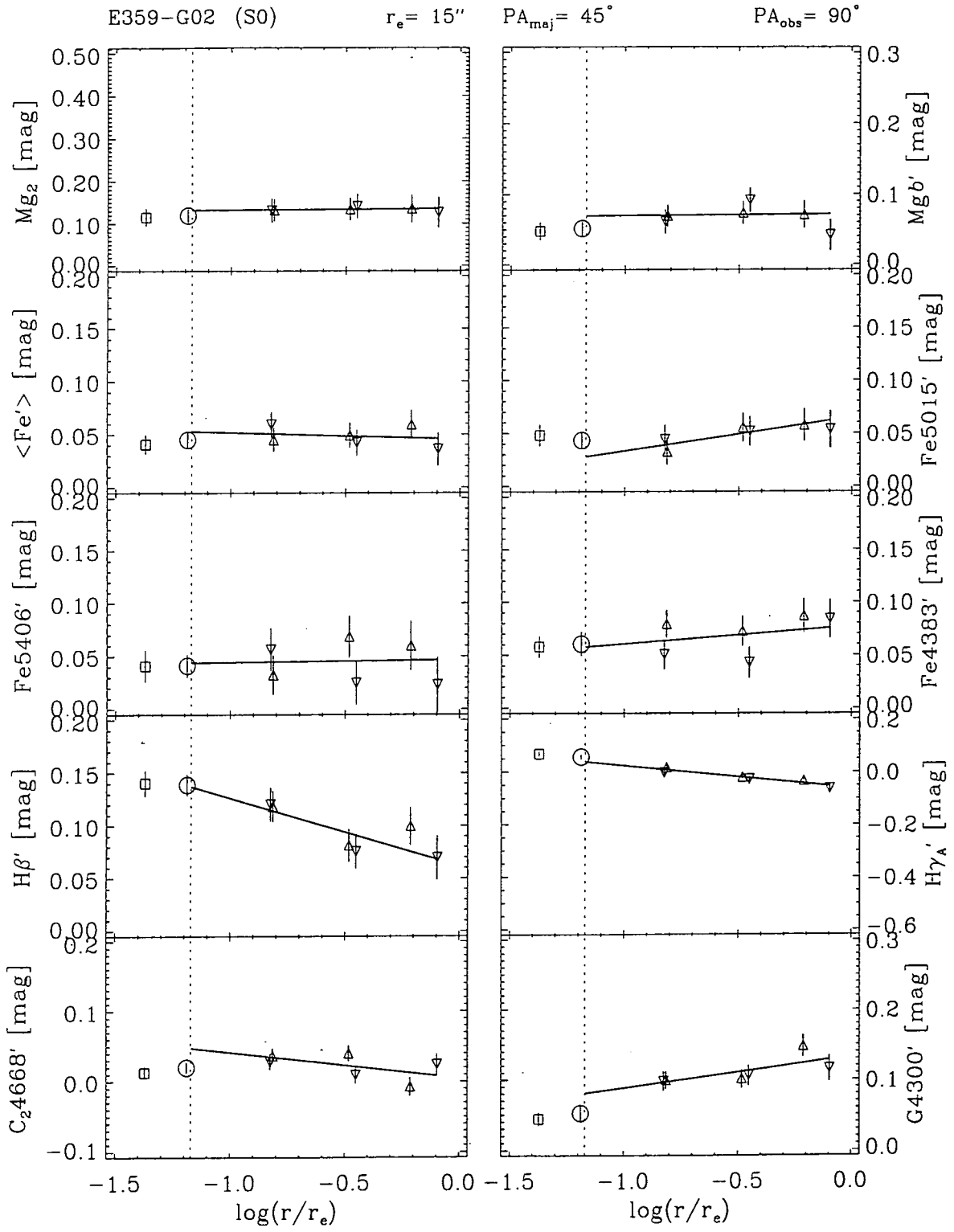

Figure B.31: Line-Strength Gradients: E359-G02 (AAT96)

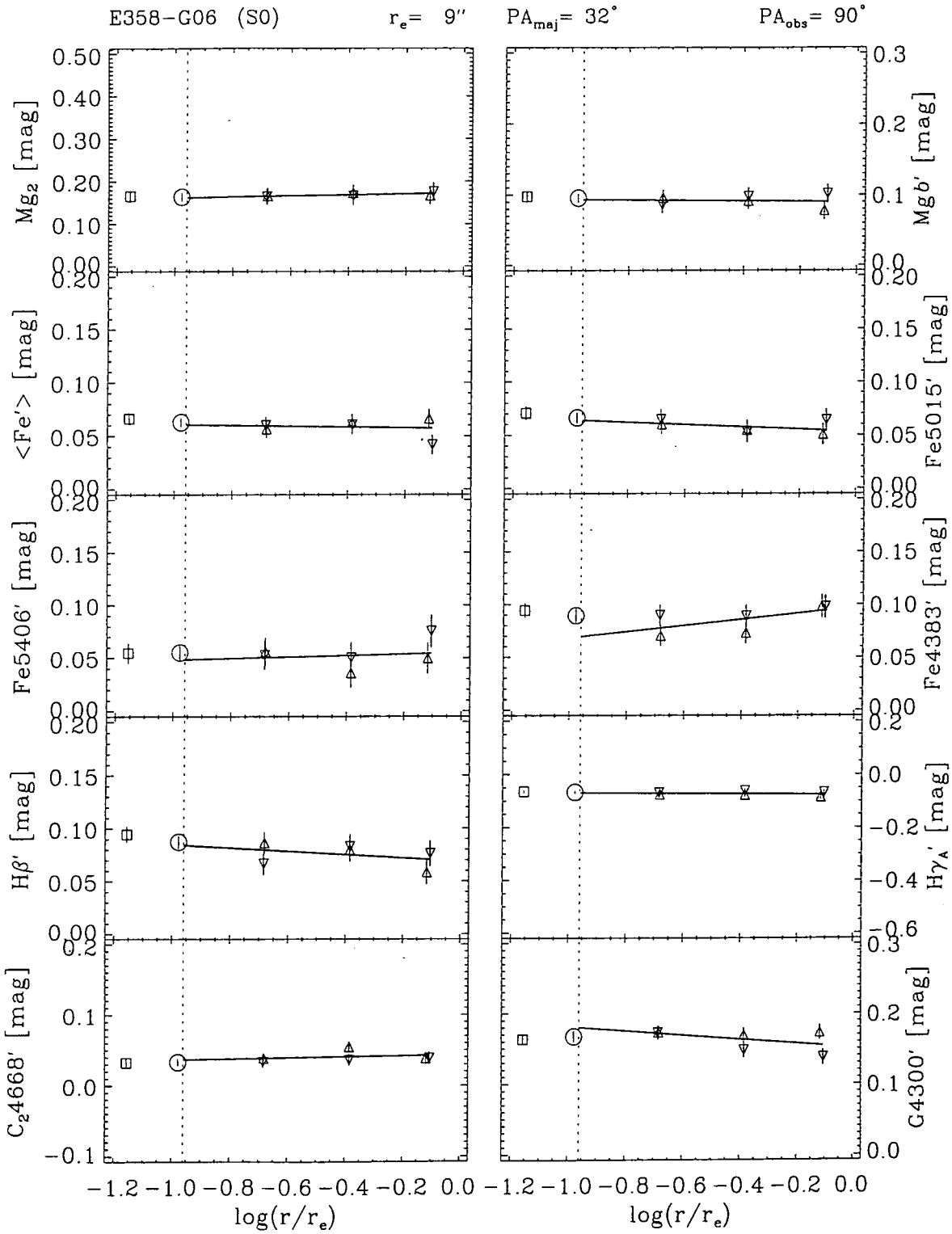

Figure B.32: Line-Strength Gradients: E358-G06 (AAT96)

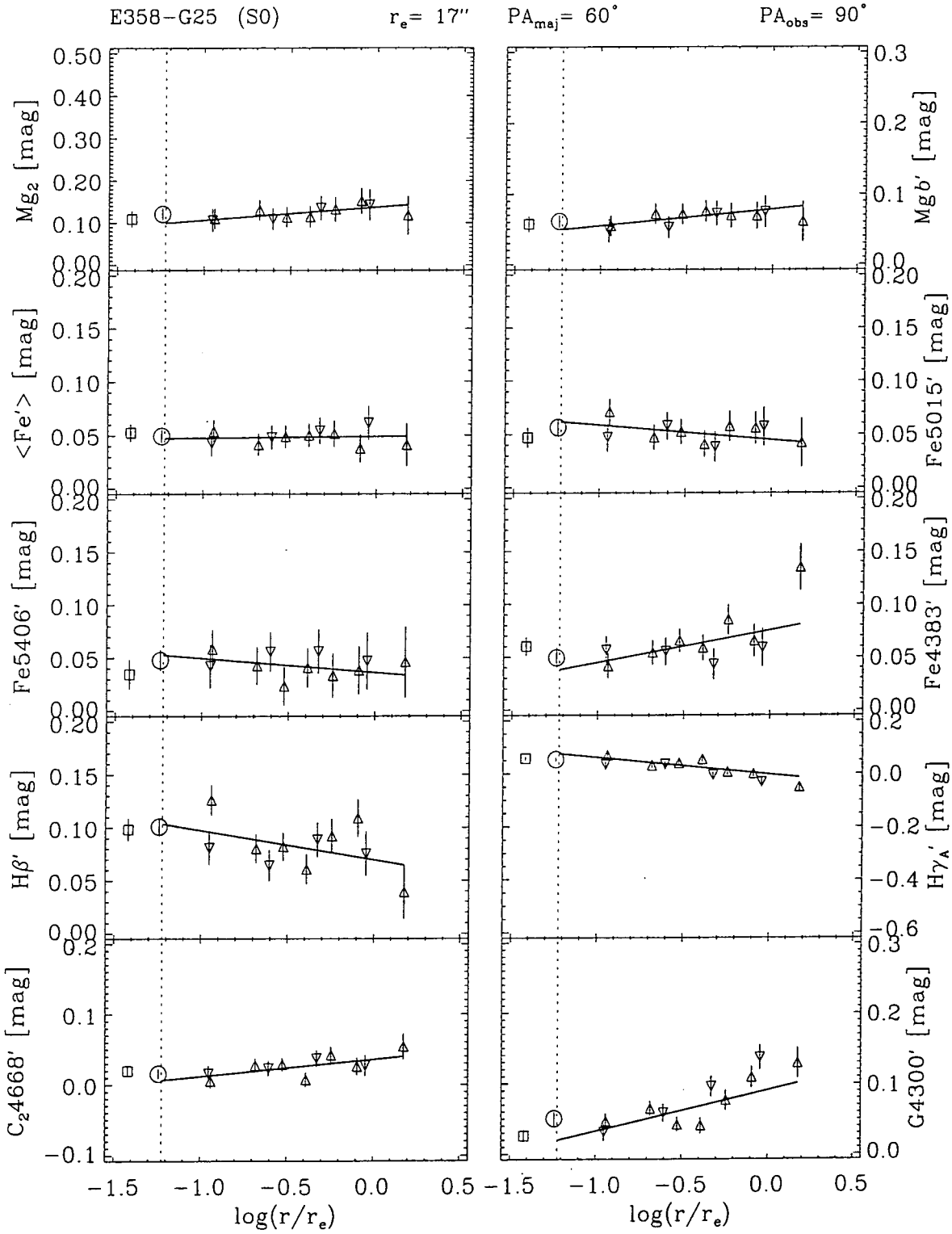

Figure B.33: Line-Strength Gradients: E358-G25 (AAT96)

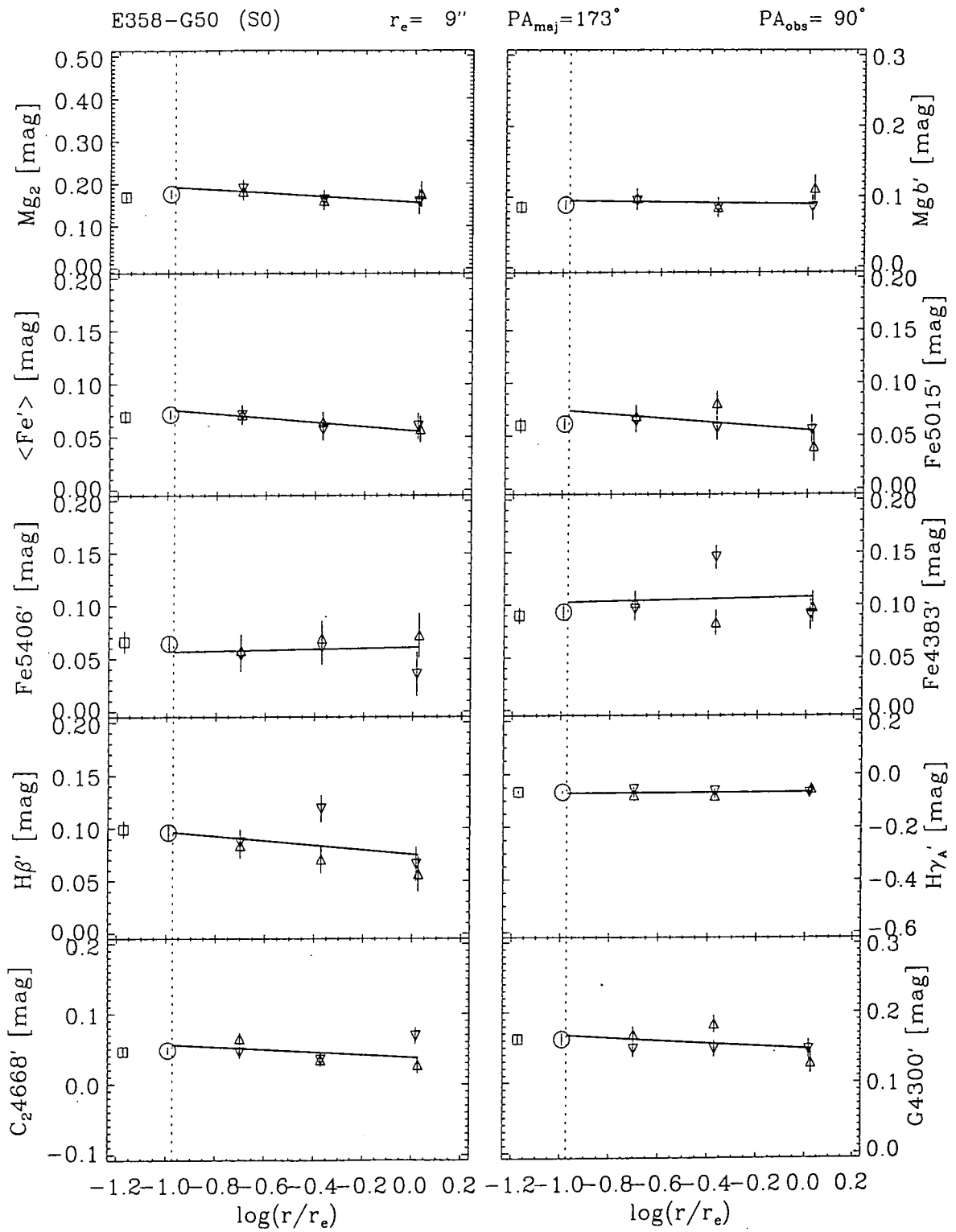

Figure B.34: Line-Strength Gradients: E358-G50 (AAT96)

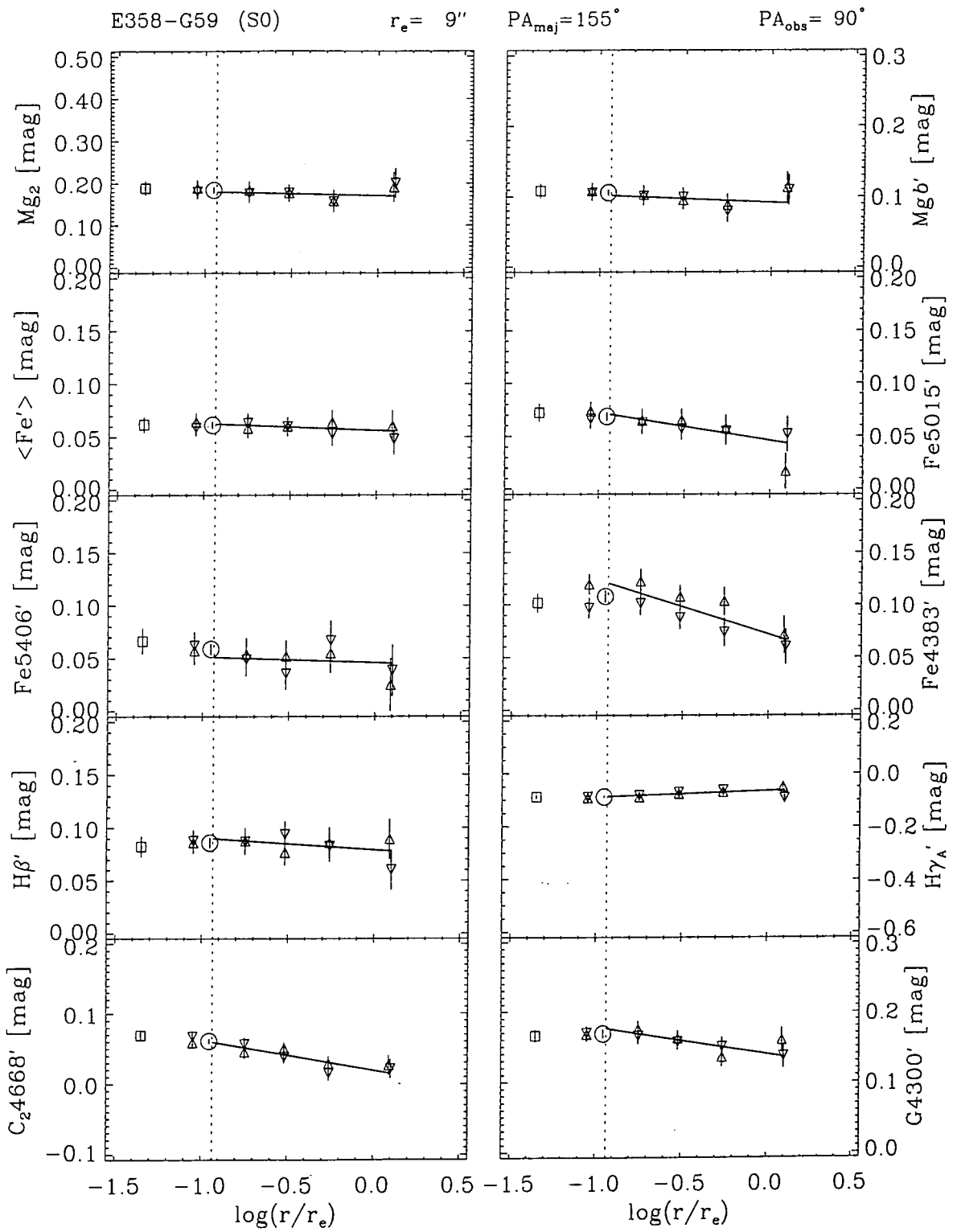

Figure B.35: Line-Strength Gradients: E358-G59 (AAT96)

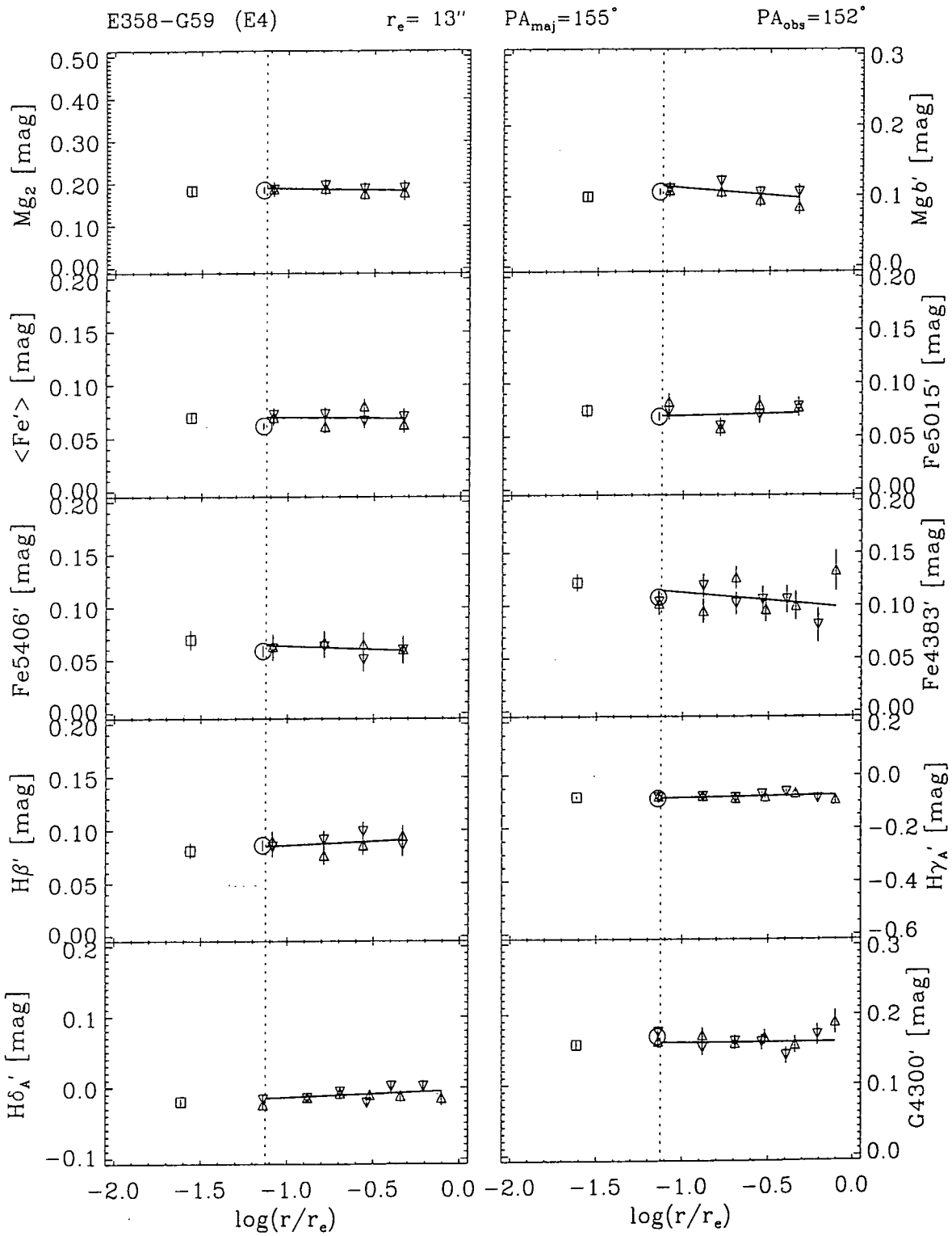

Figure B.36: Line-Strength Gradients: ESO358-G59 (NTT92)

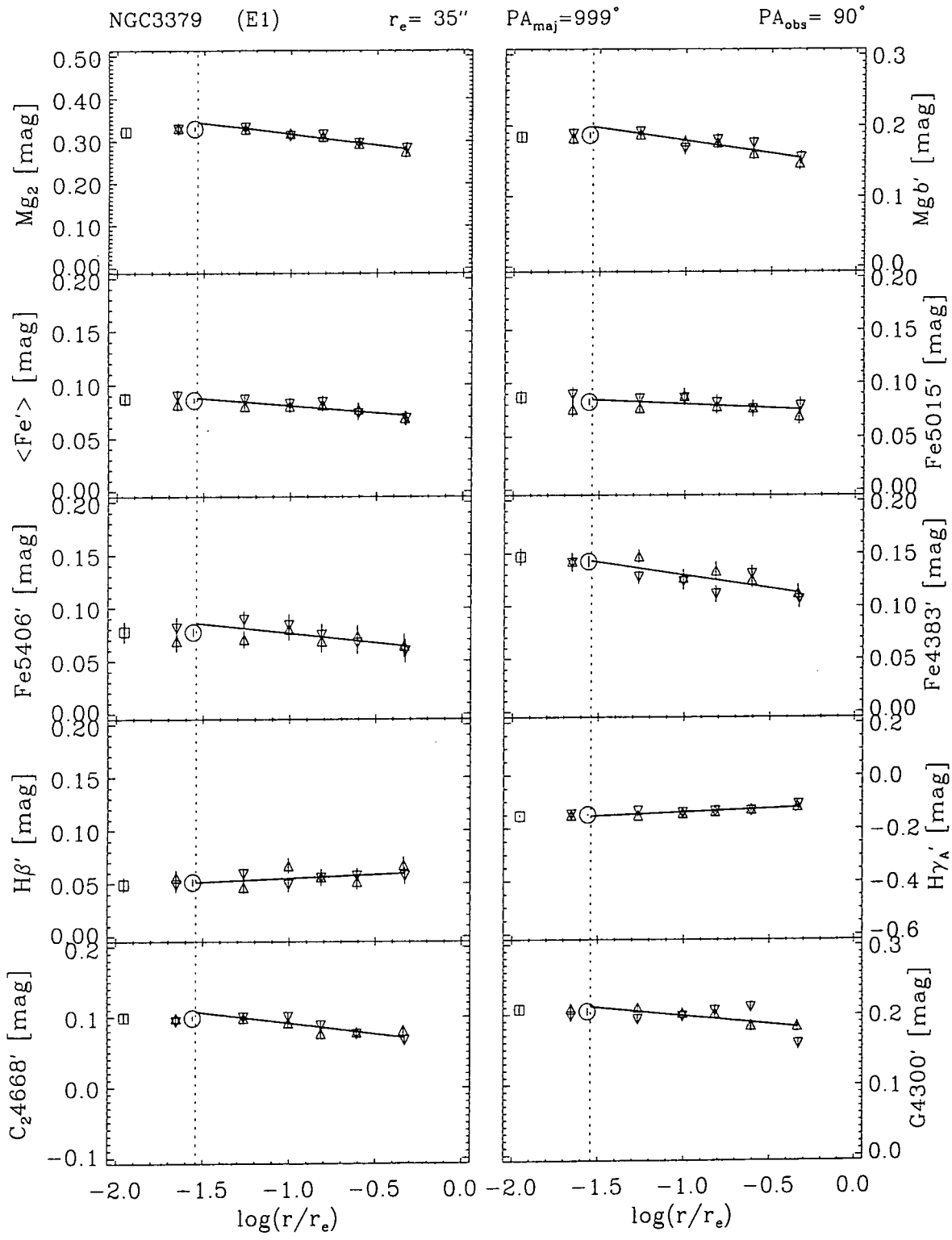

Figure B.37: Line-Strength Gradients: NGC3379 (AAT96)